Emergence of nuclear collectivity in Cd and Te isotopes from $M1$ and $E2$ observables

B. J. Coombes

A thesis submitted for the degree of
Doctor of Philosophy
The Australian National University

July 2022

Preface

This thesis presents results and interpretation of g-factor and Coulomb-excitation measurements in the Z=50 region for the purpose of investigation of the onset and nature of nuclear collectivity. The project was proposed by Prof. A. E. Stuchbery.

Coulomb-excitation measurements on the odd-mass Cd isotopes were performed using Cd beams from the 14UD Pelletron accelerator to bombard a ^{nat}C target. The accelerator was operated by the Nuclear Structure research group at the Department of Nuclear Physics and Accelerator Applications at the Australian National University with support from technical staff. The measurements made use of the hyperfine spectrometer and a Pixie16 data acquisition system. Data acquisition and processing were performed with codes developed by Drs. M. S. M. Gerathy and T. J. Gray. Analysis was performed using the CERN ROOT analysis framework and the GOSIA semiclassical Coulomb excitation code. A shell-model calculation of states in ^{111}Cd used for comparison to experimental results was provided by Dr. A. Blazhev.

Multi-step Coulomb excitation data from ^{111}Cd beam excitation on a ^{nat}Pb target were made available for analysis by Dr. J. M. Allmond. These data were taken by Dr. Allmond, Prof. A. E. Stuchbery, and a wider collaboration at the CARIBU-ATLAS facility as calibration of contaminant lines in a Coulomb-excitation measurement on ^{106}Mo. The measurements made use of GRETINA-CHICO2, a High Purity Germanium tracking array (GRETINA) and a position-sensitive parallel-plate avalanche counter (CHICO2). Analysis of these data was performed using the CERN ROOT analysis framework and a variety of codes written or adapted by the author.

The particle-vibration-model and Nilsson-model codes used in the discussion of the Cd isotopes were developed by Prof. Stuchbery.

Transient-field g-factor measurements of 4_1^+ states in $^{124-130}$Te were performed at the Australian National University Heavy Ion Accelerator Facility using the hyperfine spectrometer. The isotopically enriched, three-layer targets used in the measurement were prepared by Dr. G. Georgiev and Prof. A. E. Stuchbery. As with the single-step Coulomb excitation measurements, data acquisition was performed using a Pixie16 data acquisition system and the accelerator was operated by the Nuclear Structure group with support from technical staff. Detection of γ rays was performed with clover detectors from the CLARION array, provided and managed by Dr. J. M. Allmond. Data analysis was performed using the CERN ROOT analysis framework, and using a variety of codes, some written by the author, others written by Prof. Stuchbery, Dr. McCormick, and Dr. Gray and adapted by the author. Doppler-shift attenuation method measurements of lifetimes of states with these data were performed using codes based on the LINESHAPE program largely rewritten by the author.

The data used in the Coulomb excitation analysis of the Te isotopes were made available by Dr. Allmond. These data are from the Holifield Radioactive Ion Beam Facility of Oak Ridge National Laboratory, and were taken as calibration data for a recoil-in-vacuum g-factor measurement with Prof. Stuchbery as the spokesperson. Detection of γ rays made use of High Purity Germanium clover detectors. Particle detection used the HyBall array of CsI detectors. Analysis of these data was performed using codes written by Dr. Allmond and adapted by the author. The Coulomb-excitation analysis was performed using the GOSIA semiclassical Coulomb-excitation code.

Shell-model calculations of the Te isotopes using the jj55pn interaction were performed by the author, Prof. Stuchbery, and Dr. Gerathy. Development of the codes used in the analysis of the results of the shell-model calculations to evaluate Kumar-Cline sum rules was carried out by the author and Dr. Gray. The shell-model calculations performed using the ANTOINE code were provided by Dr. A. Gargano.

Data and analysis presented in this thesis has contributed to the following publications and conference proceedings:

- B. J. Coombes, A. E. Stuchbery, J. M. Allmond, A. Gargano, J. T. H. Dowie, G. Georgiev, M. S. M. Gerathy, T. J. Gray, T. Kibédi, G. J. Lane, B. P. McCormick, A. J. Mitchell, N. J. Spinks and B. P. E. Tee, "Emerging nuclear collectivity in $^{124-130}$Te", *EPJ Web of Conferences* **232**, 04003 (2020)

- B. J. Coombes, A. E. Stuchbery, A. Blazhev, H. Grawe, M. W. Reed, A. Akber, J. T. H. Dowie, M. S. M. Gerathy, T. J. Gray, T. Kibédi, A. J. Mitchell, and T. Palazzo, "Spectroscopy and excited-state g factors in weakly collective ^{111}Cd: Confronting collective and microscopic models", *Phys. Rev. C* **100**, 024322 (2019)

Further papers that have been coauthored:

- T. J. Gray, A. E. Stuchbery, M. W. Reed, A. Akber, B. J. Coombes, J. T. H. Dowie, T. K. Eriksen, M. S. M. Gerathy, T. Kibédi, G. J. Lane, A. J. Mitchell, T. Palazzo, and T. Tornyi "Perturbed angular distributions with $LaBr_3$ detectors: The g factor of the first 10^+ state in ^{110}Cd reexamined", *Phys. Rev. C* **96**, 054332 (2017)

- A. E. Stuchbery, B. P. McCormick, T. J. Gray, and B. J. Coombes "Pushing the limits of excited-state g-factor measurements", *EPJ Web of Conferences* **178**, 02005 (2018)

- B. P. McCormick, A. E. Stuchbery, B. A. Brown, G. Georgiev, B. J. Coombes, T. J. Gray, M. S. M. Gerathy, G. J. Lane, T. Kibédi, A. J. Mitchell, M. W. Reed, A. Akber, L. J. Bignell, J. T. H. Dowie, T. K. Eriksen, S. Hota, N. Palalani, and T. Tornyi, "First-excited state g factors in the stable, even Ge and Se isotopes", *Phys. Rev. C* **100**, 044317 (2019)

- T. J. Gray, A. E. Stuchbery, B. J. Coombes, J. T. H. Dowie, M. S. M. Gerathy, T. Kibédi, G. J. Lane, B. P. McCormick, A. J. Mitchell, and M. W. Reed, "Hyperfine fields at ^{66}Ga, ^{67,69}Ge implanted into iron and gadolinium hosts at 6 K, and applications to g-factor measurements", *Phys. Rev. C* **101**, 054302 (2020)

- M. S. M. Gerathy, G. J. Lane, A. E. Stuchbery, G. D. Dracoulis, T. Kibédi, A. Akber, L. J. Bignell, B. J. Coombes, J. T. H. Dowie, T. J. Gray, B. Q. Lee, B. P. McCormick, A. J. Mitchell, and N. Palalani, "γ-ray and conversion-electron spectroscopy of the high-spin isomer in ^{145}Sm", *Phys. Rev. C* **102**, 044319 (2020)

- M. S. M. Gerathy, G. J. Lane, G. D. Dracoulis, P. Nieminen, T. Kibédi, M. W. Reed, A. Akber, B. J. Coombes, M. Dasgupta, J. T. H. Dowie, T. J. Gray, D. J. Hinde, B. Q. Lee, A. J. Mitchell, T. Palazzo, A. E. Stuchbery, L. Whichello, and A. M. Wright, "Solenogam: A new detector array for γ-ray and conversion-electron spectroscopy of long-lived states in fusion-evaporation products", *Nucl. Instrum. Methods Phys. Res. A* **953**, 163136 (2020)

- T. K. Eriksen, T. Kibédi, M. W. Reed, A. E. Stuchbery, K. J. Cook, A. Akber, B. Alshahrani, A. A. Avaa, K. Banerjee, A. C. Berriman, L. T. Bezzina, L. Bignell, J. Buete, I. P. Carter, B. J. Coombes, J. T. H. Dowie, M. Dasgupta, L. J. Evitts, A. B. Garnsworthy, M. S. M. Gerathy, T. J. Gray, D. J. Hinde, T. H. Hoang, S. S. Hota, E. Ideguchi, P. Jones, G. J. Lane, B. P. McCormick, A. J. Mitchell, N. Palalani, T. Palazzo, M. Ripper, E. C. Simpson, J. Smallcombe, B. M. A. Swinton-Bland, T. Tanaka, T. G. Tornyi, and M. O. de Vries, "Improved precision on the experimental $E0$ decay branching ratio of the Hoyle state", *Phys. Rev. C* **102**, 024320 (2020)

- J. T. H. Dowie, T. Kibédi, A. E. Stuchbery, A. Akber, A. Avaa, L. J. Bignell, M. V. Chisapi, B. J. Coombes, T. K. Eriksen, M. S. M. Gerathy, T. J. Gray, T. H. Hoang, E. Ideguchi, P. Jones, M. Kumar Raju, G. J. Lane, B. P. McCormick, A. J. Mitchell, and B. P. E. Tee, "Evidence for shape coexistence in ^{52}Cr through conversion-electron and pair-conversion spectroscopy", *EPJ Web of Conferences* **232**, 04004 (2020)

- J. T. H. Dowie, T. Kibédi, D. G. Jenkins, A. E. Stuchbery, A. Akber, H. A. Alshammari, N. Aoi, A. Avaa, L. J. Bignell, M. V. Chisapi, B. J. Coombes, T. K. Eriksen, M. S. M. Gerathy, T. J. Gray, T. H. Hoang, E. Ideguchi, P. Jones, M. Kumar Raju, G. J. Lane, B. P. McCormick, L. J. McKie, A. J. Mitchell, N. J. Spinks, and B. P. E. Tee, "Evidence for shape coexistence and superdeformation in ^{24}Mg", *Phys. Lett. B* **811**, 135855 (2020)

Except where otherwise indicated, this thesis is my own original work, and has not been submitted in whole or in part for a degree at any university.

B. J. Coombes
13 July 2022

Acknowledgments

I would like to thank my supervisor, Andrew Stuchbery, for his consistent support and positivity, and for the insight he never fails to give.

Thanks, also, to my other two supervisors Tibor Kibédi and Greg Lane for their help in developing my knowledge and skills in nuclear physics, and for always being happy to help. My appreciation also goes to A.J. Mitchell for always checking in on me, and for his wisdom.

My sincerest gratitude to Mitch Allmond for not only providing the detectors used for the g-factor measurements, travelling to Australia to help set up the experiment, and giving help with analysis, but also for providing two extra data sets to analyse. Thanks to Georgi Georgiev and Brendan McCormick for aid in preparing for each experiment and to Georgi for his help in target preparation.

To Angelina Gargano and Andrey Blazhev, the shell-model calculations you have provided have been fascinating and your support in exploring them has been invaluable. Thank you.

My eternal appreciation to the technical staff who kept my experiments running, in particular to Peter Linardakis and Nikolai Lobanov who went above and beyond when everything started to fail in the nightmare run.

Thanks to Matthew Gerathy and Tim Gray for their help with the data acquisition and processing, and more broadly to the students of the Department of Nuclear Physics for interesting and helpful discussions of physics and analysis.

To my parents, I could never have achieved anything in life without the opportunities you have given me, and the love you've shown. Finally, to friends and family, my appreciation of your support knows no bounds.

Abstract

This thesis describes measurements of $M1$ and $E2$ observables near Z=50 and toward ^{132}Sn. Coulomb-excitation measurements of odd-mass Cd isotopes are reported with transition strengths for the low-lying states in agreement with previous measurements. Measurements were performed in inverse kinematics with Cd beams impinged on a C target. A multi-step Coulomb-excitation measurement of ^{111}Cd is described with a ^{111}Cd beam on a ^{nat}Pb target using the GRETINA and CHICO2 arrays. The observed level scheme is reported with a discussion of the nature of states. A new state is tentatively proposed and several new transitions are observed. Measured transition strengths are compared to shell-model calculations with good agreement found. Comparison is made of the low-lying structure of the Cd isotopes to the particle-vibration model with poor agreement found. Consistent with previous work, we suggest that the vibrational explanation of collective states in the Cd isotopes is insufficient. A qualitative comparison of results to the particle-rotor model is then given. Neither the particle-vibration nor the particle-rotor model is seen to give specific, accurate descriptions of these weakly collective nuclides.

Transient-field g-factor measurements on the 4_1^+ states in even-even $^{124-130}$Te are reported for the first time. Measurements were made with ^{58}Ni beams on enriched Te targets for each measured isotope. The ratio of g factors of the 4_1^+ and 2_1^+ states is seen to converge to unity away from the shell closure. The measured g factors are compared to shell-model calculations, and the observed trends are in agreement with shell-model predictions. The reported shell-model calculations show the importance of angular-momentum sharing between protons and neutrons in the development of collectivity.

Inverse-kinematics, multi-step Coulomb-excitation measurements of ^{124,126,130}Te beams on an enriched ^{50}Ti target are reported. Transition strengths for states above the 2_1^+ state are obtained to higher precision than in previous measurements in several cases, and the $4_1^+ \rightarrow 2_1^+$ transition strength in ^{130}Te measured for the first time.

Finally, a discussion of developing collectivity in the ^{132}Sn region is made with reference to shell-model calculations for both the Cd and Te measurements. The pathway to nuclear collectivity is described with nuclear deformation and triaxiality shape invariants calculated using the Kumar-Cline sum rules based on shell-model-calculated $E2$ matrix elements. Triaxiality is predicted to be an important feature of low-excitation states in the Te isotopes. Deformation of states is also seen to be smaller in higher-spin states than in lower-spin states. A suggestion is made that collectivity builds from low-excitation, low-spin states toward high-spin states.

Contents

List of Figures

List of Tables

Chapter 1

Introduction

1.1 Introduction

Collective descriptions of nuclear structure have been shown to be important in understanding most known nuclei, with the exception of spherical nuclei near doubly magic shell gaps. The exact nature of that collectivity has, however, been difficult to describe completely in the transitional regions between spherical and well-deformed nuclei. The investigation of patterns in level schemes, including energy, spin and parity, has been shown to be insufficient to isolate and characterise collective degrees of freedom. It is therefore essential to investigate electromagnetic properties, nuclear moments and transition rates for an accurate understanding of the fundamental nature of the observed structures. Modern investigations of nuclear structure are moving more towards investigation of electric-quadrupole ($E2$) transition strengths and moments. These $E2$ observables are important as low-lying collectivity is generally expressed in the quadrupole degrees of freedom. In contrast, the $M1$ moments are less well studied despite being sensitive to the underlying single-particle structure of the nuclear state. The $M1$ moments are therefore useful in tracking the development of collectivity from the seniority structures near shell closures toward clear rotational band structures in deformed nuclei. The emergence of this low-lying collectivity has not been extensively studied from the view points of both $E2$ and $M1$ observables together. This thesis will investigate the development and features of low-lying collective states in weakly-collective nuclei near the ^{132}Sn region through both $E2$ and $M1$ observables. Viewed on the nuclear chart, the nuclei studied are broadly 'west' of ^{132}Sn.

1.2 Thesis Outline

This thesis has ten chapters. Following this brief introductory chapter, Chapter 2 contains information on the research landscape that has led to the present work. The experimental techniques used in this thesis are discussed in Chapter 3. The measurements and results of Coulomb excitation measurements on the Cd isotopes are presented in Chapters 4-5 with a discussion of the observed structures in Chapter 6. Transient-field g-factor and Coulomb excitation measurements for the Te isotopes

are presented in Chapters 7-8 and discussed in Chapter 9. Finally, conclusions are presented in Chapter 10.

Chapter 2

Background and Related Work

The study of nuclear structure is often split into two separate regions: (i) spherical nuclides near closed shells with properties determined by the couplings of a few valence nucleons; and (ii) collective nuclides in which properties are largely determined by the coherent motion of many nucleons. Collective motion has traditionally been characterised as either rotations of a deformed system, or surface vibrations of spherical or deformed systems. However, exploration of the transitional regions between these two limits is also important. Recent improvements in the ability to perform microscopic calculations in larger model spaces has allowed the comparison of collective models and microscopic models in some weakly collective nuclides. This allows microscopic investigation of the origin of collective degrees of freedom. The Cd and Te nuclides investigated in this thesis lie between the spherical and deformed regions and so are ideal for investigations of the onset of collectivity and the nature of weakly collective structures. The key questions are: "How does collectivity emerge from the underlying nucleonic motion?", and "What is the nature of weakly collective nuclei?".

2.1 The nuclear shell model

2.1.1 Nuclear shells

A common basic approach to nuclear structure is to model the nucleus with a mean-field theory. The mean field, or average potential experienced by a nucleon, is the result of the combined long-range Coulomb forces and the short-range nuclear forces among the remaining nucleons. The calculations performed in these models and the resulting single-nucleon orbits in the mean field form the language used to describe the structure of nuclei. The mean field may be calculated microscopically using a Hartree-Fock type of approach, or may be parameterised more empirically, e.g. by a modified oscillator potential (the Nilsson model) or by the Woods-Saxon potential. An example set of single-particle energies in a Woods-Saxon potential with spin-orbit interactions is displayed in Fig. 2.1. At this level, the model does not provide sufficient detail for the explanation of most nuclear structure measurements, however it does give a basis from which to build more sophisticated models such as large-scale

shell-model calculations. It also allows simple predictions of basic nuclear structure properties in spherical nuclei near shell closures. Nuclei at shell closures, known as 'magic', have numbers of protons or neutrons equal to 2, 8, 20, 28, 50, 82, and 126 in stable systems. The shell structure, and hence the magic numbers, may evolve in exotic nuclei with extreme proton to neutron ratios. Odd-mass nuclides near shell closures often have properties that can be ascribed to a single unpaired nucleon. The nuclides discussed in this thesis lie near the Z=50 proton shell closure and below the N=82 neutron shell closure.

2.1.2 Large-scale shell-model calculations

Large-scale shell-model calculations begin with the single particle energies associated with occupation of the orbits in the mean-field potential. The configuration mixing due to two-body residual interactions between nucleons is then evaluated. Large-scale shell-model calculations have proven to be the most successful approach to calculate properties of nuclear states in nuclides near double-shell closures. In large-scale shell-model calculations, the possible particle configurations that can result in a given spin and parity in a large basis space, typically including all orbits in the major shell for both protons and neutrons, are allowed to mix in order to find the energies of states of that spin and parity. The configuration energies are often derived from modified nucleon-nucleon interactions using effective field theory. Experimentally derived single-particle energies can be used in shell-model calculations and may be obtained from energies of particle-like states in nuclides with a particle or hole added to the core.

Several approaches exist to obtain nucleon-nucleon interaction matrix elements for shell-model Hamiltonians. A common approach for determining two-body matrix elements is to start with the CD-Bonn potential [2], remove the repulsive core, use effective field theory to determine the residual nucleon-nucleon interactions, and possibly also fine-tune parameters to best reproduce known nuclear structure in a region. This was the approach for the interactions used in this thesis.

Ideally, these shell-model calculations would be possible without any restrictions on the possible configurations and hence could be applied across the nuclear chart. However, the configuration space required for the calculations increases combinatorially with the number of valence nucleons. In order to reduce the size of these calculations it is necessary to restrict the configuration space. The most natural way to restrict the configuration space is to only consider nucleons in specific nuclear shells. The large quantity of energy required to excite a nucleon over a shell gap restricts the population of configurations that include such excitations, and suggests removing such excitations from the configuration space as a viable truncation procedure. This is particularly effective for nuclei near closed shells. In such cases, the configurations that require excitations across a shell gap do not generally experience a strong reduction in energy from correlations and as such have little effect on the final calculated states. N=Z doubly magic nuclei like ^{16}O and ^{40}Ca have deformed multiparticle-multihole excited states at low energy, but this feature is not experi-

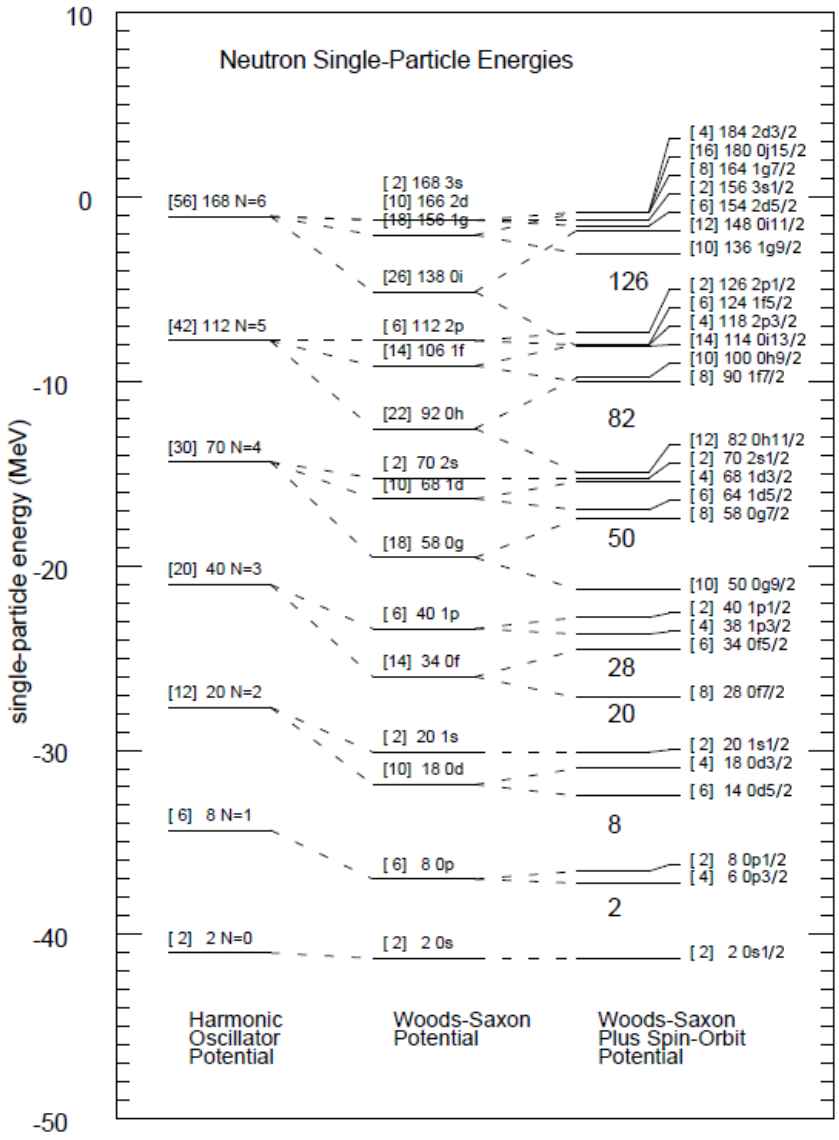

Figure 2.1: Single-particle energies as calculated by the nuclear shell model assuming a Woods-Saxon potential with spin-orbit interactions. Values in square brackets denote the degeneracies. Figure modified from Ref. [1].

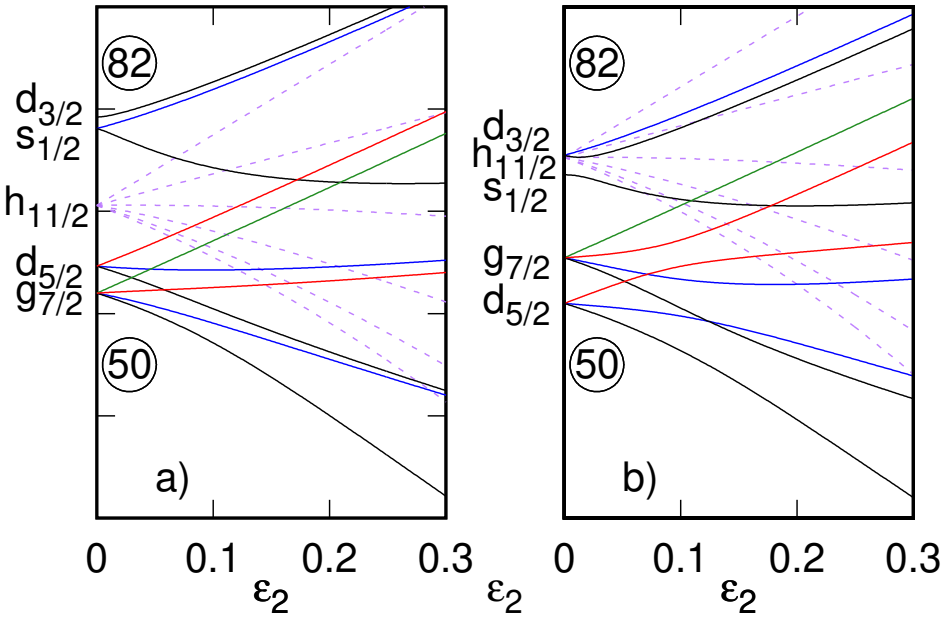

Figure 2.2: Nilsson orbits at prolate deformations are shown for the energy regions between the shell closures at 50 and 82 nucleons. Nilsson schemes for protons and neutrons are shown in panels a) and b), respectively. Nilsson orbits of positive parity and spin projection, Ω, of $1/2$ are displayed in black, $3/2$ are in blue, $5/2$ are in red, $7/2$ are in green. Negative parity states are shown in purple dashed lines.

mentally observed in ^{132}Sn and other doubly magic nuclei with $N \neq Z$.

2.1.3 Deformation and Nilsson schemes

In most nuclei the assumption of sphericity is not valid. In order to account for deformation and to extend calculations further from closed shells, the nuclear shell model has been extended to axially symmetric deformed shapes through the Nilsson model [3] and also more generally to triaxially deformed nuclei [4], that is structures associated with three independent symmetry axes rather than axial symmetry. In the Nilsson model, the energies of the angular-momentum substates in a nuclear orbit are no longer degenerate. This splits the spherical shell model j-states into $(2j+1)/2$ orbits with different projections onto the nuclear symmetry axis. The effect of deformation on the energies of the Nilsson orbits is tracked in Nilsson schemes such as those displayed in Fig. 2.2. Even small deformations can have significant impact on the nuclear structure. The changes in properties of the Nilsson orbits as deformation increases can be discussed in terms of the mixing of different spherical shell-model configurations. Deformation and the Bohr-model deformation parameters are discussed further in Sec. 2.4.1.

Nilsson orbits are specified in the form $\Omega[Nn_z\Lambda]$, where Ω is the projection of the angular momentum on to the symmetry axis, N is the major shell principal

quantum number, n_z is the number of oscillator quanta in the z-direction, and Λ is the projection of the orbital angular momentum onto the symmetry axis, $\Omega=\Lambda \pm 1/2$.

The Nilsson model is a remarkably successful model, used to describe a large range of odd-A deformed nuclides. The model predicts many of the observed properties of single-particle states in well-deformed regions and is the basis of the particle-rotor model, another highly successful model.

2.1.3.1 Triaxial projected shell model

As the number of valence nucleons increases, the model space required for shell-model calculations increases beyond what is possible using current computational techniques. In order to perform shell-model type calculations in deformed regions the projected shell model (PSM) was developed [4]. This approach uses Nilsson model basis states and reduces the number of valence nucleons considered. It has been seen to be highly successful in reproducing phenomena observed in strongly deformed regions. In recent years this approach has been extended to regions which do not exhibit strong, static deformation. Transitional nuclei are often found to have triaxiality [5]. The triaxial projected shell model was developed to describe such nuclei and uses basis states from the triaxial Nilsson potential.

Lower-mass isotopes of Te have been explored in triaxial projected shell model calculations [6] with triaxiality in the calculations chosen to reproduce the energies of the excited 2_2^+ states. The resulting energy levels are in excellent agreement with experimental levels. Unfortunately, electromagnetic properties were not included in that study.

However, relying solely on comparisons of energy spectra can be misleading as noted in the study of Garrett *et. al* [7] which casts doubt on vibrational interpretations of the Cd isotopes. In this thesis we will go beyond excited-state energies to investigate the onset of collectivity and the nature of weak collectivity through $M1$ and $E2$ observables.

2.2 Kumar-Cline sum rules

It is possible to explore the deformation, triaxiality, and γ softness of a nucleus in a model independent manner through the Kumar-Cline sum rules [8]. In this formulation the $E2$ tensor is coupled to itself to obtain a spin-zero rotationally invariant spherical tensor. Rotated into the intrinsic frame (instantaneous principal axis frame) of the nucleus, these rotational invariants can be related to a quadrupole moment parameter Q related to the deformation parameter β, and a shape parameter δ that can be related to the Bohr model axial symmetry parameter γ. The deformation parameter β determines the deformation along the symmetry axis. The parameter γ determines the shape in the plane perpendicular to the symmetry axis and specifies triaxiality.

The relation between the quadrupole moments and the quadrupole tensors is given below. Quadrupole operators are denoted $E2$; multiple tensors are coupled to

the angular momentum values in the superscript. To aid clarity, braces {} and square brackets [] are both used to indicate angular momentum coupling

$$\{E2 \times E2\}^0 = \frac{1}{\sqrt{5}} Q^2 \tag{2.1}$$

$$\{[E2 \times E2]^2 \times E2\}^0 = -\frac{\sqrt{2}}{35} Q^3 \cos 3\delta \tag{2.2}$$

$$\{[E2 \times E2]^0 [E2 \times E2]^0\}^0 = \frac{1}{5} Q^4 \tag{2.3}$$

$$\{[E2 \times E2]^0 [(E2 \times E2)^2 \times E2]^0\}^0 = -\sqrt{\frac{2}{175}} Q^5 \cos 3\delta \tag{2.4}$$

$$\{[E2 \times E2]^0 [E2 \times E2]^0 [E2 \times E2]^0\}^0 = \sqrt{\frac{1}{125}} Q^6 \tag{2.5}$$

$$\{[(E2 \times E2)^2 \times E2]^0 [E2 \times (E2 \times E2)^2]^0\}^0 = \frac{2}{35} Q^6 \cos^2 3\delta \tag{2.6}$$

The expectation value of the quadrupole invariants can be determined for a state s by introducing a sum over a complete set of intermediate states r, if the magnitude and sign of the relevant matrix elements are known. For example [9],

$$\langle s|[E2 \times E2]^0|s\rangle = \frac{(-1)^{2s}}{\sqrt{2s+1}} \sum_r \langle s||E2||r\rangle \langle r||E2||s\rangle \begin{Bmatrix} 2 & 2 & 0 \\ s & s & r \end{Bmatrix}, \tag{2.7}$$

$$\begin{aligned} &\langle s|[(E2 \times E2)^2 \times E2]^0|s\rangle = \\ &(-1)^{3s+t} \sqrt{\frac{5}{2s+1}} \sum_{rt} \langle s||E2||r\rangle \langle r||E2||t\rangle \langle t||E2||s\rangle \begin{Bmatrix} 2 & 2 & 0 \\ s & s & r \end{Bmatrix} \begin{Bmatrix} 2 & 2 & 2 \\ t & s & r \end{Bmatrix}, \end{aligned} \tag{2.8}$$

where s is the state being investigated, the sums over the set of coupled states r and t account for all available $E2$ transitions, and the terms in the braces are Wigner 6j-symbols.

While the matrix elements of all states in a nucleus cannot be measured, the matrix elements connecting the low-energy and high-energy states are small and have a smaller effect on the sums. The larger matrix elements connecting the lower-energy states can be measured through Coulomb excitation. Cline notes that a significant portion of the $E2$ strength can be found in the giant electric quadrupole resonance, particularly near closed shells, and that it has been found that in nuclei that can be considered collective >70% of the $E2$ strength is in the low-lying states [8]. It is noted in the same study that most collective models assume only a low-frequency collective mode (not including the high-frequency collectivity in the giant quadrupole resonance). In this case it is proper to only include the terms from matrix elements

between the low-energy states. In the present work, due to the proximity to shell closures, care must be taken to ensure that the Kumar-Cline sums calculated have converged.

While the Kumar-Cline sum rules are used to obtain information about the charge distributions of the states of the nucleus, they do not give information about the overall shape of these nuclear states. If the nucleus is assumed to be an ellipsoidal deformed nucleus, the shape parameters obtained through the Kumar-Cline sum rules may be used in a model-dependent way to obtain the more usual Bohr-model shape parameters (β and γ) using the formulae [9]

$$\langle Q^2 \rangle = q_0^2 \langle \beta^2 \rangle, \tag{2.9}$$

and

$$\langle Q^3 \cos 3\delta \rangle = q_0^3 \langle \beta^3 \cos 3\gamma \rangle, \tag{2.10}$$

where

$$q_0 = \frac{3}{4\pi} Z r_0^2 A^{2/3}, \tag{2.11}$$

and r_0 is the approximate radius of a nucleon, taken to be 1.2 fm. Using the same charge and mass distributions, $\cos 3\delta = \cos 3\gamma$.

2.3 Nuclear g factors

The nuclear g factor is the quantity that determines the effect of a magnetic field on a nucleus with non-zero angular momentum and is proportional to the $M1$ moment of the nuclear state, i.e.

$$g = \frac{\mu}{I}, \tag{2.12}$$

where μ is the magnitude of the magnetic dipole moment of the nucleus in units of nuclear magnetons, and I is the spin of the state in units of $\hbar$. The g factors of states corresponding to a single unpaired nucleon can be predicted from the free nucleon g factors shown in Table 2.1. There is a component due to motion of the charge (i.e. a current) associated with orbital angular momentum (ℓ) as well as a component associated with the intrinsic spin (s).

Table 2.1: Free-nucleon g factors. Data from CODATA [10].

Proton		Neutron	
ℓ	s	ℓ	s
$+1.0$	$+5.586$	0.0	-3.826

Often the free-nucleon spin g factors are quenched to $\sim 0.7 g_{\text{free}}$ in calculations of nuclear properties in order to include meson exchange and other effects, and hence to better reproduce experimental values. The total magnetic moment of a state with the g factor determined by a single nucleon is then given by the expectation of the

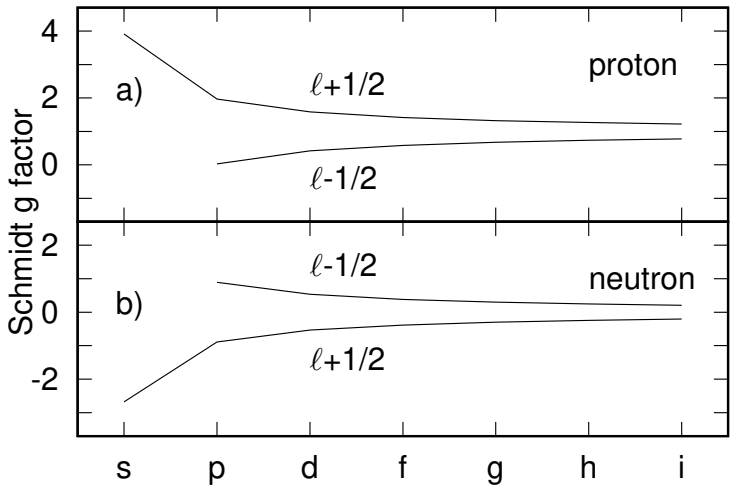

Figure 2.3: Schmidt g factors for protons and neutrons are displayed in a) and b), respectively. Spin g factors have been quenched to 0.7 of the free nucleon values.

operator

$$\hat{\mu} = \hat{\ell} g_\ell + \hat{s} g_s, \tag{2.13}$$

where $\hat{\ell}$ and $\hat{s}$ are the orbital and spin angular momentum operators of the odd nucleon, and g_ℓ and g_s are the orbital and spin g factors. Evaluation of this operator for specific orbits gives the so called "Schmidt g factors" as shown in Fig. 2.3.

The single-particle g factors can then be coupled to predict the g factors of states with multiple unpaired nucleons using the additivity relation,

$$g(I) = \frac{1}{2}(g_1 + g_2) + \frac{1}{2}(g_1 - g_2)\frac{j_1(j_1+1) - j_2(j_2+1)}{I(I+1)}, \tag{2.14}$$

where g_i and j_i are the g factor and the spin of the ith component of the coupled system with total angular momentum $I = |\vec{j_1} + \vec{j_2}|$. In the specific case when the coupled components are replaced with the orbital and spin components of an individual nucleon, i.e. g_1=g_ℓ, g_2=g_s, j_1=ℓ, and j_2=s, and the total angular momentum is given by $\vec{j} = \vec{\ell} + \vec{s}$ or equivalently j=$\ell \pm 1/2$, then we obtain the Schmidt formula.

A consequence of the additivity formula is that if a nuclear excitation has several nucleons in a single orbit, then the total g factor is equal to the g factor of the single unpaired nucleon, independent of the total spin or number of nucleons

$$g(j) = g(j^n). \tag{2.15}$$

In the case of isotopes with extra protons above the Z=50 shell closure near the N=82 shell closure, the protons enter the $g_{7/2}$ orbit. When the neutron interactions are limited, such as when the neutron shell is closed (N=82), properties of the nucleus are largely determined by the valence protons.

The measurement of g factors can be used to determine configurations for states with simple decompositions, or to determine the relative proton and neutron contributions to the state. States in which many nucleons, both protons and neutrons, contribute to an excitation tend towards a 'collective' g factor. When angular momentum is held equally amongst all nucleons in collective motion, the g factor can be approximated by assuming the charged protons contribute to the magnetic moment while the neutrons do not. If the spin components of the protons and neutrons cancel, then we obtain the hydrodynamic g factor, $g_{\text{coll}} = Z/A$. In heavy nuclei the collective g factors are usually reduced a little from this estimate, closer to $0.8Z/A$. Nuclear collectivity is discussed further in Sec. 2.5.

2.4 Transition strengths

One of the most common approaches to investigate nuclear structure beyond patterns of state energies, spins, and parities, is the measurement of γ-ray transition strengths between nuclear states. These transition strengths are generally split into the multipole components with selection rules based on the initial and final spin-parities [11]. A reduced transition strength is defined as

$$B(X\lambda; I_i \to I_f) = \frac{1}{2I_i + 1}\langle I_f||X(\lambda)||I_i\rangle^2, \tag{2.16}$$

where $X(\lambda)$ is the operator of type X, electric (E) or magnetic (M), and λ is the transition multipolarity. The transition strength can also be related to the transition probability (which depends on the inverse of the state lifetime) using the equation

$$B(X\lambda; I_i \to I_f) = \frac{\lambda[(2\lambda+1)!!]^2\hbar}{8\pi(\lambda+1)}\left(\frac{\hbar c}{E_\gamma}\right)^{2\lambda+1} P_\gamma(X\lambda; I_i \to I_f), \tag{2.17}$$

where E_γ is the energy of the transition, and P_γ is the partial transition probability for the γ-ray decay path of the given multipolarity. The partial transition probability is inversely proportional to the partial mean lifetime of the state $P_\gamma \propto 1/\tau_\gamma$. The partial transition probability is related to the total level transition probability by

$$P_\gamma(XL) = P_{\text{L}}\frac{\text{N}_\gamma}{\sum_i \text{N}_i}, \tag{2.18}$$

where $P_{\text{L}} = 1/\tau$ is the transition probability out of the state, N_γ is the number of decays through the $\gamma(XL)$ decay path and the sum includes decays from all decay paths. It is therefore possible to determine transition strengths via direct lifetime measurements. The partial lifetime for the γ-ray component of an $E2$ transition is related to the partial $E2$ lifetime by

$$\tau_{\gamma,E2} = \tau_{E2}(1 + \alpha_{E2}), \tag{2.19}$$

where α_{E2} is the $E2$ internal conversion coefficient of the transition.

Transition strengths, in particular $E2$ transition strengths, can be indicative of collectivity. The $E2$ operator is a single-particle operator, and therefore large $E2$ transition strengths are associated with multiple nucleons being involved in the transition. This increase in collectivity is more evident when strengths are expressed in single-particle or "Weisskopf" units.

Weisskopf units are approximations to the strength expected for a transition in a given nucleus if one nucleon transitions between two states [12]. The definition of a Weisskopf unit is given below:

$$B_{\mathrm{W}}(E\lambda; I_i \rightarrow I_f) = \frac{(1.2)^{2\lambda}}{4\pi}(\frac{3}{\lambda+3})^2 A^{2\lambda/3} e^2 (fm)^{2\lambda}, \tag{2.20}$$

$$B_{\mathrm{W}}(M\lambda; I_i \rightarrow I_f) = \frac{10}{\pi}(1.2)^{2(\lambda-1)}(\frac{3}{\lambda+3})^2 A^{2(\lambda-1)/3} \mu_N^2 (fm)^{2(\lambda-1)}, \tag{2.21}$$

where the conversion to Weisskopf units occurs through

$$B_{\mathrm{exp}}(X\lambda; I_i \rightarrow I_f) \text{ W.u.} = \frac{B_{\mathrm{exp}}(X\lambda; I_i \rightarrow I_f)}{B_{\mathrm{W}}(X\lambda; I_i \rightarrow I_f)}, \tag{2.22}$$

and $B_{\mathrm{exp}}(X\lambda; I_i \rightarrow I_f)$ is the experimental transition strength.

When two transition multipolarities are possible between two states, the mixing ratio squared gives the relative transition strength of each multipolarity. The mixing ratio δ is defined as [13]

$$\delta = \frac{\langle I_f || X\lambda_1 || I_i \rangle}{\langle I_f || \lambda_2 || I_i \rangle}, \tag{2.23}$$

where $\langle I_f || T(X\lambda) || I_i \rangle$ is the transition probability. For an $E2/M1$ mixed multipolarity transition (the most common mixed multipolarity transition), the partial γ-ray transition probabilities are determined by the equations

$$P_\gamma(M1) = \frac{P_{\mathrm{T}}}{1 + \alpha_{\mathrm{T}}(M1) + \delta^2(1 + \alpha_{\mathrm{T}}(E2))}, \tag{2.24}$$

$$P_\gamma(E2) = \frac{P_{\mathrm{T}}}{1 + \alpha_{\mathrm{T}}(E2) + \frac{1}{\delta^2}(1 + \alpha_{\mathrm{T}}(M1))}, \tag{2.25}$$

where $\alpha_{\mathrm{T}}(X\lambda)$ is the total internal conversion coefficient for a given transition multipolarity, and P_{T} is the partial transition probability for a transition.

Enhanced transition strengths, indicative of increased collectivity, are often seen in correlation with deformation of the nucleus.

2.4.1 Electric quadrupole moments and deformation

The electric-quadrupole moment is a measure of the charge distribution of the nucleus and is model independent. Often the deformation is discussed in a model dependent way through the Bohr-model parameters. The deformation of a rotational

ellipsoid is discussed in terms of a deformation parameter β, which can be expressed as

$$\beta = \frac{4}{3}\sqrt{\frac{\pi}{5}}\frac{\Delta R}{R_{\text{avg}}}, \tag{2.26}$$

where ΔR is the difference between the length of the semi-major and semi-minor axes, and R_{avg} is the average nuclear radius. The deformation parameter is related to the intrinsic electric-quadrupole moment Q_0 through

$$Q_0 = \frac{3}{\sqrt{5\pi}} Z R_0^2 \beta (1 + \frac{1}{8}\sqrt{\frac{5}{\pi}}\beta + \frac{1}{8}\frac{5}{\pi}\beta^2 + ...), \tag{2.27}$$

where $R_0 = r_0 A^{1/3}$ is the average radius of the nucleus. Other deformation parameters are commonly used, including β_2, δ, and ϵ. For more details and the relations between deformation parameters, see Ref. [14].

The spectroscopic electric quadrupole moment is related to the diagonal $E2$ matrix element by the equation [12]:

$$Q_S(I_i) = \frac{1}{(2I_i+1)^{1/2}} \langle I_i 2 I_i I_i | 0 I_i \rangle (\frac{16\pi}{5})^{\frac{1}{2}} \langle i || E2 || i \rangle, \tag{2.28}$$

where I_i is the spin of the state, $\langle I_i 2 I_i I_i | 0 I_i \rangle$ is a Clebsch-Gordan coefficient, and $\langle i || E2 || i \rangle$ is the reduced diagonal matrix element.

The spectroscopic electric quadrupole moment is also related to the intrinsic quadrupole moment by

$$Q_S(I_i) = Q_0(I_i) \frac{3K^2 - I_i(I_i+1)}{(2I_i+3)(I_i+1)}, \tag{2.29}$$

where K is the projection of the total angular momentum on the symmetry axis, I_i is the spin of the state, and $Q_0(I_i)$ is the intrinsic electric-quadrupole moment of the state I_i.

2.5 Collective nuclear models

Nuclei further from shell closures begin to show specific patterns in their energy levels that suggest collective motion. These patterns have traditionally been put into two categories: nuclear surface vibrations, and nuclear rotations [15]. In general, quadrupole vibrations were used to describe nuclei close to magicity. Typically, these nuclei have first-excited 2^+ state energies of several hundred keV and transition strengths of tens of Weisskopf units from the 2_1^+ state to the $0_{\text{g.s.}}^+$ ground state. Rotational motion has been used to describe highly collective states in nuclei far from magic numbers. These nuclei have first-excited 2^+ state energies of less than one hundred to a few hundred keV and can have transition strengths of up to hundreds of Weisskopf units.

As a first approximation, many nuclear excitations can be classified as being due

to rotation of an axially symmetric deformed nucleus about an axis perpendicular to the symmetry axis. Soon after the introduction of the axial rotor model it was extended to include triaxiality [16; 17]. Triaxial rotational motion has been proposed in many regions [18; 19; 20; 21; 22] and has been proffered as an alternate description of many nuclei otherwise described as vibrational or "γ soft".

2.5.1 Rotational nuclides

Even-even rotational nuclides have a low-lying 2_1^+ state between several tens of keV to a few hundred keV. There is then a sequence of states increasing in angular momentum by $\Delta I = 2$ with an energy given approximately by

$$E(I) = \frac{\hbar}{2\mathfrak{J}} I(I+1), \tag{2.30}$$

where $\mathfrak{J}$ is the moment of inertia. A typical rotational pattern is displayed in Fig. 2.4, with rotational bands built on the ground and excited states. A low-lying excited 0^+ state is often observed in rotational nuclei and interpreted as a β-vibration. A β-vibration is an oscillation of the degree of deformation along the symmetry axis [23]. On top of this second 0^+ state, another rotational band can be seen, generally with a different moment of inertia. Similarly, there is often a low-lying 2^+ state, not associated with either of the discussed rotational bands. This state has been interpreted as a γ-vibration. A γ-vibration is an oscillation in the degree of triaxiality of a nuclear shape. On top of the γ-vibration is another rotational band with spin sequence 3, 4, 5, etc. Due to reduced symmetry in the excited 2^+ state, odd-spin states are also possible in the rotational band built on the γ-vibrations. The ratio of the energy of the 4_1^+ state to the energy of the 2_1^+ state is often denoted R_{42} and is a signature used to identify the type of nuclear collectivity; for a nuclear rotation R_{42}=$\frac{10}{3}$.

The in-band $E2$ transition strengths in rigid rotational nuclei are simply related to the intrinsic quadrupole moment of the band,

$$B(E2; K, I_1 \rightarrow I_2) = \frac{5}{16\pi} e^2 Q_0^2 \langle I_1 K 20 | I_2 K \rangle^2, \tag{2.31}$$

where K is the projection of the total angular momentum on the symmetry axis, $\langle I_1 K 20 | I_2 K \rangle$ is a Clebsch-Gordan coefficient, and Q_0 is the intrinsic $E2$ moment of the band.

In an axially symmetric rotational nucleus the spectroscopic quadrupole moment of the 2_1^+ state is related to the $2_1^+ \rightarrow 0^+_{\text{g.s.}}$ transition strength as follows

$$|Q_S(2^+)| = \frac{2}{7}\sqrt{\frac{16\pi}{5} B(E2; 0^+_{\text{g.s.}} \rightarrow 2_1^+)}. \tag{2.32}$$

Not withstanding the nature of the 0^+ band for which the β vibration interpretation is disputed [24], the rotor-model has been extremely effective at describing the structure of nuclei in well-deformed regions of the nuclear chart and may be

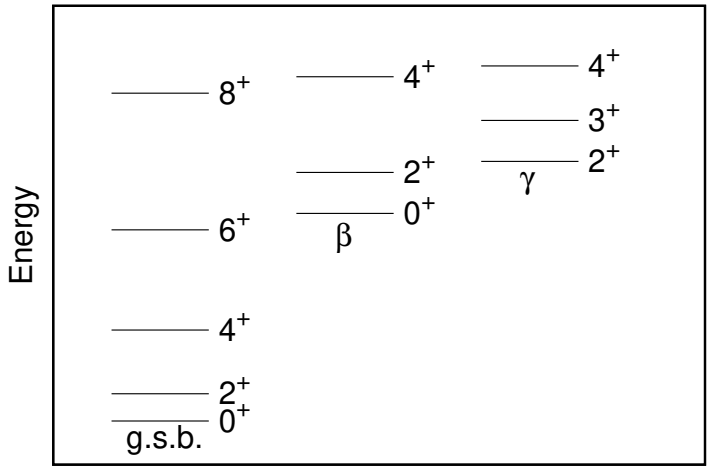

Figure 2.4: A typical rotational pattern; included are rotational bands built on the ground state, the β vibration, and the γ vibration.

considered the end point of developing collectivity. The process by which a strong deformation develops is much less well understood. In the present work we explore the development of weak collectivity in order to better understand the nature and origin of nuclear collectivity.

2.6 Weakly collective nuclides

Weakly collective nuclides are some of the least-well understood in that the interpretation of their structures remains contentious. While strongly collective well-deformed nuclei are well described by rotational models and singly or doubly magic nuclides are well described in terms of the coupling of individual valence nucleons in quite specific configurations, weakly collective nuclides have so far been resistant to simple descriptions. Several model concepts are used to describe collective motion in weakly collective nuclei. These include quadrupole vibrations, rigid-triaxial rotations, γ-soft rotations, and variable moment-of-inertia rotations. It may be that none of these collective pictures is truly applicable, especially if single-particle structures persist.

2.6.1 Quadrupole vibrations

The classical pattern observed in spherical, even-even vibrational nuclides is a low-lying 2_1^+ state with a triplet of states (0^+, 2^+, 4^+) at approximately twice the energy of the 2_1^+ state. Three-phonon states are found at triple the energy of the 2_1^+ state. For a harmonic vibration, the energy ratio of the 4_1^+ state to the 2_1^+ (R_{42}) is equal to 2, which can be used to discriminate between vibrational and rotational nuclides (R_{42}=$\frac{10}{3}$).

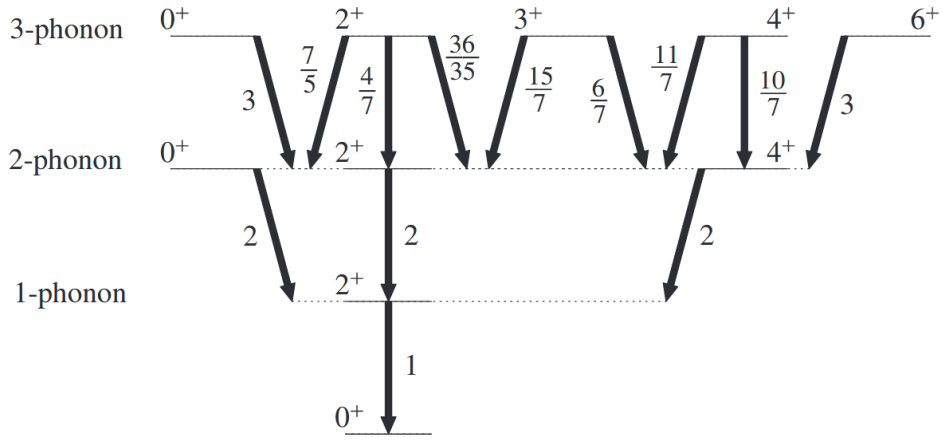

Figure 2.5: The theoretical energy level pattern for a harmonic vibrator. Transition strengths relative to the first phonon transition are shown next to transitions. Figure taken from Ref. [7].

The pattern expected for vibrational nuclides, including both the level energies and the relative $E2$ transition strengths, is displayed in Fig. 2.5. Transition strengths are given relative to the transition strength of the $2_1^+ \rightarrow 0_{\text{g.s.}}^+$ transition.

Of particular note in this harmonic-vibrator model of the nucleus is that the transitions from the highest spin state in a phonon cluster to the highest-spin state in the cluster below (what would be the ground state band in a rotational view) are expected to have transition strengths which increase linearly in phonon number; that is

$$\frac{B(E2; J = 2N \rightarrow J = 2(N-1))}{B(E2; 2_1^+ \rightarrow 0_{\text{g.s.}}^+)} = N, \tag{2.33}$$

where N is the phonon number. The transition strengths of the yrast band in harmonic vibrators and rigid axial rotors are compared in Fig. 2.6. It is worth noting that the transition strengths increase much more slowly in the rotational picture than in this vibrational picture. Transitions between states in the yrast band have been observed to have transitions strengths greater than those expected in the rotational model in several isotopes [25; 26; 27; 28].

A realistic vibration may be anharmonic and is described by perturbing the harmonic vibrator Hamiltonian by the addition of cubic and quartic terms in the phonon number. The anharmonic vibrator model can be shown to be equivalent to the U(5) symmetry of the interacting boson model [29] and has the energy relation

$$E = \epsilon n_d + \frac{1}{2}\alpha n_d(n_d - 1) + \beta(n_d - \nu)(n_d + \nu + 3) + \gamma(L(L+1) - 6n_d), \tag{2.34}$$

where n_d is the total number of d bosons, ν is the number of d bosons which are not paired to J=0, and ϵ, α, β, and γ are parameters. A spectrum calculated to reproduce the known structure of ^{110}Cd using the anharmonic-vibrator model is

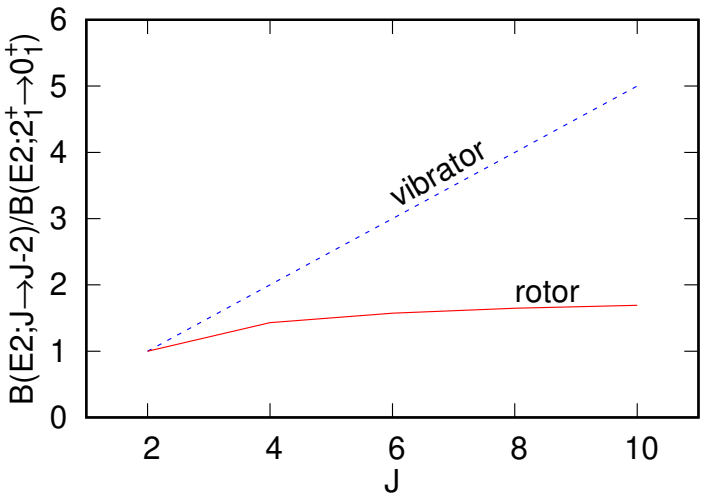

Figure 2.6: A comparison of the transition strengths between rotational states in deformed nuclei and the yrast states in spherical vibrational nuclei.

displayed in Fig. 2.7. The results are very similar to the harmonic-vibrator model, however the anharmonicities allow for the reproduction of the energy splittings of the multi-phonon states in contrast to true ideal behaviour in Fig. 2.5.

2.6.2 Particle-vibration model

The particle-vibration model is an extension of the harmonic-vibrator model that couples a single unpaired nucleon to a vibrational core [31]. The details of the core excitation such as the energy and the stiffness of the core excitation are often set to the parameters obtained from a neighbouring even-even nuclide. Coupling the unpaired nucleon in an orbit with spin j to the 2^+ core excitation leads to a multiplet of coupled states in the nucleus with spins ranging from $|j-2|$ to $j+2$.

The Hamiltonian in the particle-vibration model can be decomposed into the core Hamiltonian, the single-particle Hamiltonian, and the interaction Hamiltonian. Without the interaction between the single-particle and collective components we observe

$$(H_c + H_p)|j; NR; IM\rangle = (N\hbar\omega + E_j)|j; NR; IM\rangle, \tag{2.35}$$

where H_c is the core Hamiltonian, H_p is the unpaired particle Hamiltonian, $|j; NR; IM\rangle$ is the coupled state, N is the number of quadrupole phonons in the state, R is the core angular momentum, $\hbar\omega$ is the core excitation energy. Each of N, R, and $\hbar\omega$ are related to H_c. E_j is the energy of the single-particle excitation which is produced by H_p. I and M are the angular momentum and z-projection of the angular momentum of the coupled state.

The interaction between the core and coupled particle is then added with an

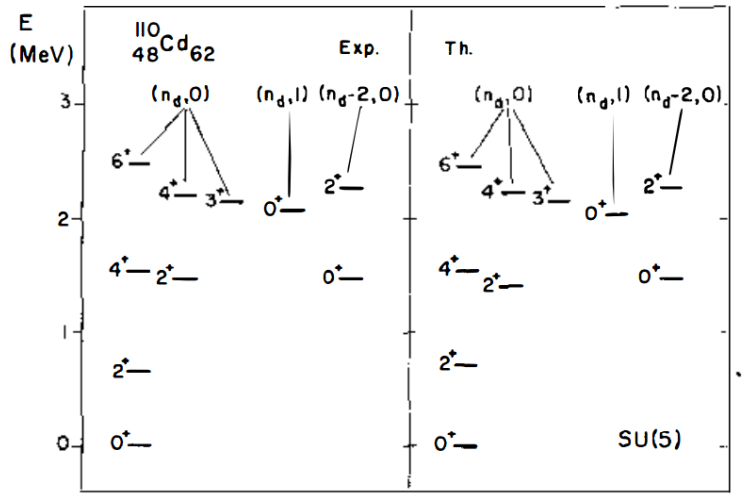

Figure 2.7: A spectrum for an anharmonic vibrator compared to the spectrum of ^{110}Cd. Figure from Ref. [30].

interaction term of the form

$$H_{\text{int}} = -\sqrt{\frac{1}{5}}\pi\xi\hbar\omega\sum_{\mu}(b_{\mu} + (-)^{\mu}b^{\dagger}_{-\mu})Y_{2\mu}(\theta,\phi), \tag{2.36}$$

where ξ is the particle-core coupling parameter, b_{μ} is the quadrupole phonon annihilation operator, and $Y_{2\mu}$ is a spherical harmonic.

As the existence of spherical vibration modes has been questioned [7], exploration of other modes of weakly collective nuclei is required.

2.6.3 Triaxial rotors

The rigid-triaxial-rotor model [17] is successful in describing a number of nuclides [32; 33; 34; 35]. Triaxial rotors are described in terms of two parameters, β and γ, which have been discussed in Section 2.1.3. As in the axial rotor model, β is the deformation parameter. The shape parameter γ determines the deviation from axial symmetry and takes values from 0° (prolate) to 60° (oblate). A spectrum calculated with the Davydov-Filippov model [17] is displayed in Fig. 2.8.

As well as the possibility of rigid triaxial rotation, another class of nuclei can be classed as γ-soft rotors [16]. In this case, the shape in the γ degree of freedom is soft; that is it does not take a rigid finite value, but can take a range of values.

A key signature of the γ-softness in triaxial nuclei is the pattern of the odd-even staggering of levels in the γ-band, defined as [36; 37; 38]

$$S(J, J-1, J-2) = \frac{(E(J) - E(J-1)) - (E(J-1) - E(J-2))}{E(2^{+}_{1})}, \tag{2.37}$$

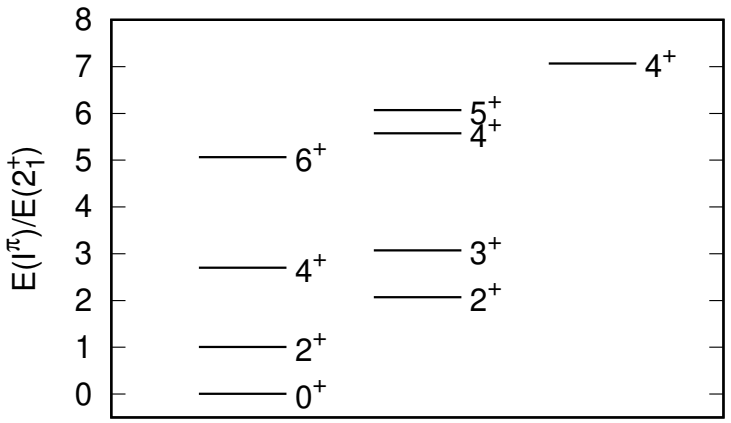

Figure 2.8: A rigid triaxial-rotor spectrum calculated using the Davydov-Filippov model [17]. The spectrum was calculated with γ=28°.

where $E(J)$ is the energy of the state J. This measure of signature splitting is often used to fix the deformation and triaxiality shape parameters for analysis of other nuclear properties.

Recent investigations of rotational nuclides with axial asymmetry in the rare earth region have determined that the Davydov-Filippov rigid triaxial rotor model is less successful than the Wilets-Jean model of γ-soft nuclei [16; 39]. In other words, γ-soft rather than γ-rigid structures appear to be more common.

2.7 Shape-coexisting intruder states

Discussions of the shape and behaviour of atomic nuclei can be complicated by the existence of multiple shapes exhibited by excited states. Excited states with different shapes from the ground state often occur via multiparticle-multihole excitation across shell gaps. Most relevant to the present study, a four-particle, two-hole excitation across the Z=50 shell gap has been identified in ^{118}Te [40]. Shape coexisting states often have a parabolic decrease in excitation energy towards the mid shell. These states fall outside of the model space in most shell-model calculations, and it must be noted that these states have a distinct structure compared with other low-lying states.

2.8 Previous studies of Cd and Te isotopes

The Cd and Te nuclides are similar in that they can be considered to have two valence protons either side of the Z=50 shell closure; the Cd isotopes have two proton holes outside of a closed Sn core while Te has two protons outside of the proton shell closure at Sn. Although the two valence particles are in different shells, when

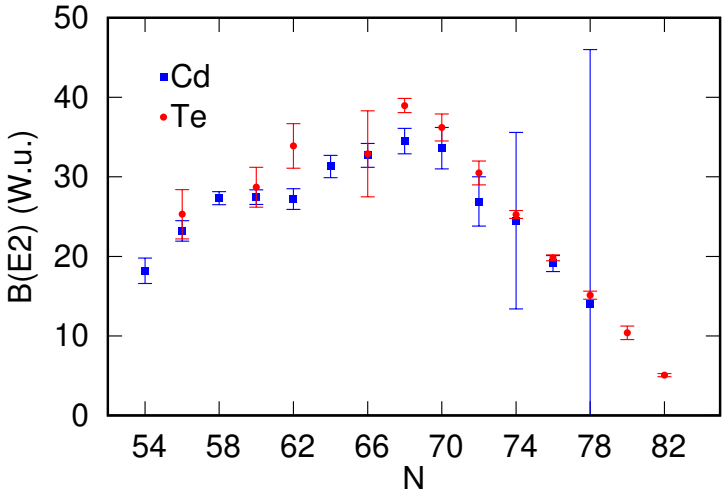

Figure 2.9: Transition strengths for the $2_1^+ \rightarrow 0_{\text{g.s.}}^+$ transitions in Cd and Te isotopes in Weisskopf units. Data obtained from the 2016 evaluation by Pritychenko *et al.* [41].

comparing the Cd and Te isotopes one might expect similar patterns to be seen, especially if collective structures emerge. The neutron model spaces in each of these species are the same, although the number of neutrons in the naturally abundant nuclei are quite different for the two elements. Previously measured $B(E2; 2_1^+ \rightarrow 0_{\text{g.s.}}^+)$ values from the 2016 evaluation by Pritychenko *et al.* [41] are given as a function of neutron number in Fig. 2.9.

Vibrational motion in the $Z = 50$ region has been extensively explored. The Cd nuclides near mid-shell in particular are often modelled as vibrational [29]. Similarly, Bucurescu *et al.* [42] found that ^{128}Te was closest to the U(5) (anharmonic vibrator) limit of the interacting boson model based on known R_{42} ratios, quadrupole moments, and transition strengths. All the Te isotopes are reasonably close to this limit.

Triaxiality has been explored experimentally and theoretically in the $Z \sim 50$ region including $^{92-110}$Mo (Z=42) [43; 44; 45; 46; 47; 22], $^{96-118}$Ru (Z=44) [47; 48; 49; 50], ^{109,115,117}Rh (Z=45) [51; 52; 53], $^{96-114}$Pd (Z=46) [20], $^{104-114}$Cd (Z=48) [54], $^{120-124}$Te (Z=52) [35], $^{128-140}$Xe (Z=54) [20], and $^{126-142}$Ba (Z=56) [55; 56; 20]. Many of these isotopes are determined to have triaxiality based on observed transition strengths, odd-even staggering in the γ-vibration band, and in a few cases, quadrupole invariants. Clearly, triaxiality is an important factor determining nuclear structure in the region near Z=50.

2.8.1 Systematics of the Te isotopes

The Te isotopes are ideal candidates for the investigation of the onset of collective motion. The heaviest naturally abundant Te isotope, ^{130}Te, has two valence protons and four neutron holes relative to the nearest doubly magic nucleus ^{132}Sn, and has been seen to maintain some single particle characteristics [57]. The lightest stable Te isotope (^{120}Te) exhibits significant collective character in that its low-excitation energy

structure appears to be vibrational. Recent advances in computational power have allowed shell-model calculations to be performed for nuclei in this region between closed shells, including for nuclei with vibration-like level structures.

The energy systematics for several low-lying states in $^{118-136}$Te are displayed in Fig. 2.10. The R_{42} ratio minimum is found in the semi magic nuclide ^{134}Te and takes the value 1.23. As neutrons are removed, the R_{42} ratio increases to the maximum value of 2.09 in ^{122}Te, close to the ratio expected in vibrational nuclei of R_{42}=2. At no point does the ratio come close to the rigid axially symmetric rotor value of $R_{42}=\frac{10}{3}$. It can also be noted that there are observed states in ^{118,120,122}Te with the spin, parity, and energy spacing expected in vibrational nuclei with 0^+, 2^+, and 4^+ states at approximately twice the 2_1^+ level energy as well as a 6^+ state at approximately three times the energy of the 2_1^+ state.

The 0_2^+, 0_3^+, and 2_3^+ states follow a parabolic trend with mass number similar to the trend expected for shape-coexisting intruder states [40]. The excited 0^+ states (or at least one of them) may therefore be expected to be deformed intruder states with associated rotational bands. These excited states have previously been identified as collective excitations on the ground state. Clearly, the existence of states with the expected spin-parity and approximately the right energy is insufficient to confirm the nature of collective excitations. Interest in the Te isotopes has led to several theoretical approaches to studying the underlying structure. These include triaxial-rotor calculations [35], anharmonic vibrator model and generalised collective model calculations [68], shell-model calculations [69], triaxial projected shell-model calculations [6], and the particle-core coupling model [70].

A recent measurement of the transition strengths and quadrupole moments in the mid-shell ^{120,122,124}Te nuclides suggested a shape parameter of γ=25°, 27.5° in ^{120,122}Te, respectively [35]. No value was given for ^{124}Te. These values suggest significant triaxiality and indeed are close to maximal triaxiality (γ=30°).

The experimentally determined $B(E2;4_1^+ \rightarrow 2_1^+)/B(E2;2_1^+ \rightarrow 0^+_{\text{g.s.}})$ values in $^{120-124}$Te have been compared to comprehensive shell-model calculations performed across the even-even Te nuclides in the N=50-82 region [69]. The results were found to have a reasonable degree of agreement, however, the pattern of large increases in the $B(E2)$ ratios towards the mid-shell is not reproduced. The same shell-model study found that the wavefunctions of low-lying states in $^{126-132}$Te were dominated by proton or neutron configurations. Of particular note is the 6_1^+ state in ^{132}Te. It is stated to be dominated by a "proton excitation", however the spin coupling given for the state is $|\phi_\pi^p(J_\pi = 0) \otimes \phi_\nu^n(J_\nu = 6)\rangle$, a neutron excitation. The magnetic moment is not discussed, but it is measured to be positive and has a magnitude that implies there is a significant proton component in its configuration [71].

2.8.2 Descriptions of Cd isotopes

The Cd nuclei near mid-shell have often been considered textbook examples of vibrational nuclei [15; 29; 72]. However, the Cd isotopes have undergone in-depth study using a variety of techniques [25; 73; 74; 75; 76], leading to a questioning of

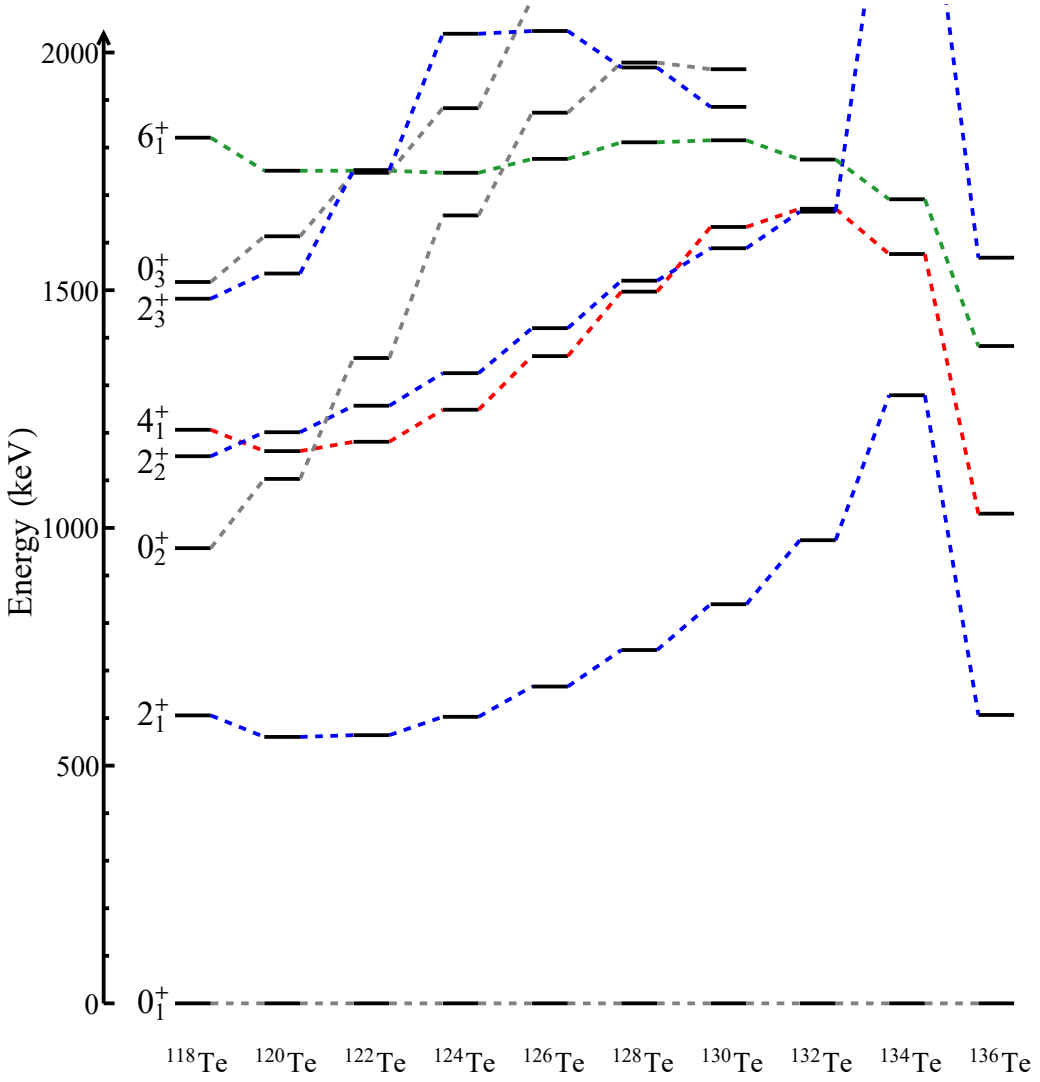

Figure 2.10: Energy systematics across the Te isotopes. Data from Nuclear Data Sheets [58; 59; 60; 61; 62; 63; 64; 65; 66; 67].

the validity of the vibrational interpretation [7]. In particular, it has been noted that the transition strengths out of the three-phonon states do not match the expected transition-strength pattern, the two-nucleon transfer rates for the coupled octupole-quadrupole phonon states are not consistent with a vibrational picture, and the g factors of the low-lying states in the odd-mass Cd isotopes are inconsistent with the harmonic vibration model. Alternate explanations for the observed nuclear structure in the Cd isotopes have been offered [77; 78; 79; 80; 81; 82; 83; 84; 85; 86]. However, these newer interpretations are not universally accepted. Several papers have recently made modifications to the vibrational model in order to explain the observed deviance [87; 88].

It has also been noted recently that the odd-mass isotopes can be particularly useful in identifying the nature of collective excitations [82; 85]. In this project, Coulomb-excitation measurements were made on ^{111,113}Cd. These nuclei will be the focus of the following discussion.

Both ^{111}Cd and ^{113}Cd have a $1/2^+$ ground state with "large" negative g factors. These states have been identified with the unpaired neutron in either the spherical $s_{1/2}$ orbit or the $1/2^+[411]$ Nilsson orbit.

However, g factors of the $1/2^+$ ground states are significantly smaller in magnitude than those predicted by the Schmidt values for an $s_{1/2}$ neutron. This has been explained through the strong mixing of spherical shell-model configurations that occurs in the $1/2^+[411]$ Nilsson state at small deformations [82]. Small deformations in the Cd isotopes are supported by the measured quadrupole moments in Cd nuclei both from $Q(2_1^+)$ in the even isotopes and from transition strengths measured for low-excitation states in odd-A nuclei [89; 90]. The $1/2^+$ ground-state g factor in ^{113}Cd is smaller in magnitude, suggesting a higher degree of deformation [82]. Larger deformations are associated with increases in collectivity. The suggestion of increased collectivity from the measured g factors is consistent with increasing transition strengths in both the even-even systematics and odd-mass Cd systematics towards the mid-shell. The increase in transition strength in the even-even Cd isotopes is displayed in Fig. 2.9.

Energy systematics of several odd-mass Cd isotopes are displayed in Fig. 2.11. The displayed energies have been shifted relative to the $1/2^+$ state. Systematic plots like that in Fig. 2.11 can be useful in the identification of origins and configurations of nuclear states near the Fermi surface.

There are a number of states at similar excitation energies with the same spin and parity in these nuclides. As such, it can be difficult to identify equivalent states across the isotopic chain. Furthermore, the spins and parities of many states in these odd-mass nuclides are unknown or tentatively assigned.

This thesis aims to explore the structure of nuclei, in particular the nature of nuclear collectivity, through the emergence of collective nuclear properties. In this chapter the concepts and experimental quantities used in the discussion of nuclear structure have been developed and discussed. The experimental investigation of the nuclear structure properties discussed in this chapter involve sophisticated measurement techniques. The techniques used in the experimental sections of this thesis

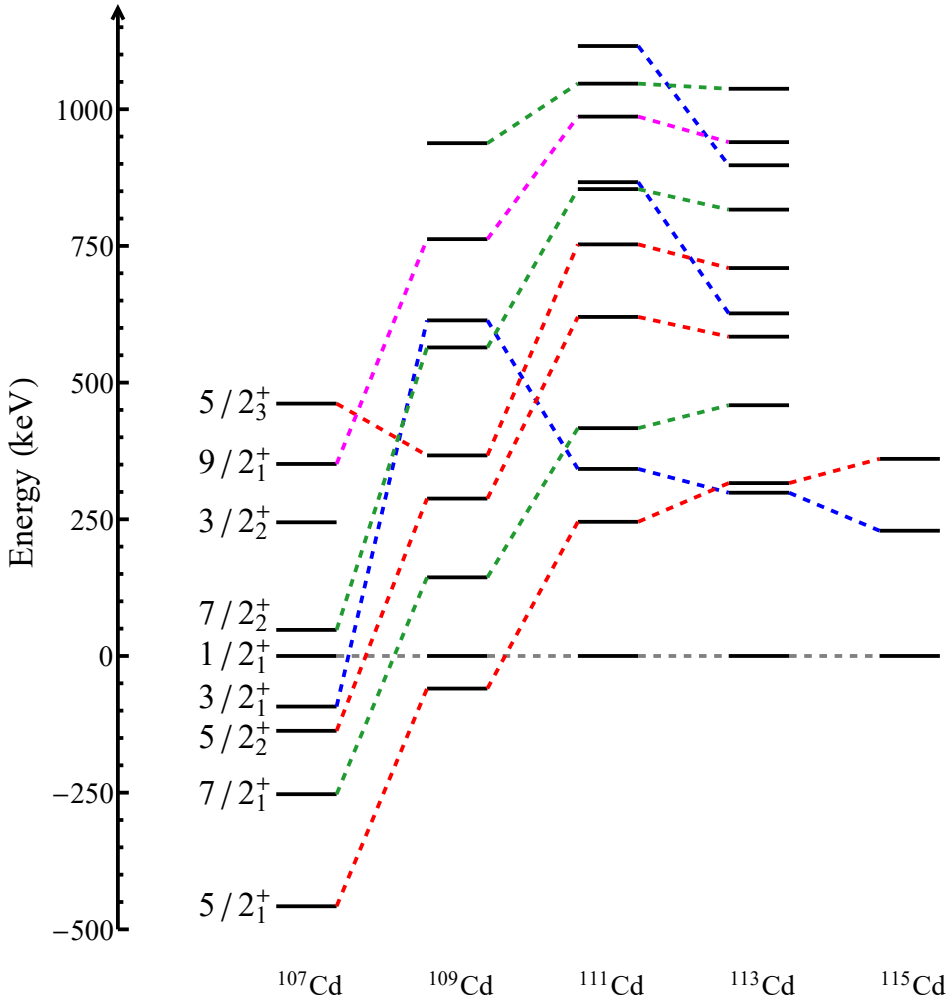

Figure 2.11: Energy systematics across the odd-mass Cd isotopes. The displayed energies have been shifted relative to the $^1/_{2_1^+}$ state. Data from Nuclear Data Sheets [91; 92; 90; 93; 94].

will be discussed in the following chapter. These techniques are used to measure $E2$ transition strengths, and $E2$ and $M1$ moments of excited nuclear states.

Chapter 3

Experimental Techniques

Several experimental techniques were used in the investigation of nuclei in this work. First, the measurement of $E2$ matrix elements through Coulomb excitation will be discussed, followed by considerations relevant to the design of such experiments. Second, a brief introduction will be given to the spatial distribution of decay radiation from aligned nuclei. This anisotropic emission can be used for the measurement of g factors as will be demonstrated by an explanation of the transient-field method. Finally, the extraction of lifetimes from Doppler-broadened lineshapes through the Doppler-shift attenuation method is discussed.

3.1 Coulomb excitation

Coulomb excitation is a process by which a nucleus moves from an initial state to a higher-excited state through interactions with electromagnetic fields.

Coulomb-excitation measurements are a sensitive and precise tool particularly for the determination of $E2$ transition matrix elements. There are two methods used in Coulomb excitation: One is low-energy or sub-barrier Coulomb excitation, in which the excitation occurs at energies well below the Coulomb barrier so that the nuclear strong force interactions play no role in the excitation. The second is intermediate energy excitation in which high-energy beams are excited on thick, heavy targets close to the barrier with particle detection restricted to low scattering angles where the nuclei remain a safe distance apart throughout the collision. The present measurements are performed by bombarding one nucleus on a target at energies well below the Coulomb barrier where strong force interactions between beam and target play no role in excitation. This low-energy interaction can be well evaluated through semi-classical Coulomb-excitation theory. The excitation can be split into several paths according to their multipolarity. Coulomb excitation occurs primarily through electric excitations [95], with low-multipolarity excitations favoured over high multipolarities. In nuclei, however, $E2$ excitation dominates over $E1$ excitations and other multipolarities. Combined with the enhancement often seen in $E2$ transition strengths due to quadrupole collectivity, and the limited transitions between states of opposite parity allowed within the major shells, other electric-multipole excitation and magnetic excitation can often be excluded from calculations. Simple

models are used to correct for the small differences in cross sections due to virtual excitation to the giant dipole resonance [96].

Single-step Coulomb excitation, in which a nucleus is excited from its ground state directly into an excited state, is favoured when the interaction between the two nuclei involved in the excitation is limited in strength, such as with light (low-Z) Coulomb-excitation partners, small scattering angles in the centre-of-mass frame, and/or low beam energy. Excitation through pathways that involve multiple states becomes more favourable when the Coulomb interaction between the nuclei is increased, i.e. by higher-Z and closer collisions (higher beam energies). While almost exclusively 2_1^+ states are excited in even-even nuclei through interactions with low-mass nuclei, it is possible to excite to high-energy and high-spin states using heavy-mass interaction partners with energies toward the Coulomb barrier.

3.1.1 The reorientation effect

The reorientation effect is a second-order process in Coulomb excitation that accounts for the effect of the quadrupole moment of a state on its excitation probability. The effect for the 2_1^+ state in an even-even nucleus can be approximated as [96]

$$P_{0^+\rightarrow 2^+} = F(\theta,\xi_{02})B(E2)[1+1.32\frac{A_B}{Z_T}\frac{\Delta E}{(1+\frac{A_B}{A_T})}Q_{2^+}K(\theta,\xi_{02})], \tag{3.1}$$

where $P_{0^+\rightarrow 2^+}$ is the excitation probability to the 2^+ state, A_B is the mass of the beam particle, A_T is the mass of the target nucleus, Z_T is the proton number of the target, ΔE is the excitation energy, Q_{2^+} is the quadrupole moment, and $F(\theta,\xi_{02})$ and $K(\theta,\xi_{02})$ are functions independent of the transition strengths and quadrupole moments but dependent on the scattering angle θ, and ξ_{02}, the adiabacity parameter defined as

$$\xi_{02} = \frac{Z_B Z_T e^2}{\hbar}(\frac{1}{v_0}-\frac{1}{v_2}), \tag{3.2}$$

where v_0 and v_2 are the initial and final projectile velocities, respectively.

The $K(\theta,\xi_{02})$ coefficient determines the magnitude of the effect of the quadrupole moment and is generally of the order of unity. The deviation of the excitation amplitude from the value obtained with a quadrupole moment of $Q_{2^+} = 0$ is close to zero in interactions with light nuclei, however it can increase to >30% in interactions with heavier nuclei.

3.1.2 Description of Coulomb-excitation measurements

In conventional-kinematics, target-excitation, Coulomb-excitation measurements a light beam is made incident upon a heavy target comprised of the isotope of interest. The scattered beam is generally measured in particle detectors around the target. The matrix elements relevant to excitation are determined by performing calculations of the yield and fitting the matrix elements such that the calculated and experimental excitation yields agree. The excitation to each state can be determined through three

methods: (i) measurement of scattered particles with sufficient energy resolution to separate inelastic scattering that populates excited states and elastic scattering, (ii) measurement of γ rays from decaying excited states, and (iii) measurement of γ rays from decaying excited states in coincidence with scattered or recoiling particles. Performing measurements using high-resolution particle spectroscopy suffers from high backgrounds due to scattering from target contaminants and poor resolution in comparison to γ-ray spectroscopy. Advantageous aspects to particle spectroscopy include a large detection efficiency and insensitivity to branching ratios, mixing ratios, and changes is γ-ray efficiency from movement away from the target of the excited nucleus (for long-lived states). In practice, measurements using particle spectroscopy alone are unsuitable for nuclei with multiple excited states, unless the states are excited with similar intensity and are well separated in energy ($\Delta E \sim 50$ keV) [96]. Measurement of γ rays alone suffers from uncertainties in integrated beam current, and Doppler-broadening of peaks. In addition, in strongly coupled systems, such as those found in multiple Coulomb excitation, the loss of information without the measurement of multiple distinct scattering angles can result in a range of valid transition strengths that give the same observed yields.

The measurement of particle-γ coincidence data solves many of these issues. High-precision, position-sensitive knowledge of particle- and γ-ray detection angles allows Doppler reconstructions of sharp peaks. The extra information gained from multiple scattering angles often allows a unique solution to be found for the $E2$ matrix elements, while the high resolution of HPGe detectors allows measurements of transitions with close energies ($\Delta E \gtrsim 3$ keV).

Many target-excitation measurements experience difficulties due to the presence of isotopic impurities in the target, leading to higher backgrounds and uncertainties from the potentially unknown isotopic composition. It is therefore useful in many cases to study the beam-like species, thereby enabling higher isotopic purities in the beam along with target materials that are naturally monoisotopic.

3.1.3 Experimental design

Due to the high sensitivity of Coulomb-excitation measurements, there are many experimental factors that must be well understood to achieve accurate results. Some important factors are beam energy, target thickness, energy loss of the beam in the target (stopping powers), scattering angles, γ-ray detection angles, and γ-ray detector efficiency.

The effect of nuclear reactions between the beam and target species should be avoided. The effects of nuclear interactions are not well understood and are not as easily calculable as the pure electromagnetic interaction. Coulomb excitation that includes nuclear overlap effects is considered "unsafe"; conversely purely electromagnetic excitation is called "safe". In order to avoid nuclear interactions, it has been found that a nuclear surface separation of at least ~ 5 fm should be maintained. A commonly used definition for the safe Coulomb-excitation beam energy in

the lab frame is therefore

$$E_{\text{safe}} = 1.44\frac{A_B + A_T}{A_T}\frac{Z_B Z_T}{1.25(A_B^{1/3} + A_T^{1/3}) + 5}\ \text{MeV}, \tag{3.3}$$

where A_B is the mass of the beam species, A_T is the mass of the target species, Z_B is the nuclear charge of the beam species, and Z_T is the nuclear charge of the target species [8].

The semiclassical approach to Coulomb excitation is only valid when the de Broglie wavelength is small compared to the distance of closest approach [96]. For a head-on collision, this can be characterised by the Sommerfeld parameter, defined as

$$\eta = \frac{Z_T Z_B e^2}{\hbar v} >> 1, \tag{3.4}$$

where v is the velocity of the beam particle, and Z_T and Z_B are the nuclear charge of the target and beam species, respectively.

In the simplified case of the three-state nucleus shown in Fig. 3.1, direct excitation to the second 2^+ state and excitation through the first 2^+ state occurs. The excitation through each path can increase or decrease the final excitation amplitudes dependent on the relative signs of the matrix elements. In the three-state case we consider a second order interference term P_3, the relevant product of terms is

$$P_3 = \langle 0^+_{\text{g.s.}}||E2||2^+_1\rangle\langle 2^+_1||E2||2^+_2\rangle\langle 2^+_2||E2||0^+_{\text{g.s.}}\rangle. \tag{3.5}$$

When $\langle 0^+_{\text{g.s.}}||E2||2^+_1\rangle$ is positive and the product P_3 is negative the final excitation amplitude of the 2^+_1 state is decreased when compared to a positive P_3. It is not possible to determine the sign of P_3 from a single measurement with a single particle detection angle, beam energy, and beam species. It is therefore important in measurements where multiple excitation paths have comparable amplitudes that multiple measurements are made under different beam and scattering conditions to determine the relative signs of matrix elements.

Coulomb-excitation measurements can also be sensitive to the diagonal matrix elements. The reorientation effect (discussed in Sec. 3.1.1) corresponds to transitions between magnetic substates of a given excited state and changes its total population in a similar way to excitation through higher excited states. In order to fix the relative signs of matrix elements, measurements with several excitation partners and beam energies are often required. Coulomb-excitation measurements with reorientation that do not change the partner species generally give more than one solution with different assumptions on the interference terms.

In Coulomb-excitation experiments where the excitation and de-excitation paths are not identical, there are nuclear structure components that must be further understood. Analysis of the decays from such states is complicated by mixed-multipolarity de-excitation. In the case of the three-state nucleus, the 2^+_1 state can be excited directly from the ground state, or indirectly through the 2^+_2 state. While the excitation of this state is largely independent of the $M1$ matrix element between these states,

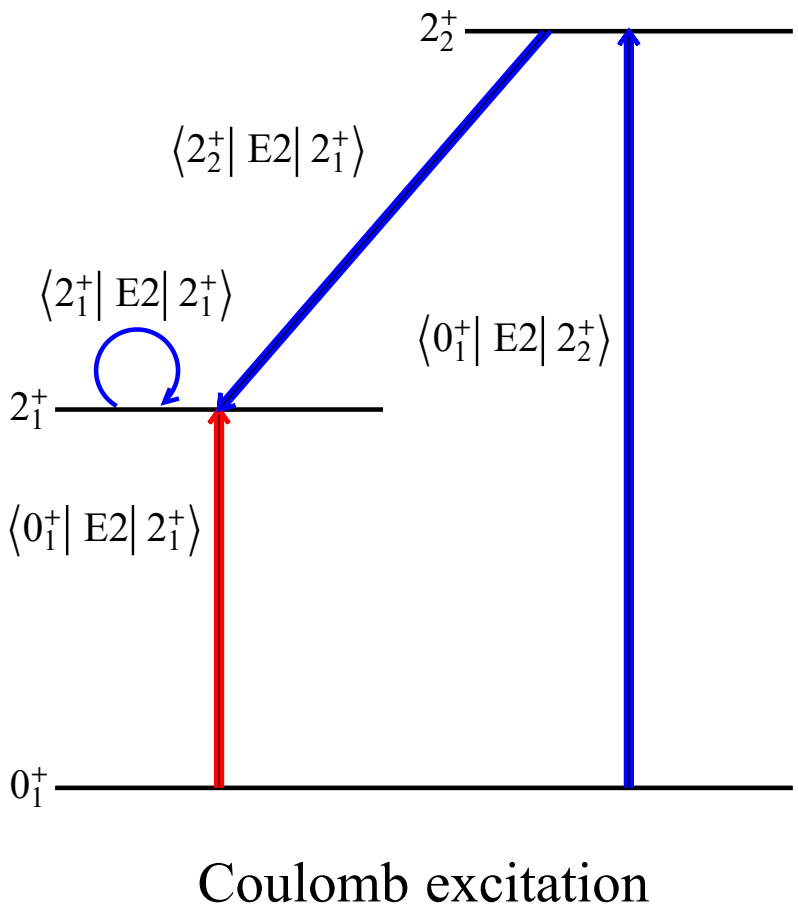

Figure 3.1: A simple, three-state system showing first- and second-order multiple-Coulomb-excitation paths to the 2_1^+ state. The first-order path is shown in red, matrix elements involved in second-order paths are shown in blue.

the observed decay yields are dependent on the decay to the 2_1^+ state through the $M1$ component. The extracted matrix elements are then dependent on the $M1$ transition strength between these two 2^+ states. The dependence of measured yields on $M1$ matrix elements becomes a bigger issue in the measurement of odd-mass nuclei, which can have many mixed transitions, often with unknown mixing ratios. Knowledge of the mixing ratios of transitions involved in Coulomb excitation is essential for the correct interpretation of observed yields.

In designing Coulomb-excitation experiments it is important to consider the effect of thicker targets on the resulting analysis. Thicker targets increase the rate of data collection, since the number of scattering centres increases. However, as the target thickness increases, the range of beam energies that are used to excite the nuclei of interest widens due to energy loss in the target. Both the absolute cross sections and the relative cross sections of the excited states can be highly sensitive to the beam energy. The thicker the target, the more dependent the measurement becomes on the assumed stopping powers. Tabulated stopping powers obtained by fitting a range of data can differ by up to $\sim$20% from measured stopping powers in specific cases. Therefore, when stopping powers are not simultaneously measured, it is useful to minimise the target thickness while maintaining the required data rate for the measurement, if possible. It can be useful to measure transition strengths relative to the known transition strengths in the interaction partner as this partially cancels errors due to the stopping powers.

3.2 Angular distribution and correlation measurements

When the angular momentum of a nuclear state favours a direction in space, i.e. the angular-momentum vector of the nucleus is oriented, the decays from that state decay probabilistically in particular spatial patterns. The angular shapes of the patterns are dependent on the population of the magnetic substates of the initial state, the spin properties of the initial and final states, and the multipolarities and mixing ratio of the transition [13]. Nuclear orientation can be obtained by the reaction mechanism or by the observation of coincident radiation from the nucleus at a known angle, or from both. When the angular momentum is determined by the reaction mechanism, the spatial pattern (usually relative to the beam axis) is known as an angular distribution; when the nuclear orientation is obtained from coincident observed radiation, the spatial pattern is called an angular correlation. The formalism for calculating angular correlations is discussed in Appendix C. Some essential details are discussed here.

The angular correlation (W) of γ radiation from an excited aligned nucleus can be expressed as

$$W(\theta_p, \theta_\gamma, \Delta\phi) = \sum_{kq} B_{kq}(\theta_p) Q_k F_k D^{k*}_{q0}(\Delta\phi, \theta_\gamma, 0), \tag{3.6}$$

where $k = 0, 2, 4$ for $E2$ and mixed $M1/E2$ transitions, q ranges over projections of k (i.e. $-k \leq q \leq k$ in integer steps), θ_p is the detection angle of the scattered particle,

θ_γ is the detection angle of the γ ray, $\Delta\phi$ is the difference in the azimuthal detection angles of the scattered particle and detected γ ray, $B_{kq}(\theta_p)$ is the statistical tensor which holds the information on the populations of magnetic substates of the initial state, Q_k is the geometrical solid angle attenuation factor due to the finite size of the γ-ray detector, D^{k*}_{q0} is the Wigner D-matrix, and F_k contains information on the initial- and final-state spins and the multipolarity of the transition.

The dependence of these distributions and correlations on spins and mixing ratios allows the measurement of these observables as a standard spectroscopic technique.

3.2.1 Alignment in Coulomb-excitation measurements

In Coulomb-excitation measurements, it is possible to calculate the expected angular-momentum substate distribution of a state and, therefore, predict the angular distributions of transitions out of that state if the spins and parities of the parent and daughter states, and the transition multipolarities and mixing ratio are known.

In transient-field measurements (discussed in Sec. 3.3), it is preferable to maximise the alignment of excited nuclei as this maximises the anisotropy of the angular correlation and increases the sensitivity of the measurement to the nuclear precession. In Coulomb-excitation measurements, the alignment is maximised for directly backscattered particles in the centre of mass frame. In the case of 180° backscattered particles, the angular momentum of the excited state is aligned perpendicular to the beam direction.

The excitation, or equivalently population, of the magnetic substates in Coulomb excitation can be related to the statistical tensor using the equation [13]

$$\rho_{kq}(N) = \frac{\sqrt{2I_N+1}}{2I_1+1} \sum_{\substack{M_N M'_N \\ M_N = M'_N + q}} (-1)^{I_N+M_N} \begin{pmatrix} I_N & I_N & k \\ -M_N & M'_N & q \end{pmatrix} \sum_{M_1} a^*_{I_N M'_N}(M_1) a_{I_N M_N}(M_1) \tag{3.7}$$

where I_N is the angular momentum of the state N, M_N is the m-substate of state N, k and q are as in Eqn. 3.6, and the factor in the brackets is a Wigner 3-j symbol. The statistical tensor ρ must be rotated from the frame in which it is calculated to the lab frame, with the beam along the z-axis, which is the usual frame in which angular distributions and particle-γ correlations are measured. The statistical tensor ρ_{kq} is related to the statistical tensor B_{kq} by [97]

$$\rho_{kq}(j) = \frac{1}{2k+1} B_{kq}(j). \tag{3.8}$$

The statistical tensors of a state fed from above (f) can be calculated from the statistical tensors of the initial state (i)

$$B_{kq}(f)_{\text{fed}} = U_k(i \to j) B_{kq}(i), \tag{3.9}$$

where the U_k coefficient is as defined in Ref. [98], and depends on the initial and final

level spins and the multipolarities and mixing ratio of the feeding transition.

3.3 Thin-foil transient-field g-factor measurements

Determination of g factors can occur through two fundamental interactions: measurement of the Zeeman splitting of the energies of the m-substates of a state, or measurement of the precession of the angular momentum of a state in the presence of a strong magnetic field. In practice, however, the energy splitting of the m-substates is small, typically $< 3 \times 10^{-8}$ eV/T of applied magnetic field, which for available magnetic fields is much smaller than the resolution of γ ray-detectors. For a selected few low-excitation states, the Mössbauer effect can be used to observe the substate splitting. Laser spectroscopy, observing the hyperfine splitting of atomic states, of the ground states in odd-mass nuclei and of long-lived isomers is also possible, however most nuclear excited states have lifetimes too short to be amenable to these methods. Hence, observation of the nuclear precession in a large magnetic field is the usual approach to measure excited-state magnetic moments.

The (Larmor) precession frequency of the nucleus, ω_L, in a magnetic field is

$$\omega_L = -gB\frac{\mu_N}{\hbar}, \tag{3.10}$$

where g is the nuclear g factor, B is the magnetic field, and μ_N is the nuclear magneton.

A nucleus recoiling through a polarised ferromagnet experiences a transient hyperfine magnetic field. The total precession angle accumulated in transit through a thin ferromagnetic layer can then be written as

$$\Delta\theta = -g\frac{\mu_N}{\hbar}\int_0^T B_{\mathrm{TF}}(t)e^{-t/\tau}dt, \tag{3.11}$$

where T is the transit time through the ferromagnet, B_{TF} is the transient magnetic field, and τ is the mean lifetime of the state being measured. B_{TF} has a time dependence due to the fact it is velocity dependent and the nucleus slows down as it transits the foil. We write this expression as $\Delta\theta = g\phi$ where

$$\phi := -\frac{\mu_N}{\hbar}\int_0^T B_{\mathrm{TF}}(t)e^{-t/\tau}dt. \tag{3.12}$$

Measurement of the precession of the angular momentum vector is possible through the measurement of anisotropic decays from excited nuclear states. The effect of the precession on the observed γ-ray decays can be expressed as

$$N_i^{\uparrow} = N_0 W(\theta - \Delta\theta), \tag{3.13}$$

where the field direction is given by an arrow ($\uparrow$), N_0 is the number of counts that would be seen in isotropic decay, $W(\theta)$ is the angular correlation function, θ is the

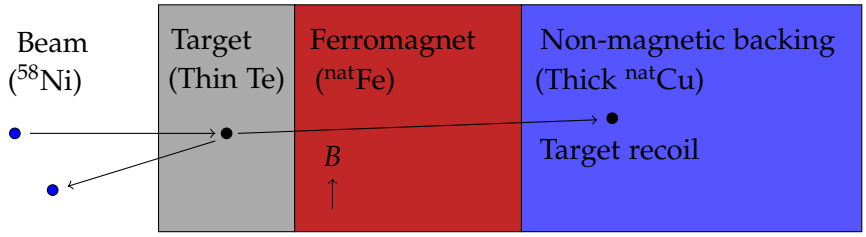

Figure 3.2: Three-layer, thin-foil target used in thin-foil transient-field g-factor measurement. A ^{58}Ni beam (blue dots) scatters from a Te target nucleus (black dots) which recoils through a ferromagnetic layer into a non-magnetic layer. A magnetic field is applied and can be periodically reversed.

angle of the γ-ray detector, and $\Delta\theta$ is the average precession angle. The number of observed decays in one γ-ray detector and one magnetic-field direction can be expressed as

$$N_i^{\uparrow(\downarrow)} = W(\theta_\gamma \pm \Delta\theta) n_T q[\uparrow(\downarrow)] \epsilon_{\gamma,i}(E_\gamma) \int_{\text{tgt}} \int_{\Omega_p} \frac{d\sigma}{d\Omega_p} \epsilon_p d\Omega_p dE, \tag{3.14}$$

where n_T is the areal number density of the target, $q[\uparrow(\downarrow)]$ is the integrated beam current in the given field direction, $\epsilon_{\gamma,i}(E_\gamma)$ is the γ-ray detector efficiency at the energy E_γ, ϵ_p is the particle detector efficiency, and the integrals are over the target thickness (in terms of energy loss dE) and the solid angle ($d\Omega_p$) over the face of the particle detector.

It is possible to remove many factors unrelated to the measurement of the angular shift by using two γ-ray detectors at complementary angles, which here means at $+\theta_\gamma$ and $-\theta_\gamma$ relative to the beam axis. We define the double ratio ρ as

$$\rho = \sqrt{\frac{N_1^\uparrow}{N_1^\downarrow} \cdot \frac{N_2^\downarrow}{N_2^\uparrow}} = \frac{W(\theta_\gamma - \Delta\theta)}{W(\theta_\gamma + \Delta\theta)}, \tag{3.15}$$

where $N_i^{\uparrow(\downarrow)}$ is the number of counts in detector i with the field in the upward (downward) vertical direction. By using two γ-ray detectors at $\pm\theta_\gamma$ the double ratio becomes insensitive to: a) differences in the integrated current in each field direction, b) differences in efficiencies, c) small offsets in the angles of the detectors or equivalently small shifts in the beam position on the target, and d) changes in data rates throughout the experiment.

Expanding the double ratio to first order in $\Delta\theta$

$$W(\theta + \Delta\theta) = W(\theta) + \Delta\theta \frac{dW}{d\theta}. \tag{3.16}$$

We then define the 'slope', S, as the logarithmic derivative of the angular distribution

or correlation evaluated at the detection angle $+\theta_\gamma$:

$$S = \frac{1}{W}\frac{dW}{d\theta}. \tag{3.17}$$

The double ratio can be written as

$$\rho = \frac{1 - S\Delta\theta}{1 + S\Delta\theta}. \tag{3.18}$$

The 'effect', ϵ, is defined as

$$\epsilon = \frac{1-\rho}{1+\rho}, \tag{3.19}$$

and the measured precession angle can be experimentally determined as

$$\Delta\theta = \frac{\epsilon}{S}. \tag{3.20}$$

Together with the factor ϕ defined in Eqn 3.12, this expression can be used to extract the g factor as

$$g = \frac{\Delta\theta}{\phi}. \tag{3.21}$$

To date, the transient field has proven impossible to calculate from first principles. In order to overcome this limitation, phenomenological models are used to estimate the magnitude and dependencies of the transient field on the ion parameters (velocity and atomic number). In general, it is preferred to perform transient-field measurements using an internal reference state in order to remove the uncertainty from the transient field strength. In the present work, measurements were made relative to a reference state in each nucleus. The assumed parametrisation of the transient field is therefore less important. Differences in the effective average transient field may still be important between states with different lifetimes; efforts were made to reduce the small effect that would occur due to differences in state lifetimes. In order to account for the effect of lifetime differences in the present measurements a parametrisation, which has been shown to reproduce observed precessions in the region, is used [99; 100]. The assumed form is

$$B_{\mathrm{TF}} = a(\frac{v}{v_0})^{p_v} Z^{p_Z}, \tag{3.22}$$

where v is the velocity of the nucleus, v_0 is the Bohr velocity, Z is the atomic number of the nucleus, and a, p_v, and p_Z are experimentally determined parameters.

The formulation based on Eqns. 3.12 and 3.21 limits the accuracy of the transient-field measurements to the precision of the parametrisation. In practice, where possible, this uncertainty is avoided by measuring g factors relative to known g factors of states excited in the same conditions. In such cases the factor ϕ is almost the same for all excited states with small differences due to the state lifetimes, which are often known from other measurements. The measured g factor relative to the reference

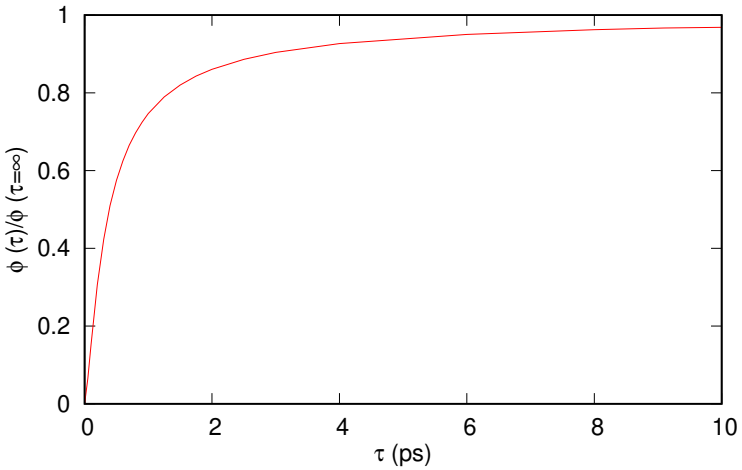

Figure 3.3: The dependence of the integrated magnetic field (ϕ) on the lifetime of an excited state given relative to the value for an infinitely long-lived state. Calculations are performed for experimental conditions similar to those used in this thesis (Chapter 7). The transit time of the nucleus through the ferromagnet is ∼600 fs. The transient-field parametrisation used is that in Ref. [100].

g factor is then expressed as

$$g_i = g_{\text{ref}} \frac{\Delta\theta_i}{\Delta\theta_{\text{ref}}} \frac{\phi(\tau_{\text{ref}})}{\phi(\tau_i)}, \tag{3.23}$$

where g_i is the g factor of the state of interest, g_{ref} is the g factor of the reference state, τ_i is the mean lifetime of the state of interest, and τ_{ref} is the mean lifetime of the reference state. The effect of the mean lifetime (τ) on ϕ with respect to the value for an infinitely long-lived state for a given recoiling nucleus and transient-field parametrisation is explored in Fig. 3.3. In the region corresponding to mean lifetimes of a few to several picoseconds, as in the present work, the value of ϕ is not strongly dependent on the lifetime.

So far we have only discussed the measurement of precessions of a directly excited state. In the present work we are specifically measuring the 4_1^+ g factor relative to the 2_1^+ state. While the 2_1^+ states are much more strongly excited than the 4_1^+ states, feeding corrections must still be applied because the 4_1^+ state decays to the 2_1^+ state. In general, feeding corrections to the observed (obs) precession angles may be applied as

$$\Delta\theta_{j,\text{obs}} = \frac{N_j^0 \frac{dW_j}{d\theta}\Delta\theta_j + \sum_{i>j} N_i^0 \frac{dW_{ij}}{d\theta}\Delta\theta_i}{N_j^0 \frac{dW_j}{d\theta} + \sum_{i>j} N_i^0 \frac{dW_{ij}}{d\theta}}, \tag{3.24}$$

where N_i^0 is the directly excited population of the state i, and $\frac{dW_j}{d\theta}$ and $\frac{dW_{ij}}{d\theta}$ are the unfed and fed angular correlations for the state j. More specifically, $\frac{dW_{ij}}{d\theta}$ is the angular correlation for the decay of the state j populated by decay from state i. We now

rewrite Eqn 3.24 in a simpler matrix form [101],

$$\Delta\theta_{j,\text{obs}} = \sum_{i \geq j} A_{ji} \Delta\theta_i, \tag{3.25}$$

where

$$A_{ji} = \frac{N_i^0 \frac{dW_{ij}}{d\theta}}{N_j^0 \frac{dW_j}{d\theta} + \sum_{i>j} N_i^0 \frac{dW_{ij}}{d\theta}}, \tag{3.26}$$

and $\frac{dW_{ii}}{d\theta} = \frac{dW_i}{d\theta}$ defined above.

In the process of experimental design it is useful to define a figure of merit to maximise the sensitivity of the experiment. For this purpose we begin with an estimate of the statistical uncertainty in the precession measurement. Using first order uncertainty propagation to obtain an uncertainty estimate for Eqn. 3.15, we obtain the expressions for the uncertainty in ρ as

$$\sigma_\rho = \sqrt{\sum_{i=1,2} \sum_{k=\uparrow,\downarrow} (\frac{\partial \rho}{\partial N_i^k})^2}, \tag{3.27}$$

and

$$\sigma_\rho \approx \frac{1}{2}\rho \sqrt{\sum_{i=1,2} \sum_{k=\uparrow,\downarrow} (\frac{\sigma_{N_i^k}}{N_i^k})^2}. \tag{3.28}$$

The change in the number of counts recorded in each detector due to the precession angle is often small. It is therefore possible to approximate the number of counts in each detector and field direction as equal in the error estimate. We denote this value N. Assuming no background, the uncertainty in the number of counts is $\sqrt{N}$. Equivalently, ρ is generally close to unity, therefore

$$\sigma_\rho \approx \frac{\rho}{\sqrt{N}} \approx \frac{1}{\sqrt{N}}. \tag{3.29}$$

The uncertainty in the effect, ϵ (Eqn 3.12), then follows without further assumptions.

$$\sigma_\epsilon = \frac{\partial \epsilon}{\partial \rho}\sigma_\rho = \sigma_\rho \frac{\partial}{\partial \rho}(\frac{1-\rho}{1+\rho}) = \frac{2}{(1+\rho)^2}\sigma_\rho, \tag{3.30}$$

and since $\rho \approx 1$, we have

$$\sigma_\epsilon \approx \frac{1}{2\sqrt{N}}. \tag{3.31}$$

Furthermore, assuming no uncertainty in the slope, we obtain from Eqn. 3.20 that

$$\sigma_{\Delta\theta} \approx \frac{1}{2}\frac{1}{S\sqrt{N}}. \tag{3.32}$$

This approximation of the uncertainty will be used later in order to investigate the optimal experimental parameters, including placement of particle and γ-ray detec-

tors, in Sec. 7.1. Note that the full error propagation was evaluated without the above approximations during data analysis.

In the course of the present transient-field measurements some damage was found for one of the particle detectors, which reduced the symmetry of the particle and γ-ray detectors. The problem was discovered and corrected, however some data were collected with the broken detector. It is therefore useful to estimate the effect of differences in the slopes that break the symmetry in ρ. Assuming the integrated beam current in each field direction is equal

$$\rho^2 = \frac{(1 - S_1\Delta\theta)(1 - S_2\Delta\theta)}{(1 + S_1\Delta\theta)(1 + S_2\Delta\theta)}, \tag{3.33}$$

where S_i is the of the angular correlation at detector i. It is more useful to consider this in terms of the average slope

$$\overline{S} = \frac{1}{2}(S_1 + S_2), \tag{3.34}$$

and the difference in the slopes

$$\Delta S = |S_1 - S_2|. \tag{3.35}$$

Using the substitution

$$S_1 S_2 = \overline{S}^2 - (\frac{\Delta S}{2})^2, \tag{3.36}$$

results in a similar expression to Eqn. 3.18

$$\rho = \frac{1 - \overline{S}\Delta\theta}{1 + \overline{S}\Delta\theta}\sqrt{\frac{1 + (\frac{\frac{1}{2}\Delta\theta\Delta S}{1-\overline{S}\Delta\theta})^2}{1 + (\frac{\frac{1}{2}\Delta\theta\Delta S}{1+\overline{S}\Delta\theta})^2}}. \tag{3.37}$$

The extra factor here can be considered a perturbation when the average slope $\overline{S}$ is used in the analysis. Evaluation of this factor with typical values (e.g. $\Delta\theta$=0.03 and ΔS <0.5) indicate that it is generally very near unity. The effect of such perturbations in the context of the measurements in this thesis is discussed in Sec. 7.1.

3.4 Doppler-Shift Attenuation Method

The Doppler-Shift Attenuation Method (DSAM) enables the measurement of lifetimes of excited nuclear states with lifetimes from some fs to a few ps. When a nucleus γ decays while moving at a relativistic velocity, there is an observable (Doppler) shift in the γ-ray energy. In experiments where excited nuclei slow or stop in a target, the detected energy of γ decays is dependent on the velocity of the nucleus and therefore on the time at which the nucleus decays. The observed lineshape for a decay can therefore be used to determine the proportion of decays that occurred at a

given velocity. This information, along with the stopping powers, which determine the velocity of the ion as a function of time, can then be related back to the lifetime of the decaying nuclear state. The stopping powers are used to convert the measured recoil velocities into a time since excitation. The DSAM technique is thus effective in determining nuclear lifetimes on the order of the stopping time ($\sim$1 ps as noted above).

The shifted energy of the observed γ ray can be calculated as

$$E_\gamma = E_0 \frac{\sqrt{1-\beta^2}}{1-\beta\cos\theta}, \tag{3.38}$$

where E_0 is the unshifted γ-ray energy, β is the velocity in units of c, and θ is the angle between the velocities of the decaying nucleus and the γ ray. For velocities of a few percent of the speed of light ($\beta \lesssim 2\%$), this expression can be approximated to first order as

$$E_\gamma = E_0(1+\beta\cos\theta). \tag{3.39}$$

The Doppler shift, and hence the experimental sensitivity, is maximised for large velocities and particle-γ angle differences of 0° or 180°. The measurements described in this thesis are as a result of data obtained in experiments primarily performed as thin-foil transient-field measurements. The γ-ray detector angles were therefore not placed at the optimal angles for DSAM measurements.

In order to appropriately interpret measured Doppler-broadened lineshapes the velocity distributions of the recoiling nuclei must be calculated. There are two commonly used approaches. The first is the Blaugrund formalism [102], that treats the ensemble of recoiling nuclei as an average nucleus that takes the expectation value for the recoil angle and velocity at a given time. This technique is typically used in cases with small recoil velocities. The second approach is to simulate the recoiling nuclei using Monte-Carlo techniques. In this approach many sample paths are simulated and these paths are used to weight the Doppler-shift as a function of time.

An accurate understanding of the stopping powers is required to convert the measured energy shifts into a "clock". Calculated stopping powers based on a parametrisation of data that is unlikely to include the specific case of interest often differ from measured stopping powers by $\sim$ 20%. It is therefore better in most cases to make a separate stopping power measurement for precise lifetime results. In cases where a separate measurement of this stopping power is not performed a significant systematic uncertainty must be applied to the results. The stopping power as a function of energy for Te in Fe using the SRIM 2013 package [103] is displayed in Fig. 3.4. The region $>0.01c$ is the electronic stopping power regime in which most of the energy loss is due to scattering from electrons in the medium. The region $<0.01c$ is the nuclear stopping regime. In this region, the energy loss of a nucleus moving through the medium is primarily due to nuclear "collisions". In the nuclear stopping regime nuclear scattering is common, which has a much larger effect on the recoil angle than electron scattering. The change in the direction of the velocity vector is the dominant factor in the change in the observed Doppler shift [102], i.e. the change in the recoil

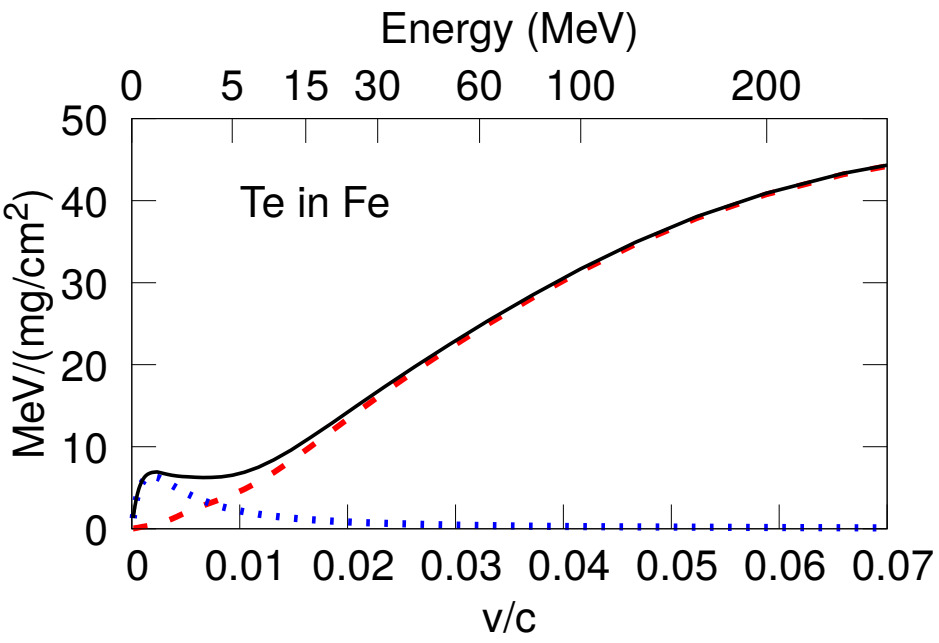

Figure 3.4: Stopping power for Te in Fe. The solid line is the total stopping power, the dashed line is the electronic component, while the dotted line is the nuclear stopping power. The stopping powers were calculated using SRIM 2013 [103].

angle from nuclear recoils has a larger effect on the measured energy than the energy loss at these recoil energies.

Another significant effect on the measured lineshape is the γ-ray angular correlation (discussed in Section 3.2) in Coulomb excitation of low-spin states. In particular, in cases where γ-ray detectors have large opening angles, such as in the present experiment, the γ-ray intensity can vary by a large amount over the surface of the detector. A calculated particle-γ angular correlation for a point-like γ-ray detector and the $2_1^+ \rightarrow 0_{\text{g.s.}}^+$ transition in ^{130}Te is displayed in Fig. 3.5. The blue lines represent the angular range sampled by the forward clover detectors used in the g-factor measurements reported in this thesis. In Fig. 3.6, the expected lineshape from a Monte-Carlo simulation for the $2_1^+ \rightarrow 0_{\text{g.s.}}^+$ transition in ^{130}Te, including and excluding angular correlation effects, is compared. In this case, not including the anisotropy changes the resulting lifetime by $\sim$20%, and the fitted lineshape is significantly altered.

In this chapter, the experimental techniques used in the investigation of the Cd and Te isotopes have been introduced. Two methods for the determination of transition strengths have been discussed: Coulomb excitation, and determination of lifetimes from the investigation of Doppler-broadened lineshapes with DSAM. In the following chapters, the measurements performed are discussed along with results, followed by a discussion in terms of the microscopic and macroscopic structures in the region 'west' of ^{132}Sn.

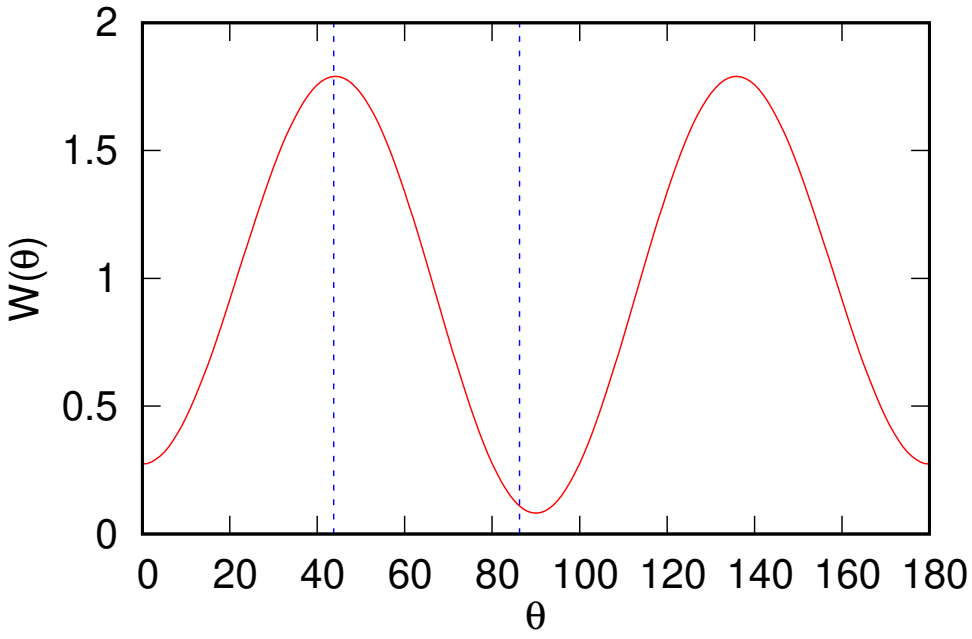

Figure 3.5: Particle-γ angular correlation for the $2_1^+ \rightarrow 0_{\text{g.s.}}^+$ transition in ^{130}Te, calculated assuming a point-like γ-ray detector. Dashed blue lines show the range of angles sampled by a clover placed at 65° in the present experiments.

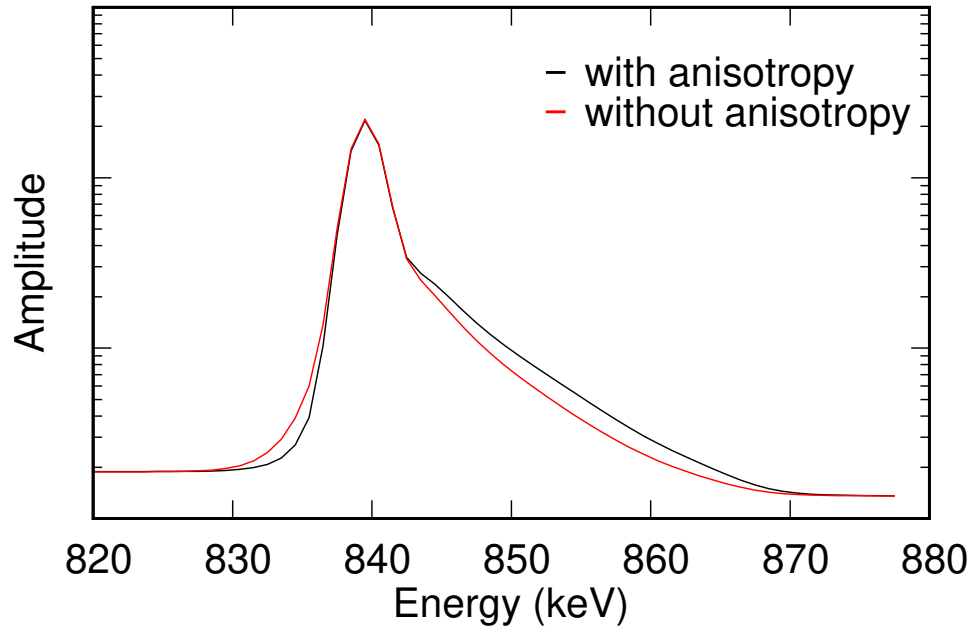

Figure 3.6: A Monte-Carlo simulation of Doppler-broadened lineshapes for the $2_1^+ \rightarrow 0_{\text{g.s.}}^+$ transition in ^{130}Te, with and without the anisotropic decay from angular correlations. The y-axis is displayed in log scale.

Chapter 4

Single-step Coulomb excitation of Cd

This chapter reports on single-step Coulomb-excitation measurements performed at the ANU on beams of ^{111}Cd, ^{112}Cd, and ^{113}Cd. The experiments are described and the results are presented. Further discussion of these results is combined with the discussion of the multi-step Coulomb-excitation measurement reported in Chapter 5. Both experiments are discussed in Chapter 6.

4.1 Single-step ^{111,112,113}Cd Coulomb-excitation experiment

4.1.1 Experimental parameters

Conventional Coulomb excitation uses a beam to excite a target comprised of the nuclei of interest [96]. Natural Cd, as used for the g-factor measurement of Chamoli *et al.* [77], contains several stable isotopes including the odd-A ^{111}Cd and ^{113}Cd of primary interest here. The natural target leads to higher Compton backgrounds from higher-lying transitions and overlapping γ-ray energies, and is not suitable for detailed Coulomb-excitation analysis on the odd-A isotopes. In order to avoid overlapping transitions and to decrease background, either a separated isotope target, or inverse kinematics, must be used. The experiment reported here was performed in inverse kinematics. The magnetic beam transport and lensing of the accelerator separates isotopes allowing measurements of a single isotope, namely the beam species.

Beams of ^{111,112,113}Cd were accelerated to 240 MeV and made incident on a ^{nat}C target with a thick Cu backing. Beams were sourced from a CdO cathode and were injected into the accelerator as CdO^- ions. The maximum energy of the accelerated Cd from the accelerator limited both the choice of target and the beam energy. Coulomb excitation increases rapidly with beam energy, therefore it is advantageous to use the maximum beam energy available within the safe Coulomb-excitation constraint discussed in Sec. 3.1.3. The choice of a low-Z target limits multi-step Coulomb excitation and the low-Z ensures a low barrier energy, closer to the experimental beam energy available from the 14UD Pelletron. Details of the beam and barrier energies are given in Table 4.1. The available experimental beam energy is $\sim$ 50% of

Table 4.1: Beam details in the Cd single-step Coulomb-excitation measurements. E_B is the beam energy, E_{safe} is the maximum safe energy for Coulomb excitation with head-on collisions particles (see text for details), and $E_{barrier}$ is the Coulomb barrier in the lab frame.

Beam	Target	E_B (MeV)	E_{safe} (MeV)	$E_{barrier}$ (MeV)
^{111}Cd	^{12}C	240.0	314.5	499.3
^{112}Cd	^{12}C	240.0	316.7	502.3
^{113}Cd	^{12}C	240.0	318.8	505.3

the barrier energy, far below the safe Coulomb-excitation beam energy.

A copper foil of thickness ∼12.5 μm was heated between Ta plates under vacuum to remove contaminants from the surface. The cleaned foil was then "painted" with a carbon suspension in isopropyl alcohol, which evaporated leaving a carbon layer with an average thickness of 0.4 mg/cm^2. The average target thickness was determined through dividing the total mass of the carbon layer by the total area of the carbon layer and is therefore subject to local variation. The thin C layer limits the range of interaction energies in the experiment and ensures enough energy in the recoiling C nuclei to pass through the backing to reach the particle detectors placed forward of the target. A thick backing was chosen in order to stop the beam particles before decay avoiding Doppler broadening and achieving a narrow γ-ray line. The copper backing was used for several reasons. Copper is easily manipulated and obtained, it is significantly heavier than C so that copper recoils will not reach the particle detectors, and it has good thermal conductivity, reducing the effects of beam heating.

4.1.2 Detection electronics

4.1.2.1 Detection of γ rays

Detection of γ rays in this experiment was enabled through the use of four high purity germanium (HPGe) detectors with properties as shown in Table 4.2. Detectors were placed such that the half-opening angles of the detectors were all 18°. The detector angles were placed near zero-gradient points in the $E2$ angular correlations in order to minimise the uncertainty in count rate from possible small-angle offsets in detector position. A picture of the HPGe detectors around the target chamber is displayed in Fig. 4.1.

4.1.2.2 Particle detectors

Recoiling particles were detected in three silicon photodiodes placed 28.9 mm downstream from the target. These detectors had an active width of 8.84 mm and an active height of 9.25 mm and were placed vertically in line with each other as shown in Fig. 4.2. The central ("Inner") particle detector was centred on the beam axis in line with the centre of the target. The remaining two ("Outer") particle detectors

Table 4.2: Detectors and angles used in the single-step Coulomb-excitation measurement of ^{111,112,113}Cd beams on a C target at 240 MeV..

Name	Angle	Diameter	Length	Rel. Eff.
Wallace	45°	62.8	72.0	$\sim$ 50%
Gromit	-45°	62.9	68.0	$\sim$ 50%
OBI-1	135°	55.8	78.7	$\sim$ 35%
OBI-2	-135°	55.8	81.5	$\sim$ 35%

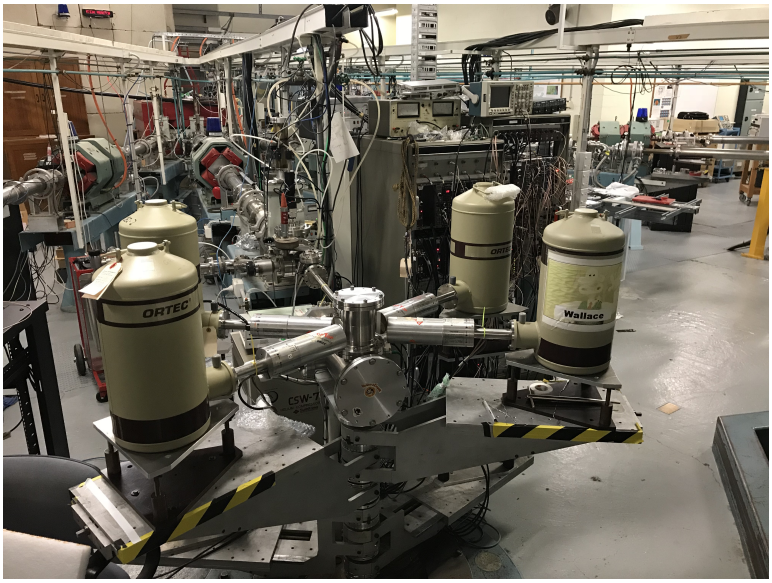

Figure 4.1: The four HPGe detectors used in the single-step Coulomb-excitation measurement of Cd placed around the target chamber.

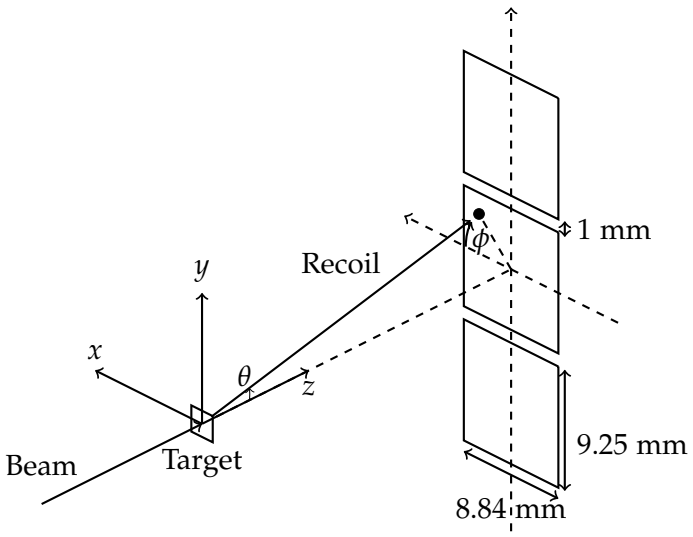

Figure 4.2: Particle-detector geometry used in the single-step ^{111,112,113}Cd Coulomb-excitation measurements.

were placed above and below the central particle detector with 1 mm offsets from the edges of the central detector.

4.1.2.3 Data acquisition system

Triggerless data were recorded using a 100-MHz Pixie-16 digital data acquisition system [104] in list mode. Event construction was performed with a 1-μs window. A single detection trigger starts event construction. All entries for 1 μs are included, and event construction times are extended to 1 μs after the final detection time.

4.2 Results

4.2.1 Efficiency correction

A relative efficiency calibration of the HPGe detectors was performed using a ^{152}Eu source, which was also used for the energy calibration. Absolute efficiency calibrations were performed with a ^{60}Co source using the cascade method [105] and checked using the known activity of the source. These two efficiency calibrations (absolute and relative) were combined to determine the absolute efficiency across the observed energy range. The cascade method using a ^{60}Co source with four HPGe detectors allows three separate measurements of the absolute efficiency at each of the γ-ray decay energies from the source in each particle detector. The efficiencies determined through these measurements vary by $\sim$2%; the source has a supplier-estimated uncertainty in the activity of 5%, however the cascade method does not require a known activity. A 2% uncertainty in the efficiency was propagated in further analysis.

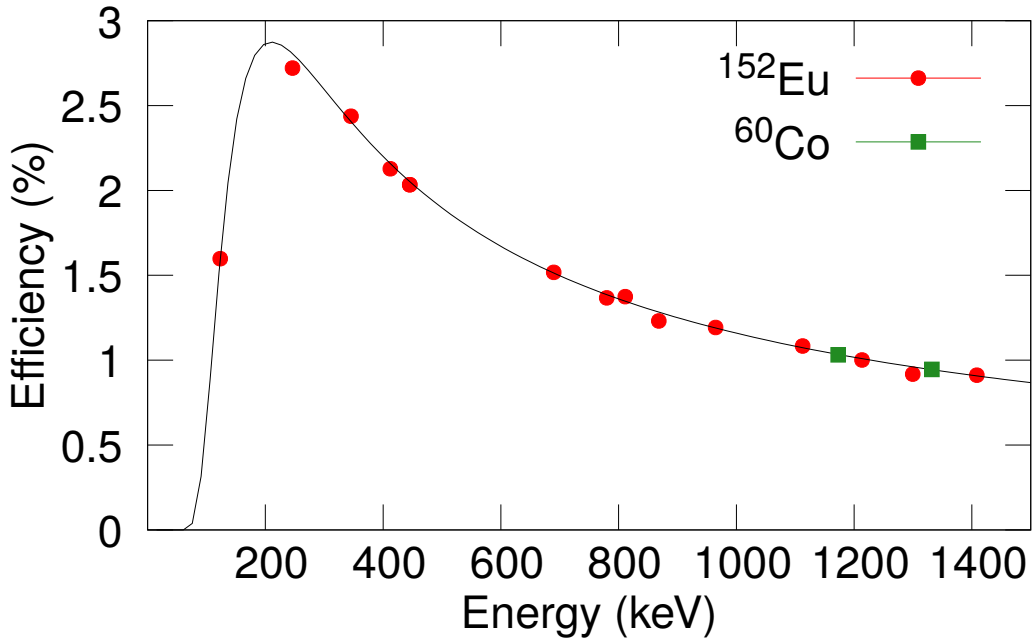

Figure 4.3: Efficiency curve used in the single-step ^{111,112,113}Cd Coulomb-excitation measurements. The absolute efficiency points from the ^{60}Co decay are shown in green squares. Relative efficiency points from the ^{152}Eu decay have been scaled to the absolute efficiency points, and are shown in red points. Uncertainties are smaller than the data points.

4.2.2 Coulomb-excitation analysis

Analysis was performed using the semiclassical Coulomb-excitation analysis code GOSIA [96]. Statistical uncertainties in measured $B(E2)$ values in the odd-mass nuclei were determined with the correlated error analysis included in GOSIA. All stopping powers were taken to be those from Ref. [106]. The internal conversion coefficients were obtained within GOSIA through the BRICC database [107].

4.2.3 ^{112}Cd

An example particle-γ coincidence energy spectrum from the ^{112}Cd measurement is displayed in Fig. 4.4. The spectrum is clean, with only the $2_1^+ \rightarrow 0_{\text{g.s.}}^+$ transition visible. Doppler broadening can be discerned around the base of the peak and is visible on both sides as the spectrum contains data from both front- and back-facing detectors. The Doppler tails can easily be included in the peak sum as there is no Compton background to obscure the tails, even with relatively low statistics.

The determined Coulomb-excitation to Rutherford ratio and corresponding $B(E2)$ values are given in Table 4.3, along with a comparison to the literature value determined in a 2016 evaluation of known $B(E2)$ values performed by Pritychenko *et al.* [41]. The present value of 37.6(5) W.u. is considerably higher than the accepted value of 31.2(14) W.u. There are few experimental parameters that could cause an overestimation of the measured $B(E2)$. One possibility may be the target properties. While the carbon paint may be expected to be close to the measured thickness on average, there may be a variable target thickness across the target. The measurements performed may not be suitable for Rutherford normalisation for this reason. However, considering the previous measurements, displayed in Fig. 4.5, it can be seen that the low value of the evaluated $B(E2)$ is largely determined by two high-statistics measurements [108; 109]. Other previous measurements of the $2_1^+ \rightarrow 0_{\text{g.s.}}^+$ transition strength in ^{112}Cd have on average been higher, although not as high as the present value. Assuming the present values are indeed too high, a satisfactory explanation for the extracted values from the present work was not found, and hence no correction could be applied to further measurements.

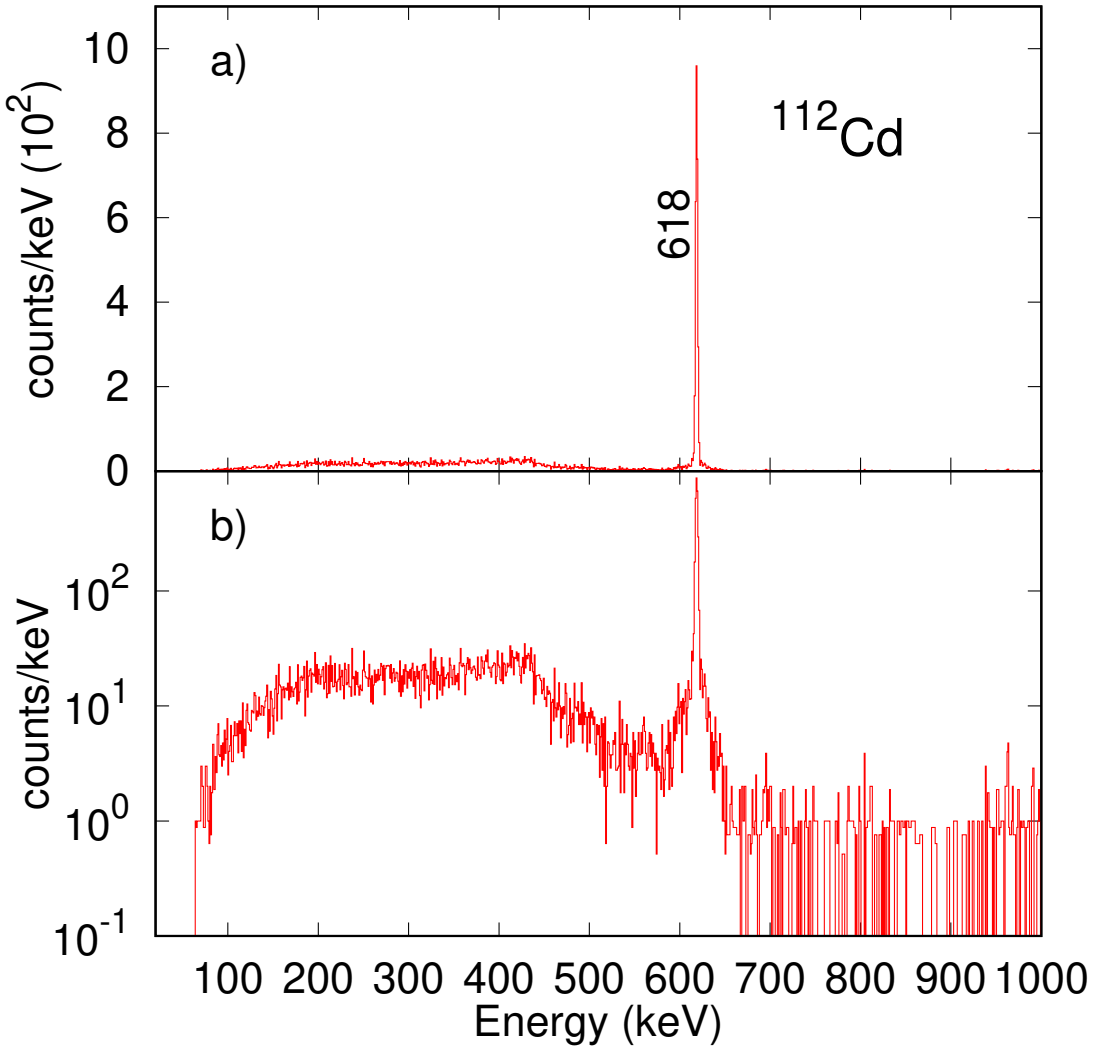

Figure 4.4: An example γ-ray spectrum from the single-step Coulomb excitation of ^{112}Cd with a) linear scale, and b) log scale. This spectrum contains combined data from all front- and back-facing HPGe detectors in coincidence with the central particle detector.

Table 4.3: Experimental $B(E2)$ values from single-step Coulomb excitation of ^{112}Cd. Literature value from Ref. [41].

E_i	I_i^π	E_γ	E_f	I_i^π	$\sigma_{\text{Coul.}}/\sigma_{\text{Ruth.}}$		$B(E2; I_i^\pi \rightarrow I_f^\pi)$	
(keV)		(keV)	(keV)		Inner ($\times 10^{-3}$)	Outer ($\times 10^{-3}$)	Present (W.u.)	Lit. (W.u.)
618	2^+	618	0	0^+	30.8(5)	25.7(5)	37.6(5)	31.2(14)

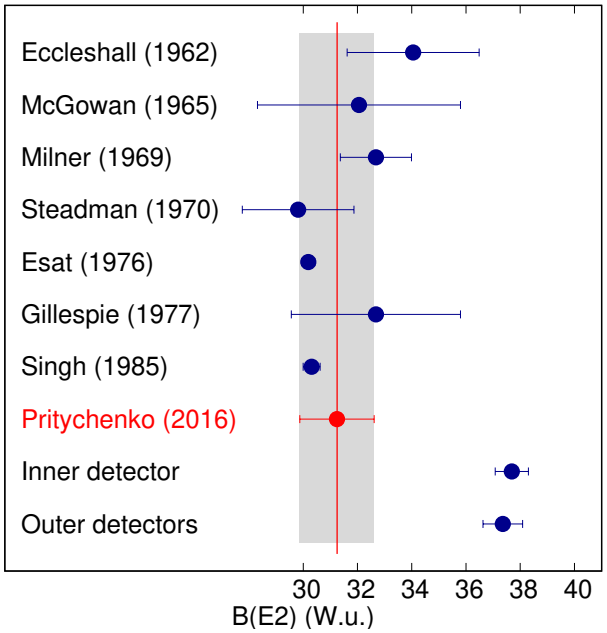

Figure 4.5: Comparison of $B(E2)$ values from the present single-step Coulomb excitation of ^{112}Cd compared to literature values from Refs. [110; 111; 112; 113; 108; 114; 109; 41]. The value from Pritychenko *et al.* (in red) is an evaluation of the literature performed in 2016. The present values from particle-γ coincidences with the inner and outer particle detectors are displayed separately.

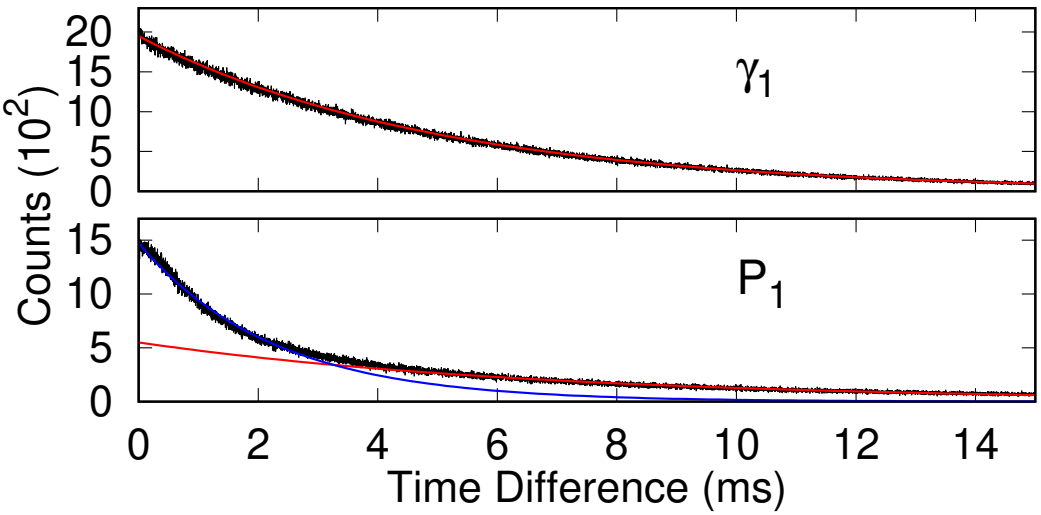

Figure 4.6: Time differences between consecutive detection events in an example γ-ray detector and an example particle-detector. The red and blue curves are exponential functions.

In pursuit of the cause of the discrepancy between the present work and the literature values, it was noted that the particle detectors had not been functioning as expected when coupled to the digital data acquisition. Examples of the time between consecutive events in both a γ-ray detector and a particle detector are displayed in Fig. 4.6. While the γ-ray detector displays the expected exponential decay based on the rate of the γ-ray detections, the time differences for the particle detectors times form a curve which is clearly non-exponential. This remains true for small subsections of the data set as well, so it is not likely to be caused by a varying particle-detection rate during the measurement. Investigating this unexpected behaviour led to the identification of low-frequency, high-amplitude, beam-induced background in the particle detectors. This beam-induced background was filtered by analog electronics in the subsequent transient-field g-factor measurements on the Te isotopes discussed in Chapter 7.

4.2.4 ^{111}Cd

An example particle-γ coincidence energy spectrum is displayed in Fig. 4.7. The measured ^{111}Cd spectrum, contains many more lines than the ^{112}Cd spectrum with high-lying states creating Compton backgrounds for peaks from lower-lying states. This can lead to the obscuring of Doppler tails. While the tails hold very little of the intensity of the transition, they can appear to be higher backgrounds, reducing the determined intensity. Where possible, background regions further away from the transition stop-peak were used to alleviate this issue. The observed intensity of the ^{110}Cd peak in the spectrum corresponds to a negligible ^{110}Cd beam contamination. As the beam is injected as $^{111}CdO^-$ the ^{110}Cd contamination may be due to

a $^{110}CdOH^-$ contamination in the injected beam. No ^{111}Cd peaks from $^{111}CdOH^-$ contamination are seen in the ^{112}Cd spectrum. Figure 4.8 shows the measured level scheme. Transition widths correspond to measured γ-ray intensities without internal conversion corrections.

It was noted in Section 4.2.3 that, due to target preparation concerns, the data may not be suitable for Rutherford normalisation analysis. In order to investigate this further, the sensitivity of the Coulomb-excitation to Rutherford ratio as a function of target thickness, or equivalently to energy loss in the target, was investigated. This ratio was found to increase by $\sim$ 1% per MeV of energy-loss difference compared to the expected energy loss from the average C thickness. In contrast, the yields of the transitions measured relative to the 342-keV transition are displayed in Fig. 4.9 and are found to be relatively insensitive to the energy loss. A change in beam-energy loss of $\sim$ 30% corresponds to a maximum difference in the relative intensities of $\sim$ 4%. Systematic uncertainty from the stopping powers are of a similar magnitude; these uncertainties are propagated in further analysis. The uncertainty from a relative measurement would therefore be largely determined by the 8% uncertainty in the literature value for the strength of the 342-keV transition. Further discussion will assume that the present measurement can be made with Rutherford normalisation. It will be shown that in this case there is very little difference in the relative results from Rutherford normalisation versus normalisation to the 342-keV transition. This is due to agreement between the transition strengths of the normalisation transitions obtained in ^{111}Cd and ^{113}Cd in the present work and literature values.

The excitation of the 342-, 620-, and 753-keV states is each dependent >95% on a single matrix element to the ground state (according to the GOSIA calculations). The yield is determined by the amount of direct excitation, the branching ratios for each transition out of each state, and feeding from above states. Precise branching ratios for each of the transitions out of these states are known from β-decay studies [115]. The final $\sim$ 5% of excitation occurs in multi-step paths through other excited states. Accurate calculation of this excitation requires knowledge of the $E2$ transition strengths between these states. These strengths can be restricted by known mixing ratios. Therefore, literature mixing ratios were used to restrict the matrix elements further [90]. The transition strengths for the transitions from the 245- and 417-keV states are highly constrained by direct lifetime measurements [90]. The literature data are summarised in Table 4.4.

The fitted $B(E2)$ values are compared with literature values in Table 4.5. The starred data were excluded from the fitting procedure; the efficiency was not well characterised at 97 keV and the 245-keV state is populated through decays from higher states and the relevant ground-state matrix element is set by direct lifetime measurements. The present value for the $3/2^+_1 \rightarrow 1/2^+_{\text{g.s.}}$ transition agrees with the previously known value; the values for the ground-state transitions of the 620- and 753-keV states are therefore not dependent on whether the normalisation is relative to Rutherford or to the 342-keV state. The measured $E2$ transition strength of the ground-state transition out of the 620-keV state agrees well with previous measurements. The $B(E2)$ of the 753-keV transition is higher than the previous measurement.

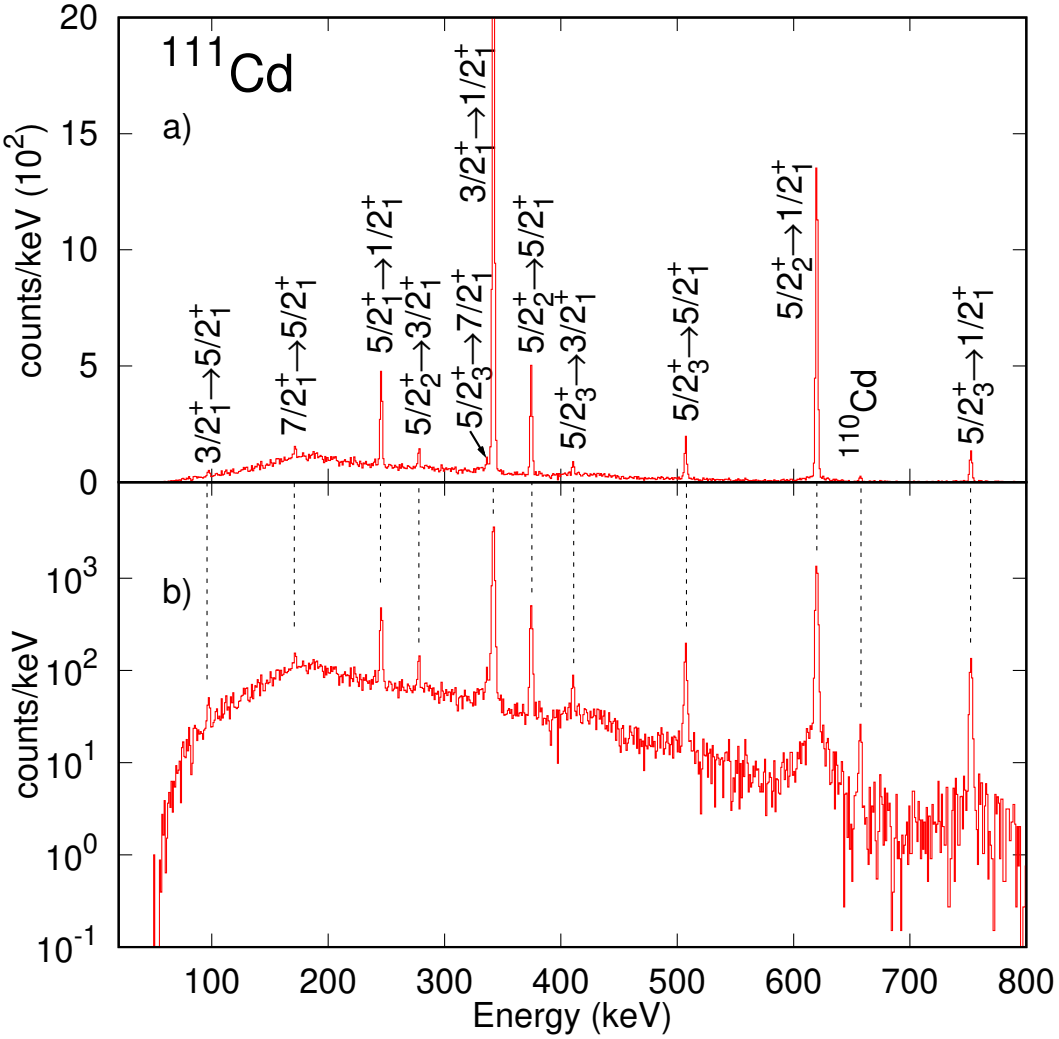

Figure 4.7: An example γ-ray spectrum from the single-step Coulomb excitation of ^{111}Cd with a) linear scale, and b) log scale. This spectrum represents all data in coincidence with the inner particle detector from all HPGe detectors.

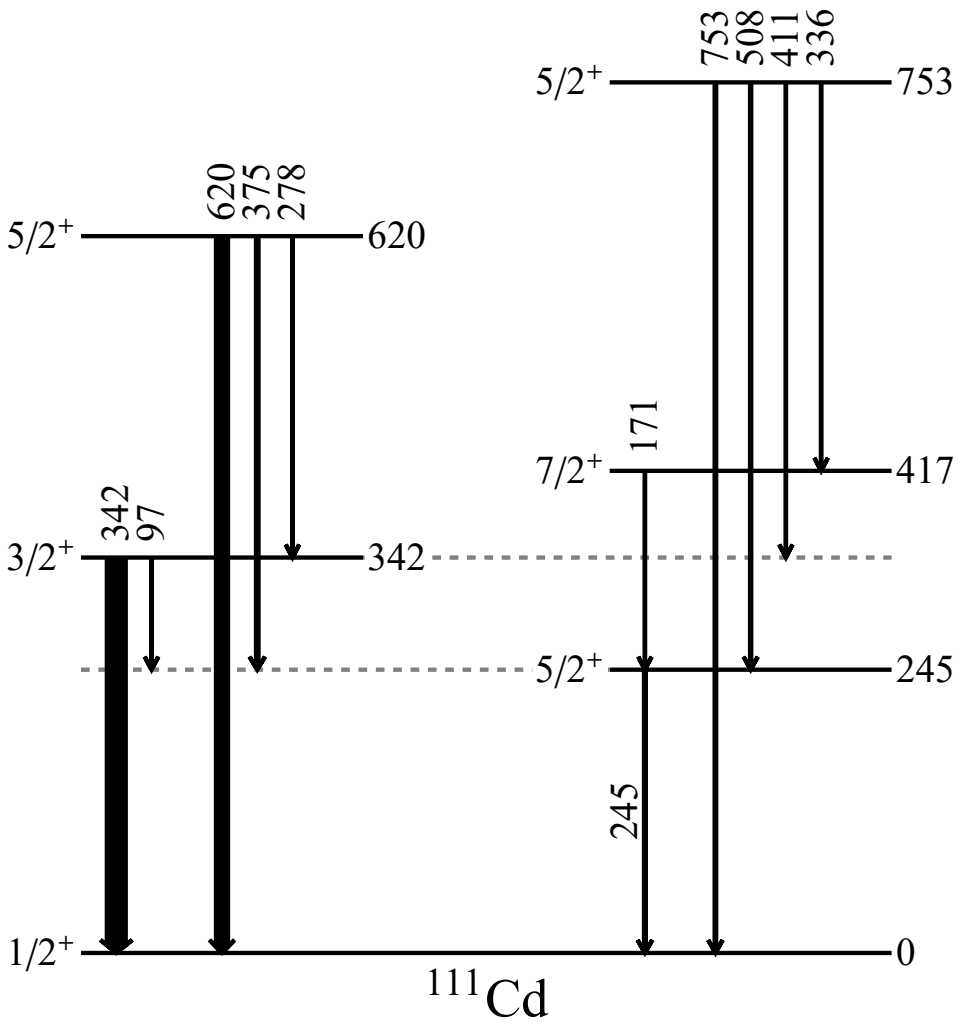

Figure 4.8: The ^{111}Cd level scheme measured in single-step Coulomb excitation. Transition width corresponds to measured γ-ray intensity.

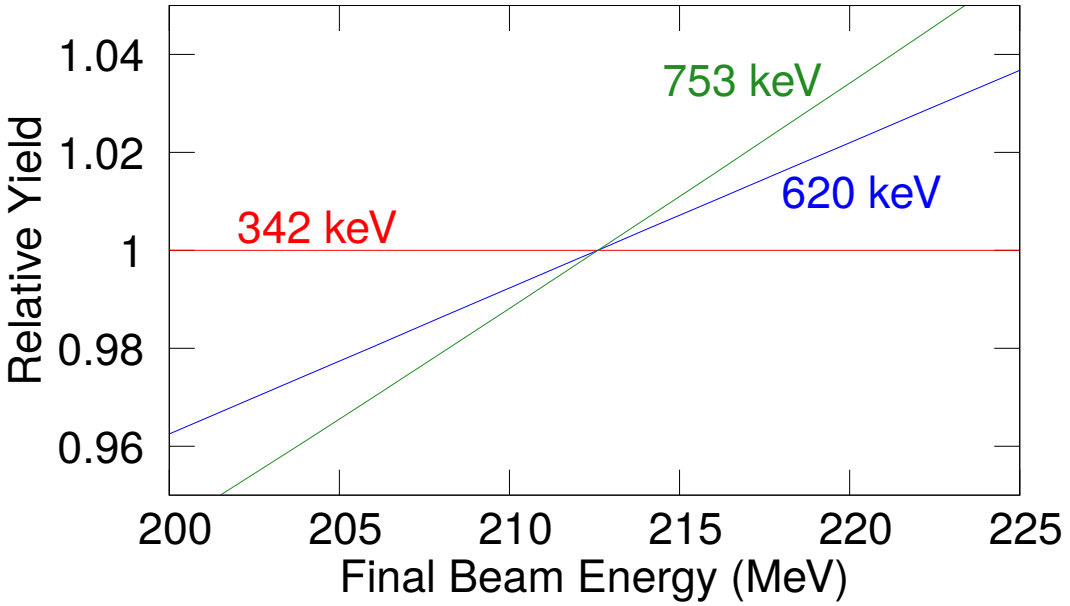

Figure 4.9: Calculated ^{111}Cd Coulomb-excitation yields of transitions, relative to the 342-keV transition, as a function of the beam energy on exit from the C layer. The crossover point is determined by the energy loss of the average target thickness.

Table 4.4: Literature data used in GOSIA fitting of $B(E2)$ values in single-step Coulomb excitation of ^{111}Cd. Data are taken from Refs. [90; 115].

E_i (keV)	τ	I_i^π	E_γ (keV)	E_f (keV)	I_i^π	$X\lambda$	δ	BR
0		$\frac{1}{2}^+$						
245	121.9(6) ns	$\frac{5}{2}^+$	245	0	$\frac{1}{2}^+$	$E2$		100
342		$\frac{3}{2}^+$	97	245	$\frac{5}{2}^+$	$M1+E2$	0.12(4)	1.46(3)
			342	0	$\frac{1}{2}^+$	$M1+E2$	+0.36(2)	100(1)
417	173(43) ps	$\frac{7}{2}^+$	171	245	$\frac{5}{2}^+$	$M1+E2$	-0.144(3)	100
620		$\frac{5}{2}^+$	278	342	$\frac{3}{2}^+$	$M1+E2$		4.9(9)
			375	245	$\frac{5}{2}^+$	$M1+E2$	+2.8(5)	27.2(9)
			620	0	$\frac{1}{2}^+$	$E2$		100(1)
753		$\frac{5}{2}^+$	336	417	$\frac{7}{2}^+$	$(M1+E2)$		13(2)
			411	342	$\frac{3}{2}^+$	$M1+E2$	-0.05(3)	41(4)
			508	245	$\frac{5}{2}^+$	$(M1+E2)$		100(2)
			753	0	$\frac{1}{2}^+$	$E2$		99(2)

The new value is in better agreement with a recent DSAM measurement that found a lifetime equivalent to an 11(5) W.u. transition strength [85].

Table 4.5: Experimental data used in GOSIA fitting of $B(E2)$ values and fitted $B(E2)$ values from single-step Coulomb excitation of ^{111}Cd. Starred data were excluded from the fitting routine (see text for details). Data are taken from present measurements and Ref. [90].

E_i	I_i^π	E_γ	E_f	I_f^π	$\sigma_{\text{Coul.}}/\sigma_{\text{Ruth.}}$		$B(E2; I_i^\pi \to I_f^\pi)$	
(keV)		(keV)	(keV)		Inner detector ($\times 10^{-4}$)	Outer detector ($\times 10^{-4}$)	Present (W.u.)	Lit. (W.u.)
0	$\frac{1}{2}^+$							
245	$\frac{5}{2}^+$	245	0	$\frac{1}{2}^+$	8.3(4)*	6.6(3)*		0.2374(12)
342	$\frac{3}{2}^+$	97	245	$\frac{5}{2}^+$	3.2(8)*	2.1(7)*		
		342	0	$\frac{1}{2}^+$	87(1)	70.7(9)	17.4(12)	17.4(14)
417	$\frac{7}{2}^+$	171	245	$\frac{5}{2}^+$	1.7(4)	0.7(3)		21(6)
620	$\frac{5}{2}^+$	278	342	$\frac{3}{2}^+$	2.1(3)	1.2(3)		
		375	245	$\frac{5}{2}^+$	11.4(4)	10.4(4)		
		620	0	$\frac{1}{2}^+$	55.4(9)	43.6(8)	15.4(11)	15.9(23)
753	$\frac{5}{2}^+$	336	417	$\frac{7}{2}^+$				
		411	342	$\frac{3}{2}^+$	1.9(2)	1.5(3)		
		508	245	$\frac{5}{2}^+$	5.7(3)	5.4(3)		
		753	0	$\frac{1}{2}^+$	6.9(4)	5.6(3)	5.5(4)	4.4(8)

Table 4.6: Literature data used in GOSIA fitting of $B(E2)$ values in single-step Coulomb excitation of ^{113}Cd. Data are taken from Ref. [93].

E_i (keV)	τ	I_i^π	E_γ (keV)	E_f (keV)	I_i^π	$X\lambda$	δ	BR
0		$\frac{1}{2}^+$						
299	15.6(4) ns	$\frac{3}{2}^+$	299	0	$\frac{1}{2}^+$	$M1+E2$	+0.30(3)	100
316		$\frac{5}{2}^+$	316	0	$\frac{1}{2}^+$	$E2$		100
459		$\frac{7}{2}^+$	143	316	$\frac{5}{2}^+$	$M1+E2$	-0.04(3)	100
584		$\frac{5}{2}^+$	268	316	$\frac{5}{2}^+$			1.4(2)
			285	299	$\frac{3}{2}^+$			2.5(2)
			584	0	$\frac{1}{2}^+$	$E2$		100
681		$\frac{3}{2}^+$	365	316	$\frac{5}{2}^+$	$M1+E2$	-0.02(7)	20.1(4)
			382	299	$\frac{3}{2}^+$	$M1+E2$	+0.16(15)	20.0(4)
			97	584	$\frac{5}{2}^+$	$(M1+E2)$		5.2(3)
			681	0	$\frac{1}{2}^+$	$M1+E2$	-1.8(1)	100(1)
709		$\frac{5}{2}^+$	393	316	$\frac{5}{2}^+$	$M1+E2$	-0.24(4)	13(2)
			709	0	$\frac{1}{2}^+$	$E2$		41(4)

4.2.5 ^{113}Cd

An example of a particle-γ coincidence energy spectrum from the ^{113}Cd measurement is displayed in Fig. 4.10. The measured level scheme can be seen in Fig. 4.11. Transition widths correspond to the measured γ-ray intensities.

The same procedures as discussed in Sec. 4.2.4 were followed. The relevant nuclear structure information from the literature is presented in Table 4.6. This nuclear structure information was taken from Refs. [93; 116].

The transition strengths determined in the present work are given in Table 4.7. Once again, the transition strengths are in good agreement with the literature values [93].

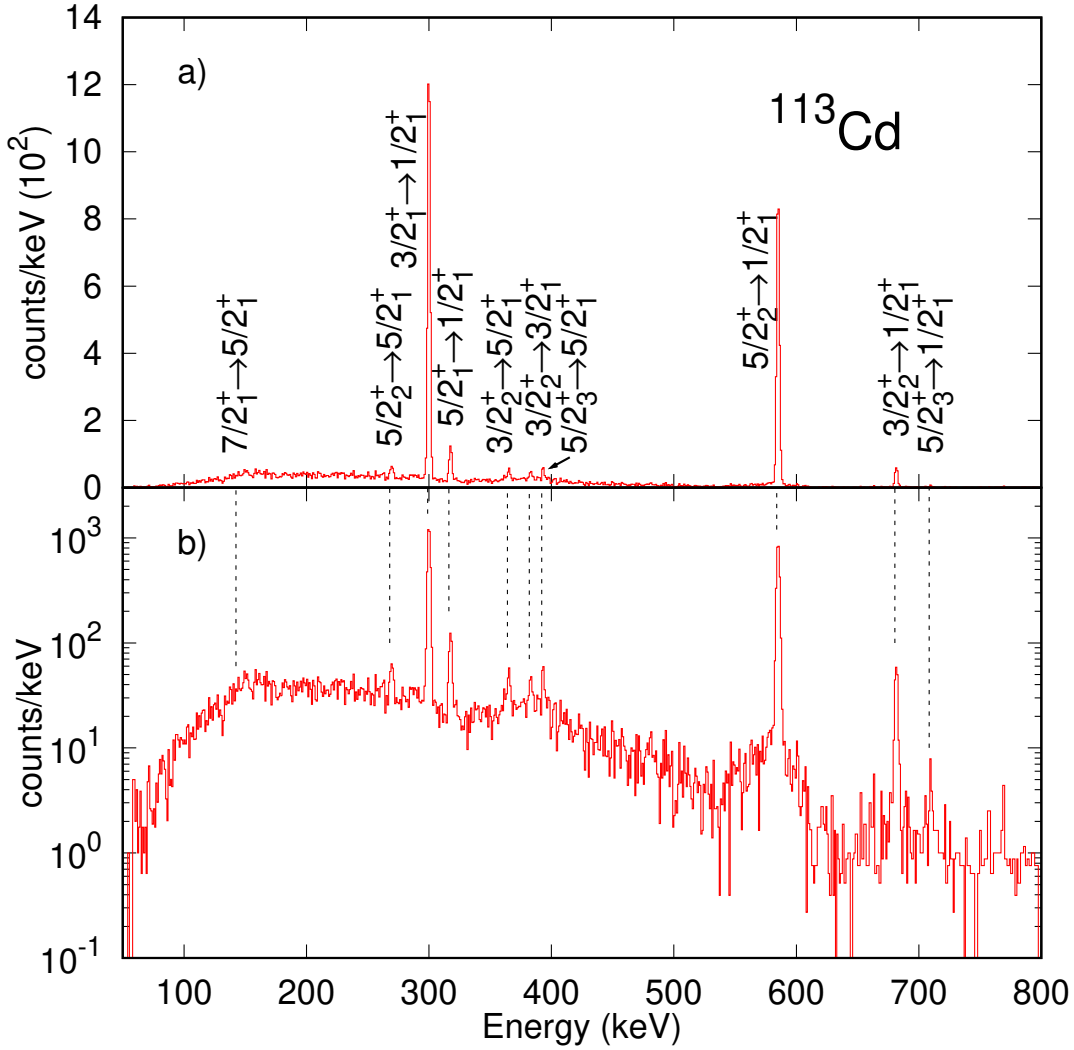

Figure 4.10: An example γ-ray spectrum from single-step Coulomb excitation of ^{113}Cd with a) linear scale, and b) log scale. This spectrum represents all data in coincidence with the inner particle detector from all HPGe detectors.

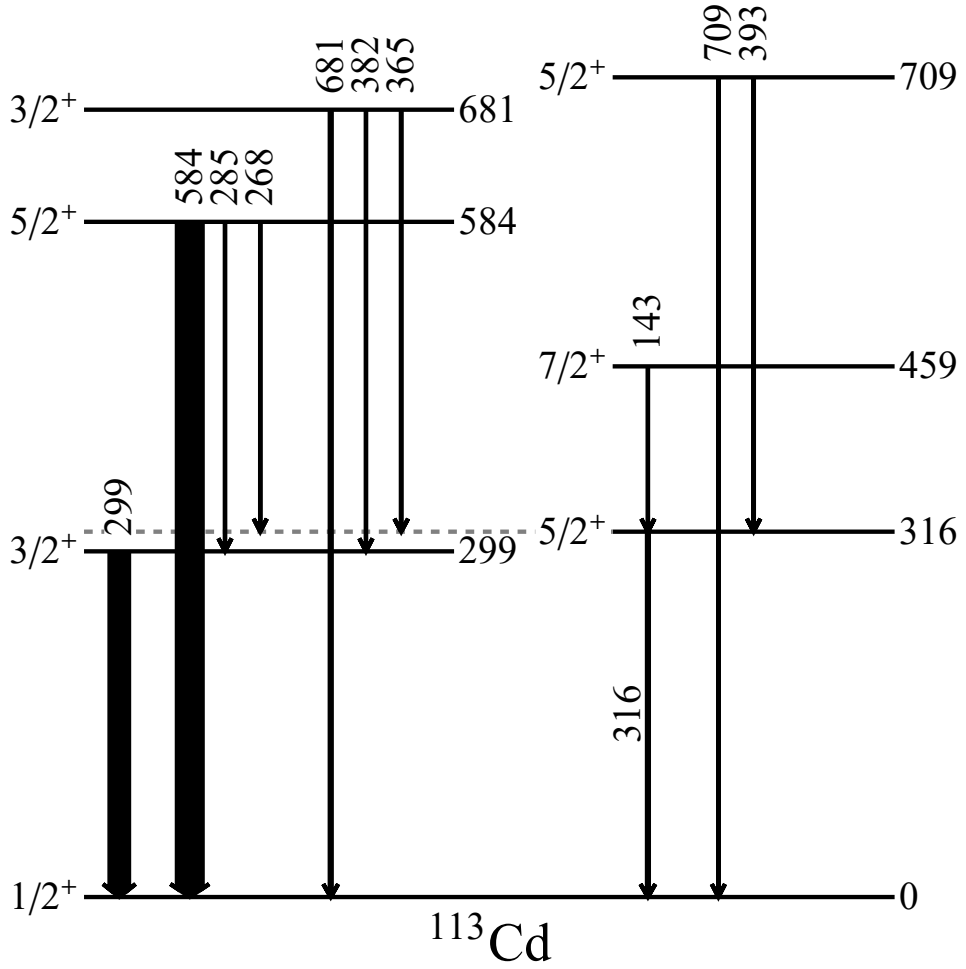

Figure 4.11: Measured ^{113}Cd level scheme in single-step Coulomb excitation.

Table 4.7: Experimental data used in GOSIA fitting of $B(E2)$ values and fitted $B(E2)$ values from single-step Coulomb excitation of ^{113}Cd. Data are taken from present measurement and Refs. [93; 116].

E_i	I_i^π	E_γ	E_f	I_f^π	$\sigma_{\text{Coul.}}/\sigma_{\text{Ruth.}}$		$B(E2; I_i^\pi \to I_f^\pi)$	
(keV)		(keV)	(keV)		Inner detector ($\times 10^{-4}$)	Outer detector ($\times 10^{-4}$)	Present (W.u.)	Lit. (W.u.)
0	$\frac{1}{2}^+$							
299	$\frac{3}{2}^+$	299	0	$\frac{1}{2}^+$	90(2)	72.7(15)	22.8(15)	20(8)
316	$\frac{5}{2}^+$	316	0	$\frac{1}{2}^+$	8.6(6)	6.2(5)		0.372(25)
459	$\frac{7}{2}^+$	143	316	$\frac{5}{2}^+$				
584	$\frac{5}{2}^+$	268	316	$\frac{5}{2}^+$	2.5(5)	1.3(5)		
		285	299	$\frac{3}{2}^+$				
		584	0	$\frac{1}{2}^+$	119(2)	98(2)	35.7(24)	34(8)
681	$\frac{3}{2}^+$	365	316	$\frac{5}{2}^+$	3.1(5)	2.5(5)		
		382	299	$\frac{3}{2}^+$	1.3(6)	2.4(5)		
		681	0	$\frac{1}{2}^+$	8.9(6)	9.5(7)	12(1)	11(2)
709	$\frac{5}{2}^+$	393	316	$\frac{5}{2}^+$	3.8(6)	2.1(5)		
		709	0	$\frac{1}{2}^+$	1.1(2)	1.0(2)	2(1)	

In this chapter, measurements of $E2$ strengths in transitions from the low-lying energy levels in ^{111}Cd and ^{113}Cd have been reported. Although the increased transition strengths measured in ^{112}Cd have not been explained in a way that can be applied to data from the ^{111}Cd and ^{113}Cd measurements, the transition strengths in ^{111}Cd and ^{113}Cd reported in the present work are in good agreement with previous results, but with generally smaller uncertainties. The measured uncertainties in the transition strengths of strongly excited states from the Rutherford-normalised analysis are limited by the uncertainty in the target thickness and the presence of Doppler broadening, future measurements with a target of known, consistent thickness or with a thin target and high-precision position sensitivity in particle and γ-ray detection could reduce the measured uncertainties. In the next chapter, the level scheme of ^{111}Cd excited in multi-step Coulomb excitation is explored. The results of these measurements are then combined for discussion in Chapter 6.

Chapter 5

Multi-step Coulomb excitation of ^{111}Cd

In this chapter the results of a multi-step Coulomb-excitation measurement on ^{111}Cd are discussed. The measurement used GRETINA, the first stage of the HPGe Gamma-Ray Energy Tracking Array (GRETA), and the position-sensitive CHICO2 particle-detector array. The use of the position-sensitive detectors for detailed Coulomb-excitation measurements on odd-mass nuclides and the considerations, requirements and limitations for such experiments are explored in this chapter.

5.1 Multi-step ^{111}Cd Coulomb-excitation experiment

5.1.1 Experiment background

The data for this analysis were obtained as a by-product of a radioactive-ion beam measurement on Coulomb excitation of ^{106}Mo at the CARIBU/ATLAS facility [117] with Dr. J. M. Allmond as the spokesperson. In that measurement, there was a significant ^{111}Cd contaminant in the beam. It was not possible to separate the detected ^{106}Mo and ^{111}Cd due to overlap in the particle-identification metric. Additionally, the key $2_1^+ \rightarrow 0_{\text{g.s.}}^+$ transition in ^{106}Mo at 171.5 keV overlaps with the $^{7}/_{2}^+_1 \rightarrow {}^{5}/_{2}^+_1$ transition at 171.3-keV in ^{111}Cd. In order to account for the contaminant line, a specific measurement of stable ^{111}Cd was performed. The calibration run was short, which allows limited analysis of the data, however this is the first multi-step Coulomb-excitation experiment performed for ^{111}Cd. Thus, any new information that can be extracted from the data is of interest, and limitations on what can be extracted will inform the planning of future experiments.

5.1.2 Experimental parameters

The beam-excitation experiment was performed in conventional kinematics with a ^{111}Cd beam on a 1.1 mg/cm^2 $^{\text{nat}}$Pb target. The beam energy was chosen to match the beam energy of the contaminant ^{111}Cd in the ^{106}Mo measurement. The ^{106}Mo beam was at 408 MeV. As the split-ring resonators in the ATLAS accelerate nuclei moving through the machine to the same velocity, the ^{111}Cd beam was therefore at

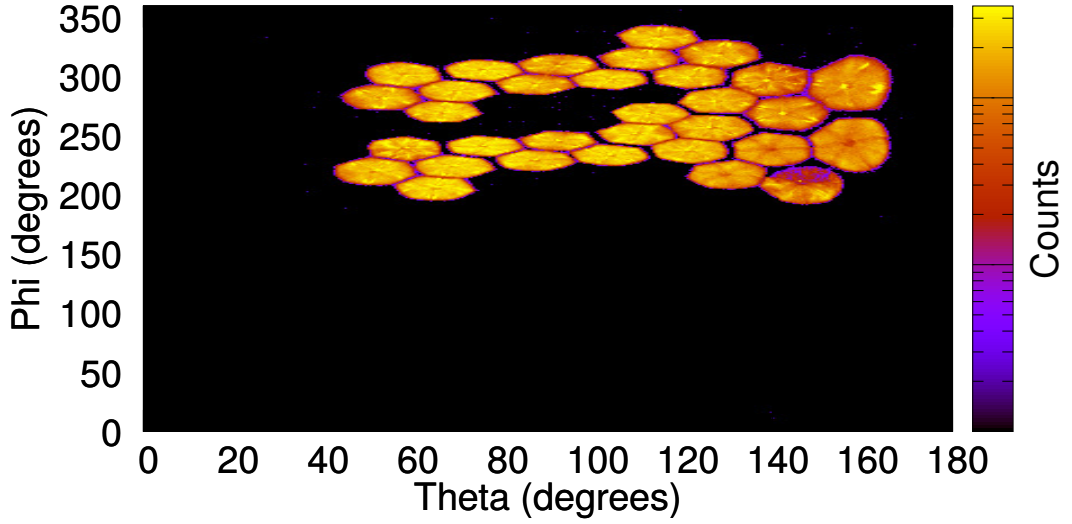

Figure 5.1: GRETINA hit map showing the angular coverage for γ-ray detection.

427 MeV. The total data were accumulated in one ∼90 min run. The safe Coulomb-excitation energy as defined in Sec. 3.1.3 for backscattered particles (head-on collisions) is 472 MeV; therefore, all scattering angles correspond to safe Coulomb excitation.

5.1.3 Detection electronics

5.1.3.1 GRETINA tracking array

GRETINA is the first stage of a HPGe array currently under development, the 4π Gamma-Ray Energy Tracking Array (GRETA) [118]. In the present measurement it consisted of 32 segmented coaxial germanium crystals. The segmentation of the individual germanium crystals along with the waveform analysis allows precise, sub-crystal determination of the position of the primary γ-ray interaction. The positional sensitivity of the detectors in the array has been determined to be ∼2 mm. Another advantage of the array is the large efficiency; GRETINA covers a large solid angle as displayed in the heat map of Fig. 5.1.

5.1.3.2 CHICO2 particle-detector array

Particles were detected by the CHICO2 (Compact Heavy Ion COunter) detector array [119]. CHICO2 is a pixelated parallel-plate avalanche counter with a θ resolution, from the pixelated cathode plate, of ∼1.6° and a ϕ resolution, from the segmented anode, of ∼2.5°. The particle detectors cover angles between 20-167° as shown in Fig. 5.2.

Forward-scattered particles were detected with a coincidence requirement that two segments of CHICO2 must detect particles in the same plane. In this way, both

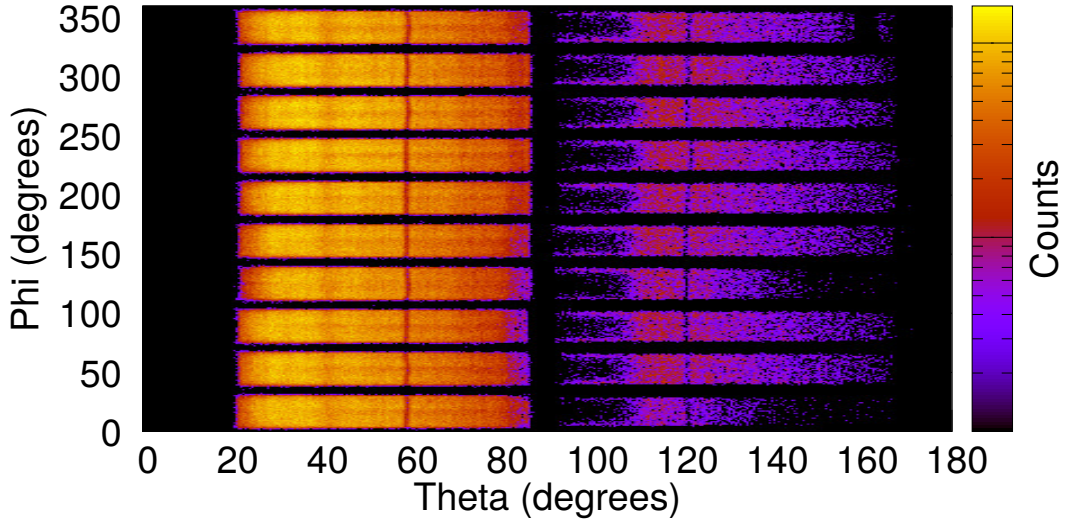

Figure 5.2: Particle hit map as a function of angle for the CHICO2 detector. The x-projection on to the θ coordinate is displayed in Fig. 5.5.

scattering partners are detected. Analysis of the time difference of these particle detections for a given scattering angle allows particle identification of the Cd/Pb pairs used in this experiment. An example plot of this particle-identification statistic is shown in Fig. 5.3. Backscattered ^{111}Cd nuclei were detected with no particle coincidence requirement.

Particle singles and particle-particle coincidence signals from CHICO2 were processed through a CAEN V812 constant fraction discriminator before the signal was input into a CAEN V1495 programmable logic module which handled coincidence logic. The anode and cathode timing were determined using a CAEN V1190A time-to-digital converter.

5.1.4 Velocity and energy-loss calibration

The stopping powers and energy loss of the beam in the target were calibrated using the measured energies of the Doppler shifted γ-rays of the 620 keV transition. The measured velocities are displayed in Fig. 5.4. The red line is calculated assuming no energy loss in the target. The blue line corresponds to scattering in the centre of the target using the Ziegler 1985 [106] stopping powers scaled by a factor of 0.94. A reduction in the scattered beam velocity is observed around 90° due to the greater distance travelled by the nuclei within the target at the scattered angle. The target stands at an angle $\sim$90° to the beam.

5.1.5 Scattering angle divisions

Population of excited states in multi-step Coulomb excitation can occur through multiple paths, and often there are multiple possible solutions that reproduce the mea-

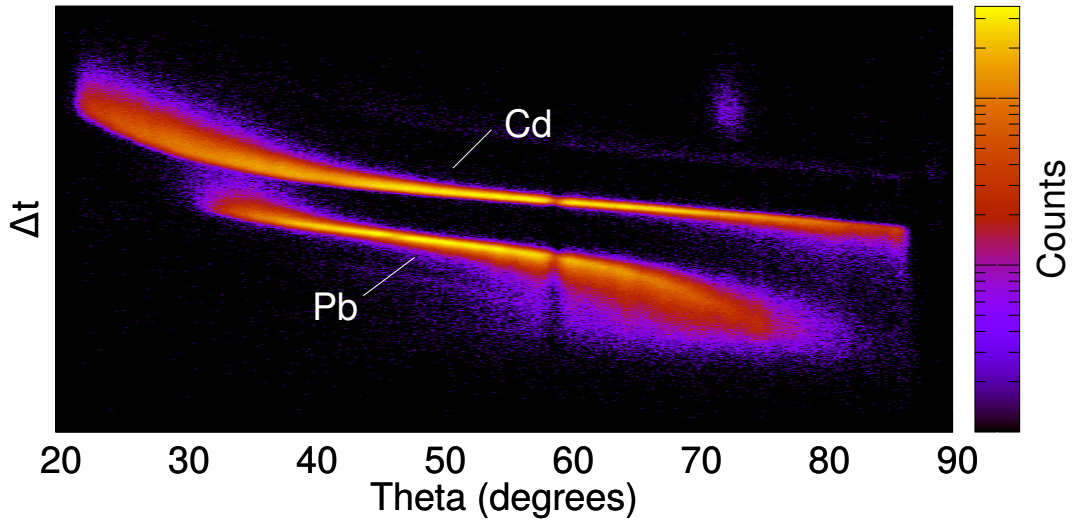

Figure 5.3: The particle-identification statistic used in the identification of scattering partners in CHICO2. The x-axis is the lab-frame scattering angle of an arbitrarily chosen observed particle of the required two coincident particles. The other observed particle is analysed separately. The y-axis is the time difference between the observation of the two particles in CHICO2.

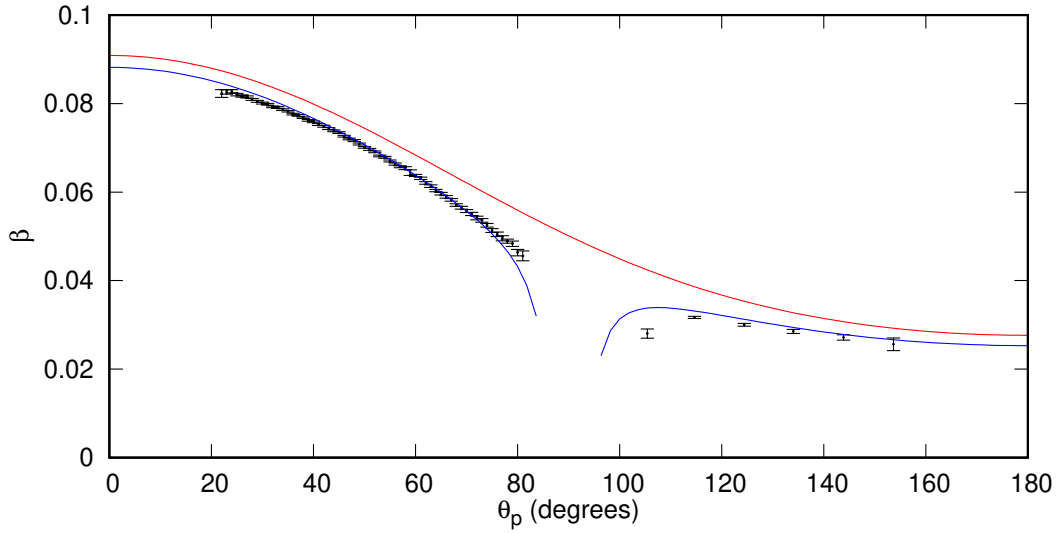

Figure 5.4: Measured velocity of ^{111}Cd from Doppler-shift measurements from the 620-keV transition. The red line is the velocity of the scattered ^{111}Cd ignoring energy loss in the target. The blue line accounts for energy loss using the Ziegler 1985 stopping powers [106] scaled to reproduce the data, and assumes scattering takes place at the centre of the target.

sured excitation yields. Measuring those yields at multiple scattering angles reduces the range of matrix element possibilities that reproduce experiment. The scattering angles are split into divisions over finite ranges in the particle detector. Smaller divisions increase sensitivity, but will be more limited by lower statistics. The scattering angle ranges used in the Coulomb-excitation analysis are presented in Fig. 5.5; the measured particle energy spectrum is split into angular ranges (divisions) by colour. It is clear that at small angles and angles near 90° the particle detectors are not fully efficient as the observed curve should appear smooth. Angle ranges were chosen such that the loss of efficiency in four of the scattering angle divisions (divisions 2,3,5,6) was minimised. Division 1 is quite narrow and so the excitation cross section will vary less over the range. A dip is observed above 40° in division 2. A Cd particle which scatters at these angles corresponds to a recoil angle of the complementary Pb particle of around 60° which is a region in which the particle detectors are not sensitive. Division 4 has few statistics, and is unlikely to contribute significantly to the measurement results.

The scattering angle of the beam particles changes the absolute and relative excitation of the excited states and the relative excitation of internal substates of the excited states. An angular-dependent change in the efficiency causes the effective angle of the measurements to be changed. The analysis must take the varying angle-dependent efficiency into account. The angle-dependent loss of efficiency has two effects in the Coulomb-excitation analysis. The first is that the relative excitation yields of the states are altered; this has the direct effect of changing the determined transition strengths as the angular coverage of particle detectors used to calculate the excitation will not be accurate. The second effect is the change to the statistical tensors that determine the angular correlation of decays. The change to the angular correlations and the corrections due to anisotropic decays can have large effects on the extracted matrix elements. The wide range of angles sampled by γ-ray detectors in GRETINA generally averages the observed yields over the angular correlation to get a value close to the average over the total 4π solid angle, which mitigates the effect of the changed angular correlations on the extracted excitation yields. The alignment (and therefore the anisotropy) is maximised at scattering angles close to 180°, while most data are measured at smaller scattering angles. The loss of efficiency is largely at angles which do not produce large anisotropies, which further reduces the limited effect of the anisotropies on extracted matrix elements. It is possible to account for the efficiency of the particle detectors by defining reduced ϕ coverage at specific polar scattering angles (θ) in the excitation calculations, mimicking experiment.

5.2 Results

The observed particle-γ energy spectrum is displayed in Fig. 5.6. A summary of the observed transitions is given in Table 5.1. It was not possible to obtain an intensity for the 245-keV transition due to the long state lifetime. The transition is observed as a sharp peak before Doppler correction. This implied that the ^{111}Cd is stopping before

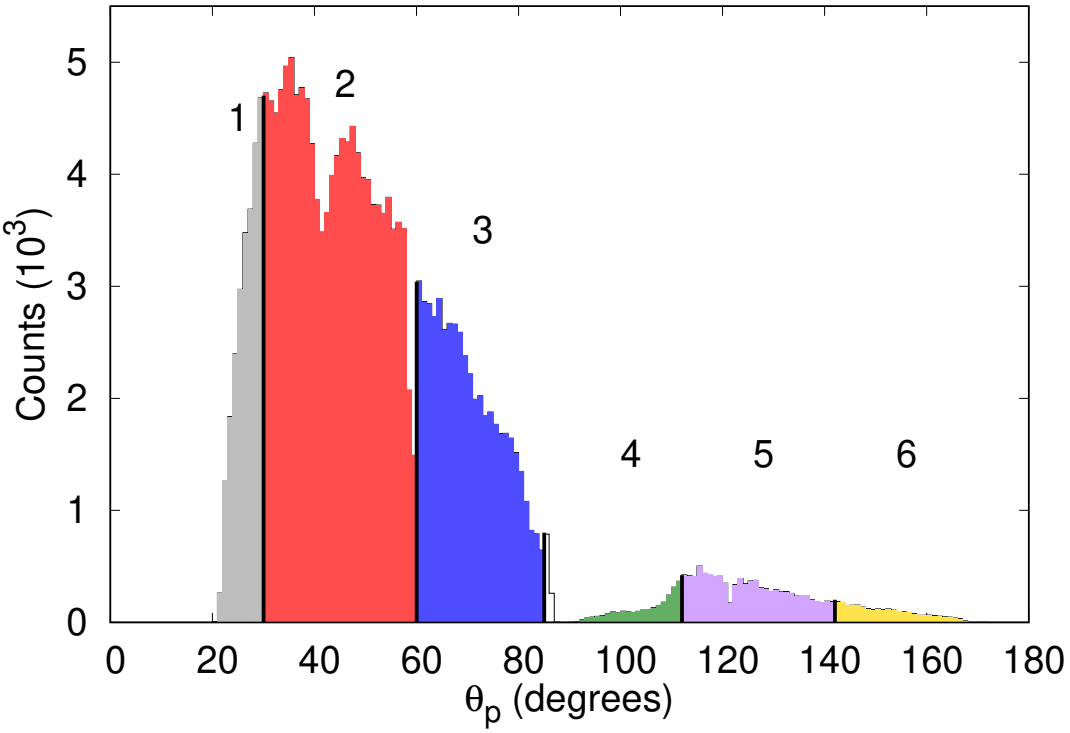

Figure 5.5: Scattering angle divisions for multi-step Coulomb-excitation analysis of ^{111}Cd. The range of scattering angles have been labelled by the integers 1-6 and are separated by colour. The observed angles of the Cd-like particles in valid Cd-Pb pairs in coincidence with an observed γ-ray is displayed in Fig. 5.2.

decaying and the decays are occurring far from the target position. The efficiency is not well defined when the decaying nucleus is not close to the target position.

Table 5.1: Observed states and transitions in multi-step Coulomb excitation of ^{111}Cd. Unresolved doublet intensities are tagged as D, intensities determined from coincidence γ-ray spectra are given the tag C, and new transitions are given the tag N. Unplaced transitions from the states ∼1552 keV, discussed in the text, have been given the tag A. Where possible, level energies, level spin-parities, transition multipolarities, and mixing ratios have been taken from Nuclear Data Sheets [90]. Transition energies are those experimentally determined in the present measurement. The experimental uncertainty in the measured transition energies is of the order of ∼0.2 keV.

E_i	I_i^π	E_γ	E_f	I_f^π	Tags	Intensity	$X\lambda$	δ
0	$\frac{1}{2}^+$							
245.4	$\frac{5}{2}^+$	245.4	0	$\frac{1}{2}^+$			$E2$	
342.1	$\frac{3}{2}^+$	97	245.4	$\frac{5}{2}^+$			$M1$+$E2$	+0.12(4)
		342.2	0	$\frac{1}{2}^+$		10000(90)	$M1$+$E2$	+0.36(2)
416.7	$\frac{7}{2}^+$	171.4	342.1	$\frac{3}{2}^+$		461(10)	$M1$+$E2$	-0.144
620.2	$\frac{5}{2}^+$	203.5	416.7	$\frac{7}{2}^+$		26(4)		
		278.1	342.1	$\frac{3}{2}^+$		303(9)	$M1$+$E2$	$+0.45(^{+25}_{-13})$ or $-1.2(^{+2}_{-4})$
		374.8	245.4	$\frac{5}{2}^+$		1774(16)	$M1$+$E2$	+2.8(5)
		620.2	0	$\frac{1}{2}^+$	C	6094(53)	$E2$	
680.5	$(\frac{9}{2}^-)$	283.6	396.2	$\frac{11}{2}^-$		29(6)	$M1$+$E2$	+0.16(1)
752.8	$\frac{5}{2}^+$	336.9	416.7	$\frac{7}{2}^+$		236(6)		
		410.8	342.1	$\frac{3}{2}^+$		417(10)	$M1$+$E2$	
		507.6	245.4	$\frac{5}{2}^+$		1083(13)		$-0.05(3)$
		753.1	0	$\frac{1}{2}^+$		942(15)	$E2$	
853.9	$\frac{7}{2}^+$	436.9	416.7	$\frac{7}{2}^+$		79(8)		
		609.0	245.4	$\frac{5}{2}^+$		128(5)		

Continued on next page.

Table 5.1 continued.

E_i	I_i^π	E_γ	E_f	I_f^π	Tags	Intensity	$X\lambda$	δ
855.6	$\frac{3}{2}^+$	855.1	0	$\frac{1}{2}^+$		11(2)	$M1$+$E2$	
866.6	$\frac{3}{2}^+$	524.6	342.1	$\frac{3}{2}^+$		61(3)	$M1$+$E2$	+2.4(4)
		621.0	245.4	$\frac{5}{2}^+$	C	243(39)	($M1$+$E2$)	
		866.6	0	$\frac{1}{2}^+$		135(6)	$M1$+$E2$	
986.5	$\frac{9}{2}^+$	569.6	416.7	$\frac{7}{2}^+$		41(6)		
		742.1	245.4	$\frac{5}{2}^+$		15(2)	$E2$	
1016.8	$\frac{3}{2}^+$	1017.5	0	$\frac{1}{2}^+$		8(2)	$M1$+$E2$	$-3.2(6)$
1046.8	$\frac{7}{2}^+$	427.3	620.2	$\frac{5}{2}^+$		73(8)		
		630.2	416.7	$\frac{7}{2}^+$	N			
		704.8	342.1	$\frac{3}{2}^+$		388(9)		
		800.7	245.4	$\frac{5}{2}^+$	D	188(7)		
1078.3	$\frac{3}{2}^+$	833.0	245.4	$\frac{5}{2}^+$		26(2)	$M1$+$E2$	+0.20(4)
		1078.5	0	$\frac{1}{2}^+$	D	41(3)	$M1$+$E2$	$+0.27(^{+4}_{-3})$
1115.6	$\frac{3}{2}^+$	495.8	620.2	$\frac{5}{2}^+$		58(4)	$M1$+$E2$	
		773.9	342.1	$\frac{3}{2}^+$		82(4)	$M1$+$E2$	$+2.8(^{+6}_{-4})$
		1115.7	0	$\frac{1}{2}^+$		232(7)	$M1$+$E2$	$-0.17(3)$
1118.4	$\frac{1}{2}^+$	872.8	245.4	$\frac{5}{2}^+$		48(4)		
1185.7	$\frac{1}{2}^+$	1186.0	0	$\frac{1}{2}^+$		50(3)		
1256.6	$\frac{11}{2}^+$	839.7	416.7	$\frac{7}{2}^+$		14(2)		
1274.7	$(\frac{5}{2})^+$	932.3	342.1	$\frac{3}{2}^+$	D	109(6)		
		1029.1	245.4	$\frac{5}{2}^+$		10(2)		

Continued on next page.

Table 5.1 continued.

E_i	I_i^π	E_γ	E_f	I_f^π	Tags	Intensity	$X\lambda$	δ
1298.6		882.2	416.7	$\frac{7}{2}^+$		20(2)		
		1053.6	245.4	$\frac{5}{2}^+$		33(3)		
1321.6		1322.0	0	$\frac{1}{2}^+$		36(3)		
1340.7	$(\frac{1}{2}, \frac{3}{2})$	721	620.2	$\frac{5}{2}^+$		18(2)		
		1341.1	0	$\frac{1}{2}^+$		15(2)	$M1+E2$	+0.21(9) or $-3.0(^{+7}_{-14})$
1341.3	$(\frac{5}{2})$	924.5	416.7	$\frac{7}{2}^+$		10(2)		
		999.3	342.1	$\frac{3}{2}^+$		27(3)		
1473.0	$\frac{3}{2}^+$	720.2	752.8	$\frac{5}{2}^+$		18(2)		
		1130	342.1	$\frac{3}{2}^+$			$M1+E2$	$-0.21(3)$ or +64(22)
		1226.1	245.4	$\frac{5}{2}^+$		7(1)		
		1471.8	0	$\frac{1}{2}^+$		14(2)		
1511.6		463	1046.8	$\frac{7}{2}^+$	N			
		657.8	853.9	$\frac{7}{2}^+$	N	12(4)		
		891.5	620.2	$\frac{5}{2}^+$		49(3)		
		1095.7	416.7	$\frac{7}{2}^+$		17(2)		
		1267.1	245.4	$\frac{5}{2}^+$		22(2)		
1552.1	$\frac{3}{2}^+$	698	853.9	$\frac{7}{2}^+$	N A	45(3)		
		800.7	752.8	$\frac{5}{2}^+$	D N A	188(7)		
		1210.2	342.1	$\frac{3}{2}^+$		7(1)		
		1306.5	245.4	$\frac{5}{2}^+$		22(2)		
		1551.5	0	$\frac{1}{2}^+$		10(2)		

Continued on next page.

Table 5.1 continued.

E_i	I_i^π	E_γ	E_f	I_f^π	Tags	Intensity	$X\lambda$	δ
1552.4	$(\frac{7}{2}^+, \frac{9}{2}^+)$	698	853.9	$\frac{7}{2}^+$	N A	45(3)		
		800.7	752.8	$\frac{5}{2}^+$	D N A	188(7)		
		932.3	620.2	$\frac{5}{2}^+$	D	109(6)	$M1+E2$	$-0.16(2)$
		1134.7	416.7	$\frac{7}{2}^+$		66(3)		
1692.0	$\frac{3}{2}^+$	1692.1	0	$\frac{1}{2}^+$		5(1)	$M1+E2$	$+0.34(^{+1}_{-2})$ or $-5.0(2)$
1701		1078.5	620.2	$\frac{5}{2}^+$	D N	41(3)		
		1357.6	342.1	$\frac{3}{2}^+$	N	6(1)		
		1454.8	245.4	$\frac{5}{2}^+$	N	8(2)		
		1700.7	0	$\frac{1}{2}^+$	N	7(2)		
1826.7	$(\frac{9}{2}, \frac{11}{2})^+$	778.0	1046.8	$\frac{7}{2}^+$		23(4)		
1971.8	$\frac{7}{2}^-$	1577.5	396.2	$\frac{11}{2}^-$		9(2)	$E2$	
		1292.2	680.5	$\frac{9}{2}^-$	D	26(2)		
Unplaced		748.0				36(5)		
		1155.7				11(2)		
		1178			N	4(2)		
		1242.2				7(1)		

The FWHM of the observed transitions against the decay energy is displayed in Fig. 5.8. The FWHM of transitions were fitted in local energy regions based on transition density using a single value for each transition in the region. The red line is a quadratic fit to the FWHM, and most values lie on the fitted line. Some notable exceptions include the 427- and 436-keV transitions which are weak transitions. The transition around 800 keV has a larger FWHM as it is a composite peak comprised of transitions from the 1552-keV state and the 1047-keV state. The transitions above 1400 keV are further from the line; however these transitions are also quite weak.

Gamma-ray concidence spectra, projected from the particle-γ-γ coincidences, are shown in Fig. 5.9 for selected transitions. Such concidence spectra were important in establishing the placement of new transitions as well as confirming the existence of weak decay paths.

The observed level scheme from the present experiment is shown in two parts in Fig. 5.10 and Fig. 5.11. The line widths of the transitions are proportional to the intensities of the observed transitions. New transitions and levels are displayed in red.

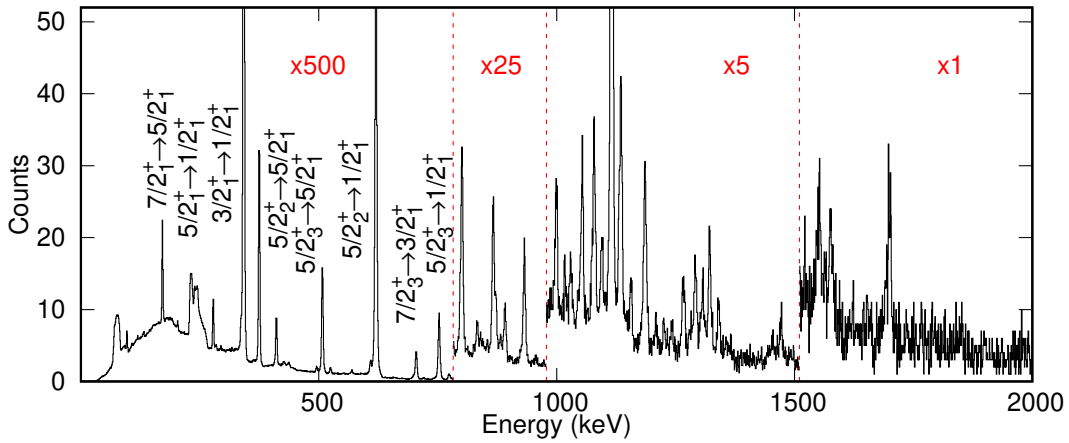

Figure 5.6: Total γ-ray energy spectrum from particle-γ coincidences including all data taken. Doppler-shift corrections have been applied for Cd-like recoils. Dashed lines separate regions with different scaling factors.

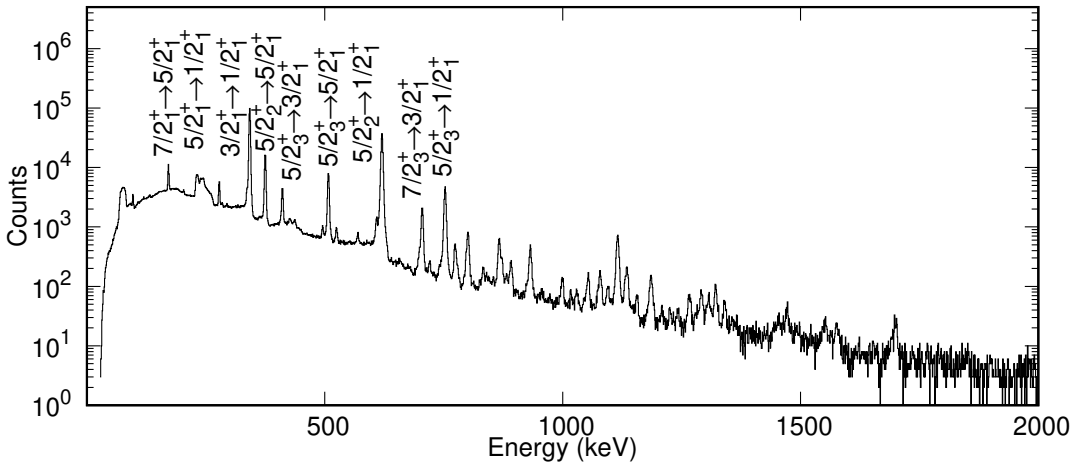

Figure 5.7: Total log-scale γ-ray energy spectrum from particle-γ coincidences including all data taken. Doppler-shift corrections have been applied for Cd-like recoils.

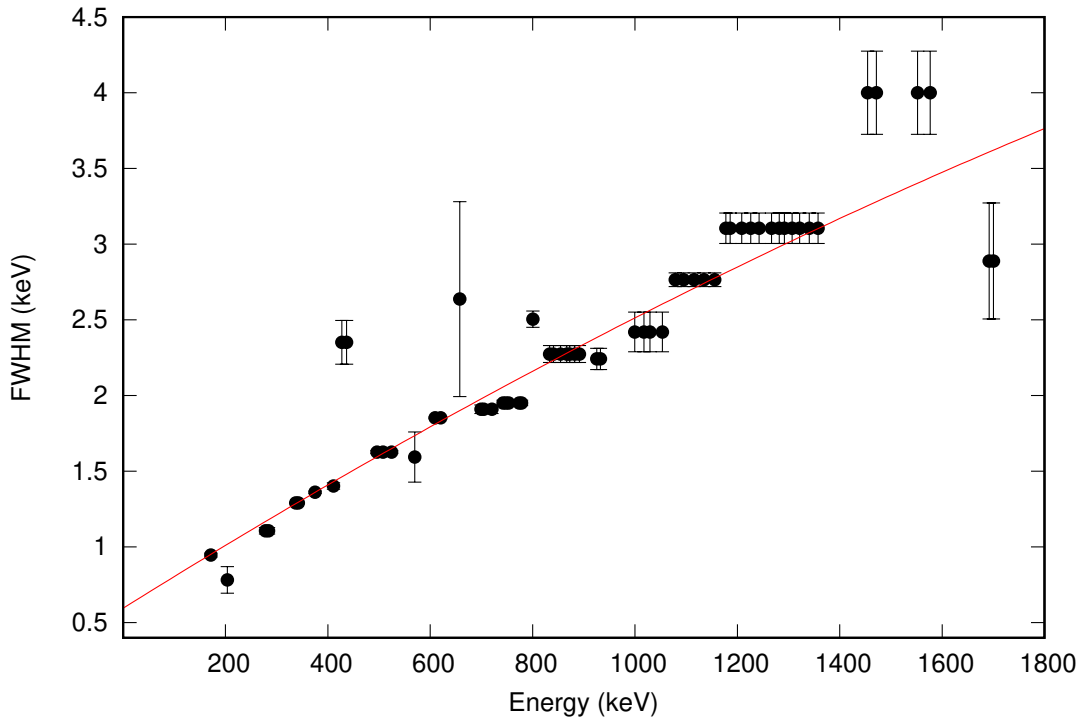

Figure 5.8: The FWHM of observed γ-ray peaks for each transition energy. The width of peaks were fitted in regions using a single shared value. The red line corresponds to a quadratic fit as a function of transition energy of the form FWHM=$ax^2 + bx + c$.

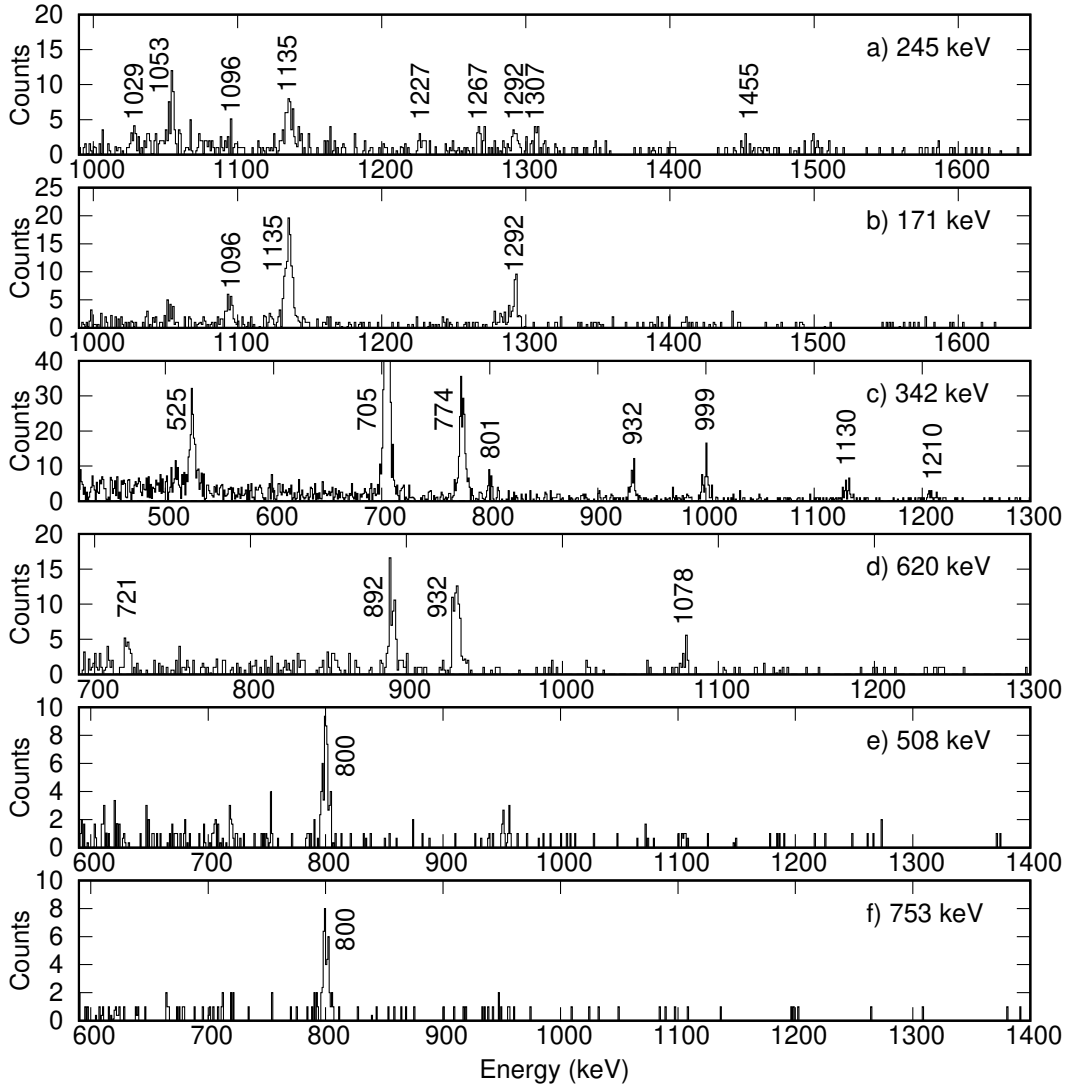

Figure 5.9: Gamma-ray coincidence spectra projected from particle-γ-γ coincidence data. Gates are placed on a) the 245-keV transition, b) the 171-keV transition, c) the 342-keV transition, d) the 620-keV transition, e) the 508-keV transition, and f) the 753-keV transition.

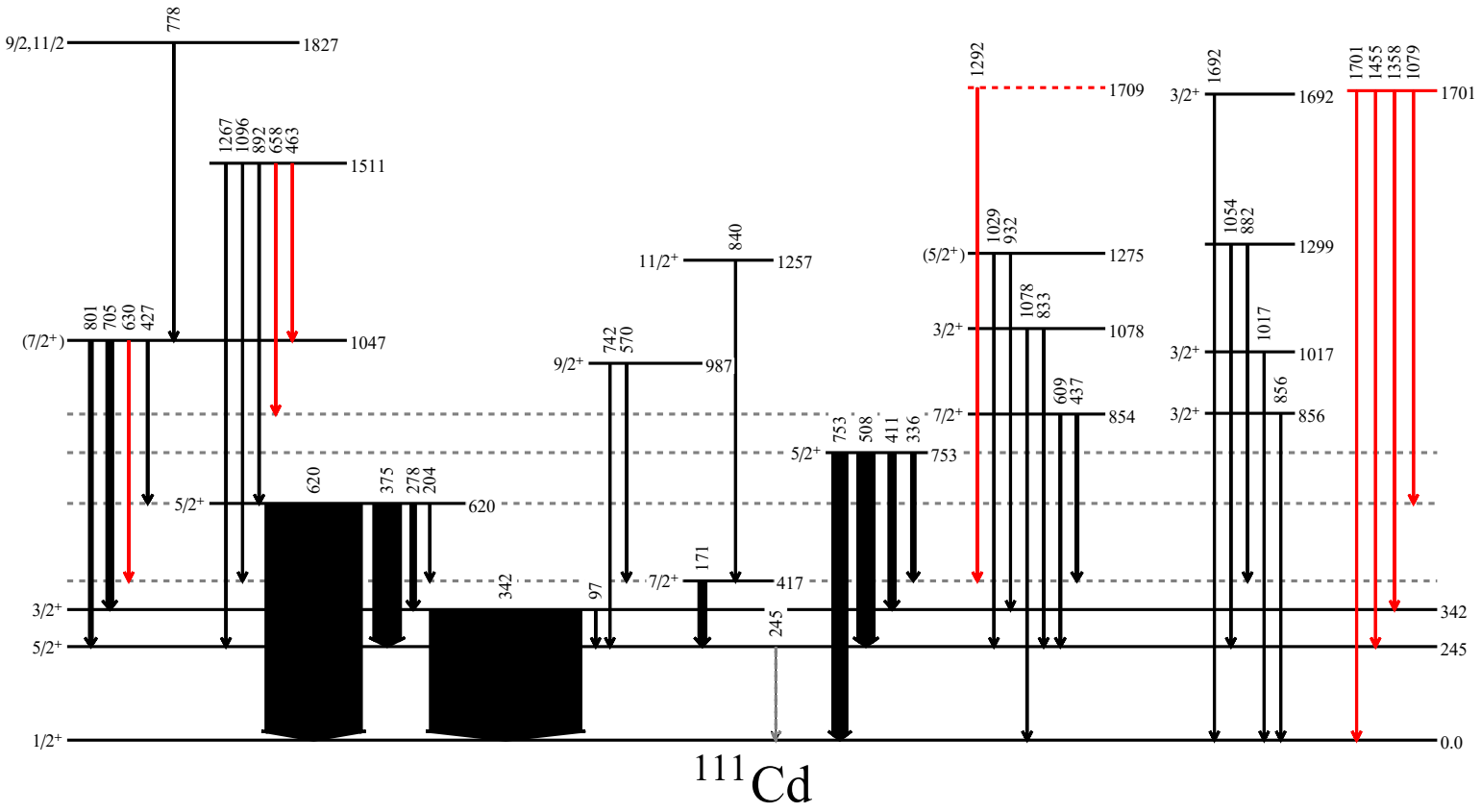

Figure 5.10: Partial level scheme deduced from observed transitions in ^{111}Cd multi-step Coulomb excitation. New states and transitions are shown in red. The dotted red state at 1709 keV is a tentatively proposed new state. Other dashed lines extend levels to show where transitions feed and decay.

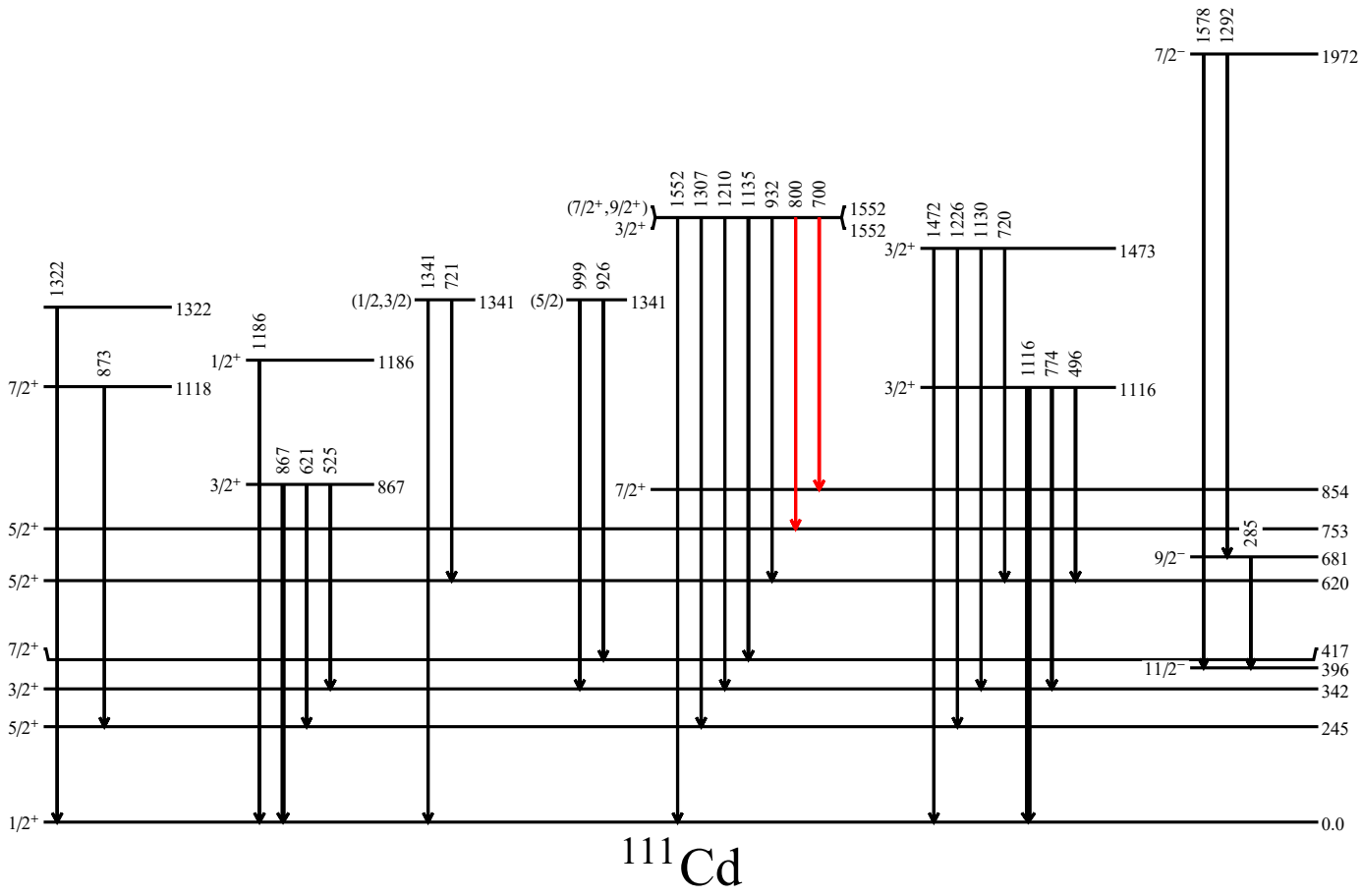

Figure 5.11: Partial level scheme deduced from observed transitions in ^{111}Cd multi-step Coulomb excitation.

5.2.1 Assigning transitions

Much of the known, low-spin structure from the nuclear data evaluators has been confirmed in the present measurement. The states listed in Nuclear Data Sheets [90] that were not observed in the present measurement, largely, were not observed in previous neutron capture and neutron scattering measurements [120]. This section discusses particular transitions and their assignments.

5.2.1.1 The 463- and 658-keV transitions

Two new transitions from the 1511-keV state, displayed in Fig. 5.10, were observed. A 658-keV transition was observed in coincidence with the 609-keV transition from the $^{7}/_{2}^{+}$, 854-keV state, and a 463-keV transition was observed in coincidence with the 705-keV and 801-keV transitions from the $^{7}/_{2}^{+}$ state at 1047 keV. Both of these transitions are to $^{7}/_{2}^{+}$ states; the 1511-keV state decays to states with a minumum spin of $^{5}/_{2}^{+}$ suggesting a high spin.

5.2.1.2 The 630-keV transition

A previously unobserved transition has been seen in coincidence with the 171- and 245-keV transitions from the 417- and 245-keV states, displayed in Fig. 5.10. This transition has therefore been identified as originating from the $^{7}/_{2}^{+}$ state at 1047 keV.

5.2.1.3 The 855-keV transition

A weak transition at 855 keV (shown in Fig. 5.10) may correspond to the reported level at 856 keV [90]. The reported level has a single decay to the ground state and has been observed only in a Coulomb-excitation measurement by protons [109] which did not observe the $^{3}/_{2}^{+}$ state at 867 keV. Notably, transitions corresponding to a state at 855 keV were not observed in the (n,γ) and $(n,n'\gamma)$ measurements reported by Baskova [120]. It is here suggested that the 856-keV state reported in Ref. [109] corresponds to the known 867-keV state. In this case the origin of the observed 855-keV transition is unknown. The 856-keV state has been left in the proposed level scheme.

5.2.1.4 The 1292.2-keV transition

Multiple $\sim$1292-keV transitions have been observed previously in ^{111}Cd and have been attributed to transitions from the 2045-keV state to the 753-keV state, and from the 1972-keV state to the 681-keV state. The 1292.2-keV transition measured in the present work is observed in coincidence with the 245- and 171-keV transitions and not seen in coincidence with other transitions, so it cannot be identified with either of these previously reported transitions. Neither the 1972-keV state, nor the 1972-keV state have been displayed in the level schemes in Figs. 5.10 and 5.11. The 1292.2-keV transition may be from a newly observed 1709-keV state, however there is no known

state at this energy. Since only a single transition is observed, the proposal of a state at 1709 keV must remain tentative. The assigned state is shown in Fig. 5.10.

5.2.1.5 The 1577.5-keV transition

A known transition [90] from the 1972-keV $^{7}/_{2}^{-}$ state to the 396-keV $^{11}/_{2}^{-}$ state is observed. The negative parity states are displayed in Fig. 5.11. No transition is seen in coincidence with the 1577-keV transition in the present measurement. This is consistent with the known data as no coincidences would be expected due to the 49 min half-life of the $^{11}/_{2}^{-}$ state.

5.2.2 Unplaced transitions

Transitions discussed in this section have not been placed in the present measurement and so are not in the level schemes in Figs. 5.10 and 5.11.

5.2.2.1 The 1155.7-keV transition

The 1155.7-keV transition is a known transition [120; 121], however it has not previously been placed in the ^{111}Cd level scheme. There are no coincident γ-rays observed in the present measurement that place this transition in the level scheme. Further measurements with measurements of either feeding transitions or the energy of particles directly exciting the state with this decay are required to place the transition.

5.2.2.2 The 1242.2-keV transition

There is a known transition at ∼1243 keV from a $(^{5}/_{2}^{+}, ^{7}/_{2}^{+})$ state at 2097 keV to the $^{7}/_{2}^{+}$ 854-keV state. The second-strongest transition from this state would appear at 1343 keV connect to the $^{5}/_{2}^{+}$ 753-keV state; such a transition could be hidden under the observed 1342-keV transition. No transition is observed in coincidence spectra and so the observed transition has not been placed in the present measurement.

5.2.3 Excited states

5.2.3.1 The 1321.6-keV state

The 1321.6-keV state (see Fig. 5.10) decays via two known transitions: a 1321.6-keV ground-state transition, and a 979.5-keV transition to the 416.7-keV state. Only the ground-state transition was observed in the present measurement. The reported intensity ratio [90] for the 979.5-keV transition relative to the 1322-keV transition is 0.04(1), which may be too weak to be observed in the present measurement.

5.2.3.2 The 1552.1-keV state

A reported doublet of excited states appears in Nuclear Data Sheets at 1552 keV [90], displayed in Fig. 5.11. A $^{3}/_{2}^{+}$ state at 1552.1-keV state has been observed in previous

Table 5.2: The experimental intensities of the transitions out of the 1552-keV states relative to the 342-keV transition are compared as a double ratio between scattering angle ranges of 112-170° and 28-80°.

E_i	I_i^π	E_γ	E_f	I_f^π	$R_{112-170}/R_{28-80}$
1552.1	$\frac{3}{2}^+$	1134.7	416.7	$\frac{7}{2}^+$	1.9(3)
		1210.2	342.1	$\frac{3}{2}^+$	20(9)
		1306.5	245.4	$\frac{5}{2}^+$	2.2(5)
		1551.5	0	$\frac{1}{2}^+$	9(4)
1552.4	$(\frac{7}{2}^+, \frac{9}{2}^+)$	932.3	620.2	$\frac{5}{2}^+$	
		1134.7	416.7	$\frac{7}{2}^+$	1.9(3)
Unplaced		698	853.9	$\frac{7}{2}^+$	1.8(4)
		800.7	752.8	$\frac{5}{2}^+$	

measurements [122; 120]; however, in a ^{110}Pd(^{3}He,2nγ)^{111}Cd measurement, the large gradient of the excitation function of a transition from a 1552-keV state was noted and interpreted as a 1552.4-keV ($7/2^+$,$9/2^+$) state. The review of (n,γ) and (n,$n'\gamma$) studies by Németh [121] confirms the $9/2^+$ spin assignment for one member of the doublet.

Previously unobserved transitions were observed in the present measurement decaying from a state at ∼1552 keV. It may be possible to identify the origin of the observed transitions by analysing the intensity of these transitions in different beam-scattering angle ranges and comparing to the intensity of a normalising transition. In Table 5.2 the intensity of a transition in a scattering angle range, relative to the intensity of the 342-keV transition in the same range, is denoted $R_{\theta_1-\theta_2}$. The double ratios of $R_{\theta_1-\theta_2}$ from two scattering angle ranges are given in Table 5.2. The 932- and 800-keV transitions are doublets and so have not been given intensity ratios. The intensity ratios of the 698-, 1135-, and 1307-keV transitions are ∼2. The 1210- and 1552-keV transitions are higher, however, they have large uncertainties. The intensity ratio seen for the 1135-keV transition attributed to the $(\frac{7}{2}^+, \frac{9}{2}^+)$ state is consistent with the majority of the transitions attributed to the 1552.1-keV $3/2^+$ state. No transition assignments were made based on the information in Table 5.2. All transitions from states at 1552 keV have been assumed to be as stated in Ref. [121] with previously unobserved transitions unplaced. In Table 5.1 the unplaced transitions have been placed with both the 1552.1-keV $3/2^+$ and 1552.4-keV $(7/2^+, 9/2^+)$ states.

5.2.3.3 The 1701-keV state

Numerous transitions were seen in coincidence with transitions from low-lying states with energies that sum to an energy of ∼1700 keV. A new state is proposed at 1701 keV, however, while the existence of this state is clear, further experimentation must take place to characterise this state. At present the 1701-keV state spin is

constrained to be $^1/_2{}^+$, $^3/_2{}^+$, or $^5/_2{}^+$. Transitions are seen to the $^1/_2{}^+$ ground state as well as $^5/_2{}^+$ excited states. No transitions are observed to $^7/_2{}^+$ states. Based on the (reasonable) assumption that the transitions observed from this state are $M1$ and $E2$ in character, the transition to the $^1/_2{}^+$ ground state limits the maximum spin to $^5/_2{}^+$. No limit is placed on the minimum spin.

5.3 Coulomb-excitation analysis

An attempt was made to use Coulomb-excitation analysis to determine $E2$ matrix elements in ^{111}Cd. While it is possible to reproduce the observed yields with a range of transition strengths, the limited knowledge of nuclear structure from previous spectroscopic measurements, and the relatively low statistics for most states excited in the present measurement, means that a unique solution is not possible. It is possible to reproduce the experimental yields using the matrix elements obtained in Chapter 4 with a range of values for other matrix elements. Many of the states excited in the present work have unknown spins and parities and most transitions have both $M1$ and $E2$ components with unknown mixing ratios. The low statistics also prevent the measurement of angular correlations to determine spins, parities, and mixing ratios.

The planning of future multi-step Coulomb-excitation measurements should be performed with the complexity of the nucleus in mind. Coulomb-excitation measurements must be performed starting from single-step Coulomb excitation such as performed in Chapter 4, before increasing the mass and energy of the exciting nucleus to incrementally populate higher-excited states and higher spins. Further measurements are likely to be required in order to simplify the analysis of the excitation and de-excitation pathways. Several states excited in the present measurement have unknown spins and parities. The mixing ratios of mixed transitions in ^{111}Cd are also largely unknown, including for transitions out of key states such as the strongly excited 753- and 1047-keV states. As such, the analysis of ^{111}Cd would benefit from measurements specifically aimed at the measurement of mixing ratios. This is possible through angular distribution or angular correlation measurements following Coulomb excitation or nucleon scattering. Clarification of much of the observed structure could be obtained from $(n, n'\gamma)$ measurements. Furthermore, this could provide lifetime measurements [123] for many states using the Doppler-shift attenuation method. New measurements could be combined with the present data to provide greater sensitivity.

Chapter 6

Interpretation of Coulomb excitation measurements on ^{111,113}Cd

The Cd isotopes have long been seen as textbook examples of vibrational nuclei [15], however, the validity of this model has been brought into question [7]. In particular, the $E2$ transition strengths in the even-even isotopes for multi-phonon states do not agree with model predictions, and the g factors in the odd-mass isotopes cannot be explained in the particle-vibration model [82; 85]. The particle-rotor model is given as an alternative to describe the odd-mass Cd isotopes with some success observed. Both the particle-vibration model and particle-rotor model explain some of the features observed in these nuclides, however the nuclei may not be fully collective and therefore it may be more accurate to attempt a microscopic approach. Recent advances in computational power have allowed large-basis shell-model calculations to be performed on the Cd isotopes. In this chapter, the predictions of the particle-vibration model, the particle-rotor model, and shell-model calculations are compared to experimental data.

The $^{3}/_{2}^{+}_{1}$ and $^{5}/_{2}^{+}_{2}$ states in ^{111}Cd can be identified as a 2^{+} core excitation coupled to an $s_{1/2}$ neutron in the weak coupling limit of the particle-vibration model, or as a $K=1/2^{+}$ band in the particle-rotor model. The relative $E2$ strengths of the $^{3}/_{2}^{+} \rightarrow {}^{1}/_{2}^{+}$ and $^{5}/_{2}^{+} \rightarrow {}^{1}/_{2}^{+}$ transitions are predicted to be equal in both models [82]. The experimental observation of approximately equal $E2$ strengths of these transitions in ^{111}Cd allows for either theoretical interpretation to be considered valid. First, we consider the rotor model applied to the Cd isotopes.

6.1 Particle-rotor interpretation

Previous attempts have been made to interpret ^{111}Cd as a deformed nucleus with rotational excitations built on Nilsson orbits [124; 82; 85]. While this interpretation has some merit and can explain some aspects of these nuclei, the states and associated transitions observed in the present multi-step Coulomb excitation of ^{111}Cd suggest that this interpretation is not sufficient for characterisation of the nuclear structure.

In this section, the levels will be discussed in terms of the particle-rotor model, assuming states can be described in terms of rotational bands, before interpretations with other models are discussed.

6.1.1 Ground-state band

The ground-state "band" in ^{111}Cd can be identified with a $1/2^+_{g.s.}$ band head with rotational states above, including a $3/2^+$ state at 342 keV, a $5/2^+$ state at 620 keV, and a $7/2^+$ state at 1047 keV. The measured transition strengths for the $3/2^+_1 \rightarrow 1/2^+_{g.s.}$ and $5/2^+_2 \rightarrow 1/2^+_{g.s.}$ transitions are 17.4(12) W.u. and 15.4(11) W.u., respectively. These enhanced $B(E2)$ values are indicative of collectivity and may indicate that these are the rotational states. These transition strengths are not large on the scale of known rigid rotations and so deformation would be small in a rotational interpretation of ^{111}Cd. It is further proposed that in the particle-rotor interpretation, the state at 1511 keV, with unknown spin, may be the $9/2^+$ state of the ground-state band. Transitions from the 1511-keV state are only seen to states with known spin-parity assignments of $5/2^+$ and $7/2^+$. Since no transitions are observed to lower-spin states it is likely that excitation of this state occurs through multi-step Coulomb excitation. The observation of this high-energy, (likely) high-spin state is therefore suggestive of a sequence of collective transitions. An alternative candidate for the $9/2^+$ member of the ground-state band could be the reported $9/2^+$ state at 1552 keV. The presence of the $3/2^+$ state, also at 1552 keV, hides this potentially higher-spin state that was reported in a ^{110}Pd(^{3}He,2nγ)^{111}Cd reaction based on the observed gradient of the excitation function [124]. Further measurement of this nucleus in order to determine the spins of these states could resolve these two potential interpretations.

In the discussion of the ^{110}Pd(^{3}He,2nγ)^{111}Cd measurement [124], it was proposed, based on variable moment-of-inertia particle-rotor calculations, that the $(9/2^+, 11/2^+)$ state at 1827 keV is the $9/2^+$ state of the ground-state band. We instead propose here that the 1827-keV state is the $11/2^+$ member of the ground-state band. The 1827-keV state is the highest-energy identified excited state in the present Coulomb-excitation measurement. Combining the fact of its high spin and multi-step excitation, it is likely to be a member of the ground-state band.

6.1.2 245-keV state K=$5/2^+$ band

The 245-keV state can be interpreted as a $5/2^+$ single-particle like state. The band built on this state is extended in the present work. The $7/2^+$ state at 417 keV has a single transition to the 245-keV state. An $E2$ transition could exist to the 342-keV state, however it would appear at 75 keV, which is at the same energy as a Pb x-ray. It is worth noting that no transition is known between the $7/2^+_1$ state in ^{113}Cd and the $3/2^+_1$ state which is at lower energy than the $5/2^+_1$ state and so should be favoured energetically. The $9/2^+$ state in the $5/2^+_1$ band is seen at 987 keV with observed transitions only to the 245- and 417-keV states. Finally, an $11/2^+$ state appears at 1256 keV with a transition only to the $7/2^+$ state at 417 keV. Another $E2$ transition is possible to

the $^{7}/_{2}^{+}$ state at 854 keV, however this would be relatively hindered due to the much lower energy of the transition (E_γ=402 keV).

6.1.3 753-keV state

It is not clear whether the 753-keV state is single-particle-like in nature. The transition strength to the ground state is $B(E2)$=5.5(4) W.u. which is larger than the $\sim$1-W.u. transition strength expected for a single-particle transition. The 753-keV state is strongly excited in the multi-step Coulomb-excitation measurement, and is an important state in the subsequent excitation of higher excited states. Many of the states higher in energy than the 753-keV, $^{5}/_{2}^{+}$ state do not have known spins and parities. Further, observed transitions out of the higher-lying states do not have known mixing ratios. It is therefore difficult to assign more states to a band built on the 753-keV state.

6.1.4 Particle-rotor decomposition

A decomposition of the low-lying level scheme in ^{111}Cd, is presented in Fig. 6.1, which includes positive-parity states up to 1047 keV, excluding the 856-keV and 1017-keV $^{3}/_{2}^{+}$ states. Inset is a Nilsson scheme calculated for ^{111}Cd. Following the discussion in Ref. [85], a qualitative description of much of the low-lying spectrum is possible with reference to rotational bands built on Nilsson orbits. The presence of the extra $\frac{3}{2}^{+}$ states at 856 and 1017 keV may be explained by the $^{3}/_{2}[422]$ and $^{3}/_{2}[402]$ Nilsson states, although the observed energies are low compared to what would be expected for these excitations. The evidence for these states is quite weak in the literature, therefore other placements for the single transitions from each of these states may be possible. The presence of other observed states are well explained by the particle-rotor model, however transition information does not readily lead to band descriptions as discussed above.

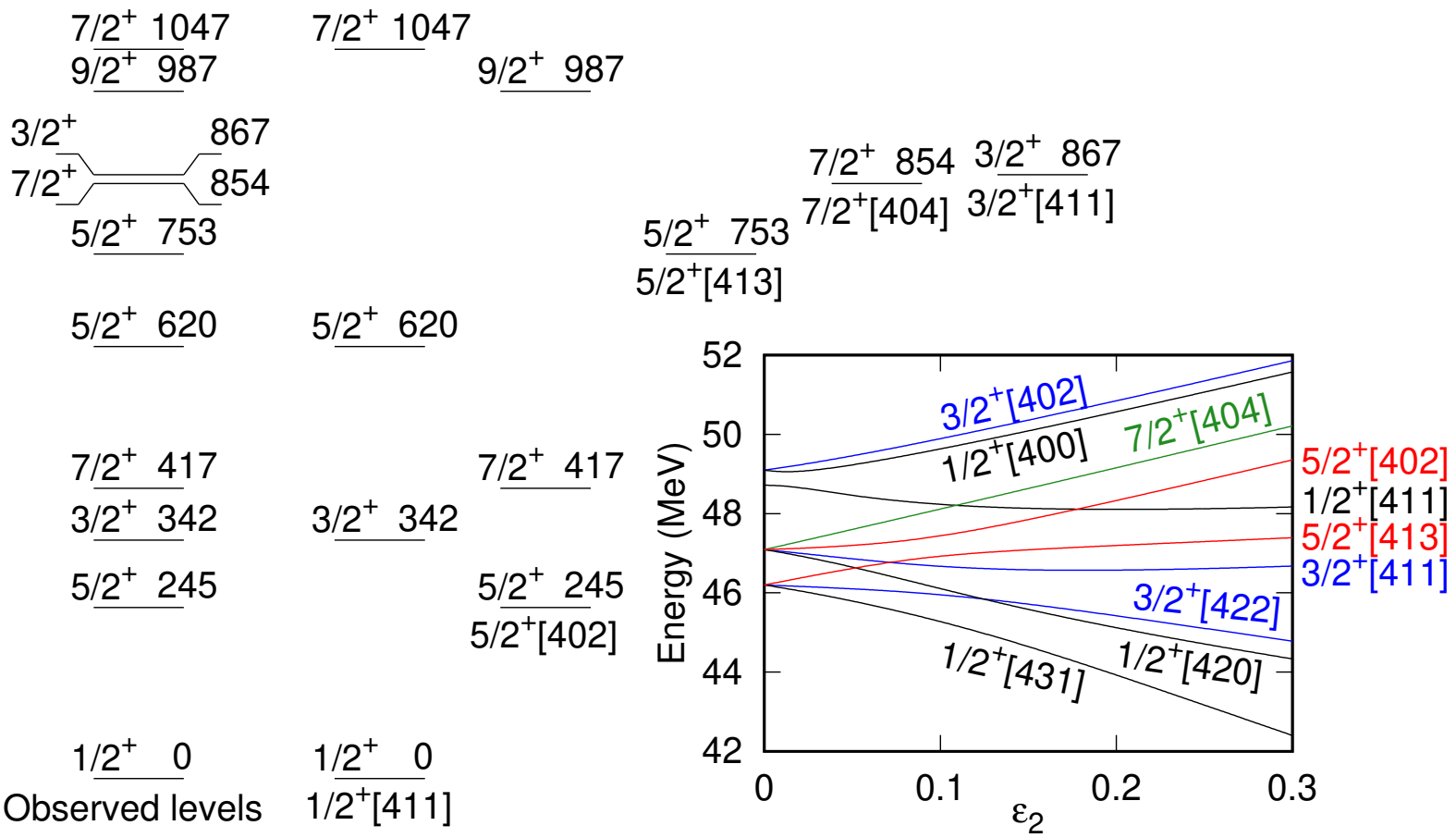

Figure 6.1: A decomposition of a selection of observed levels in ^{111}Cd into a particle-rotor level scheme. Level energies are given in keV. Inset is a Nilsson scheme calculated for ^{111}Cd; positive-parity orbits only are included.

6.1.5 Intruder bands in odd-mass nuclei

Intruder states have been observed in odd-mass nuclides at similar energies to the shape-coexisting states in the neighbouring even-even isotopes [40]. In ^{110}Cd and ^{112}Cd, the lowest-energy shape-coexisting states occur at 1473 keV and 1224 keV, respectively [125]. It might therefore be expected that a shape-coexisting $1/2^+$ state may appear in ^{111}Cd at around these energies. Several states are seen in this region, however none of these states have a known spin-parity assignment of $1/2^+$, two states have completely unknown spin, and one state has a tentative $(1/2, 3/2)$ assignment [90]. Measurements of $E0$ transition strengths would likely be required to identify any shape coexisting states [40]. It is worth noting that the shape-coexisting state may not have a spin-parity of $1/2^+$, other couplings are possible, and may be favourable at the altered deformation.

6.1.6 Moment-of-inertia plots

In Fig. 6.2 the transition energies are compared to the initial state spin I_i for known states in ^{110}Cd and ^{112}Cd. In a rigid, axially symmetric rotor, the energy of the transitions is proportional to the initial spin I_i and inversely proportional to the moment of inertia and should lie on a straight line as a function of angular momentum. The lowering of the gradient of the transition energies is a sign of an increasing moment of inertia if the nucleus is interpreted as a rotor. In a classical picture of the nucleus, the high energy of the 2_1^+ state is indicative of a small deformation and hence a low moment of inertia. In order to gain two units of angular momentum, the nucleus must rotate more rapidly, which can cause further deformation, and an increase of the moment of inertia. This effect is sometimes called centrifugal stretching. The transition energies in ^{112}Cd rapidly begin to decrease. This cannot be explained by a statically deformed rotor. A possible explanation of the decreasing energy is that the shape of ^{112}Cd is softer than ^{110}Cd and the centrifugal stretching is increased in ^{112}Cd. Usually centrifugal stretching is associated with much smaller changes in the moment of inertia of well-deformed rotors. The term is used "qualitatively" rather than "quantitatively" here. An alternative explanation of the decreased transition energies at higher spins could be that they result from interactions with intruder bands. It has been recently noted that many of the features in ^{110}Cd and ^{112}Cd can be explained through the inclusion of multiple shape coexisting structures [125]. The addition of the odd nucleon can give insights from observing the interaction between the odd nucleon and states in the core, however, it adds complexity, which makes an overall picture of the nucleus elusive. One may expect that similar shape coexisting structures may be present in the odd-mass Cd isotopes.

It is difficult to perform the analysis of the moment of inertia of the odd-mass isotopes due to a lack of knowledge of the spins and parities of excited states. However, based on the level scheme proposed in Sec. 6.1.4, the E_γ versus I_i plot for ^{111}Cd is displayed in Fig. 6.3. The blue points correspond to the ground-state band starting with the $5/2_2^+ \rightarrow 1/2_{\text{g.s.}}^+$ transition, the red squares correspond to the other transition

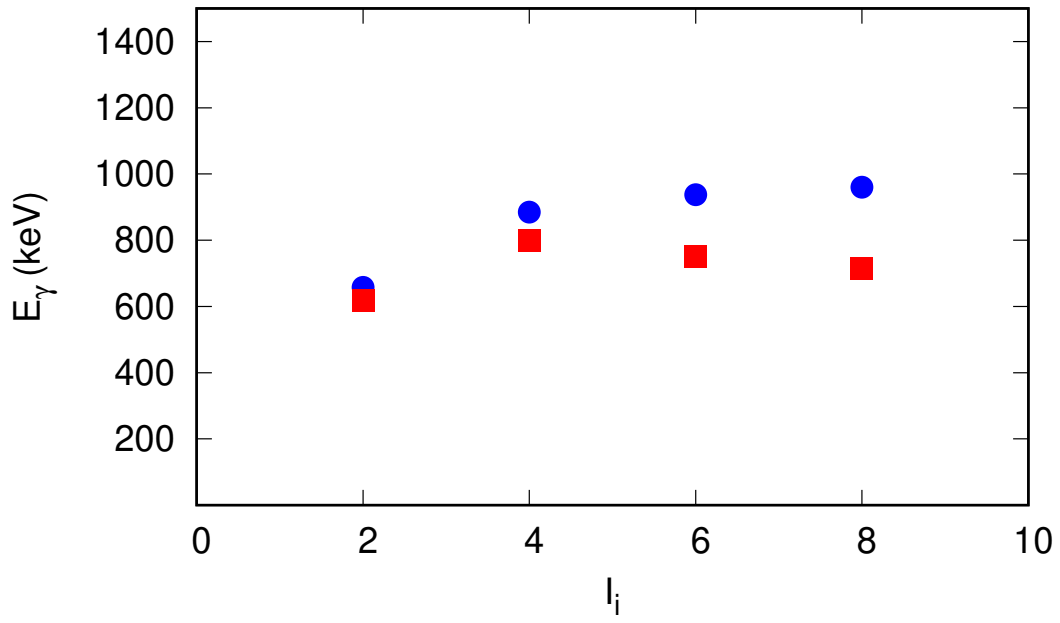

Figure 6.2: $E2$ γ-ray energies E_γ against the transition-parent spin (I_i) for the low-lying yrast sequence in ^{110}Cd (blue dots), and ^{112}Cd (red squares).

sequence of the ground-state band, starting at the $^{7}/2_2^+ \rightarrow {}^{3}/2_1^+$. Insufficient transitions are known for the $^{5}/2_1^+$ band to observe trends, however, the $^{9}/2_1^+ \rightarrow {}^{5}/2_1^+$ transition is displayed with a green downward-facing triangle and the $^{11}/2_1^+ \rightarrow {}^{7}/2_1^+$ transition is displayed with a black upward-facing triangles. The trends observed in the odd mass isotopes are very similar in nature to those observed in the even-even isotopes. Comparing to Fig. 6.2, the odd-A system appears to have a similar moment of inertia to its even-even neighbours. The apparent difference in the moment of inertia of the two 'signatures' of the ground-state band is not without precedent and invites further investigation.

6.1.7 Particle-rotor conclusions

The increasing transition strengths from ^{111}Cd to ^{113}Cd, reported here, would correspond to increased deformation in the particle-rotor model. This is consistent with increased transition strengths observed along the chain in the even-even isotopes. The possible centrifugal stretching or other shape change/coexistence observed in the even-even isotopes must be considered in the discussion of deformation in these isotopes. The $E2$ transition strengths of the $^{3}/2_1^+ \rightarrow {}^{1}/2^+_{\text{g.s.}}$ and $^{5}/2_2^+ \rightarrow {}^{1}/2^+_{\text{g.s.}}$ transition strengths are approximately equal in ^{111}Cd, consistent with the predictions for a K=1/2 band in the particle-rotor model. The $^{5}/2_2^+ \rightarrow {}^{1}/2^+_{\text{g.s.}}$ transition strength is significantly larger than the $^{3}/2_1^+ \rightarrow {}^{1}/2^+_{\text{g.s.}}$ transition strength in ^{113}Cd; however this is not sufficient to exclude a rotor description of ^{113}Cd.

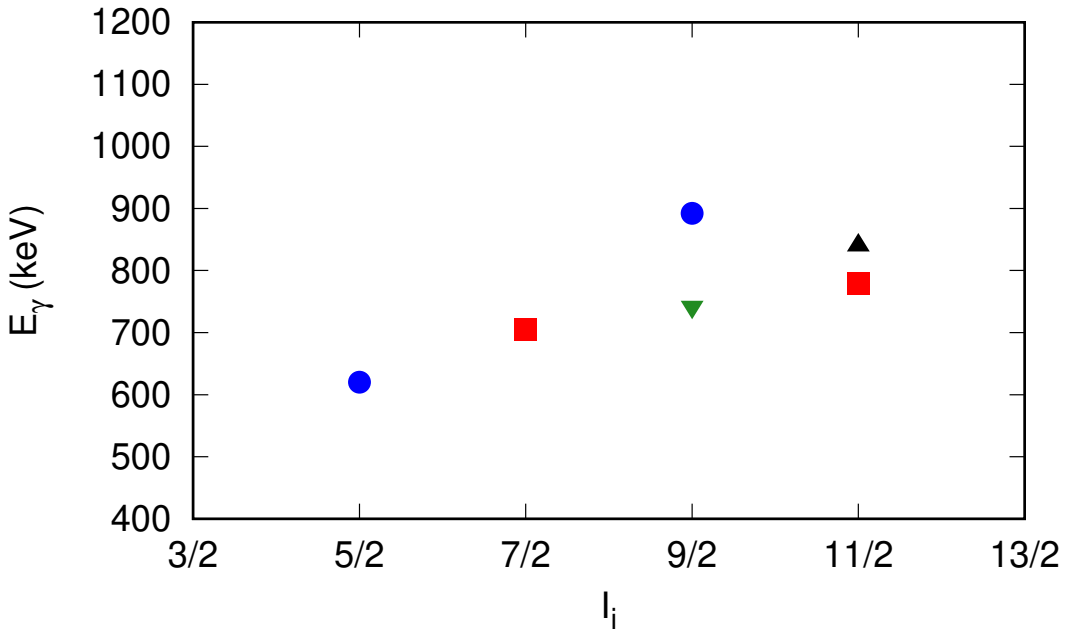

Figure 6.3: $E2$ γ-ray energies against the transition-parent spin (I_i) for transitions in ^{111}Cd. The blue points correspond to the ground-state band starting at the $^5/2^+_2 \rightarrow {}^1/2^+_{\text{g.s.}}$ transition, the red points correspond to the ground-state band starting at the $^7/2^+_3 \rightarrow {}^3/2^+_1$ transition. Values for transitions within the $^5/2^+_1$ band are also displayed: the $^9/2^+_1 \rightarrow {}^5/2^+_1$ transition is displayed with a green downward-facing triangle, and the $^{11}/2^+_1 \rightarrow {}^7/2^+_1$ transition is displayed with a black upward-facing triangle.

Table 6.1: Parameters used in particle-vibration calculations.

^{A}X	ξ	$\hbar\omega$ (keV)	$E(s_{\frac{1}{2}})$ (keV)	$E(d_{\frac{5}{2}})$ (keV)	$E(d_{\frac{3}{2}})$ (keV)	$E(g_{\frac{7}{2}})$ (keV)	C (MeV)
^{111}Cd	2.2	460	0	330	1100	367	55.9
^{113}Cd	2.2	438	0	400	1100	437	55.9

Tentative band assignments have been made for several states in ^{111}Cd. However, without spectroscopic measurements to determine the spin-parities of excited states, further band assignments are not possible. A preferential decay pattern within the band sequence, characteristic of rotation, is not observed. It appears that the observed states are strongly mixed. This may be due to strong Coriolis mixing associated with small deformations.

The particle-rotor model must account for the weak deformation of these isotopes, a changing moment of inertia, and possibly strong Coriolis mixing, which complicate the model significantly compared to the simple rigid-rotor model. Furthermore, observations of characteristics consistent with triaxiality in the region may suggest that triaxial shapes should be considered beyond the axial-rotor model.

A qualitative assignment of observed states to particle-rotor states is possible, but a quantitative description is hard to achieve.

6.2 Particle-vibration calculations

Particle-vibration calculations, described in Sec. 2.6.2, were performed for ^{111}Cd and ^{113}Cd with the parameters given in Table 6.1. The stiffness parameter C is a scaling factor for the $E2$ transition strengths and was set based on the transition strength in the neighbouring even-even ^{112}Cd in both calculations. Single-particle energies were initially set to the energy of the observed levels before being varied along with the coupling parameter and core-excitation energy to best reproduce the experimental level scheme. The $d_{3/2}$ orbit does not appear to be necessary to explain the low-lying spectrum. Hence, the energy of the $d_{3/2}$ single-particle state was put to 1100 keV, outside of the relevant observed energy region in both isotopes. The fitted excitation energy of the core ($\hbar\omega$) in both odd-A isotopes is significantly below the energy of the core excitation in ^{112}Cd, for which the 2_1^+ state lies at 618 keV. It has previously been noted that the g factors of the low-lying states, including the ground state, are in general not well reproduced by the particle-vibration model [82; 85]. In this section we will largely be concerned with the predictions for transition strengths and their comparison with the newly measured experimental results.

Particle-vibration calculations for ^{111}Cd and ^{113}Cd as a function of the particle-vibration coupling parameter ξ are displayed in Figs. 6.4 and 6.5, respectively. In the two figures, panel a) compares the calculated energy levels and experimental data. The level energies in ^{111}Cd agree quite well, however the proximity of the two $^{5}/_{2}^{+}$ states at low energy in ^{113}Cd is not reproducible while also describing the large

energy splitting of the $s_{1/2} \otimes 2^+$ states to reproduce the $^3/2_1^+$ energy. Attempting to fit the $^5/2^+$-state energies leads to a strong interaction between the $^5/2^+$ states of $d_{5/2} \otimes 0^+$ parentage and $s_{1/2} \otimes 2^+$ parentage, which shares the collective transition strength, which is not seen in experiment. Transition strength comparisons are made in panel b) of both figures. The strength of the collective $s_{1/2} \otimes 2^+ \rightarrow s_{1/2} \otimes 0^+$ transition is shared with the transition from the lower-energy state of $d_{5/2}$ parentage. This causes discrepancies in not only the transition strength of the lowest $^5/2^+$ state, but also in the transition strength of the collective $^5/2_2^+$ state. Experimentally, the $^5/2^+$ state is isomeric in both isotopes. It has a transition strength of 0.2218(19) W.u. [90] from direct lifetime measurements in ^{111}Cd. Similarly, the transition strengths of the ground-state transitions from the $^5/2_3^+$ state in ^{111}Cd and the $^3/2_2^+$ state in ^{113}Cd are seen to have large disagreements between the experimentally found values and the values from the particle-vibration model using the parameters in Table 6.1.

6.2.1 Particle-vibration conclusions

The particle-vibration model cannot explain the observed level energies, g factors, or $E2$ transition strengths even for states that can be naively identified as deriving from coupling of the odd neutron in its ground state to the first phonon. This is a major issue for the harmonic vibrator model in these nuclei. The addition of deformation may go some way to reconciling the differences between experimentally observed g factors and the model predictions [85], however, the also model appears unsatisfactory in other respects. If neither the particle-rotor model, nor the particle-vibration model are capable of completely describing the nucleus, it may be useful to take a microscopic approach to describe structures in these nuclei.

6.3 Shell-model calculations

Large-scale shell-model calculations on ^{111}Cd were performed using the M-scheme code KSHELL [126] with the SR88MHJM Hamiltonian [127; 128; 129; 130]. The core used in these calculations was ^{88}Sr. The orbits included in the shell-model calculations are $\pi(p_{1/2}, g_{9/2})\nu(d_{5/2}, g_{7/2}, d_{3/2}, s_{1/2}, h_{11/2})$. The interaction is based on the CD-Bonn potential with renormalization of the G-matrix [131; 132; 133]. The residual two-body matrix elements were adjusted to reproduce experimental energies in the tin isotopes. Effective charges of $e_\pi = 1.7e$ and $e_\nu = e$ were used in the evaluation of electromagnetic properties.

6.3.1 Comparison to Coulomb-excitation results

Transition strengths adopted in the present work are compared to shell-model calculations in Table 6.2. If the ordering of the $^5/2_2^+$ and $^5/2_3^+$ levels predicted by the shell model is swapped, better agreement is seen between shell-model $^5/2_2^+ \rightarrow {}^1/2_{\text{g.s.}}^+$ and $^5/2_3^+ \rightarrow {}^1/2_{\text{g.s.}}^+$ transition strengths and experiment. This observation is consistent with recent g-factor measurements performed on excited states in ^{111}Cd [85], although it

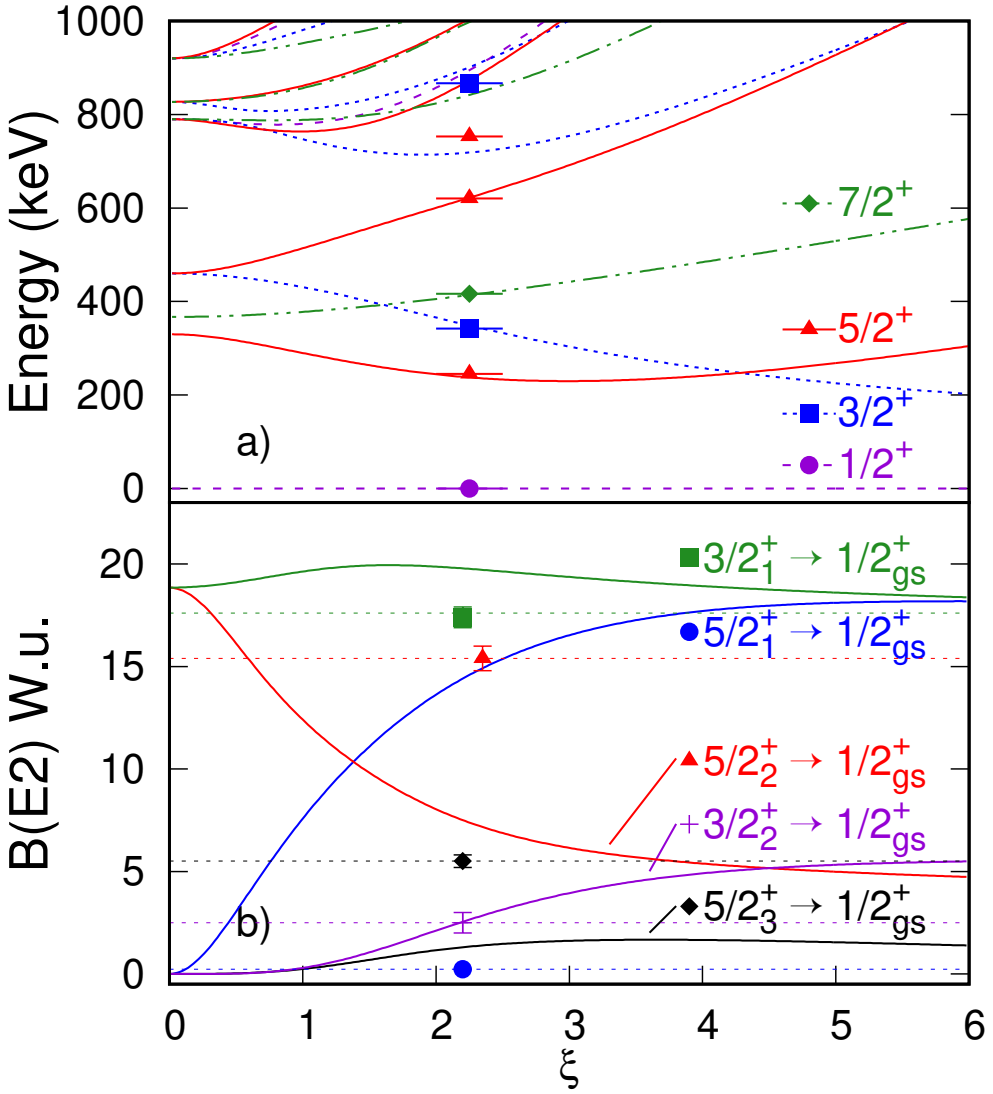

Figure 6.4: Results of particle-vibration model calculations for ^{111}Cd for a range of particle-vibration coupling parameters (ξ) are displayed with level energies in a), and transition strengths in b). Experimental results are shown as data points at the 'best fit' ξ value and as horizontal dotted lines.

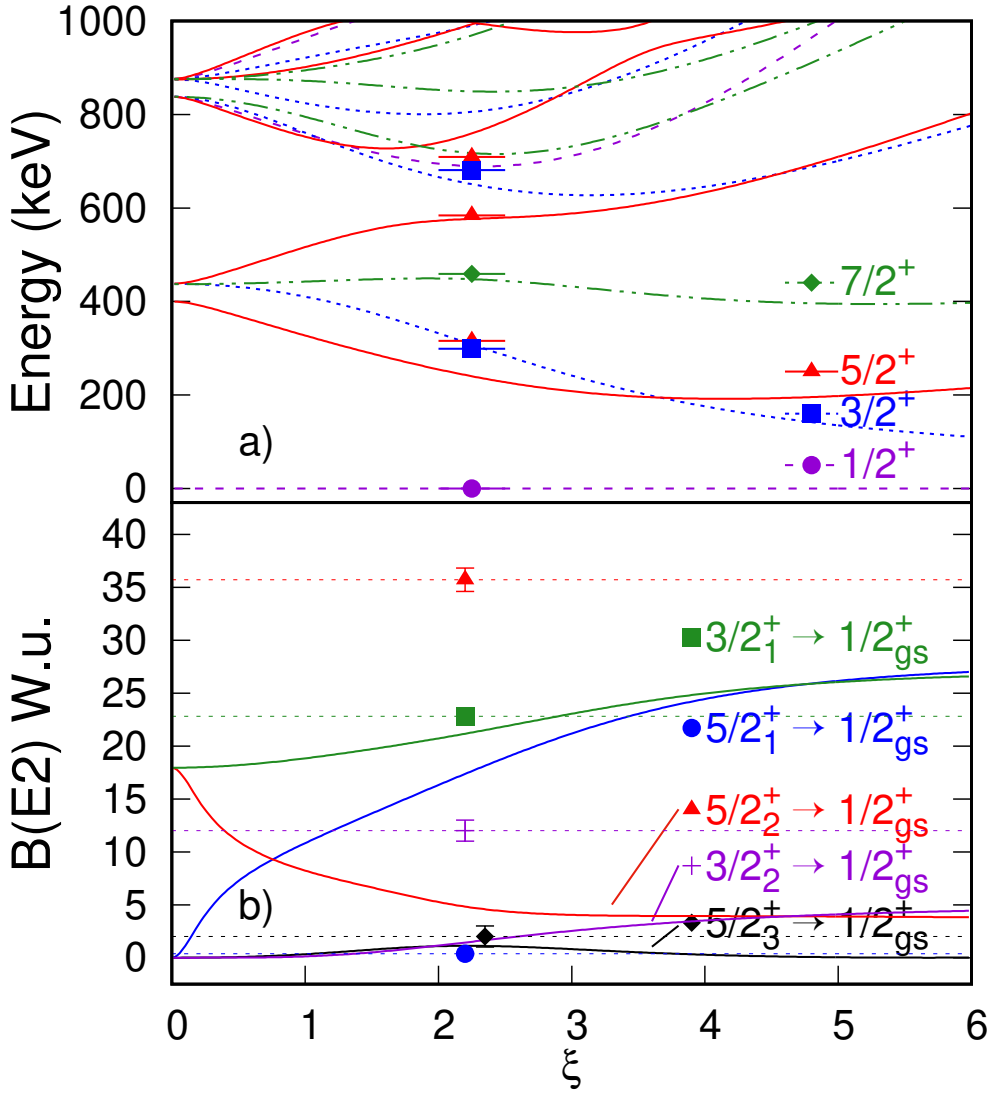

Figure 6.5: Results of particle-vibration model calculations for ^{113}Cd for a range of particle-vibration coupling parameters (ξ) are displayed with level energies in a), and transition strengths in b). Experimental results are shown as data points at the 'best fit' ξ value and as horizontal dotted lines.

Table 6.2: Adopted transition strengths in ^{111,112,113}Cd; results for ^{111}Cd are compared to shell-model calculations. Experimental data on ^{111}Cd and ^{113}Cd are from the present work, the value for ^{112}Cd is from Ref. [41].

^{A}X	I_i^+	E_γ	I_f^+	$B(E2)$ (W.u.)	
		(keV)		Adopted	SM
^{111}Cd	$\frac{3}{2}^+$	342	$\frac{1}{2}^+$	17.4(12)	14.1
	$\frac{5}{2}^+$	620	$\frac{1}{2}^+$	15.4(11)	7.5
	$\frac{5}{2}^+$	753	$\frac{1}{2}^+$	5.5(4)	15.0
^{112}Cd	2^+	618	0^+	31.3(14)	
^{113}Cd	$\frac{3}{2}^+$	299	$\frac{1}{2}^+$	22.8(15)	
	$\frac{5}{2}^+$	584	$\frac{1}{2}^+$	35.7(24)	
	$\frac{3}{2}^+$	681	$\frac{1}{2}^+$	12(1)	
	$\frac{5}{2}^+$	709	$\frac{1}{2}^+$	2(1)	

is worth noting that the calculated g factors for the $^5/2_2^+$ and $^5/2_3^+$ states are close ($g(^5/2_2^+) = +0.162$ and $g(^5/2_3^+) = +0.134$) and the uncertainties on the measured g factors are quite large ($g(^5/2_2^+) = +0.22(4)$ and $g(^5/2_3^+) = +0.5(2)$).

6.4 Collectivity in ^{111,113}Cd

A recent self-consistent deformed Hartree-Fock+BCS with Skyrme forces study of the charge radii and charge distributions in the Cd isotopes [134] predicted a trend of decreasing quadrupole deformation for the $^1/2^+_{\text{g.s.}}$ states in the Cd isotopes from prolate deformed in ^{111}Cd to slightly oblate in ^{119}Cd. The same study predicted that the even-even isotopes are prolate in their ground state with a sudden increase in deformation around A=116. This predicted decrease in deformation from ^{111}Cd to ^{113}Cd is not consistent with the observation of larger transition strengths between nominally collective states observed in ^{113}Cd compared to those in ^{111}Cd.

While the experimental $^3/2_1^+ \rightarrow {}^1/2^+_{\text{g.s.}}$ and $^5/2_2^+ \rightarrow {}^1/2^+_{\text{g.s.}}$ transition strengths increase from ^{111}Cd to ^{113}Cd, the $^5/2_3^+ \rightarrow {}^1/2^+_{\text{g.s.}}$ transition strength decreases from ^{111}Cd to ^{113}Cd. Despite the superficial similarities between ^{111}Cd and ^{113}Cd, the $^5/2_3^+$ state may have a different structure in ^{111}Cd and ^{113}Cd. The proportion of the wavefunction of the $^5/2_3^+$ state which originates from the $^5/2^+$ state of the ground-state band in ^{111}Cd may be larger than in ^{113}Cd. In the latter case, the rotational collectivity is consolidated in the more collective $^5/2_2^+$ state.

There is no clear decay pattern of the excited states observed in the Coulomb-excitation measurements. In a rotational nucleus the intra-band transitions are usu-

ally strong and favoured over inter-band transitions. The excited-state structures of the Cd nuclei are clearly strongly mixed; the reason the weakly collective models used for transitional nuclei are not seen to accurately predict the nuclear structure may be due to the persistence of shell-model-like structures for many states, rather than the development of truly collective structures.

Measurements of $E2$ transition strengths in ^{111}Cd and ^{113}Cd largely affirm previously reported values. The particle-vibration model does not reproduce the measured transition strengths in either ^{111}Cd or ^{113}Cd and has trouble explaining the observed energy levels in the Cd isotopes. While the particle-rotor model qualitatively explains the characteristics of low-lying levels in the Cd isotopes, the level scheme determined from the multi-step Coulomb-excitation measurement does not easily lend itself to a particle-rotor description. Both of the commonly used collective models for these weakly collective nuclei have difficulties explaining the observed nuclear structure. Some success has been found in describing the transition strengths in ^{111}Cd, however more work must be done both theoretically and experimentally to further compare shell-model and experimental results. Weakly collective nuclei remain a challenge for both shell-model and collective descriptions. More details on the nature of collectivity in this region may be obtained from the study of its emergence closer to the shell closures at ^{100}Sn and ^{132}Sn. In the following sections the emergence of collectivity from particle-like structures is explored through Coulomb-excitation and g-factor measurements on the stable, even-even Te isotopes.

Chapter 7

Transient-field g-factor measurements on ^{124,126,128,130}Te

In this chapter, transient-field g-factor measurements of the 4_1^+ states in the Te isotopes are discussed.

As discussed in Chapter 2, the properties of states can often be well understood on one hand as the excitations of a few coupled nucleons or on the other hand as strongly collective excitations. However, the transition from few-particle-like states to multiparticle collective states is not well understood. A previous study of the relative g factors in the stable Te isotopes [135] found that the 2_1^+ g factors rapidly converge to the collective limit moving away from the singly magic ^{134}Te toward the lower-mass stable isotopes. This is not necessarily indicative of the development of collectivity; however, it does imply a significant increase in the fraction of the angular momentum carried by neutrons. While the 4_1^+ states were populated in Ref. [135], the statistics were not sufficient to obtain a measurement of the 4_1^+-state g factors.

A recent paper has discussed the onset of collectivity through study of the Xe isotopes (Z=54) [136] and speculates that the onset of collectivity may start with the lower-spin, low-excitation states and progress through to the higher-spin, higher-excitation states. The natural next step in these studies is to explore the Te (Z=52) isotopes in a similar fashion. As Te is closer to the Z=50 shell closure than Xe, it may be expected that the onset of collectivity will be slower in Te since the p-n interaction, often cited as the driving force of collectivity, will be weaker in the Te isotopes, which have fewer valence protons. Shell-model calculations predict $g(4_1^+) \gg g(2_1^+)$ in the Te isotopes near N=82 [137; 138]; in this chapter the convergence of $g(4_1^+)$ to the collective limit, and relative to $g(2_1^+)$, is measured in order to explore the onset of nuclear collectivity.

7.1 Te g-factor measurements

7.1.1 Experimental parameters

Transient-field g-factor measurements require the measurement of small changes in relative γ-ray intensities as a result of small precession angles and therefore require

Table 7.1: State and transition energies in ^{124,126,128,130}Te. Data from Nuclear Data Sheets [61; 62; 63; 64].

Isotope	$E(2_1^+)$	$E(4_1^+)$	$E(4_1^+ \rightarrow 2_1^+)$
^{124}Te	602.7	1248.6	645.9
^{126}Te	666.4	1361.4	695.0
^{128}Te	743.2	1497.0	753.8
^{130}Te	839.5	1633.0	795.5

a high statistical precision in each detector. In a previous measurement of ^{130}Te, the excitation to the 4_1^+ state was less than ∼6% of the excitation to the 2_1^+ state. The difficulty of exciting the 4_1^+ state increases as the transition strength between states decreases closer to the shell closure. The energy of the excited states also increases towards the shell closure, further decreasing the excitation probability.

The energies of the relevant transitions in the Te isotopes are given in Table 7.1. An additional challenge is that the energy difference between the $4_1^+ \rightarrow 2_1^+$ and $2_1^+ \rightarrow 0_{\text{g.s.}}^+$ transitions is small enough that portions of the transitions overlap due to Doppler broadening, particularly in the case of ^{128}Te.

As described in Chapter 3, Section 3.3, the precision achievable in transient-field measurements is proportional to the slope of the angular correlation, further increasing the required measurement time for accurate g-factor measurements on the 4_1^+ states in the Te isotopes. Along with the low probability of excitation, the slope S (as discussed in Sec. 3.3) of the $4_1^+ \rightarrow 2_1^+$ transition is less than half the slope of the $2_1^+ \rightarrow 0_{\text{g.s.}}^+$ transition, implying a four-fold increase in measurement time, all else being equal. Among the stable isotopes, ^{130}Te is the least collective case and requires the most measurement time. In this case, the $4_1^+ \rightarrow 2_1^+$ transition lies below the $2_1^+ \rightarrow 0_{\text{g.s.}}^+$ transition, increasing the Compton background in the measurement of the intensity of the $4_1^+ \rightarrow 2_1^+$ transition. With many factors increasing the uncertainty in the measurement, much of the experimental design focussed on maximising sensitivity.

7.1.1.1 Choice of beam parameters

Beams of ^{58}Ni were provided by the ANU 14UD Pelletron accelerator. In order to maximise multiple Coulomb excitation, a high-Z beam species that the accelerator can produce readily at the safe Coulomb-excitation limit should be chosen. This also maximises the recoil velocities of the Te nuclei, allowing thicker Fe foils to be used while ensuring that all recoiling Te nuclei are implanted in the copper backing. Additionally, in order to reduce the background from beam excitation, doubly or singly magic beams (which have higher excitation energies and lower transition strengths) are preferred. Finally, the backscattered beam particles are required to have enough energy to be observed by the particle detectors. This final condition provides an upper limit on the mass of the beam particles. Combining all these considerations, the beam species was chosen to be ^{58}Ni; it is also an easily produced beam. The

Table 7.2: Beam and γ-ray detector details in the Te g-factor measurements.

Target	Run	Run time (days)	Beam	θ_γ Front	θ_γ Back	E_B (MeV)	E_{safe} (MeV)	$E_{barrier}$ (MeV)
^{124}Te	A	3	^{58}Ni	±65°	±125°	200	191.5	277.9
^{126}Te	B	3	^{58}Ni	±65°	±125°	205	190.1	275.7
^{128}Te	C	4	^{58}Ni	±65°	±125°	205	188.8	273.5
^{128}Te	D	4	^{58}Ni	±65°	±115°	205	188.8	273.5
^{130}Te	E	6	^{58}Ni	±65°	±125°	198	187.5	271.4
^{130}Te	F	4	^{58}Ni	±65°	±115°	205	187.5	271.4

beam energy was chosen to be close to the safe Coulomb-excitation energy given in Table 7.2 as defined in Section 3.1.3. The beam energy is slightly above the safe energy in all cases, however this does not significantly affect the statistical tensors and so does not affect the g-factor analysis. The statistical tensors used in the analysis have been tested experimentally via angular correlation measurements as will be described later in this chapter. The beam current was maintained at ∼1.5 pnA, with rates of ∼5000 Hz in the segments of the clover detectors and ∼500 Hz in the particle detectors.

7.1.1.2 Target preparation

For each isotope studied, isotopically enriched Te material was evaporated onto an annealed Fe foil of ∼5 mg/cm^2 thickness. The Fe foil was then bonded to a copper backing thick enough to stop recoiling Te isotopes with a thin layer of evaporated indium (∼1 mg/cm^2). Details of the targets are given in Table 7.3. Targets were prepared by Dr. Georgiev and Prof. Stuchbery. Isotopically enriched targets were required as the natural isotopic abundances do not lead to balanced statistics across the measured isotopes. The enrichment ensured simple, clean spectra with (largely) well separated peaks. Although the lower stopping power of gadolinium allows larger integrated transient magnetic fields, iron was used for kinematic reasons. It is not kinematically possible for a ^{58}Ni beam bombarding ^{nat}Fe to backscatter, therefore any detected, backscattered particles will be from the Te target layer. Because the average atomic mass of the gadolinium target (157.25) exceeds the masses of the Te isotopes, the ^{58}Ni beam ions backscatter from a gadolinium backing with higher energy than from the Te target. This would create a background under the particles scattered from the Te target. Coulomb excitation of the rather collective Gd isotopes would potentially interfere with the weakly collective Te excitation of interest.

7.1.1.3 Hyperion

A diagram of the hyperfine spectrometer (Hyperion) [139] is given in Fig. 7.1. An electromagnet provided a localised magnetic field of 0.08 T that was used to align the magnetization of the annealed iron foil. The direction of the polarising mag-

Table 7.3: Target details in the Te g-factor measurements.

Isotope	Te (mg/cm^2)	Fe (mg/cm^2)	Cu (mg/cm^2)
^{124}Te	0.42	4.76	9.4
^{126}Te	0.59	5.29	5.3
^{128}Te	0.57	5.33	6.0
^{130}Te	0.72	4.53	5.9

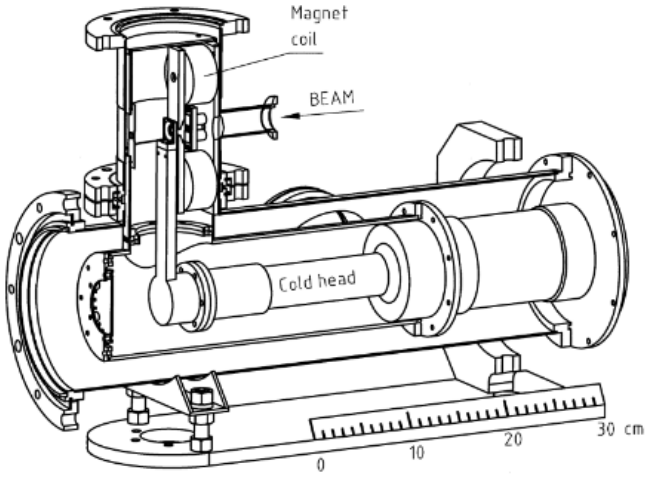

Figure 7.1: Diagram of the inside of the vacuum chamber, adopted from Ref. [139].

netic field was flipped approximately every 15 minutes, with data collection in the change-over period (a few seconds) tagged and removed from further analysis. The target temperature was maintained at a constant ∼4 K by a Sumitomo RDK-408D cryocooler. Tellurium has a low melting point (449.5° C) and is prone to target degradation under beam. Cooling the target helped maintain target quality throughout the measurements, although there was evidently some gradual loss of target material.

7.1.2 Detection electronics

7.1.2.1 Clover detectors

The γ rays produced in this experiment were detected by four clover detectors from the CLARION array [140]. These detectors are constructed from four, originally cylindrical, central-contact HPGe crystals with a diameter of 50 mm and a length of 80 mm. The crystals are planed on the sides nearest other crystals by 6 mm in order to allow a tighter geometry with less unused solid angle. The crystals are arranged in a pattern that resembles a four-leaf clover as displayed in Fig. 7.2. The primary energy signal is taken from central contacts within each crystal. The individual crystals are further electrically connected to outputs on the side and in the centre of the clover detectors which can be used to get a more precise position

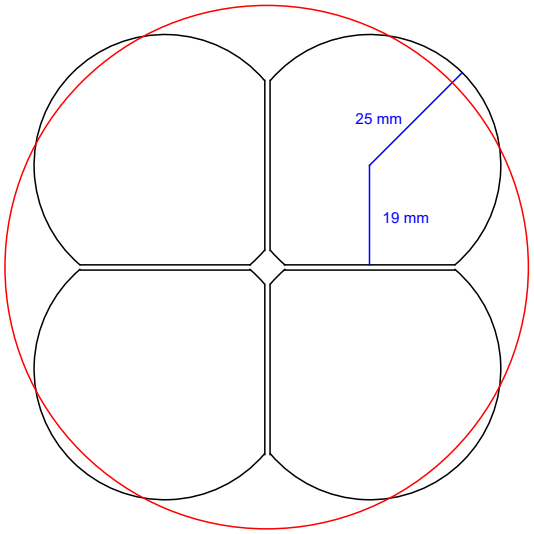

Figure 7.2: Geometry of the CLARION clover detectors. The black lines indicate the front face of the crystals that make up the clover detectors and face the target. The red line shows the approximation to a cylindrical geometry as described in the text.

for γ-ray detections based on the relative charge on the side channels of the crystal. However, this capability was not used due to an increase in noise in some crystals when the side channels were input to the data acquisition system. Two crystals were not functioning during parts of the experiment; these crystals were placed at back angles in equivalent (symmetrical) positions in order to maximise the number of working crystal pairs in optimal positions for the transient-field measurement and analysis. The clover detectors around the target chamber are displayed in Fig. 7.3.

Addback of Compton scattered γ rays was performed within each single clover detector. If two segments within a clover detector fired coincidentally, the energies of the two detection events were added to create a single detection event in the clover. This serves both to reduce the Compton background and increase the efficiency of the detectors.

Each clover had an energy resolution of $\sim$2 keV at 1 MeV γ-ray energy. The front faces of the clover detectors were placed 11.3 cm from the target position in the g-factor measurements. Some crystals experienced changes in gain over the run time. An example of the gain drift in one crystal over a 78 minute interval is displayed in Fig. 7.4. Corrections were made to the energy calibrations to account for this drift, see, for example, the green line in the figure.

The close geometry of the clover detectors decreases the amplitude of the slope of the angular correlation, however this decrease in sensitivity is more than recovered by the increasing absolute detection efficiency. The angles of the clover detectors used for the transient-field g-factor measurement are given in Table 7.2. The angles were chosen to be close to the maximum sensitivity for the precession measurement on the 4^+ state, with the back-angle detectors offset to account for non-functioning

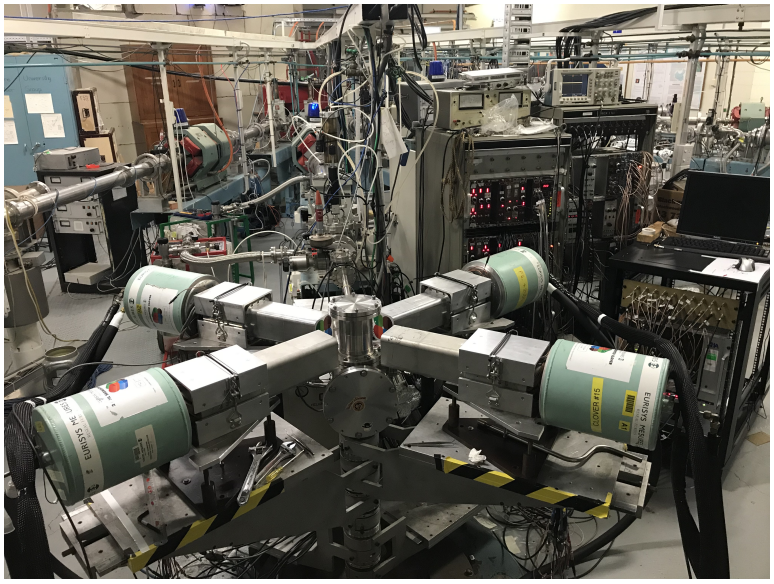

Figure 7.3: The clover detectors on the beam line as set up during the Te g-factor measurements.

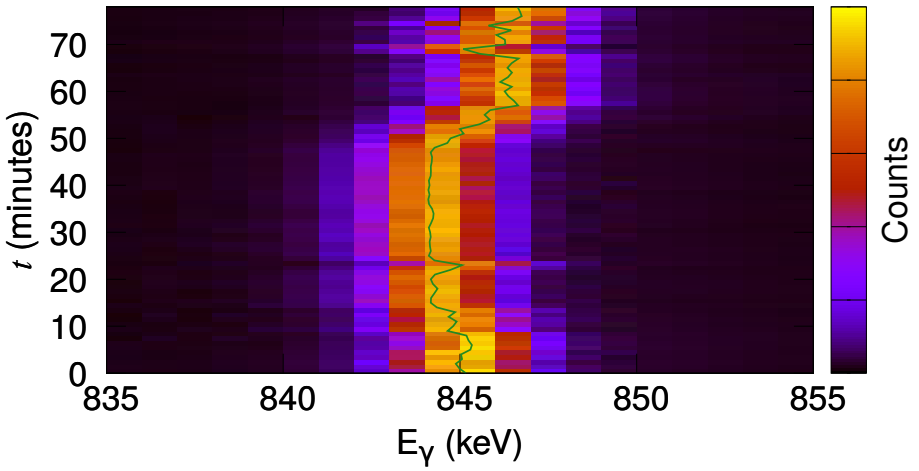

Figure 7.4: The energy of some clover crystals had significant drift. In the displayed crystal, the energy shifted by ∼2 keV over the 78 minute segment shown. The green line shows the centroid position over time that was used to correct for this gain drift.

crystals and enhance the sensitivity of the working crystals. The experimental sensitivity of the transient-field measurement can be approximated as $S^2W\sigma$, as discussed in Section 3.3. Sensitivity graphs as a function of angle with an example angular correlation for the $2_1^+ \rightarrow 0_{\text{g.s.}}^+$ and $4_1^+ \rightarrow 2_1^+$ transitions are presented in Figs. 7.5 and 7.6, respectively. In Fig. 7.7 and Fig. 7.8 experimental sensitivities as a function of distance, together with example angular correlations at specific distances are displayed for typical $2^+ \rightarrow 0^+$ and $4^+ \rightarrow 2^+$ transitions, respectively. In both figures, panel b) displays the proportional change in sensitivity, relative to the experimental distance, as a function of the distance of the crystal faces from the target position. It can be seen that distances closer than the 11.3 cm used in the present measurement would result in larger sensitivities, however, the position of other γ-ray detectors and the size of the target chamber meant that 11.3 cm was the smallest distance possible. Closer, and the adjacent detectors would touch.

Additional measurements were made at a range of detection angles in order to perform particle-γ correlation measurements. The angular correlation measurements confirm that the theoretically calculated statistical tensors (and hence angular correlations) used to determine the slopes in the g-factor analysis were correct. These measurements also check for angular offsets in the γ-ray detector position. If the layers of the target had come apart during the experiment and a gap had been created, the anisotropy would have been reduced by the vacuum deorientation process; the measurement of the angular correlation therefore also checks the integrity of the target.

7.1.2.2 Particle detectors

Backscattered particles were detected in two silicon photodiodes placed 16.2 mm upstream from the target and with their edges vertically offset above and below the beam by 3.8 mm as displayed in Fig. 7.9. The silicon photodiodes had a width of 25.2 mm and a height of 9.25 mm. Larger-area detectors were used in this measurement than in the recent simultaneous measurement of the stable even-even Te isotopes [101] in order to increase the sensitivity of the experiment. The increased angular coverage and smaller scattering angles (θ) lead to a reduced slope; however, the larger integrated cross section achieved with the larger detector is the dominant factor and increases sensitivity.

The sensitivity of the measurement to particle detector position is explored in Fig. 7.10. In all panels, the γ-ray detectors are placed at θ =65° and ϕ =0°, and the transition is assumed to be the $4_1^+ \rightarrow 2_1^+$ transition in ^{130}Te excited by ^{58}Ni at 198 MeV. Dashed red lines correspond to a point detector in the same ϕ plane as the γ-ray detector, solid green lines correspond to a point detector with $\Delta\phi$=90°, where $\Delta\phi$ is the ϕ or azimuthal angle between the γ-ray and particle detection angles, and dot-dashed purple lines correspond to annular particle detectors. Annular approximations are used in order to explore the effect of large angle finite detector sizes. The particle detectors used in this measurement cover a sizeable portion of the available scattering angles toward 180°. In panel a) the slope of the particle-γ cor-

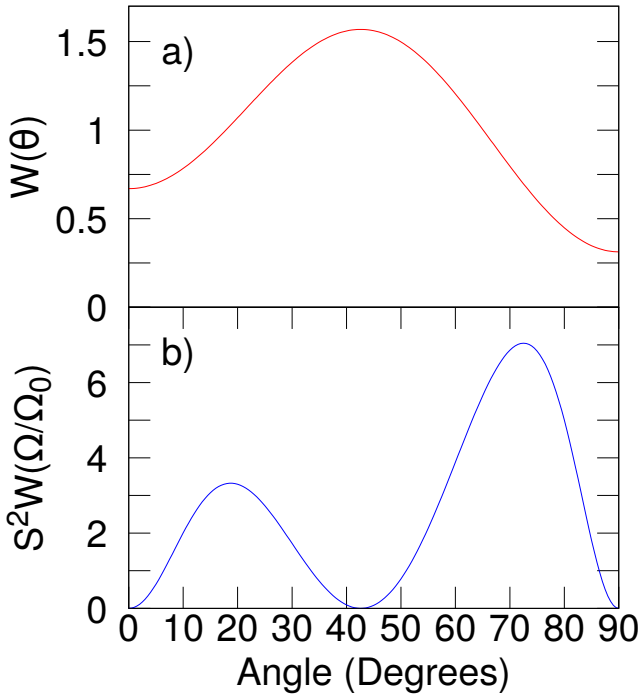

Figure 7.5: In panel a) an example of a calculated angular correlation is shown, in this case for the $2^+ \rightarrow 0^+$ transition in ^{130}Te. Panel b) contains a sensitivity plot for a $2^+ \rightarrow 0^+$ transition as a function of γ-ray detector angle. The front of the γ-ray detector is assumed to be 11.3 cm from the target as used in the experiment.

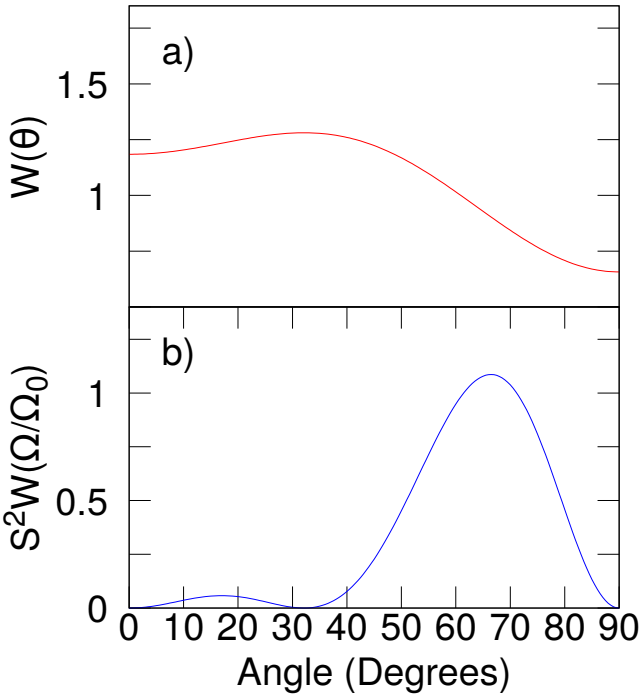

Figure 7.6: In panel a) an example of a calculated angular correlation is shown, in this case for the $4^+ \rightarrow 2^+$ transition in ^{130}Te. Panel b) contains a sensitivity plot for a $4^+ \rightarrow 2^+$ transition as a function of γ-ray detector angle. The front of the γ-ray detector is assumed to be 11.3 cm from the target as used in the experiment.

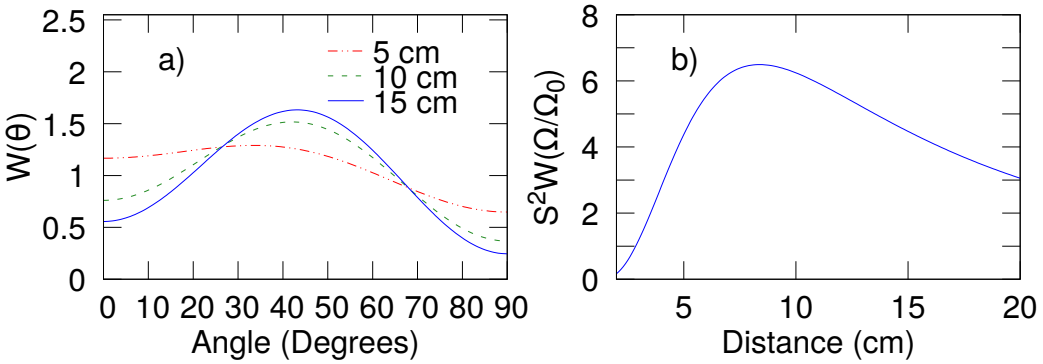

Figure 7.7: Angular correlations and sensitivity for $2^+ \rightarrow 0^+$ transitions as a function of the distance from the γ-ray detector to the target. In panel a) the angular correlations are given for a number of target-detector distances. In panel b) the sensitivity versus distance is shown, assuming a detector angle of 65°.

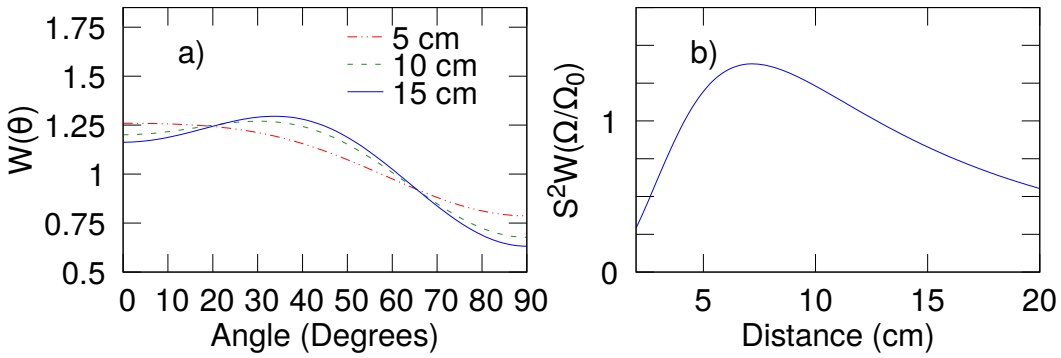

Figure 7.8: Angular correlations and sensitivity for $4^+ \rightarrow 2^+$ transitions as a function of the distance from the γ-ray detector to the target. In panel a) the angular correlations are given for a number of target-detector distances. In panel b) the sensitivity versus distance is shown, assuming a detector angle of 65°.

relation is presented. When $\Delta\phi$=90°, the predicted slope of the angular correlation is seen to be insensitive to the scattering angle (θ) of the incident ^{58}Ni. The sensitivity of the measurement excluding the increased cross-section at lower scattering angles is presented in panel b). In this case it remains high for a large portion of backscatter angles. Forward scattering angles are experimentally unavailable as thin-foil transient-field measurements are performed with a thick, non-magnetic backing, which would stop the scattered ^{58}Ni before reaching the particle detectors. Angles around θ=90°, $\Delta\phi$=90° are experimentally unavailable due to the magnet poles and coils used to magnetise the iron foil. In panel c) the value for an annular counter is multiplied by $2\pi\sin\theta$, which represents the total solid angle available at a given scattering angle. In panels d) and e) the excitation cross-section of the 4_1^+ state is taken into account. The total cross section for the 4_1^+ is larger at smaller scattering angles due to the larger Rutherford cross section; this pushes the maximum sensitivity to smaller scattering angles, in particular around $\Delta\phi$=90°.

As noted above, the particle detectors used in the present measurement had a width of 25.2 mm and a height of 9.25 mm, which fit in the chamber without shadowing from magnet poles. The sampled scattering angles and the associated sensitivities for the $2_1^+ \rightarrow 0^+_{\text{g.s.}}$ and $4_1^+ \rightarrow 2_1^+$ transitions are displayed in Fig. 7.11 and Fig. 7.12, respectively. The particle detector angles in the current and previous measurements [101] are indicated by the yellow and green lines, respectively. The range of scattering angles sampled was from 132°-167° with an average scattering angle of 152°. The particle detectors cover a large portion of the available scattering angles. The sensitivity of the measurement as a function of detector width is given in Fig. 7.13.

During part of the ^{124}Te and 198 MeV ^{130}Te measurements a section of one particle detector broke off. The red line corresponds to the broken edge of the particle detector for positive θ_γ detectors. The red line is mirrored around $\Delta\phi$=90° for negative θ_γ detectors. It is therefore necessary to estimate the effect of the missing section on the

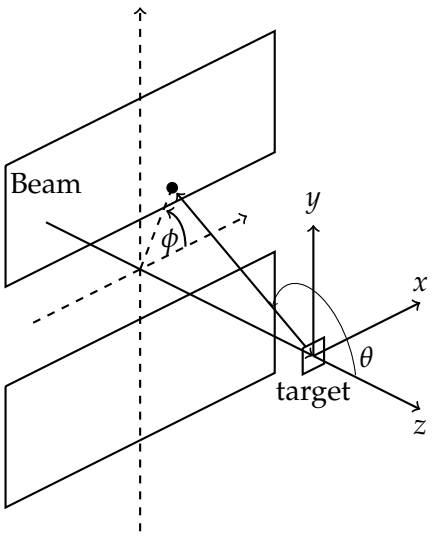

Figure 7.9: Particle-detector geometry used in the transient-field g-factor measurements on $^{124-130}$Te.

measured double ratio ρ as defined in Section 3.3. Using Eqn. 3.37 and integrating the relevant sections in Figs. 7.11 and 7.12, the change to ρ can be estimated to be $< 10^{-4}$% for the $2^+ \rightarrow 0^+_{\text{g.s.}}$. Since the statistical uncertainty is much larger than this, the effect of the broken detectors will not be discussed in further analysis.

7.1.2.3 Particle detector signal preprocessing

Timing outputs from the two particle detectors were first processed through Ortec 474/863 timing filter amplifiers and Ortec 935 constant fraction discriminators. Energy signals from the particle detectors were processed through Ortec 855 spectroscopy amplifiers and Ortec 542 linear gate and stretchers. The processed signals were input to the digital data acquisition. This analog pre-processing was required to filter out large amplitude oscillations as discussed in Section 4.2.3. A coincidence requirement between energy and timing outputs was included in as part of the data processing.

7.1.2.4 Data acquisition system

The data acquisition was performed using two 16-channel 100 MHz Pixie-16 digital data acquisition cards [104]. List-mode, triggerless data were collected; offline event construction used a dynamic 1-μs window, starting from the first trigger and including all events within 1 μs, with the event construction window extending to 1 μs past the last detected event. The CFD algorithm available on the Pixie-16 system was disabled, with fast-trigger timing determined to a precision corresponding to a 10 ns timestep.

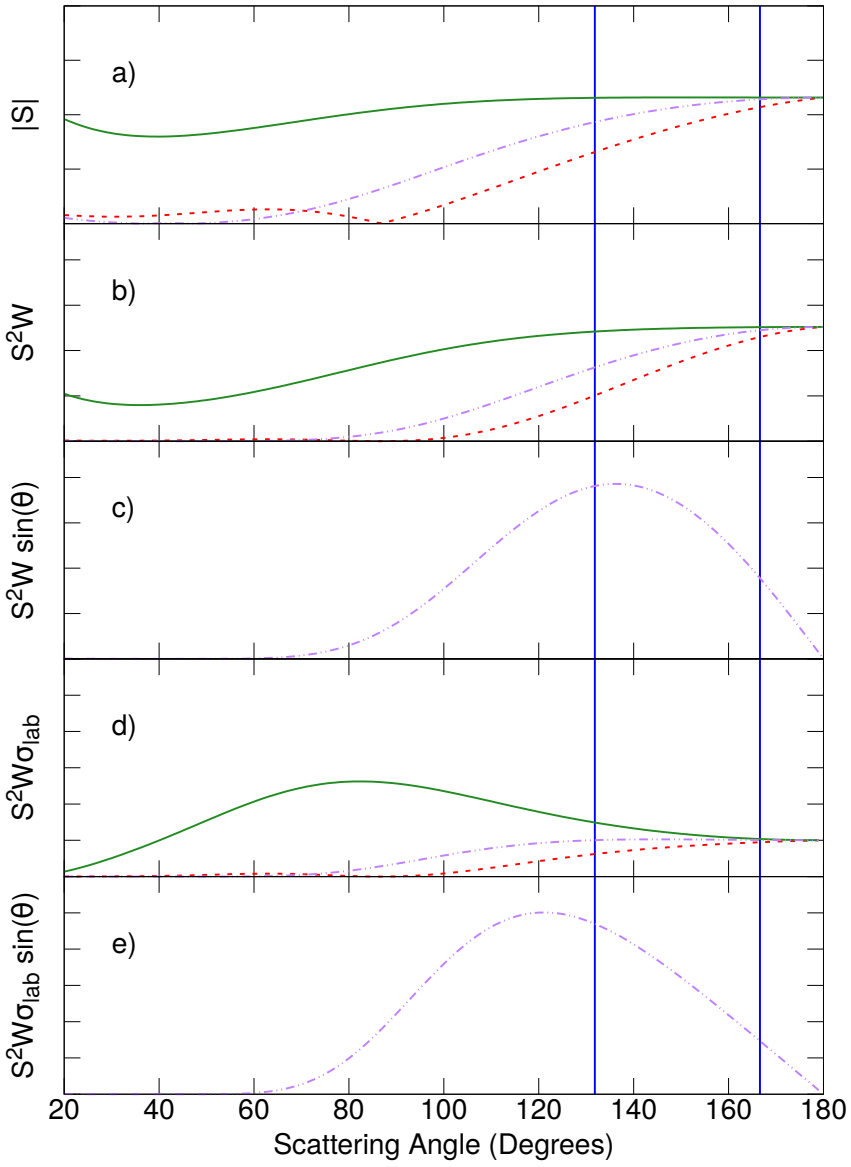

Figure 7.10: Sensitivity plots for the $4^+ \rightarrow 2^+$ transition in ^{130}Te calculated to understand the particle detector placement. Solid green and dashed red lines correspond to $\Delta\phi$=90° and $\Delta\phi$=0°, respectively, where $\Delta\phi$ is the azimuthal angle between the γ-ray and particle detectors. Dot-dashed purple lines represent annular particle detectors. The blue lines correspond to angles partially covered in the present measurement. Information on the panels is as follows: a) is the absolute value of the slopes; b) S^2W is proportional to the experimental sensitivity; c) S^2W is multiplied by $2\pi\sin\theta$ to obtain the total value of a single scattering at angle θ; d) is S^2W as in panel b) scaled by the Coulomb-excitation cross section of the 4_1^+ state; e) is as in d) scaled by $2\pi\sin\theta$ to obtain the total value of a scattering angle around all ϕ.

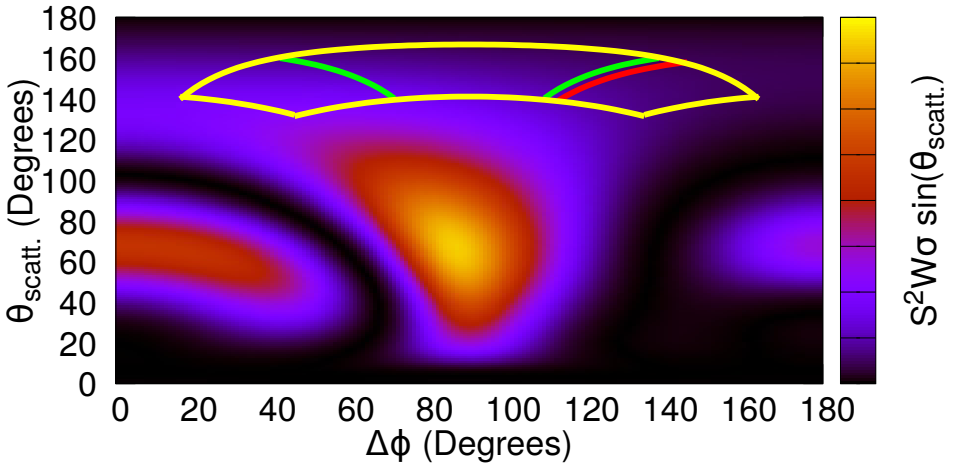

Figure 7.11: Sensitivity of the transient-field measurements for the $2^+ \rightarrow 0^+$ transition as a function of particle scattering angle. The clover γ-ray detector is assumed to be a CLARION clover (as in the experiment) at θ_γ=65°, ϕ_γ=0°, and 11.3 cm distance. The region marked by yellow lines is the solid angle covered by the particle detectors. The green lines correspond to the widths of the particle detectors in the previous measurement. The red line corresponds to the broken edge of the particle detector for positive θ detectors (see text for details). The red line is mirrored around $\Delta\phi$=90° for negative θ_γ detectors.

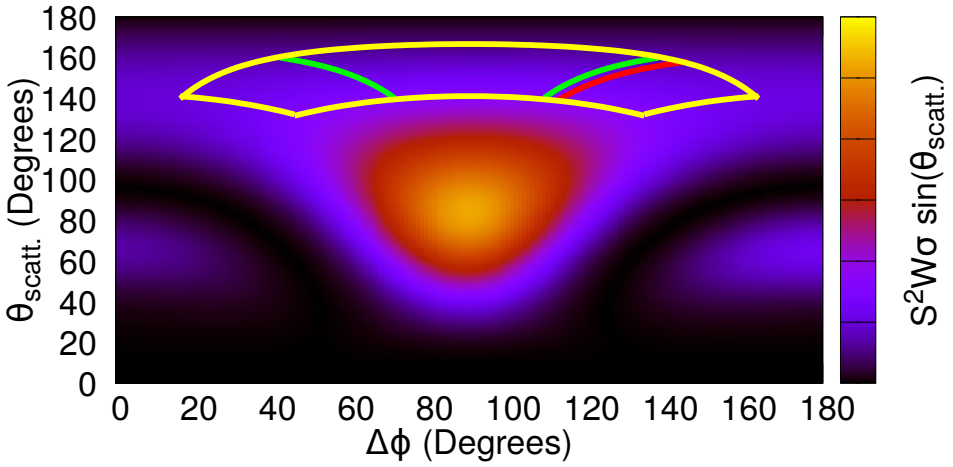

Figure 7.12: Sensitivity plot $4^+ \rightarrow 2^+$. The γ-ray detector is assumed to be a CLARION clover (as in the experiment) at θ_γ=65°, ϕ_γ=0°, and 11.3 cm distance. The region marked by yellow lines is the solid angle covered by the particle detectors. The green lines correspond to the widths of the particle detectors in the previous measurement. The red line corresponds to the broken edge of the particle detector for positive θ detectors (see text for details). The red line is mirrored around $\Delta\phi$=90° for negative θ detectors.

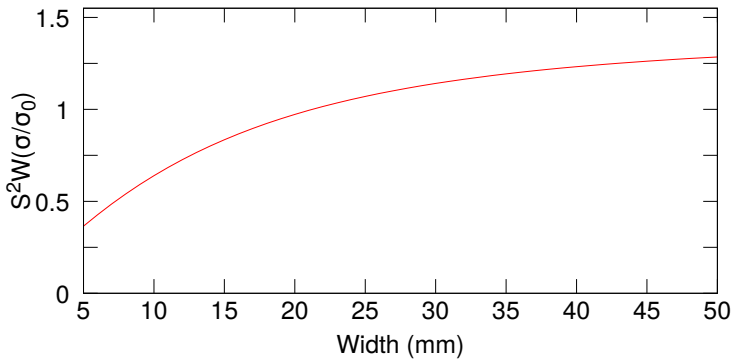

Figure 7.13: The sensitivity is given as a function of particle-detector width for an example $4^+ \rightarrow 2^+$ transition. The sensitivity of the measurement continues to increase out to large detector widths, but there is only a modest gain beyond 25 mm. Thus, the detectors used were near optimal.

7.1.3 Analysis procedures

A particle-energy spectrum and corresponding gate from Run F (See Table 7.2) is shown in Fig 7.14. The particle energy spectra have no observed background. Low-amplitude noise was eliminated by the linear gate and stretchers.

A particle-γ time difference spectrum from Run F is displayed in Fig. 7.15. The γ-detection time is subtracted from the particle detection time; the later the γ detection is after the particle-detection time, the further negative the time difference. Examples of the true and random gates used for random subtraction are shown. The tail to the left of the prompt peak in this spectrum is from low-energy γ rays.

Angular-correlation measurements were performed on ^{124,128,130}Te. Experimental correlations were fit to theoretically calculated angular correlations. In cases of a single multipolarity such as in the $E2$ transitions $4_1^+ \rightarrow 2^+$ and $2_1^+ \rightarrow 0_{\text{g.s.}}^+$ this reduces fitting to two parameters, an amplitude value; and a small angular offset. Statistical tensors were calculated using the de Boer-Winther program [141]. As the angular correlations can be calculated reliably, the angular correlation measurements are not strictly necessary to determine the slope of the angular correlation used in g-factor measurements. However the measurements are useful confirmation of the calculated statistical tensors and verification of the experimental set up and analysis procedures. Angular correlations are presented in Sec. 7.2.1.

Standard thin-foil transient-field analysis procedures were followed (see Sec. 3.3 for details). As the recoiling Te nuclei traverse the ferromagnetic layer a portion of the nuclei decay. There are two ways to deal with this. It is possible to take the total area of the particle-γ coincidence peaks and scale the measured precession by the average magnetic field experienced by recoiling nuclei before decay. In order to do this, the Doppler-broadened tails must be included in the measured peak areas. Including the Doppler-broadened tails increases the uncertainty a little from both the potentially unknown shape of the tails and from the smaller peak to background

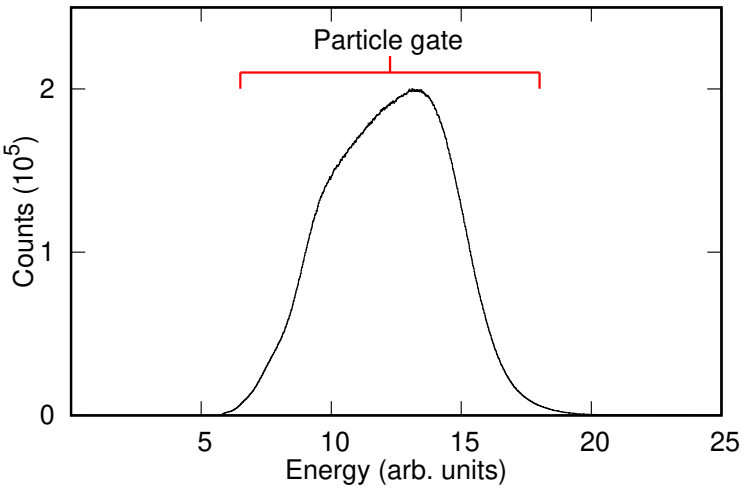

Figure 7.14: The particle-energy spectrum from a single particle detector in Run F. Data shown represent the total data taken. The particle energy gate used in the selection of particle-γ coincidences is indicated with a red line. The shape of the spectrum reflects the Rutherford backscattering cross section and energy loss of the beam in the target.

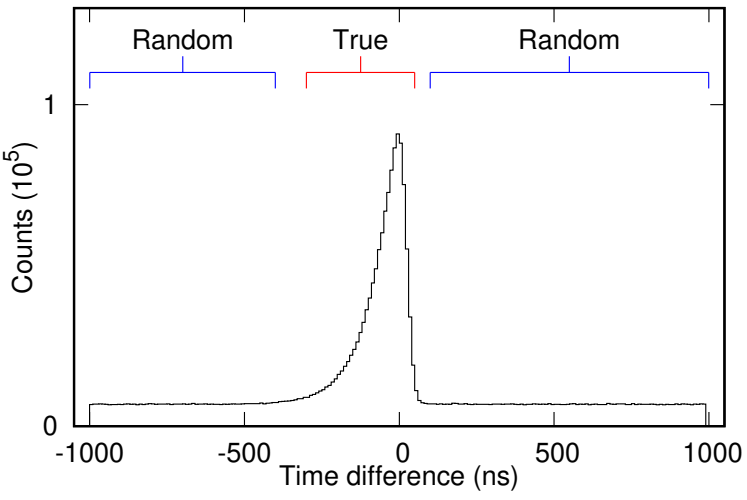

Figure 7.15: The time-difference spectrum from Run F between particle and γ-ray detections; later γ-ray detections are more negative. Time random subtraction was performed using the displayed true and random gates.

ratio in the tail region. A further complication occurs if there is overlap of the tails with other transitions that appear close in energy. In order to avoid these issues another approach was taken: namely, only the stop peak was included in the measured areas. Ideally, the stop peak would solely contain radiation from nuclei which had experienced the full transient-field precession from traversing the ferromagnetic layer. Unfortunately, due to the large solid angle coverage of the clover detectors used in this experiment, a portion of the unshifted γ-ray energies detected are from particle-γ angles close to 90°. The measured energy from such a transition would have energy close to the unshifted energy of the peak, contaminating the stop peak. A mitigating factor is that close to $\Delta\theta_{p-\gamma}$=90°, the angular correlation is much smaller than at smaller angles, decreasing the number of counts observed at the unshifted energy from moving nuclei. However, it is still necessary to estimate the maximum effect of this contamination.

In order to determine the transient field experienced by the Te nuclei, a simulation of the recoil events was performed. The level properties, reaction kinematics, and simulation results for recoiling Te nuclei are given in Table 7.4. The precession per unit g factor ($\phi(\tau)$) was calculated assuming a transient field parametrisation that has been shown to be accurate in the region [99; 100] and is also given in Table 7.4. Stopping powers used in calculations were taken from Ref. [106]. The calculated precession is a weak function of the lifetime. Unknown 4^+ state lifetimes for $^{126-130}$Te were estimated assuming $B(E2; 4_1^+ \rightarrow 2_1^+) = B(E2; 2_1^+ \rightarrow 0_{\text{g.s.}}^+)$. This assumption here is consistent with shell-model calculations discussed in Sec. 9.1.1 and is similar to the observed transition strengths in ^{124}Te [35]. Comparing the ratio of $\phi(2_1^+)$ to $\phi(4_1^+)$ (Eqn. 3.12) we see a maximum effect on the resulting ratio from the entire lineshape, including Doppler-broadened tails, of ∼2%. This is already much smaller than the statistical uncertainty in the measurements and, accounting for the procedures taken to minimise this effect, it is expected to be negligible. For this reason, uncertainty from this factor was not included in the overall uncertainty assigned to the measurements.

Table 7.4: Transient-field simulation details in Te g-factor measurements. E_B is the beam energy, E_n is the energy of the excited state n, I_n^π is the spin-parity of the excited state, τ is the state lifetime, $\langle E_i \rangle$ is the average initial energy of recoiling Te entering the Fe foil, $\langle E_e \rangle$ is the average energy of recoiling Te nuclei as they exit the Fe layer, $\langle v_i/v_0 \rangle$ and $\langle v_e/v_0 \rangle$ are the average initial and final velocities of the recoiling ion entering and exiting the Fe foil, $\langle v/v_0 \rangle$ is the average ion velocity through the Fe layer, t_{Fe} is the effective time that the Te experiences a magnetic field in the Fe layer, $\phi(\tau)$ is the calculated transient-field precession per unit g factor, and $\phi(\infty)$ is the limiting value as $\tau \to \infty$. $v_0 = c/137$ is the Bohr velocity. Unknown lifetimes (marked with *) are estimated by assuming the transition strength out of the 4^+ state is equal to the transition strength out of the 2^+ state. Data are taken from Refs. [41; 35].

Target	E_B (MeV)	E_n (keV)	I_n^+	τ (ps)	$\langle E_i \rangle$ (MeV)	$\langle E_e \rangle$ (MeV)	$\langle v_i/v_0 \rangle$	$\langle v_e/v_0 \rangle$	$\langle v/v_0 \rangle$	t_{Fe} (fs)	$-\phi(\tau)$ (mrad)	$-\phi(\infty)$ (mrad)
^{124}Te	200	603	2_1^+	9.1(5)	169.7	20.4	7.29	2.57	4.54	599	73.1	75.6
		1249	4_1^+	5.5(3)	169.8	20.3	7.29	2.57	4.56	586	71.6	75.7
^{126}Te	205	666	2_1^+	6.5(1)	159.0	13.5	7.13	2.08	4.07	726	84.0	89.0
		1361	4_1^+	5.3*	158.8	13.5	7.13	2.08	4.08	717	82.9	89.0
^{128}Te	205	743	2_1^+	4.7(9)	158.5	13.4	7.06	2.05	4.04	724	83.4	90.5
		1497	4_1^+	4.4*	158.3	13.3	7.06	2.05	4.04	720	83.0	90.5
^{130}Te	198	839	2_1^+	3.3(1)	148.8	20.1	6.79	2.50	4.33	564	66.3	73.1
		1634	4_1^+	4.4*	148.6	20.1	6.79	2.49	4.31	580	67.9	73.2
^{130}Te	205	839	2_1^+	3.3(1)	155.6	22.1	6.92	2.62	4.47	548	66.5	73.1
		1634	4_1^+	4.4*	154.3	22.0	6.92	2.61	4.45	562	68.1	73.2

Feeding corrections were applied as discussed in Section 3.3. The relevant measured initial populations, angular correlation gradients, and assumed g factors are in Table 7.5. Unknown g factors were assumed to be equal to $g(2_1^+)$. This is not expected to be a good assumption, in particular for the 6^+ states, so it is worth exploring the effect of a larger g factor (as expected) for these states. Changing the g factors of any state with an unmeasured g factor by a factor of two (similar to the largest predicted differences in shell-model calculations) has $<\sim$1% effect on the resulting observed precession of the 2^+ state. Similarly, changing the g factors of states feeding the 4_1^+ states by a factor of two had $<\sim$2% effect in ^{126,130}Te and less than $\sim$4% in ^{124,128}Te. These percentage uncertainties were added in quadrature to the relevant experimental uncertainties.

Table 7.5: Parameters used to obtain feeding correction factors for the 2_1^+ and 4_1^+ precessions. $N^0_{i,j}$ is the proportion of decays from feeding through the directly populated state I_i^π, the fed statistical tensors of the state I_j^π are then used to calculate the gradient of the angular correlation ($\frac{dW(\theta)}{d\theta}$), and these values along with the relative g factors ($g_j/g(2_1^+)$) are used to calculate $A_{i,j}$, which is as defined in Sec. 3.3.

Isotope	I_i^π	I_j^π	$N^0_{i,j}$	$g_j/g(2_1^+)$	$\frac{dW(\theta)}{d\theta}$	$A_{i,j}$	$\frac{dW(\theta)}{d\theta}$	$A_{i,j}$
			65°		65°		125°	
^{124}Te	2_1^+	2_1^+	77.4	1	−2.66	0.93	+1.87	0.94
		4_1^+	12.4		−0.94	0.05	+0.85	0.06
		2_2^+	8.5	1	−0.29	0.01	+0.06	0.00
		0_2^+	0.8	0	0	0.00	0	0.00
		6_1^+	0.8	1	−0.75	0.00	+0.72	0.00
		4_2^+	0.0	1	−0.93	0.00	+0.63	0.00
		4_2^+	0.0	1	−0.63	0.00	+0.84	0.00
	4_1^+	4_1^+	93.9		−0.93	0.96	+0.85	0.95
		6_1^+	6.1	1	−0.75	0.04	+0.72	0.05
		4_2^+		1	−0.68	0.00	+0.63	0.00
^{126}Te	2_1^+	2_1^+	82.2	1	−2.41	0.95	+1.72	0.96
		4_1^+	9.9		−0.88	0.04	+0.81	0.04
		2_2^+	7.5	1	−0.27	0.01	+0.05	0.00
		6_1^+	0.4	1	−0.70	0.00	+0.68	0.00
		0_2^+		0	0	0.00	0	0.00
	4_1^+	4_1^+	96.0		−0.87	0.97	+0.81	0.97
		6_1^+	4.0	1	−0.70	0.03	+0.68	0.03
^{128}Te	2_1^+	2_1^+	91.7	1	−2.41	0.98	+1.86	0.97

Continued on next page.

Table 7.5 continued.

Isotope	I_i^π	I_j^π	$N_{i,j}^0$	$g_j/g(2_1^+)$	$\frac{dW(\theta)}{d\theta}$	$A_{i,j}$	$\frac{dW(\theta)}{d\theta}$	$A_{i,j}$
			65°		65°		125°	
		4_1^+	3.4		−0.87	0.01	+0.85	0.02
		2_2^+	4.6	1	−0.26	0.00	+0.05	0.00
		6_1^+	0.3	1	−0.70	0.00	+0.72	0.00
		0_2^+		0	0	0.00	0	0.00
		4_2^+		1	−0.60	0.00	+0.64	0.00
		4_2^+		1	−0.88	0.00	+0.86	0.00
	4_1^+	4_1^+	92.1		−0.80	0.94	+0.79	0.95
		6_1^+	7.8	1	−0.70	0.06	+0.72	0.04
		4_2^+		1	−0.60	0.00	+0.38	0.01
^{130}Te	2_1^+	2_1^+	93.0	1	−2.34	0.99	+1.85	0.98
		2_2^+	1.9	1	+0.43	−0.00	−0.11	−0.00
		4_1^+	4.5		−0.88	0.02	+0.85	0.02
		2_3^+	0.4	1	+0.72	−0.00	−0.18	−0.00
		0_2^+	0.1	0	0	0.00	0	0.00
		4_2^+	0.08	1	−0.61	0.00	+0.65	0.00
		4_2^+	0.08	1	−0.88	0.00	+0.86	0.00
	4_1^+	4_1^+	98.1		−0.88	0.99	+1.30	0.98
		4_2^+	1.9	1	−0.61	0.01	+0.65	0.02

It is possible to perform a separate analysis based on the γ-ray detector crystals at specific angles rather than as full clover detectors. This reduces the effect of averaging over many angles. When the weighted average of the many particle-γ combinations is taken, it slightly decreases the overall uncertainty. However, when splitting the clover into its four components, a coincident Compton event between the two crystals at different polar angles does not have a clear position to be assigned and must be discarded. This reduces the total efficiency of the detector. Analysis was performed with both the full clovers and with the component detectors. Similar results were obtained. The results of the analysis with separate crystals were adopted to ensure no effect from the absent faulty crystals.

There have been several codes released for Doppler-broadened lineshape analysis recently [142; 143]. Doppler-broadened lineshape analysis was performed using a program based on the LINESHAPE program [144] using the procedures outlined in Section 3.4. The electronic stopping powers were calculated using the SRIM SR module [103]. It is also possible to gain sensitivity in these measurements by separating the data into clover segments and performing analysis on data taken in crystals with angles closer to 0° or 180°. However, the programs do not currently support arbi-

Table 7.6: Observed transitions in the ^{124}Te g-factor measurement. I_i^π and I_f^π are the spin and parity of the initial and final states, respectively. E_i and E_f are the energies of the initial and final states, respectively. E_γ is the transition energy. $I_\gamma(65^\circ)$ is the observed transition intensity, and I_γ is the transition intensity after corrections for the angular correlations have been applied. Level energies are taken from Ref. [61], and γ-ray energies are those measured in the present work.

I_i^π	E$_i$ (keV)	E$_\gamma$ (keV)	I_f^π	E$_f$ (keV)	$I_\gamma(65^\circ)$	I_γ
2^+	602.7	602.8	0^+	0	100(1)	100(1)
4^+	1248.6	645.7	2^+	602.7	13.1(5)	14.5(6)
2^+	1325.5	722.4	2^+	602.7	7.9(5)	7.0(5)
		1325.7	0^+	0	0.94(3)	0.95(3)
0^+	1657.3	1054.7	2^+	602.7	0.78(3)	0.80(3)
6^+	1747.0	498.3	4^+	1248.6	0.70(3)	0.78(3)
0^+	1882.9	556.9	2^+	1325.5		
4^+	1957.9	∼710	4^+	1248.6		
		∼1350	2^+	602.7		

trary γ-ray detector geometries (e.g. with the detector axis not pointing directly at the target) and so this analysis was not performed.

7.2 Results

Particle-γ energy spectra from the even-even $^{124-130}$Te measurements are displayed in Fig. 7.16. Transitions observed from the even-even $^{124-130}$Te isotopes are listed in Tables 7.6-7.9. Transitions from other isotopes populated by transfer reactions are given in Appendix A. The beam energies used in the excitation are slightly above the safe Coulomb-excitation limit; this does not affect the g-factor measurement. The transfer reactions occured at very low rates and were only visible in the present measurements due to the low Coulomb-excitation cross section and the high statistics obtained.

7.2.1 Angular correlations

While angular correlations were numerically integrated over the detector to calculate the slopes for the g-factor analysis, in order to reduce computation requirements in the angular correlation analysis, the clover detectors were approximated as cylindrical detectors with a radius of 5 cm. The real shape of the clover detectors compared

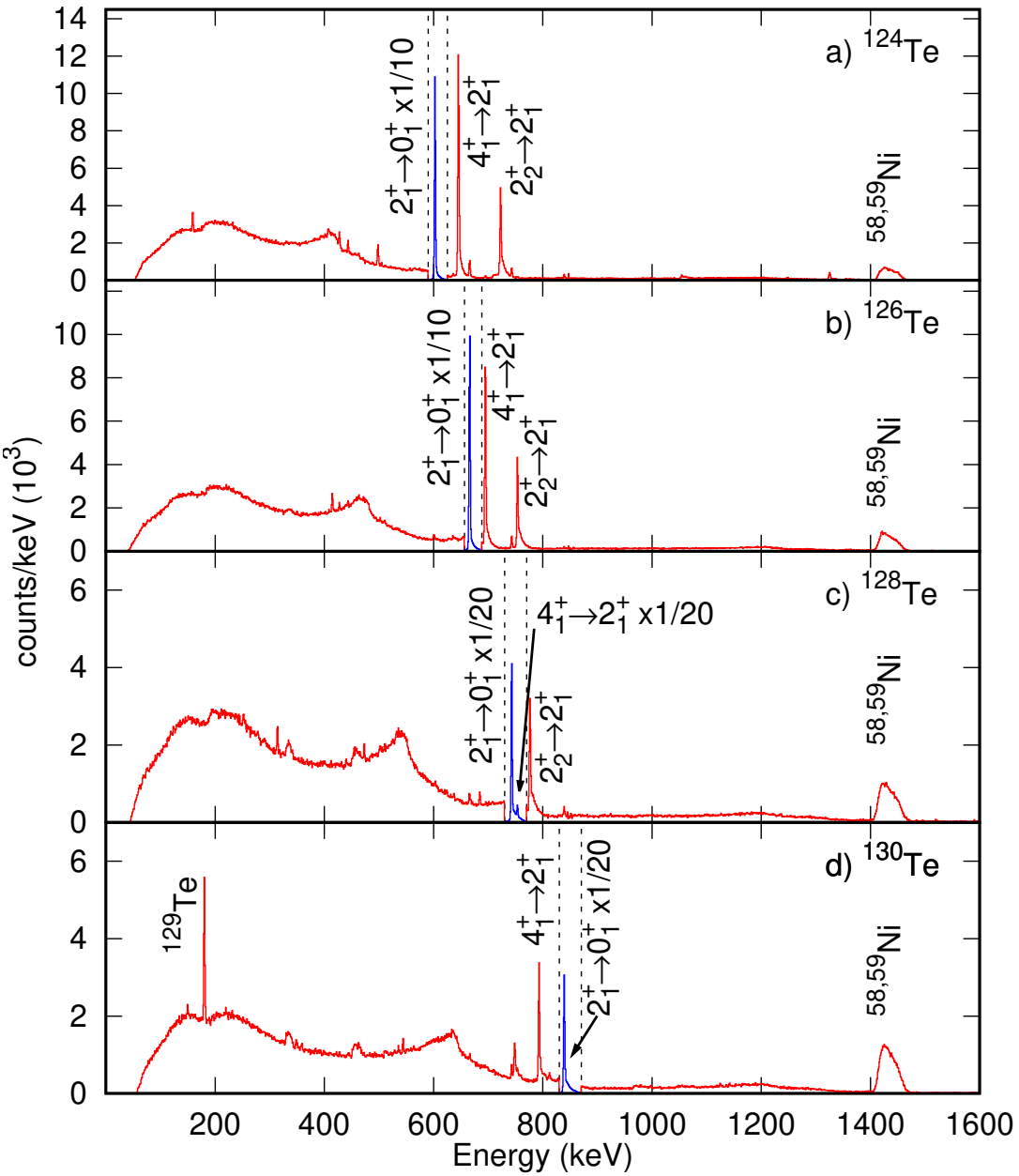

Figure 7.16: Particle-γ coincidence γ-ray spectra from ^{124,126,128,130}Te g-factor measurements. The displayed spectra contain all data from the clover detector at 65° in coincidence with the upper particle detector. The $2^+_1 \rightarrow 0^+_{\text{g.s.}}$ transitions have been scaled down by a factor of 10 for the ^{124,126}Te data and a factor of 20 for the ^{128,130}Te spectra.

Table 7.7: Observed transitions in the ^{126}Te g-factor measurement. I_i^π and I_f^π are the spin and parity of the initial and final states, respectively. E_i and E_f are the energies of the initial and final states, respectively. E_γ is the transition energy. $I_\gamma(65°)$ is the observed transition intensity, and I_γ is the transition intensity after corrections for the angular correlations have been applied. Level energies are taken from Ref. [62], and γ-ray energies are those measured in the present work.

I_i^π	E$_i$ (keV)	E$_\gamma$ (keV)	I_f^π	E$_f$ (keV)	$I_\gamma(65°)$	I_γ
2_1^+	666.4	666.4	0_1^+	0	100(1)	100(1)
4_1^+	1361.4	694.9	2_1^+	666.4	9.7(1)	10.6(1)
2_2^+	1420.2	753.8	2_1^+	666.4	7.0(1)	6.2(9)
		1420.2	0_1^+	0		
6_1^+	1776.2	414.7	4_1^+	1361.4	0.49(3)	0.54(3)
0_2^+	1873.4	1207.3	2_1^+	666.4	0.12(2)	0.12(2)
2_3	2045.2	2045.2	0_1^+	0	0.36(6)	0.36(6)

Table 7.8: Observed transitions in the ^{128}Te g-factor measurement. I_i^π and I_f^π are the spin and parity of the initial and final states, respectively. E_i and E_f are the energies of the initial and final states, respectively. E_γ is the transition energy. $I_\gamma(65°)$ is the observed transition intensity, and I_γ is the transition intensity after corrections for the angular correlations have been applied. Level energies are taken from Ref. [63], and γ-ray energies are those measured in the present work.

I_i^π	E$_i$ (keV)	E$_\gamma$ (keV)	I_f^π	E$_f$ (keV)	$I_\gamma(115°)$	I_γ
2_1^+	743.2	742.9	0_1^+	0	100(1)	100(1)
4_1^+	1497.0	753.6	2_1^+	743.2	6(1)	7(1)
2_2^+	1520.0	776.4	2_1^+	743.2	4.8(1)	4.9(1)
		1520.3	0_1^+	0	0.09(1)	0.09(1)
6_1^+	1811.1	314.0	4_1^+	1497.0	0.28(3)	0.31(3)
0_2^+	1978.8	1235.6	2_1^+	743.2	0.12(2)	0.12(2)
4_2^+	2027.8	530.7	4_1^+	1497.0		
		1284.6	2_1^+	743.2	0.03(2)	0.03(2)

Table 7.9: Observed transitions in the ^{130}Te g-factor measurement. I_i^π and I_f^π are the spin and parity of the initial and final states, respectively. E_i and E_f are the energies of the initial and final states, respectively. E_γ is the transition energy. $I_\gamma(65^\circ)$ is the observed transition intensity, and I_γ is the transition intensity after corrections for the angular correlations have been applied. Level energies are taken from Ref. [64], and γ-ray energies are those measured in the present work.

I_i^π	E_i (keV)	E_γ (keV)	I_f^π	E_f (keV)	$I_\gamma(65^\circ)$	I_γ
2_1^+	839.5	839.4	0_1^+	0	100(1)	100(1)
2_2^+	1588.3	748.4	2_1^+	839.5	1.7(1)	2.2(1)
		1588.0	0_1^+	0	0.03(1)	0.03(1)
4_1^+	1633.0	793.3	2_1^+	839.5	4.3(2)	4.8(2)
2_3^+	1885.7	∼1045	2_1^+	839.5	0.35(3)	0.38(3)
$(0)_2^+$	1964.8	1125.2	2_1^+	839.5	0.13(2)	0.13(2)
4_2^+	1981.5	348.6	4_1^+	1633.0	0.06(3)	0.07(3)
	1981.5	1142.9	4_1^+	839.5	0.10(2)	0.11(2)

to the approximation is presented in Fig. 7.2. Measured angular correlations with γ-ray detectors at distances of 11.3 cm and 15.2 cm from the target are displayed in Fig. 7.17 and Fig. 7.18, respectively. A second measurement of ^{130}Te in close geometry was performed in order to increase statistics over the first measurement. The relatively large angular offset observed in the close-geometry ^{130}Te correlation measured in Run F in Fig. 7.17 at negative angles is due to the crystal that was not working. The $2_1^+ \rightarrow 0_{\text{g.s.}}^+$ angular correlations are largely well reproduced. The only significant deviation in these correlations occurs in the ^{130}Te measurement at the larger distance (Fig. 7.18). It is unclear what is causing this discrepancy as it was taken soon after the far-geometry ^{128}Te data in the same run. The $4_1^+ \rightarrow 2_1^+$ transitions have much larger uncertainties. There is a possible flattening of the correlation between positive and negative angles in the ^{124}Te measurement. This trend may also appear in the close-geometry ^{130}Te measurements, although it is somewhat obscured by the larger uncertainties. This trend is not observed in the far-geometry measurements, which are governed by the same statistical tensors, and so it will be assumed to be statistical in origin and ignored in further analysis. As the mechanisms that govern that statistical tensors for the $2_1^+ \rightarrow 0_{\text{g.s.}}^+$ transition and the $4_1^+ \rightarrow 2_1^+$ transition are the same, the agreement between the measured and calculated angular correlations for the $2_1^+ \rightarrow 0_{\text{g.s.}}^+$ transition ensures valid slopes from the $4_1^+ \rightarrow 2_1^+$ transition.

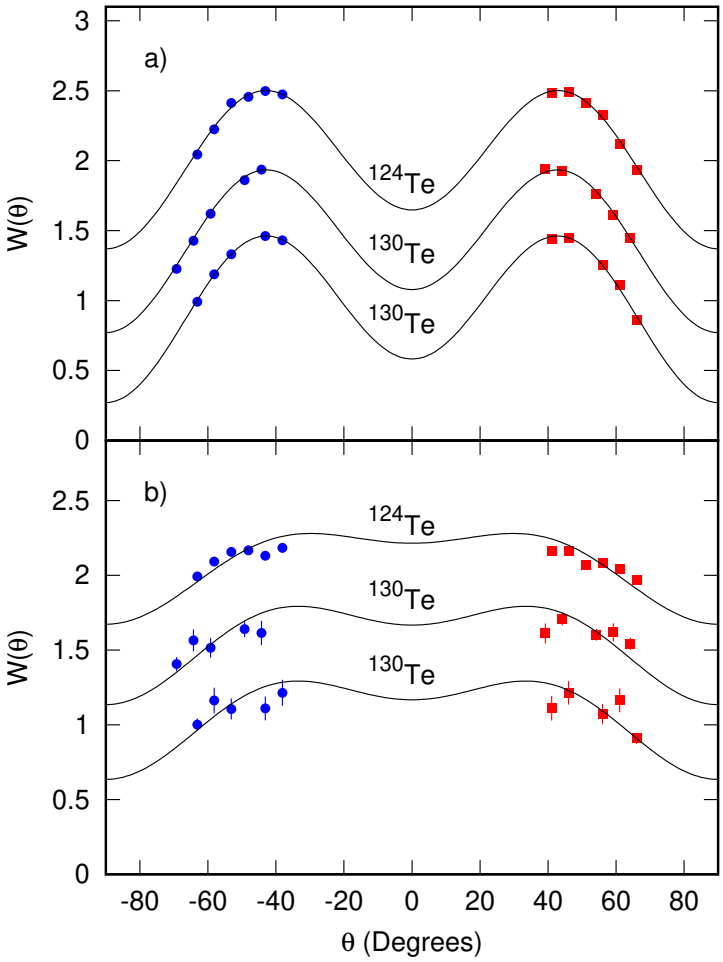

Figure 7.17: Measured angular correlations with γ-ray detectors at 11.3 cm from the target for transitions from the 2_1^+ states in panel a), and from the 4_1^+ states in panel b). Data from separate measurements have been offset for presentation. The two ^{130}Te measurements correspond to Run E (centre correlation in the figure) and Run F (lower correlation in the figure).

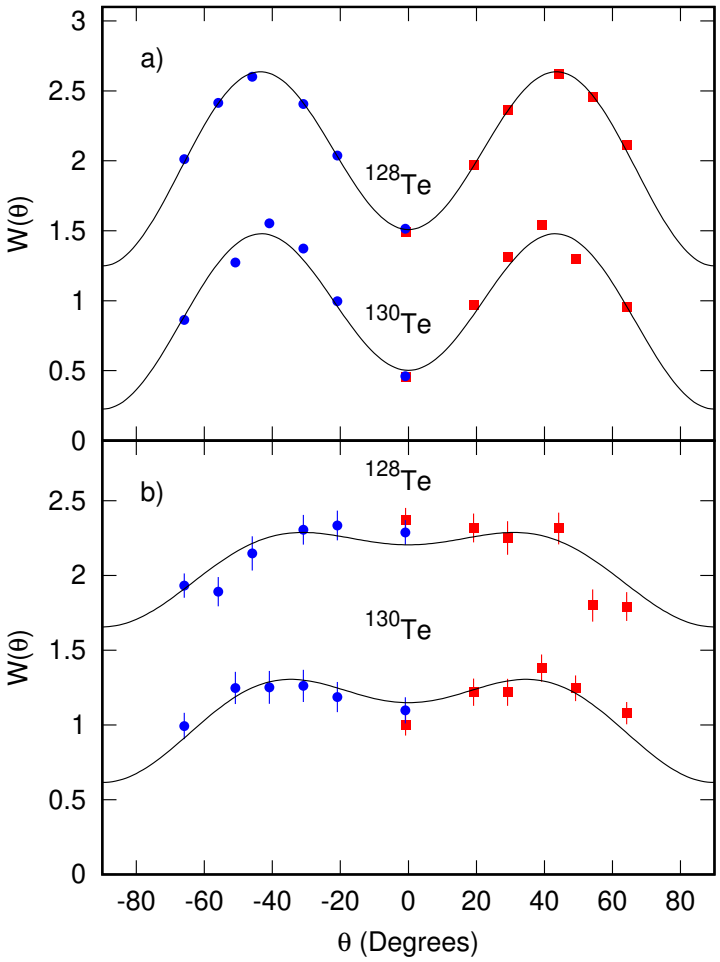

Figure 7.18: Measured angular correlations with γ-ray detectors at 15.2 cm from the target for transitions from the 2_1^+ states in panel a), and from the 4_1^+ states in panel b). Data from separate measurements have been offset for presentation.

7.2.2 Experimental g factors

Results from the g-factor measurements using the full and partitioned clover detectors are listed in Tables 7.10 and 7.11, respectively. The resulting g-factor ratios are consistent between the two separate analyses. The $\Delta\theta$ values obtained show discrepancies outside of statistical uncertainties in several cases, in particular the $\Delta\theta(2_1^+)$ values in the forward and backward detectors in the ^{124}Te measurement differ significantly (20.8(5) vs 27.2(8) mrad). In each case, the $^{\Delta\theta(4_1^+)}/_{\Delta\theta(2_1^+)}$ ratio is consistent between forward and backward detectors. The precession values $\Delta\theta$ are generally more consistent between detectors placed at similar angles than between forward and backward detectors. This may be due to angular offsets in the angles of the γ-ray detectors.

Table 7.10: Full-clover transient-field measurement results in the Te isotopes. Data are given for both the 2_1^+ and 4_1^+ measurements. The pairs of clover detectors used in the analysis have centres at $\pm\theta_\gamma$. The effect (ϵ) is given in milliunits, the slope of transitions, including feeding effects, (S_{fed}) are given for the positive-angle detectors. $\Delta\theta$ is the experimentally determined precession angle. Corrections to the g-factor ratio $g(4^+)/g(2^+)$ due to feeding have been applied. Angles marked with * include a clover detector with a faulty crystal.

Isotope	$\pm\theta_\gamma$	$\epsilon \times 10^3$	S_{fed} (rad^{-1})	$\Delta\theta$ (mrad)	$\epsilon \times 10^3$	S_{fed} (rad^{-1})	$\Delta\theta$ (mrad)	$g(4^+)/g(2^+)$
		2^+			4^+			
^{124}Te	65°	44.9(10)	−2.16	−20.8(5)	22(3)	−1.03	−22(3)	1.09(10)
	125°*	−31.2(9)	+1.14	−27.2(8)	−23(3)	+0.79	−29(4)	
^{126}Te	65°	50(2)	−2.22	−22.6(10)	15(8)	−1.03	−14(7)	1.15(12)
	125°*	−29(2)	+1.17	−24.9(19)	−25(8)	+0.79	−32(10)	
	65°	42.5(9)	−2.22	−19.2(4)	22(3)	−1.03	−21(3)	
	125°*	−26.7(10)	+1.17	−22.9(8)	−25(4)	+0.79	−31(4)	
^{128}Te	65°	45.4(10)	−2.45	−18.6(4)				1.39(20)
	125°*	−29.0(10)	+1.25	−23.2(8)	−21(5)	−0.79	−27(6)	
	65°*	38.5(11)	−2.45	−15.7(4)				
	115°	−38.5(10)	+2.45	−15.7(4)	−22(4)	+1.03	−22(4)	
^{130}Te	65°	48.2(13)	−2.46	−19.6(5)	34(7)	−1.03	−33(7)	1.85(22)
	125°*	−26.7(13)	+1.26	−21.2(11)	−48(9)	−0.79	−61(11)	
	65°*	42.8(18)	−2.44	−17.6(7)	31(8)	−1.03	−30(8)	
	115°	−35.8(14)	+2.44	−14.7(6)	−22(7)	+1.03	−21(7)	

Table 7.11: Clover-segment transient-field results in the Te isotopes. The pairs of clover crystals used in the analysis have average angles $\pm\theta_\gamma$. The effect (ϵ) is given in milliunits, the slope of transitions, including feeding effects, (S_{fed}) are given for the positive-angle crystals. $\Delta\theta$ is the experimentally determined precession angle. Corrections to the g-factor ratio $g(4^+)/g(2^+)$ due to feeding have been applied. Data are given for both the 2_1^+ and 4_1^+ measurements.

Isotope	$\langle\pm\theta_\gamma\rangle$	$\epsilon\times10^3$	S_{fed} (rad^{-1})	$\Delta\theta$ (mrad)	$\epsilon\times10^3$	S_{fed} (rad^{-1})	$\Delta\theta$ (mrad)	$g(4^+)/g(2^+)$
		2^+			4^+			
^{124}Te	57°	26.3(13)	−1.48	−17.8(9)	11(4)	−0.92	−12(5)	1.02(11)
	73°	78.4(19)	−3.53	−24.0(6)	33(5)	−1.16	−29(4)	
	117°	−54.1(13)	+2.25	−22.2(5)	−25(4)	+1.12	−22(4)	
	132°	−9.3(14)	+0.37	−25(4)	−20(5)	+0.53	−37(9)	
^{126}Te	57°	30(3)	−1.51	−20(2)	20(11)	−0.93	−21(12)	1.19(13)
	73°	85(4)	−3.68	−22.4(15)	17(12)	−1.16	−15(10)	
	117°	−52(4)	+2.31	−23.2(12)	−46(12)	+1.12	−42(11)	
	132°	−6(4)	+0.38	−17(10)	−10(14)	+0.53	−19(26)	
	57°	28.0(13)	−1.51	−18.5(9)	26(5)	−0.93	−29(5)	
	73°	73(2)	−3.68	−19.6(7)	23(6)	−1.16	−20(5)	
	117°	−45.2(15)	+2.31	−19.8(5)	−23(5)	+1.12	−21(5)	
	132°	−5.2(17)	+0.38	−14(4)	−21(7)	+0.53	−40(12)	
^{128}Te	57°	27.7(13)	−1.62	−17.1(8)				1.31(19)
	73°	82.2(20)	−4.31	−19.1(6)				
	117°	−48.3(15)	+2.53	−19.1(5)	−22(7)	+1.12	−20(6)	
	132°	−8.0(17)	+0.39	−20(4)	−23(8)	+0.53	−43(14)	
	57°	23.9(17)	−2.53	−18.5(9)				

Continued on next page.

Table 7.11 continued.

Isotope	$\langle \pm\theta_\gamma \rangle$	$\epsilon \times 10^3$	S_{fed} (rad^{-1})	$\Delta\theta$ (mrad)	$\epsilon \times 10^3$	S_{fed} (rad^{-1})	$\Delta\theta$ (mrad)	$g(4^+)/g(2^+)$
		2^+			4^+			
	73°	69(2)	−4.31	−19.6(7)				
	107°	−66(2)	+4.31	−19.8(5)	−26(7)	+0.93	−22(6)	
	123°	−25.9(13)	+2.53	−14(4)	−21(6)	+1.16	−23(7)	
^{130}Te	57°	30.2(17)	−1.63	−18.5(10)	33(10)	−0.93	−35(11)	1.97(22)
	73°	84(2)	−4.35	−17.3(8)	47(11)	−1.16	−40(9)	
	117°	−44.0(19)	+2.54	−19.4(6)	−45(11)	+1.12	−40(10)	
	132°	−4.0(23)	+0.40	−10(6)	−28(17)	+0.54	−52(31)	
	57°	18.4(26)	−1.62	−11.3(16)	62(15)	−0.93	−67(15)	
	73°	71(3)	−4.28	−14.5(6)	27(12)	−1.16	−23(10)	
	107°	−62(3)	+4.28	−16.5(7)	−26(11)	+1.16	−31(9)	
	123°	−24.3(18)	+1.62	−15.0(11)	−5(10)	+0.93	−6(11)	

7.2.3 Doppler-broadened lineshape results

Fitted lineshapes from the Doppler-broadened lineshape analysis at forward and backward angles are displayed in Fig. 7.19 and Fig. 7.20, respectively. The corresponding fitted lifetimes are given in Table 7.12. Most calculated lineshapes are seen to recreate experimental data reasonably well, however the lineshape for the $2_1^+ \rightarrow 0_{g.s.}^+$ transition in ^{126}Te (panel c in Fig. 7.19) has a larger discrepancy. The cause of this is not clear, however it may be due to a less well-defined background from the proximity of the $4_1^+ \rightarrow 2_1^+$ transition. The statistical errors are small in the analysis of the 2^+ states. However, other (less well-known) factors are important in the final determination of lifetimes from the data. A major source of uncertainty is the assumed stopping power. Calculated stopping powers often differ from experimental stopping powers on the order of 20%. This problem is compounded when complex targets are used, like those in the present measurements.

The data used for this analysis were obtained as a by-product of the transient-field measurement. As such, the placement of the detectors was not optimal for a DBLS measurement. In these measurements, the angular correlation can change the proportion of γ-ray detections at a given angle across the face of the detector. Modifications were therefore made to the analysis codes to account for the angular correlation.

The statistical errors were added in quadrature to a flat 20% uncertainty from potential systematic effects. The resulting mean lifetimes are given in Table 7.12 and the corresponding transition strengths are given in Table 7.13.

The transition strengths corresponding to the measured lifetimes are presented in Table 7.13. The lifetime of the 4_1^+ state in ^{130}Te is measured here for the first time. (A further measurement of the corresponding transition strength is presented in Chapter 8.) The observed lineshapes largely agree with the simulated results for both forward- and backward-facing detectors with the exception of the transition from the 2_1^+ state in ^{126}Te in detectors placed at forward angles. The cause of this discrepancy is not clear, however, the lifetime obtained in forward- and backward-facing detectors are in good agreement and the lifetime can largely be determined by the ratio of counts in the Doppler tail to the stop peak so it is unlikely to have significantly affected the derived mean lifetime. Measurement of the lifetime of the 4_1^+ state in ^{128}Te was not possible due to significant overlap of the transition and the Doppler tail of the transitions from the 2_1^+ and 4_1^+ states. The lifetimes presented in this section are in agreement with the transition strengths measured in Coulomb excitation presented in Chapter 8 and with previous measurements [41; 61; 62; 63; 64; 35]. In future discussions the values will be taken from the Coulomb-excitation analysis due to a higher precision, however the measured lifetimes are useful for confirmation of results.

The g factors and transition strengths reported in this chapter provide a solid basis for a discussion of the emergence of collectivity away from the N=82 shell closure. A clear departure from the proton-dominated excitations is observed as more neutron holes are involved in the nuclear structures. In the next chapter, further

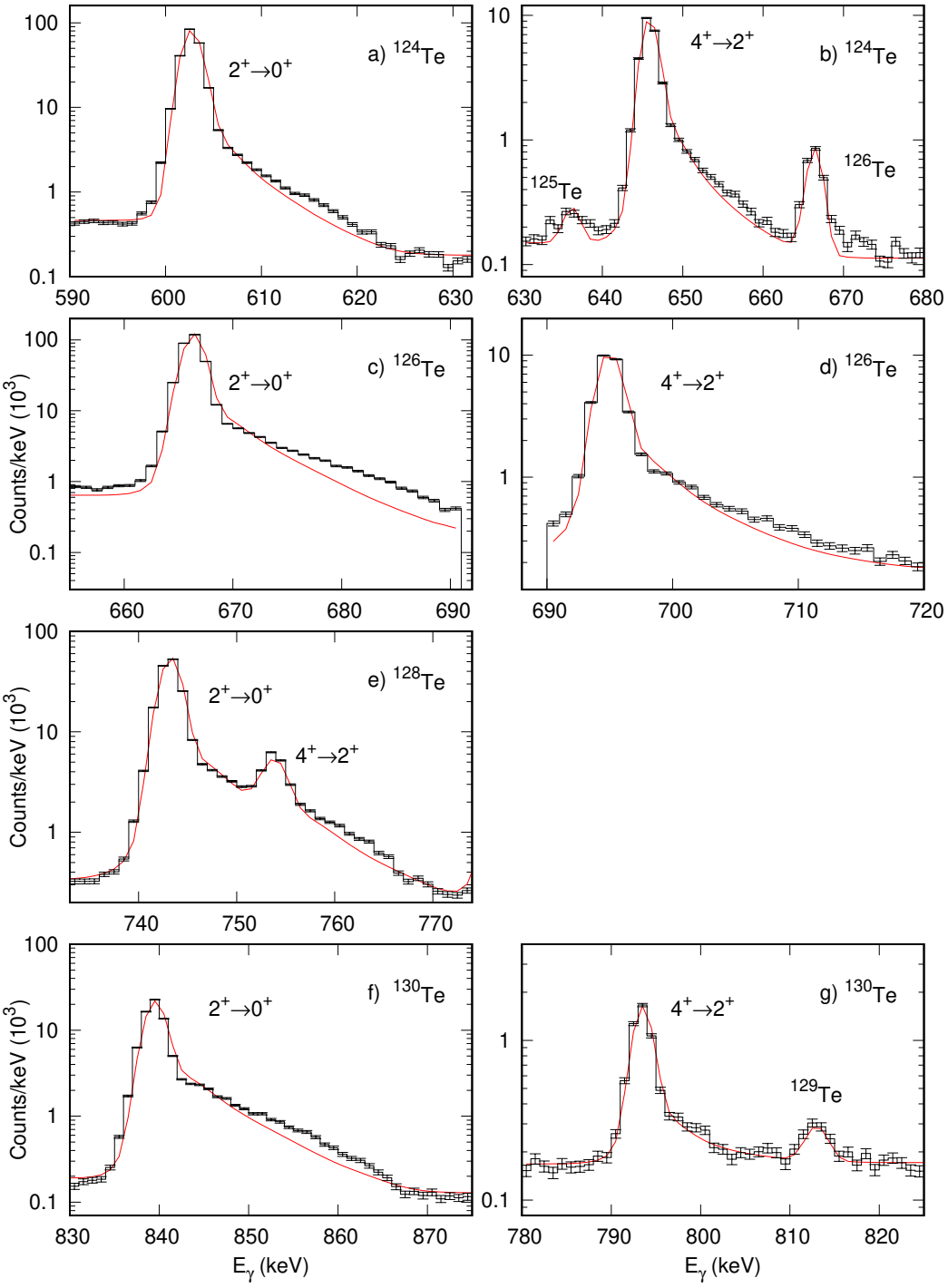

Figure 7.19: Fitted lineshapes from a Doppler-broadened lineshape analysis for 2_1^+ and 4_1^+ states in $^{124-130}$Te for the clover at 65°. The transition from the 4_1^+ state in ^{128}Te does not have a corresponding image as it sits on the tail of the $2_1^+ \rightarrow 0_{g.s.}^+$ transition. Contamination from the $2_1^+ \rightarrow 0_{g.s.}^+$ transition in ^{126}Te and the $^5/2_2^+ \rightarrow {}^3/2_1^+$ transition in ^{125}Te can be seen in panel b), and contamination from ^{129}Te is seen in panel g).

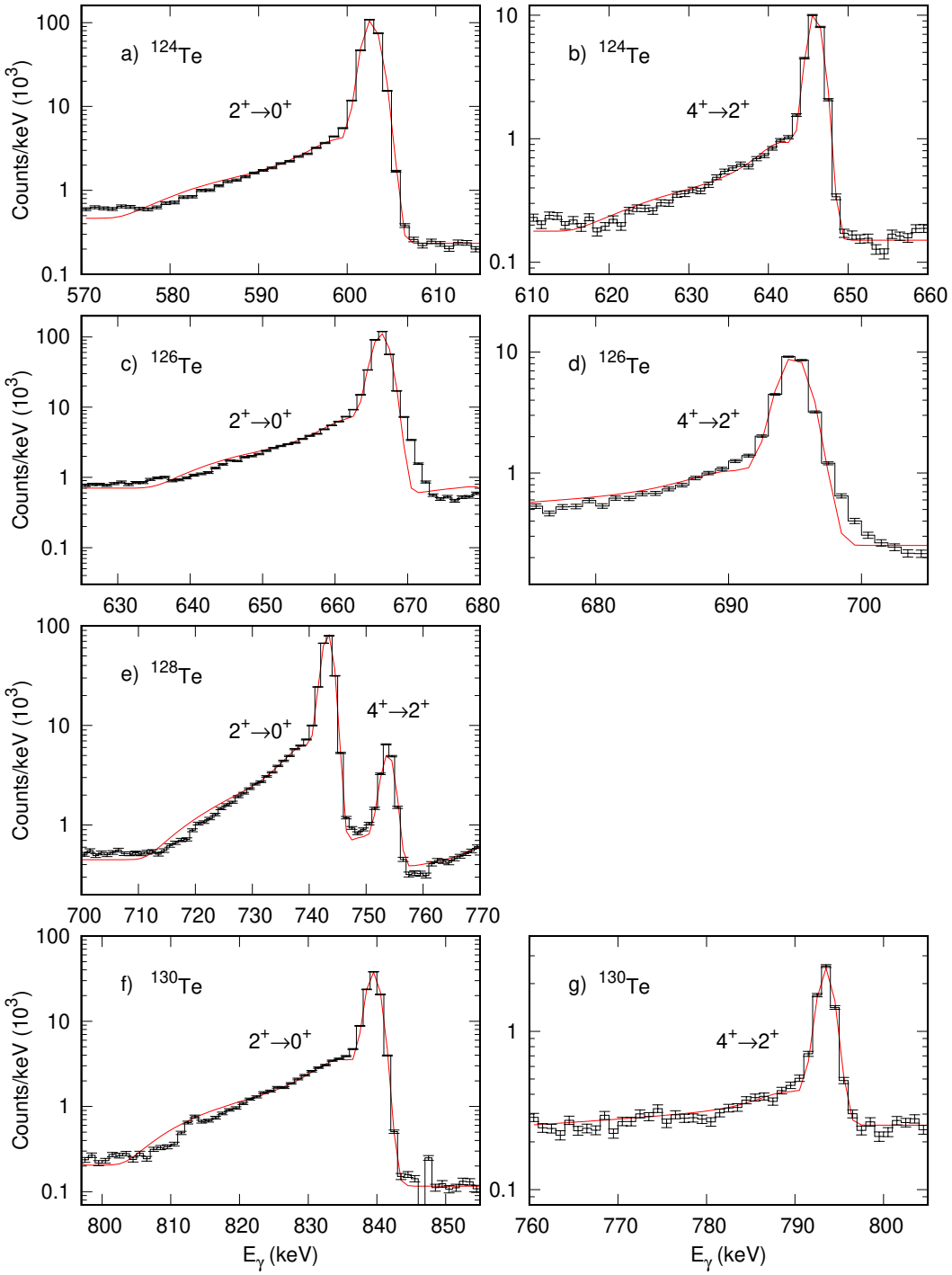

Figure 7.20: Fitted lineshapes from a Doppler-broadened lineshape analysis for 2_1^+ and 4_1^+ states in $^{124-130}$Te. The γ-ray detectors were placed at angles of 125° in the ^{124}Te and ^{126}Te measurements, and 115° in the ^{128}Te and ^{130}Te measurements. The transition from the 4_1^+ state in ^{128}Te does not have a corresponding image as its tail lies under the $2_1^+ \rightarrow 0_1^+$ transition.

Table 7.12: Mean lifetimes from the DSAM analysis of transitions in ^{124,126,128,130}Te. Literature values from Nuclear Data Sheets and previous Coulomb-excitation measurements [41; 61; 62; 63; 64; 35]. Back-angle detectors were placed at 125° in the ^{124}Te, ^{126}Te and ^{130}Te (Run E)) measurements and at 115° in the ^{128}Te and ^{130}Te (Run F) measurements.

Isotope	$\tau(2_1^+)$ (ps)			$\tau(4_1^+)$ (ps)		
	65°	125°/115°	Lit.	65°	125°/115°	Lit.
^{124}Te	9.3(21)	9.0(19)	8.94(14)	4.5(11)	4.9(10)	5.5(3)
^{126}Te	6.2(14)	6.0(13)	6.52(14)	3.9(9)	4.8(10)	4.0(17)
^{128}Te	4.7(11)	4.9(10)	4.76(4)			
^{130}Te	3.8(8)	3.3(7)	3.32(8)	3.8(9)	4.0(10)	
^{130}Te (Run F)	3.7(7)	3.5(7)	3.32(8)	4.8(11)	5.2(11)	

Table 7.13: Equivalent $E2$ transition strengths from DSAM lifetime measurements of 2_1^+ and 4_1^+ states in $^{124-130}$Te. Literature values are taken from Nuclear Data Sheets and previous Coulomb-excitation measurements [41; 61; 62; 63; 64; 35].

Isotope	$B(E2; 2_1^+ \rightarrow 0^+_{\text{g.s.}})$ (W.u.)		$B(E2; 4_1^+ \rightarrow 2_1^+)$ (W.u.)	
	Present	Lit.	Present	Lit.
^{124}Te	30(7)	30.5(15)	42(11)	35.9(17)
^{126}Te	27(6)	25.3(5)	31(7)	34(16)
^{128}Te	20(5)	19.8(4)		
^{130}Te	14(3)	15.1(5)	15(4)	

measurements of the $E2$ transition strengths in the Te isotopes are reported. This is then followed by a more complete discussion of the development of collectivity in the Te isotopes and combined with the Cd results in order to explore the emergence and nature of collectivity 'west' of ^{132}Sn in Chapter 9.

Chapter 8

Multi-step Coulomb excitation of ^{124,126,130}Te

Radioactive-ion beam (RIB) measurements can be challenging and often require calibration measurements of stable beams to model interactions, contaminants or peak shapes that are unclear in low-statistics RIB measurements. This calibration data often contains interesting and previously unknown information on the structure of the stable nuclei. Measurements of the transition strengths and electromagnetic moments in ^{136}Te required calibration data for the attenuation coefficients used in the recoil-in-vacuum (RIV) measurement of the 2_1^+-state g factor [145]. Coulomb-excitation measurements were therefore performed on several stable Te isotopes. In this chapter we discuss the measurement of transition strengths and quadrupole moments in ^{124,126,130}Te, based on these Coulomb-excitation experiments.

8.1 Experimental description

Coulomb-excitation measurements on ^{124,126,130}Te were performed at the Holifield Radioactive Ion Beam Facility (HRIBF) in inverse kinematics. Beams of ^{124,126,130}Te were Coulomb excited on a $\sim$1.5 mg/cm^2, isotopically enriched, ^{50}Ti target. Details of the target composition are given in Table 8.1. The enriched semi-magic ^{50}Ti target was chosen to reduce the excitation of, and hence the Compton background from, the $2_1^+ \rightarrow 0_{\text{g.s.}}^+$ transitions in the target nuclei.

The enriched target was chosen for the purposes of the RIV calibration, however an isotopically-enriched ^{48}Ti target would not significantly improve the experiment. Statistics of the normalisation transition were more than sufficient, the relative uncertainties in the enriched isotope and ^{48}Ti were similar, and the increased Compton background from the ^{48}Ti Coulomb excitation would have detracted from the measurement.

Particle detection was performed by rings 2-4 of the HyBall detector array [146]. Angular ranges of the array are given in Table 8.2. The HyBall array consists of rings of CsI detectors at a given polar angle range. The rings are segmented in the azimuthal angle to give position information for Doppler reconstruction and angular correlation measurements.

Table 8.1: Composition of the enriched ^{50}Ti target as measured by inductively coupled plasma mass spectrometry (ICP-MS). The quoted γ-ray energies (E_γ) correspond to the γ-ray transition from the state expected to be most strongly excited in each nucleus.

Isotope	^{46}Ti	^{47}Ti	^{48}Ti	^{49}Ti	^{50}Ti
Percentage	1.64(3)	1.35(3)	12.09(12)	3.52(4)	81.40(81)
E_γ (keV)	889.3	159.4	983.5	1542.2	1553.8

Table 8.2: Angular coverage, in the polar axis, of the particle-detector rings in the HyBall array in the ^{124,126,130}Te Coulomb-excitation measurements.

	Ring 2	Ring 3	Ring 4
Angle range	14-28°	28-44°	44-60°
Number of detectors	10	12	12

Kinematic information for each experiment is given in Table 8.3. The safe distance condition discussed in Sec. 3.1 can be used to determine which rings are considered to give safe Coulomb-excitation data. The safe distance is related to the scattering angle. In inverse kinematics, small detection angles, closer to head-on collisions, have smaller distances of closer approach. The beam loses energy through the target. The distance of closest approach will therefore be smaller at the front of the target than at the back. The distance of closest approach at the beam energy in Ring 2 is found to be smaller than the safe Coulomb-excitation distance at the beam energy, however, the distance of closest approach in Ring 2 becomes equal to the minimum safe distance with $\sim$20 MeV energy loss. The energy loss through the target is $>$ 80 MeV in each isotope and so the excitation of the beam particle largely occurs at safe energies. Ptolemy calculations [147] for excitation at the beam energy predict a $<$ 1% effect on the cross section of the 2_1^+ states at the minimum scattering angle in Ring 2. The effect of the Coulomb nuclear interference has therefore not been included in further analysis.

Detection of γ-rays was performed by six clover detectors from the CLARION array [140]. Three detectors were placed at a 90° angle relative to the beam axis, and three detectors were placed at a 131.75° angle. Side channel energy detection was used to constrain the detection position further for Doppler reconstruction; the γ-ray

Table 8.3: Experimental details in ^{124,126,130}Te Coulomb-excitation measurements.

Isotope	E_B	Safe distance	Minimum distance (fm)		
	(MeV)	(fm)	Ring 2	Ring 3	Ring 4
^{124}Te	385	15.84	15.12	15.88	17.81
^{126}Te	390	15.87	15.10	15.86	17.78
^{130}Te	400	15.94	15.05	15.81	17.74

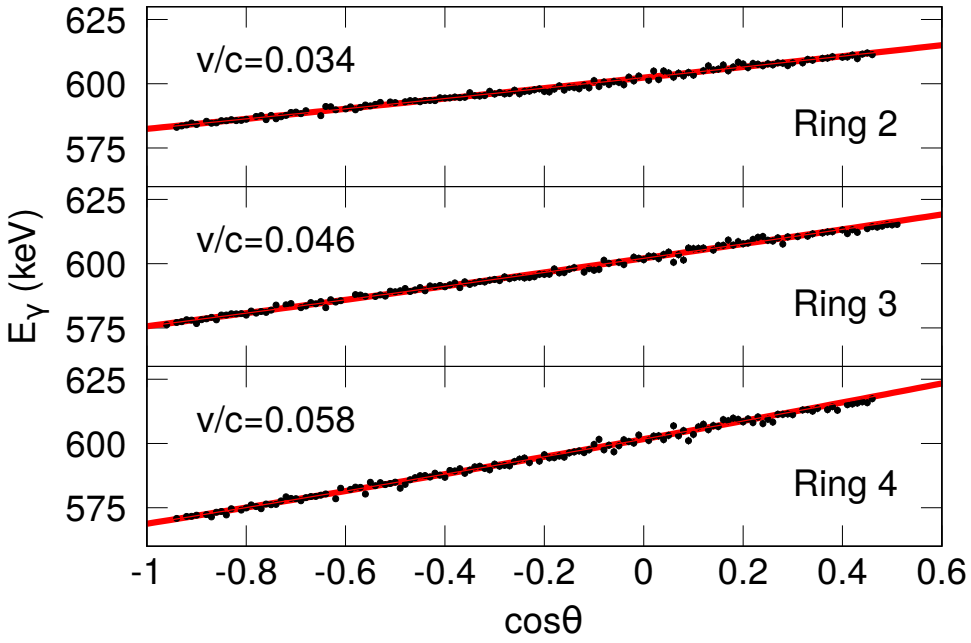

Figure 8.1: Measured Doppler shift in ^{124}Te Coulomb-excitation. Red lines correspond to fitted ^{124}Te velocities. Velocities were independently determined and results are given in Table 8.4. A large number of angular differences are available for the calibration from the segmentation of the particle and the localisation of γ-ray detection events to sub-crystal precision from side-channel energies; see text for details.

detection was assumed to be in the section of the crystal closest to the side channel with the largest energy. The dependence of detected γ-ray energies on the angular difference between the motion of the scattered Te ions and the detected γ rays in the ^{124}Te measurement is displayed in Fig. 8.1. The fitted velocities from the equivalent analysis for each isotope were used to perform Doppler reconstructions of γ-ray energy, and to calibrate the energy loss of the Te beam in the target, as discussed below.

Compton-scattering addback was performed by adding all detections in a single clover detector into a single event as in Sec. 7.1.2.1. When multiple crystals detect a γ-ray it is assumed that the multiple detections are due to Compton scattering within the detector. The calibrated energies of the γ rays in each crystal are summed to a single "detection". Addback increases the efficiency of the clover detectors and removes background from the Compton events under peaks.

8.2 Analysis procedures

Random subtraction was performed using usual procedures. Examples of prompt and background time gates are presented in Fig. 8.2. A particle ID (PID) statistic is

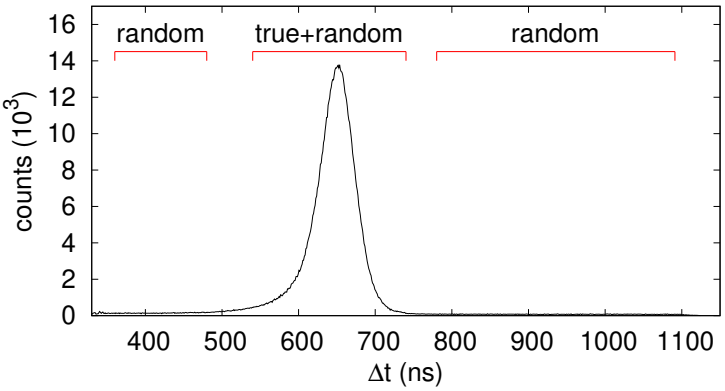

Figure 8.2: The time-difference spectrum between particle and γ-ray detections; later γ-ray detections are more negative. Time-random subtractions between coincident particles and γ-rays were performed using the prompt and random gates indicated.

used to identify the type of events detected in the particle detector. The PID statistic is determined through the relative measurement of the slow and fast components of the waveform in a detection due to the fast and slow decay times in the CsI(Tl) crystal. An example PID vs. energy plot in a CsI crystal from the ^{124}Te measurement is displayed in Fig. 8.3. The Ti-like recoils are marked by an example gate shown in white. The separation of the heavy ion like particles from the lower mass particles (e.g. electrons) allows clean determination of particle singles and particle-γ coincidences. The clear separation of the particle group would also allow Coulomb-excitation-to-Rutherford measurements for absolute normalisation, however, dead-time measurements were not performed and these have been observed to be too large to neglect in similar experiments. Normalisation of the beam excitation to excitation of ^{48}Ti in the target was performed relative to the ^{48}Ti present in the target. The excitation of the 2_1^+ states occurs at similar rates in ^{48}Ti and ^{50}Ti since the higher excitation cross section of ^{48}Ti compensates for its lower abundance in the target. An analysis using a ^{50}Ti normalisation is complicated by the overlap of observed transitions from the $2_1^+ \rightarrow 0^+_{\text{g.s.}}$ transition in ^{50}Ti and the $^{11}/_{2_1^-} \rightarrow {}^{7}/_{2^-_{\text{g.s.}}}$ transition in ^{49}Ti.

Coulomb-excitation analysis was performed using the analysis code GOSIA [96]. Internal-conversion coefficients used in the GOSIA analysis were sourced through the BRICC database [107]. For each isotope, best fit values were obtained through the internal fitting routine of the program using the intensities from the present measurement with corrections due to target composition and angular correlations, described below. Uncertainties were obtained through creating a χ^2 surface by fixing a value of the matrix element of interest and allowing the program to fit other matrix elements and using the values at $\chi^2 + 1$ as 1σ values.

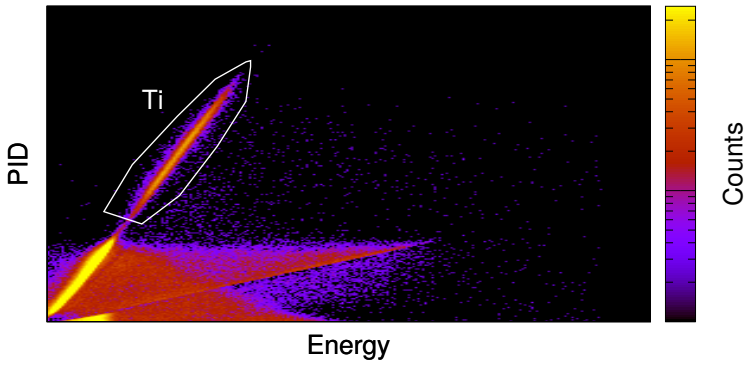

Figure 8.3: The particle-identification statistic (as discussed in Sec. 8.2) is plotted against the energy observed in a single CsI crystal in Ring 2. Heavy-ion like Ti particles are marked by an example gate shown in white. Electron and γ-ray events are seen below the heavy-ion-like events.

Table 8.4: Energy-loss calibration details as determined through measurement of the Doppler shifts of γ-ray energies in the Coulomb-excitation measurements of ^{124,126,130}Te and the simulation used to reproduce the experimentally determined velocities.

Isotope	E_B	v/c_{Exp} (%)			$v/c_{sim.}$ (%)			E_{loss}
	(MeV)	Ring 2	Ring 3	Ring 4	Ring 2	Ring 3	Ring 4	(MeV)
^{124}Te	385	3.41(3)	4.58(3)	5.76(3)	3.41	4.55	5.75	88(2)
^{126}Te	390	3.49(2)	4.64(2)	5.81(2)	3.50	4.63	5.81	85(2)
^{130}Te	400	3.54(2)	4.65(2)	5.84(2)	3.54	4.64	5.81	87(2)

8.3 Efficiency calibration

An efficiency measurement was performed using a ^{152}Eu source placed directly behind the target. The efficiency curve used in the analysis is shown in Fig. 8.4. The majority of the states explored are in the energy region from 600-1000 keV where the relative efficiency is well characterised. De-excitation γ rays from the 3^- states in ^{124,126}Te require an extrapolation of the measured curve above the well characterised region. The transitions from the 3^- states are too weak to extract meaningful results and are not discussed further in the present work.

8.4 Energy loss calibration

The energy-loss calibration was performed by simulating the kinematics and energy loss through the target using the Ziegler 1985 stopping powers [106], then scaling these stopping powers by a constant factor to reproduce the observed Doppler shift. Details of this analysis are presented in Table 8.4.

The stopping powers calculated with SRIM change slowly through the full range

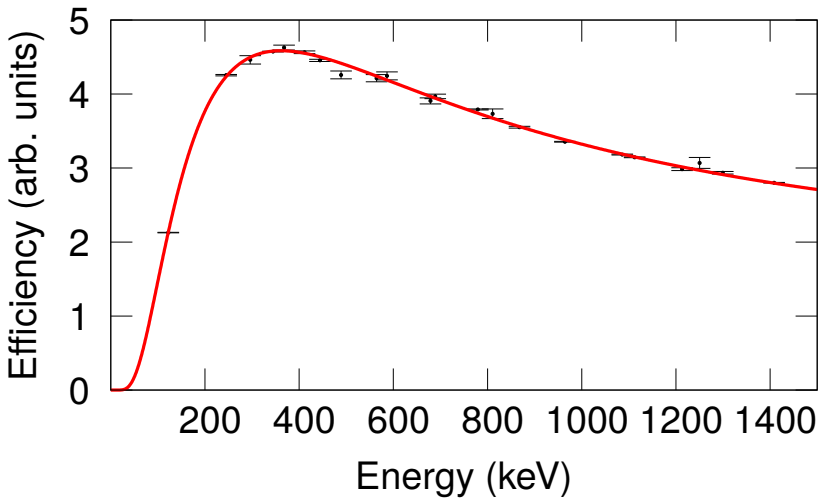

Figure 8.4: The relative γ-ray detection efficiency determined using the full clover array. The calibration was determined up to ∼1400 keV. This was used in the Te Coulomb-excitation analysis.

of energies experienced by the beam particles (∼ 4% over a 90 MeV energy loss) and are expected to be similar for each isotope (<1% difference) in the region of interest. A previous measurement of the energy loss of a 410 MeV ^{136}Te beam through the target used in this experiment was made using a Bragg detector; it found an energy loss of 86(2) MeV [145], consistent with the energy loss determined in this measurement through the Doppler shifts and shown in Table 8.4. A weighted average of all four energy loss measurements (including the Bragg detector measurement) of 86.5(10) MeV was adopted in the Coulomb-excitation analysis with GOSIA.

8.5 Target composition corrections

Excitation calculations were made assuming a 100% ^{50}Ti target, however, ^{50}Ti only comprises 81.40(81)% of the target. Interactions with different Ti isotopes result in different Coulomb-excitation-to-Rutherford ratios. A correction factor must therefore be calculated to account for the target composition. The Rutherford and Coulomb-excitation quantities were calculated for each isotope and each ring. The correction factors were found to be largely independent of the HyBall ring investigated (< 0.1% effect). The final correction factors are presented in Table 8.5.

8.6 Recoil in vacuum calibration

When the nucleus is excited in Coulomb excitation it is in an aligned state. The angular distribution from this aligned state impacts the observed transition intensities. The initial statistical tensors governing the shape of the particle-γ angular correlations can be calculated. While GOSIA is capable of calculating these statistical

Table 8.5: Excitation correction factors accounting for Te excitation from Ti isotopes other than ^{50}Ti.

Beam species	2_1^+	4_1^+	2_2^+
^{124}Te	1.02	1.05	1.05
^{126}Te	1.03	1.05	1.05
^{130}Te	1.03	1.06	1.06

tensors and correcting for them, the initial angular distributions are quenched due to interactions from electrons around the nucleus. This is accounted for in GOSIA using a simple two-state model [148], however, the magnitude of the quenching must be fitted. Two approaches were taken to account for this. Angular distributions were formed using the two polar angles with HPGe detectors for each particle-detector ring. The two state model parameters were adjusted manually to reproduce the ratio of these data points. The second approach taken was to construct $\Delta\phi$ distributions and fit the vacuum deorientation coefficients G_2 and G_4. Fitted angular correlations are presented in Figs. 8.5-8.7 and parameters determined from the fits are presented in Table 8.6. The relationship between G_2 and G_4 was fixed in this fitting procedure using the Abragam-Pound fluctuating field model [149]. Note that an accurate description of the RIV mechanism is not required here; all that is needed is a good fit to the angular correlation data. These data, presented here, have previously been used to calibrate a recoil in vacuum g-factor measurement of the first-excited state of ^{136}Te for the analysis presented in Refs. [135; 145].

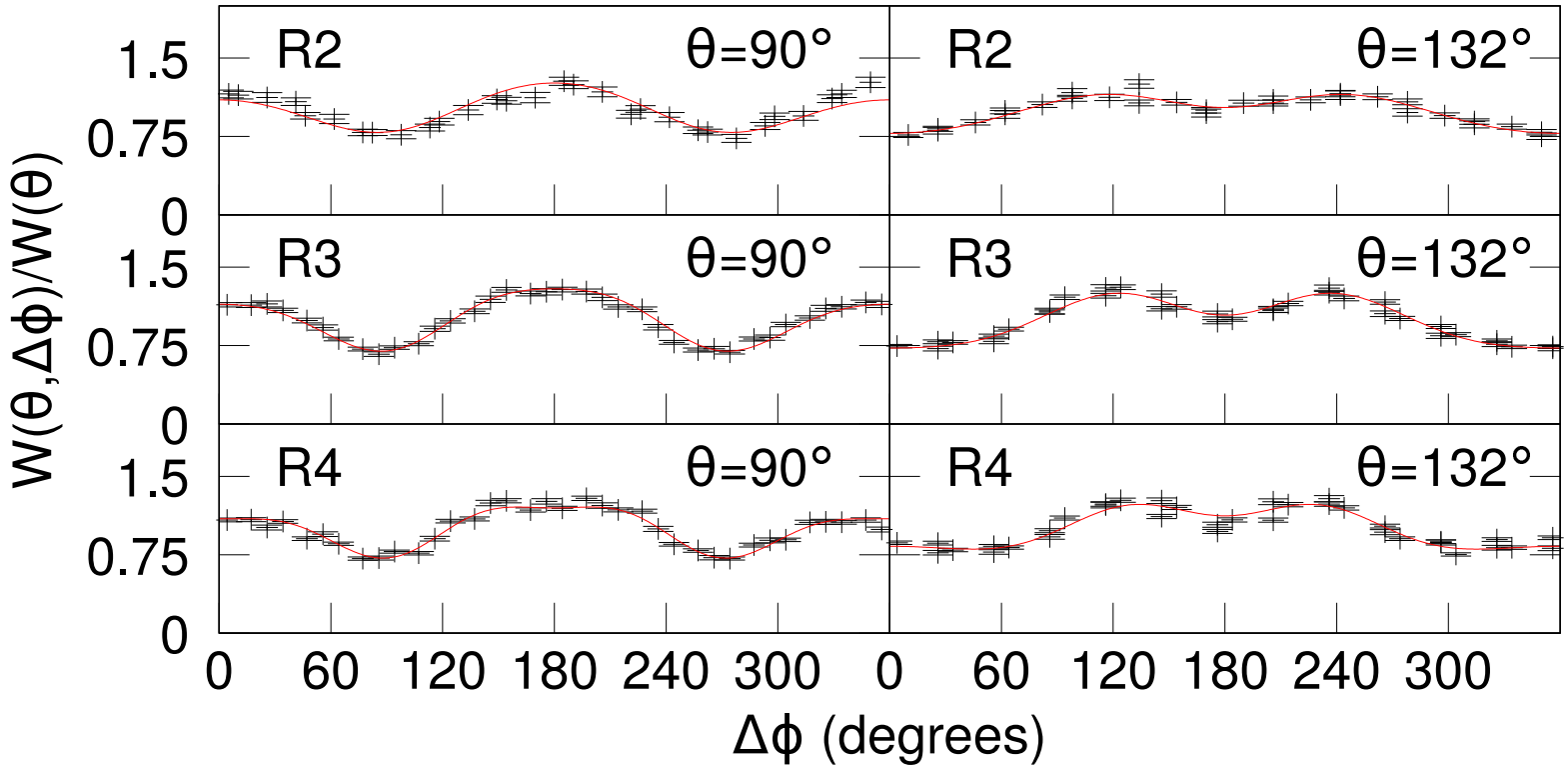

Figure 8.5: Angular distributions around $\Delta\phi$ for ^{124}Te. Red lines correspond to fitted distributions. $W(\theta)$ is the average value of the angular distribution around $\Delta\phi$.

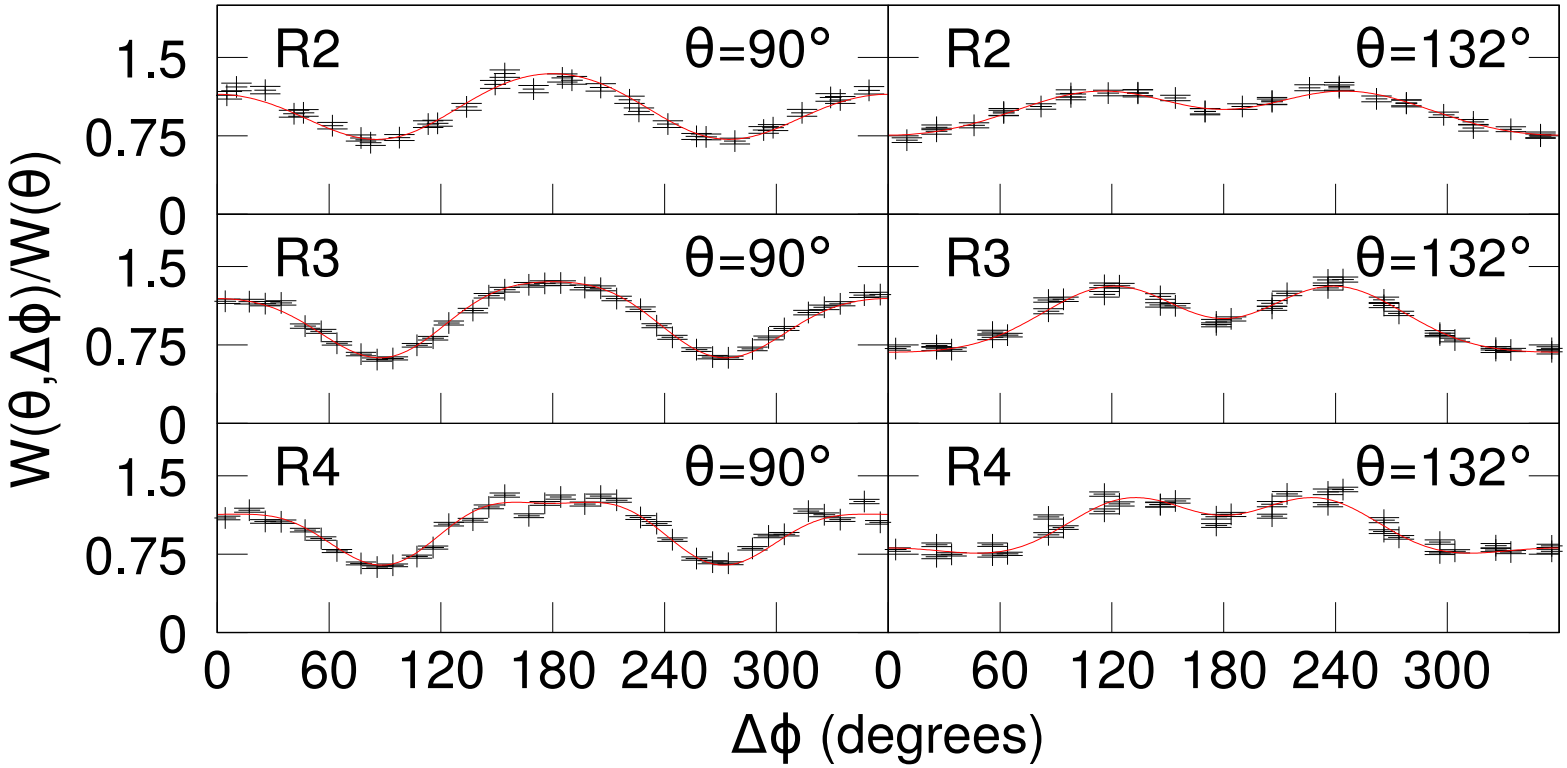

Figure 8.6: Angular distributions around $\Delta\phi$ for ^{126}Te. Red lines correspond to fitted distributions. $W(\theta)$ is the average value of the angular distribution around $\Delta\phi$.

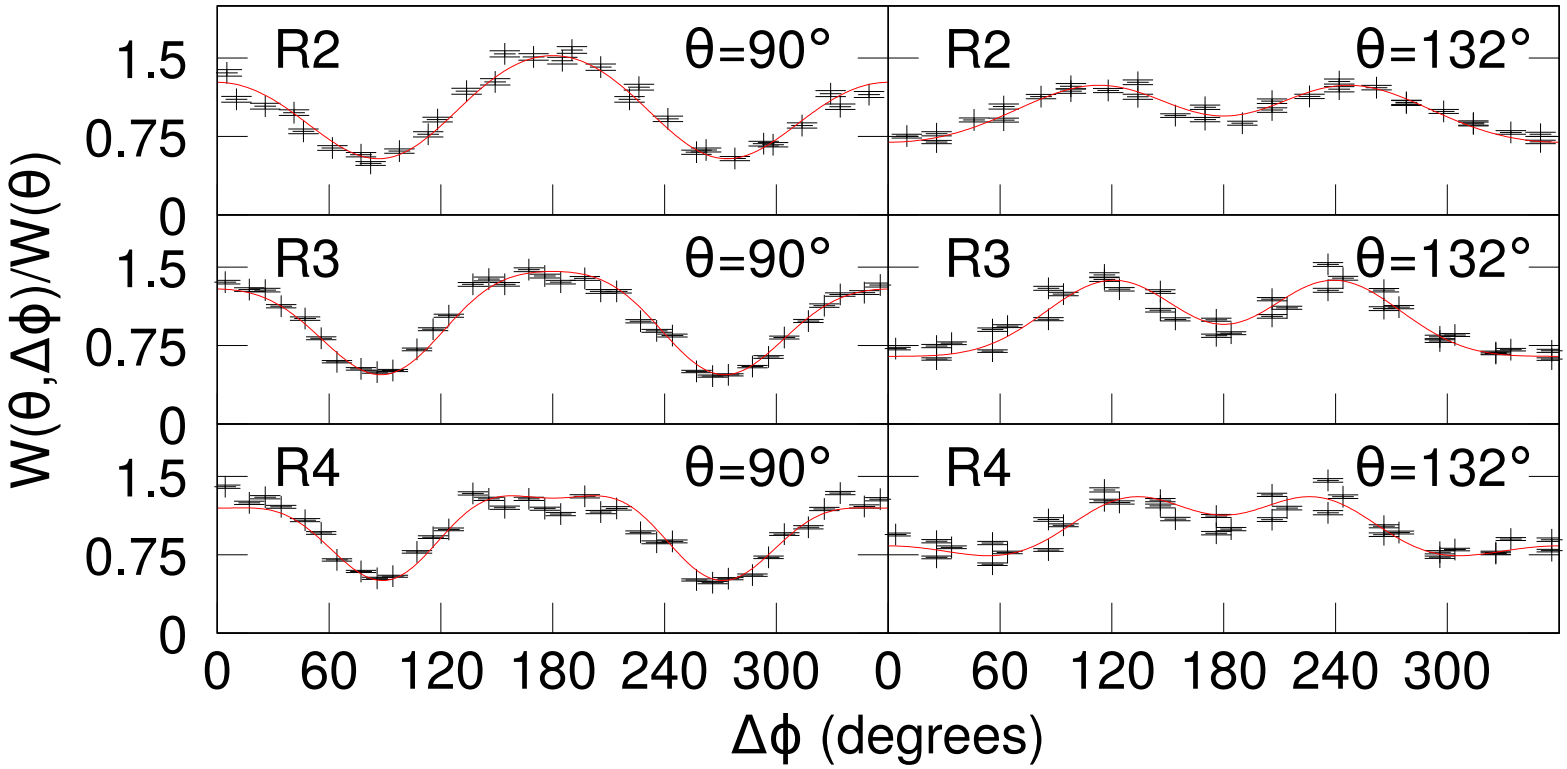

Figure 8.7: Angular distributions around $\Delta\phi$ for ^{130}Te. Red lines correspond to fitted distributions. $W(\theta)$ is the average value of the angular distribution around $\Delta\phi$.

Table 8.6: Vacuum deorientation parameters fitted using the $\Delta\phi$ distributions (see text for details).

Beam	θ_γ	Ring 2		Ring 3		Ring 4	
species		G_2	G_4	G_2	G_4	G_2	G_4
^{124}Te	90°	0.666(14)	0.374(15)	0.607(7)	0.317(7)	0.497(8)	0.228(6)
	131.75°	0.678(27)	0.387(30)	0.577(10)	0.290(8)	0.473(10)	0.212(7)
^{126}Te	90°	0.753(9)	0.477(12)	0.683(5)	0.392(6)	0.588(6)	0.300(5)
	131.75°	0.763(20)	0.492(28)	0.684(8)	0.394(8)	0.592(8)	0.303(7)
^{130}Te	90°	0.864(4)	0.657(8)	0.807(3)	0.556(5)	0.735(4)	0.455(5)
	131.75°	0.875(11)	0.678(21)	0.785(5)	0.523(7)	0.670(7)	0.379(8)

8.7 Uncertainty estimates

8.7.1 Target composition

The isotopic composition of the target is given Table 8.1. The uncertainty in each component is quite small, on the order of a few percent. The errors from the corrections to the relative yields due to the target composition (given in Table 8.5) are also small, on the order of a percent. The uncertainty introduced by these correction factors on the evaluated, internally normalised $B(E2)$ values, is expected to be negligible and so has not been included. However, the evaluation of the $2_1^+ \rightarrow 0_{\text{g.s.}}^+$ transition strengths in Te relative to the ^{48}Ti yield is linearly dependent on the isotopic fraction of ^{48}Ti in the target. The ∼1% uncertainty contributed to the transition strengths from the target composition was added in quadrature to other sources of uncertainty.

8.7.2 Energy loss

The value taken as the energy loss through the target can have a significant effect on the yields calculated through the target. It therefore becomes necessary to estimate the effect on the relative yields from the uncertainty in the energy loss (E_{loss}=86.5(10) MeV). A 1 MeV change in energy loss was found to change the yields of the 4_1^+ and 2_2^+ states relative to the transition from the 2_1^+ state in each Te isotope by ∼0.4%. The uncertainty from the energy loss was added in quadrature to the internally normalised results. In contrast, the relative yields of the 2_1^+ states in each Te isotope and ^{48}Ti remained largely unchanged with a change in energy loss. Therefore, the uncertainty from this effect was not included in measurement of the 2_1^+ transition strength.

8.7.3 Matrix elements in ^{48}Ti

The transition strengths between the excited states in ^{48}Ti are known from direct lifetime measurements and scattering measurements. However, the excitation of

the 2_1^+ state in ^{48}Ti is highly dependent on the sign of the P_3 interference term, $\langle 0^+_{\text{g.s.}}|E2|2_1^+\rangle\langle 2_1^+|E2|2_2^+\rangle\langle 2_2^+|E2|0^+_{\text{g.s.}}\rangle$. Switching the sign of the $0^+_{\text{g.s.}} \rightarrow 2_2^+$ matrix element changes the excitation yield of the 2_1^+ state in ^{48}Ti calculated using GOSIA by $\sim$10%. In order to account for this effect, the $0^+_{\text{g.s.}} \rightarrow 2_2^+$ matrix element was left at zero, taking close to the centre of the two possibilities, with a 5% uncertainty added in quadrature to the $B(E2; 0^+_{\text{g.s.}} \rightarrow 2_1^+)$ measurement to account for this effect.

8.7.4 Vacuum deorientation correction

The calculated yields were found to be largely insensitive to the G_k coefficients assumed in the calculations. Changing the assumed g factor used in the recoil-in-vacuum model used by GOSIA by a factor of two caused a change in the calculated yield in Ring 2 in the ^{124}Te experiment of $\sim$ 2%. Performing the same test in the ^{130}Te calculations yielded a <1% change in the calculated yield. The calibration described in Sec. 8.6 allowed accurate determination of the G_k coefficients, see Table 8.6. Hence, no uncertainty was included from this effect in the reported $B(E2)$ values.

8.8 Results

The observed γ-ray energy spectra in the three experiments (^{124,126,130}Te) are displayed in Figs. 8.8 and 8.9 with Doppler corrections made for Te-like particles and Ti-like particles, respectively. The reconstructed $2^+ \rightarrow 0^+$ transitions in the Te isotopes have a FWHM of $\sim$7 keV. Most of the observed transitions are well separated in energy. There are two notable exceptions: the $2_2^+ \rightarrow 2_1^+$ and $4_2^+ \rightarrow 4_1^+$ transitions in ^{124}Te; and the $2_1^+ \rightarrow 0^+_{\text{g.s.}}$ transitions in ^{130}Te and ^{46}Ti. In neither case does a large change in the area of the Te transitions occur. The effect of the overlap with the $2_1^+ \rightarrow 0^+_{\text{g.s.}}$ in ^{46}Ti has been estimated by the relative excitation of the 2_1^+ state in ^{48}Ti and the isotopic composition of the target.

Lists of the measured γ-ray intensities are given in Tables 8.7-8.9. As expected, fewer transitions are observed in the higher-mass, less-collective isotopes.

The transition strength in ^{48}Ti used for normalisation was taken from the 2016 Pritychenko evaluation [41], $B(E2; 2_1^+ \rightarrow 0^+_{\text{g.s.}})$=0.0662(29) eb. Other transition strengths and the quadrupole moment for the 2_1^+ state in ^{48}Ti were taken from Nuclear Data Sheets [150]. In almost all cases, the transition strengths obtained in the present measurement, presented in Table 8.10, are consistent with previous measurements, where previous measurements exist. A notable exception is the $2_2^+ \rightarrow 2_1^+$ transition in ^{130}Te. This value (τ=2.32(34) ps [151]) was obtained through a DSAM measurement with $(n, n'\gamma)$. This measurement is at the limit of the applicability of the method because the low-mass neutron does not impart enough momentum to the heavy nucleus to create a sensitive DSAM measurement for a state with such a lifetime. A new evaluation of $(n, n'\gamma)$ data with the DSAM gives τ>2.97 ps [152]. A firmer value is therefore available from the present measurement. The $B(E2)$ of the $4_1^+ \rightarrow 2_1^+$ transition in ^{130}Te has been measured for the first time.

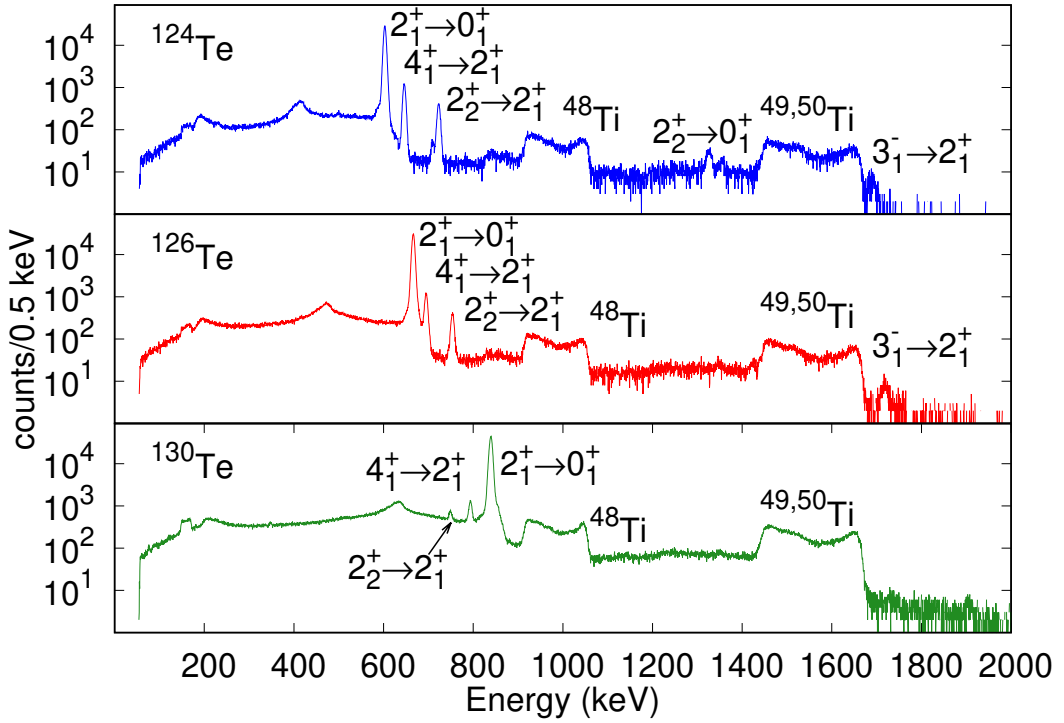

Figure 8.8: Measured energy spectra from ^{124,126,130}Te Coulomb excitation, Doppler corrected for Te-like nuclei. Data from all γ-ray and particle detectors for the entire run time are displayed.

Table 8.7: Observed transitions in the Coulomb-excitation measurement of ^{124}Te. Transition intensities are normalised to the $2^+ \rightarrow 0^+$ transition intensity.

I_i^π	E_i	E_γ	I_f^π	E_f	I_γ		
	(keV)	(keV)		(keV)	Ring 2	Ring 3	Ring 4
2^+	602.7	602.7	0^+	0	100(1)	100(1)	100(1)
4^+	1248.6	645.9	2^+	602.7	7.2(1)	5.55(7)	2.80(4)
2^+	1325.5	722.8	2^+	602.7	3.45(8)	2.10(4)	0.96(3)
		1325.5	0^+	0	0.41(4)	0.25(2)	0.14(2)
0^+	1657.3	1054.6	2^+	602.7	0.22(3)		
6^+	1747.0	498.4	4^+	1248.6	0.23(5)	0.25(3)	
4^+	1957.9	709.3	4^+	1248.6	0.25(3)	0.18(2)	0.08(1)
		1355.2	2^+	602.7	0.12(2)		
3^-	2293.7	1691.0	4^+	602.7	0.31(4)	0.22(2)	0.11(2)

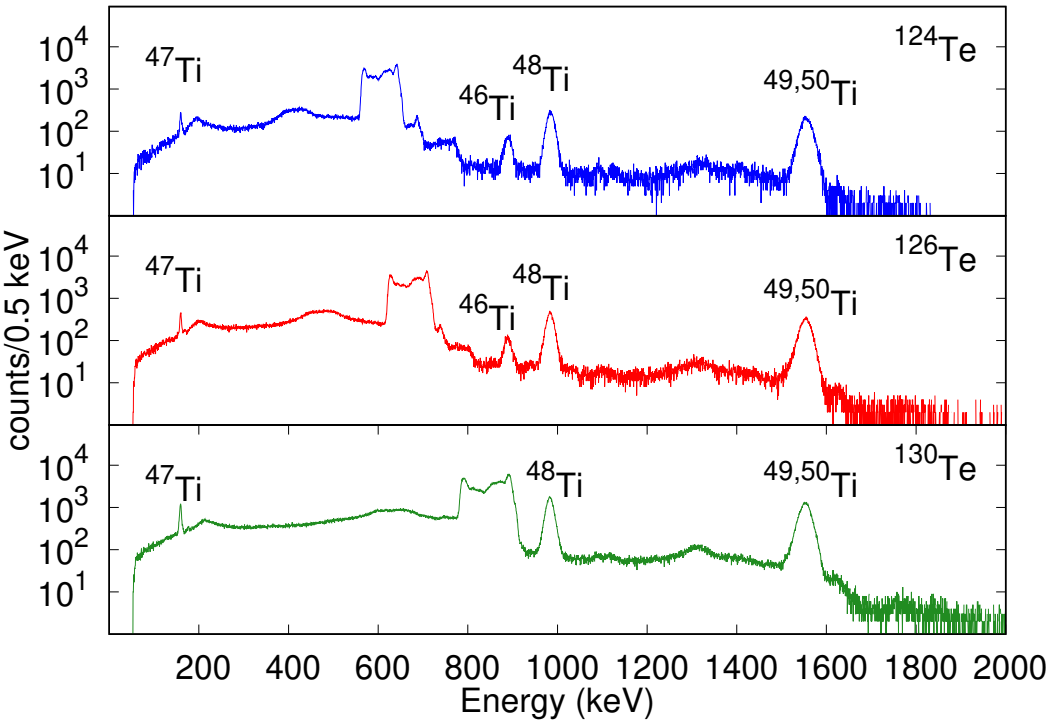

Figure 8.9: Measured energy spectra from ^{124,126,130}Te Coulomb excitation, Doppler corrected for Ti-like recoils. Data from all γ-ray and particle detectors for the entire run time are displayed.

Table 8.8: Observed transitions in the Coulomb-excitation measurement of ^{126}Te. Transition intensities are normalised to the $2^+ \rightarrow 0^+$ transition intensity.

I_i^π	E_i	E_γ	I_f^π	E_f	I_γ		
	(keV)	(keV)		(keV)	Ring 2	Ring 3	Ring 4
2^+	666.4	666.4	0^+	0	100(1)	100(1)	100(1)
4^+	1361.4	695.0	2^+	666.4	5.7(1)	4.37(6)	2.38(5)
2^+	1420.2	753.8	2^+	666.4	3.00(7)	1.70(4)	0.77(2)
3^-	2385.8	1719.5	2^+	666.4	0.09(2)	0.09(1)	0.08(1)

Table 8.9: Observed transitions in the Coulomb-excitation measurement of ^{130}Te. Transition intensities are normalised to the $2^+ \rightarrow 0^+$ transition intensity.

I^π	E_i	E_γ	I_f^π	E_f	I_γ		
	(keV)	(keV)		(keV)	Ring 2	Ring 3	Ring 4
2^+	839.5	839.4	0^+	0	100(2)	100(2)	100(2)
2^+	1588.3	748.4	2^+	839.5	2.51(7)	2.08(4)	0.97(3)
4^+	1633.0	793.3	2^+	839.5	1.09(5)	0.64(3)	0.25(3)

Table 8.10: Measured transition strengths in ^{124,126,130}Te. Literature data from Refs. [41; 151; 153; 154; 35; 68]. Where two values are listed from the same reference, these correspond to two possible mixing ratios leading to two possible conversions from lifetime to $E2$ strength for the transition.

^{A}X	I_i^π	E_i (keV)	E_γ (keV)	I_f^π	E_f (keV)	$B(E2)_{\text{exp}}$ (W.u.)	$B(E2)_{\text{lit.}}$ (W.u.)	Ref.
^{124}Te	2^+	602.7	602.7	0^+	0	26.1(14)	30.5(15)	[41]
	4^+	1248.6	645.9	2^+	602.7	39.9(9)	35.9(17)	[35]
	2^+	1325.5	722.8	2^+	602.7	41.5(13)	34(5)	[35]
							$22.1(^{+45}_{-43})$	[68]
							$55.5(^{+109}_{-99})$	[68]
							$29.9(^{+17}_{-12})$	[154]
							114(4)	[154]
^{126}Te	2^+	666.4	666.4	0^+	0	25.4(21)	25.26(50)	[41]
	4^+	1361.4	695.0	2^+	666.4	29.8(4)	34(16)	[155]
	2^+	1420.2	753.8	2^+	666.4	43.5(10)	$45(^{+5}_{-4})$	[153]
^{130}Te	2^+	839.5	839.4	0^+	0	13.3(10)	15.12(51)	[41]
	2^+	1588.3	748.4	2^+	839.5	14.5(5)	27(3)	[151]
							<10	[152]
	4^+	1633.0	793.3	2^+	839.5	15.3(3)		

The excitation of the 2_1^+ state depends on both the $E2$ matrix element between the ground state and the 2_1^+ state, and the diagonal matrix element of the 2_1^+ state in a correlated manner. Analysis was performed in the manner described in Ref. [156]. A chi-squared plot used to determine the diagonal $\langle 2_1^+||E2||2_1^+\rangle$ matrix element in ^{130}Te is shown in Fig. 8.10. The black lines show the previous measured values [41; 89] with uncertainties displayed as dashed lines. The quadrupole moments were determined through analysis of the best values of the quadrupole moment for a given $\langle 0_{\text{g.s.}}^+||E2||2_1^+\rangle$ matrix element, and values for ^{124,126,130}Te are presented in Table 8.11. Similar approaches can be used to deduce other matrix elements and for other Te nuclides. As the present measurement was performed to calibrate the recoil-in-vacuum effect for another measurement, limited care was taken to ensure that the data would be useful for a detailed Coulomb-excitation analysis. It was later recognised that the Coulomb-excitation and $B(E2)$ data on the Te isotopes were scarce. As the experimental parameters were not optimised for Coulomb-excitation experiments, the data rates were high enough to induce significant dead-time effects. The dead time would usually be measured simultaneously, as Coulomb-excitation data are taken, however in the present measurement this was not done. Additionally, the most sensitive Coulomb-excitation data would be obtained from the largest scattering angles in the centre of mass. This corresponds to Ring 1, which was not included in the present measurement. Lastly, the heavy-ion group seen in the particle detectors is not fully separated from the group of lower-mass particles in the PID statistic for Ring 4. All of this taken together, causes problems in the measurement of the absolute values of

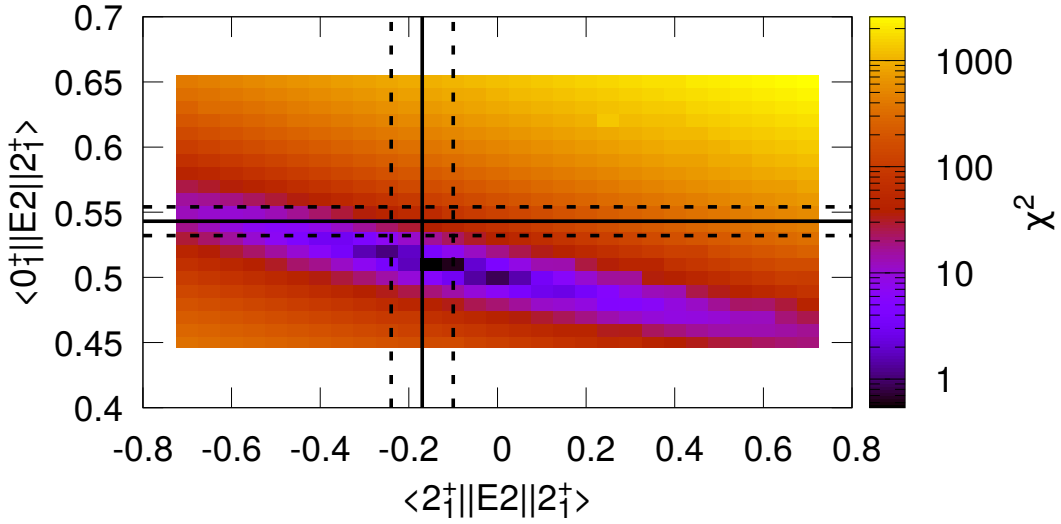

Figure 8.10: Total chi squared over all detectors plotted as a function of the $\langle 0^+_{\text{g.s.}}||E2||2^+_1\rangle$ and $\langle 2^+_1||E2||2^+_1\rangle$ matrix elements for ^{130}Te. Solid black lines represent literature values with uncertainties displayed as dashed lines.

Table 8.11: Measured electric quadrupole moments in ^{124,126,130}Te. Literature data from Ref. [89].

Isotope	$Q(2^+_1)_{\text{exp}}$ (eb)	$Q(2^+_1)_{\text{lit.}}$ (eb)
^{124}Te	-0.30(15)	-0.45(5)
^{126}Te	-0.40(15)	-0.23(5)
^{130}Te	-0.14(15)	-0.12(5)

the transition strengths and quadrupole moments.

If quadrupole moments were sought, a series of measurements on ^{12}C targets would also be valuable, as would data corresponding to scattering at the furthest back angles in the centre-of-mass frame. The quadrupole moments determined in the present measurement in Table 8.11 have very large uncertainties due to a lack of sensitivity. The resulting quadrupole moments may also be suspect due to the implied difference in the presently measured transition strength compared to the literature $2^+_1 \rightarrow 0^+_{\text{g.s.}}$ transition strength, as displayed in Fig. 8.10. The $Q(2^+_1)$ values, discussed in the following sections, are therefore adopted from the Stone evaluation [89].

8.9 Conclusions

Measurements of the $B(E2;4^+_1 \rightarrow 2^+_1)$ and $B(E2;2^+_2 \rightarrow 2^+_1)$ transition strengths in ^{124,126,130}Te were performed through Coulomb excitation with measurements of some values obtained for the first time. Further experiments, including measurements

with lighter targets and at larger scattering angles, would allow measurements of quadrupole moments with greater precision. The results of the Coulomb-excitation measurements in this chapter are combined with the results of the g-factor measurements discussed in Chapter 7 and the Coulomb-excitation measurements on the Cd isotopes in Chapters 4 and 5 in order to discuss the development of nuclear collectivity in the ^{132}Sn region in the next chapter.

Chapter 9

Discussion

Nuclear quadrupole collectivity evidently emerges when the long-range component of the nucleon-nucleon interaction becomes dominant over the short-range nuclear pairing forces. There are several factors that can be considered indicators for the emergence of collectivity. The first indicator for the development of collectivity is the fragmentation of the shell-model wavefunctions of states in the nucleus. Further, the fragmentation must occur in a coherent way. This means that the correlated motion of the many involved nucleons enhances the $E2$ strength of transitions between collective states. Increasing $B(E2)$ values are generally correlated with another indicator, namely increasing deformation. Additionally, the angular momentum of a collective state must be shared between the protons and neutrons which will affect the g factors of the states. Finally, the emergence of collective structure may involve the breakdown of the nuclear shell structure. Excitations across shell closures may give rise to deformed structures, and the involvement of the core nucleons becomes more common in collective excitations.

In this chapter the emergence of collectivity is discussed, first, through a discussion of shell-model-calculated wavefunctions for the Te isotopes. These are discussed in terms of proton and neutron spin components, and in terms of the fragmentation of the wavefunctions. The observed trends are related to the known 2_1^+ g factors and to the 4_1^+ g factors measured in the present work. This discussion is then extended to transitional nuclei more widely. The present Coulomb-excitation results for ^{124,126,130}Te are then combined with known transition strengths [41] and the implications for developing collectivity are explored. The deformation is then discussed in relation to previously measured quadrupole moments [89] and shape invariants calculated using the Kumar-Cline sum rules [8] with $E2$ matrix elements obtained from the shell-model calculations. It is noted that lower-spin states are calculated to develop deformation more rapidly than higher-spin states. Signatures of the development of collectivity in the Cd isotopes are then discussed with a focus on the transition strengths measured in the present work and the level scheme developed from the multi-step Coulomb-excitation data. Lastly, combining the discussion of the Cd and Te nuclides, development of collectivity in the $Z = 50$ region is discussed and it is suggested that the reason that models of weakly collective nuclei have not been successful is that collectivity develops individually in states at different rates which is not accounted for in the commonly applied models.

9.1 Emergence of Collectivity in $^{124-134}$Te

The measurement of the characteristics of a chain of transitional isotopes allows an investigation of the stages toward the development of nuclear collectivity. The stable Te isotopes are an ideal case to study, since the highest-mass naturally abundant isotope ^{130}Te exhibits a largely seniority structure, while the lowest-mass stable isotope ^{120}Te exhibits a clearly vibrational-like collective structure. By combining theory and experiment, it is possible to extract information on the increases in transition strengths, the development of deformation, the correlated motion of protons and neutrons, wavefunction fragmentation, and the breakdown of the nuclear shells, across these stable isotopes. The experimental data give indicators of the progress of each of these factors, however the interpretation of the experimental data can be difficult without reference to a specific model or microscopic calculation. Comparisons with shell-model calculations, in particular, are useful in the extraction of the microscopic origins of the macroscopic properties measured.

9.1.1 Shell-model calculations

Shell-model calculations were performed using the large-scale shell-model codes ANTOINE and NUSHELLX@MSU. In both cases, calculations were performed with a ^{100}Sn core and no restrictions placed on proton or neutron occupation, in the full ($g_{7/2}$, $d_{5/2}$, $d_{3/2}$, $s_{1/2}$, $h_{11/2}$) model space. For the Te nuclei studied experimentally in the present work, there are two protons in the lower part of the shell and a few to modest number of neutron holes in the upper part of the shell. Two-body matrix elements derived from the CD-Bonn potential were used in both cases, however alternative procedures for obtaining the interaction Hamiltonians were used, resulting in somewhat different effective interactions. The jj55pn interaction [157] was used in the NUSHELLX@MSU calculations. The process used to obtain the interaction used in the ANTOINE calculations is described in Ref. [158].

Due to limitations in computational power, calculations for the lower-mass Te isotopes were not able to be performed using the NUSHELLX@MSU code. Using this program, calculations were performed for ^{128,130,132,134}Te using the jj55pn interaction. The single-particle energies were set based on the low-energy excitations in ^{131}Sn and ^{133}Sb.

The neutron effective charge was varied so that the $2^+_1 \rightarrow 0^+_{\text{g.s.}}$ transition strength in ^{130}Sn reported in Ref. [159] was reproduced; the value obtained was e_n=0.62(7)e. A recent study of ^{132}Xe [136] found that an effective neutron charge of $e_n \sim 0.8e$ reproduced the $10^+_1 \rightarrow 8^+_1$ transition strength in ^{130}Sn and the $2^+_1 \rightarrow 0^+_{\text{g.s.}}$ transition strengths in ^{126}Sn and ^{128}Sn. The same study notes that the $10^+_1 \rightarrow 8^+_1$ transition strength in ^{128}Sn is reproduced with an effective neutron charge of e_n=0.46(1)e but disregarded this value due to the more complex wavefunction of the states involved. The present value of e_n=0.62(7)e sits between those presented in Ref. [136]. The 2^+_1 state in ^{130}Sn is calculated to be quite mixed with the largest component being the 56.4% $\nu h^{-2}_{11/2}$ configuration. It may be reasonable to use the value obtained from the

$10^+_1 \rightarrow 8^+_1$ transition strength in ^{130}Sn (e_n=0.8e) as both the 10^+_1 and 8^+_1 states are calculated to be pure $\nu h^{-2}_{11/2}$ configurations. Alternatively, since the investigated transitions are from low-spin states, the values obtained from the low-spin state transitions could be used in calculations. The results of both assumptions will be discussed below.

The proton effective charge used in the shell-model calculations in the jj55pn interaction was set by comparison to the experimentally known $2^+_1 \rightarrow 0^+_{\text{g.s.}}$ transition strength in ^{134}Te, which leads to an effective proton charge of e_p=1.74(3)e. A similar analysis performed for the $6^+_1 \rightarrow 4^+_1$ transition in ^{134}Te leads to an effective proton charge of e_p=1.54(2)e. In this case a proton charge of e_p=1.7e was used in evaluations for consistency with other shell-model studies in the region [136; 138].

Calculations were performed for ^{124,126,128,130}Te using the ANTOINE code. Effective charges of e_p=1.7e and e_n=0.9e were used in the ANTOINE calculations, which reproduce the $B(E2; 2^+_1 \rightarrow 0^+_{\text{g.s.}})$ values in ^{134}Te and ^{128}Sn.

9.1.1.1 Discussion of wavefunctions

An initial interpretation of the level schemes of the Te isotopes is to treat the proton and neutron systems as uncoupled and to compare these uncoupled states in the related singly magic isotope and isotone. These comparisons are presented in Fig. 9.1. In most cases, the 4^+_1 and 6^+_1 states are seen to be at similar energies to those found in ^{134}Te. The 4^+_2 and 6^+_2 states are found close in energy to the 4^+_1 and 6^+_1 states in the corresponding Sn isotone. It may therefore be expected that these states in the investigated Te isotopes may largely be formed by the same excitations as those in the singly magic nuclides. Immediately it is apparent, however, that the 2^+ states are not reproduced in this approach unless they are strongly mixed. Additionally, away from the N=82 shell closure, excited 0^+ states begin to occur with no corresponding states in either singly magic nuclide. Further investigation of the characterisation of the excited states as separate proton and neutron states is possible by examining the spin of proton and neutron configurations in the shell-model wavefunctions.

In Fig. 9.2 the fragmentation of the 2^+_1 wavefunction is displayed. Each wavefunction component, in the form $(\nu j_n \otimes \pi j_p)^J$, is plotted at the squared amplitude of the configuration along the x axis, with the height of the bar corresponding to the summed size of all components with that amplitude. In panel a) the calculated amplitudes associated with each individual configuration are given. In order to investigate the activity of protons and neutrons in excitations, we plot the amplitudes of the neutron and proton configurations separately. The total probability of each neutron configuration, ignoring proton configurations, is presented in panel b). Similarly, the total probability in each proton configuration, without separating different neutron configurations, is presented in panel c). To illustrate this, for ^{132}Te in panel c), the two dominant proton configurations can be seen, each are $[g^2_{7/2}]$ with the larger component coupled to 2^+ and the smaller component coupled to 0^+. In panel b) the neutron configurations are much more split, many neutron configurations are present with smaller amplitude (contributions are shown lower on the

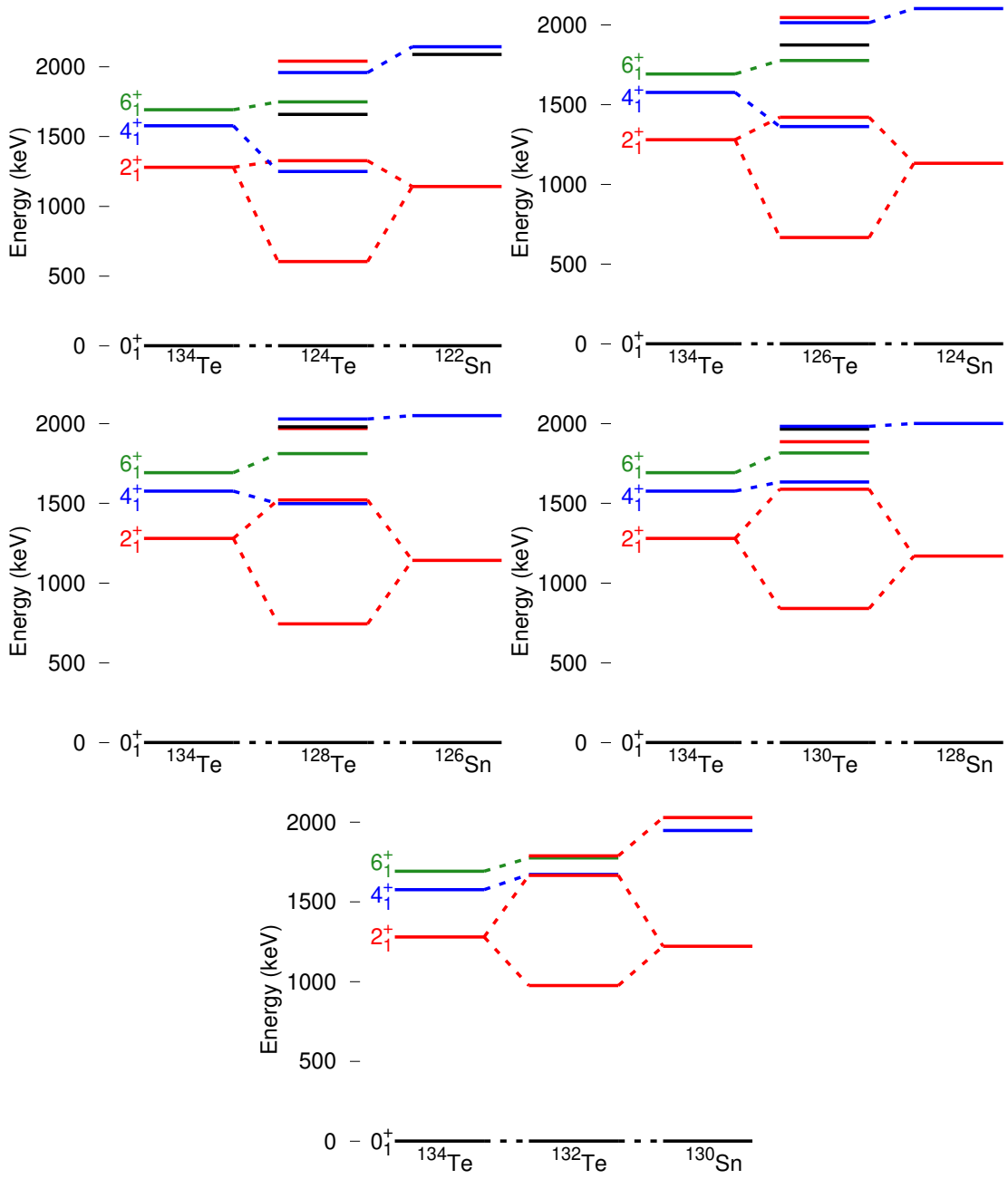

Figure 9.1: Experimental energy levels of the Te isotopes compared with the singly magic, "parent" isotope and isotones. States of the same spin and similar energies are connected to show potential proton or neutron parentage. States with angular momentum of 0^+ are shown in black, 2^+ are shown in red, 4^+ are shown in blue, and 6^+ are shown in green.

x axis); multiple contributions are summed and shown in a single bin. In panel a) each total configuration is separated and it can be seen that a large number of small amplitude configurations are present. In ^{134}Te the only active nucleons are the two valence protons with the dominant configuration ($[\pi^2 g_{7/2}]^2$) comprising >95% of the wavefunction. The completeness of this display is limited as NushellX@MSU only provides an output for a spin coupling if the total proportion contained in all proton and neutron configurations is greater than 1%. The proton components of the wavefunction split into two dominant configurations with the $[\pi g^2_{7/2}]^0$ becoming dominant in lower-mass isotopes. In ^{132}Te (two valence neutron holes), the neutron configurations are highly fragmented with no dominant neutron configuration observed. In the isotopes with more neutron holes, the wavefunction is highly fragmented (panels a) while the proton configurations remain dominated by a few configurations (panels c). The neutrons are responsible for the majority of the developing fragmentation (panels b).

The fragmentation in the 4^+_1 states in $^{128-134}$Te is displayed in Fig. 9.3. The fragmentation of these states increases less rapidly away from the closed shell than the 2^+_1 states shown in Fig. 9.2. It is worth noting again here that the protons remain largely in the $\pi g^2_{7/2}$ configuration, coupled to either 4^+, 2^+ or 0^+, while the fragmentation of neutron configurations occurs much more rapidly. The 4^+_1 state in ^{128}Te is highly fragmented with almost half of the wavefunction composed of configurations with less than 1% of the total wavefunction.

The wavefunction fragmentation of the 6^+_1 states can be seen in Fig. 9.4. In the 6^+_1 states the protons are calculated to remain largely in the $\pi g^2_{7/2}$ configuration coupled to 6^+ from ^{134}Te to ^{128}Te. In ^{128}Te, a significant $\pi g_{7/2} \pi d_{5/2}$ component coupled to 6^+ is indicated. Even in ^{128}Te, the fraction of the wavefunction with neutrons coupled to zero spin is >50%.

9.1.2 Comparison to g-factor results

The calculated and experimentally determined g factors displayed in Fig. 9.5 are essential to developing a correct understanding of the onset of collectivity in the Te isotopes. The 2^+_1 g factors decrease rapidly as neutrons are removed, starting from the N=82 shell closure. The observed g factors of the 2^+_1 and 6^+_1 in singly magic ^{134}Te [66] are consistent with majority $\pi g^2_{7/2}$ configurations. The Schmidt model g factor for a $g_{7/2}$ proton with spin g factor quenched to 70% of the free value is $g(g_{7/2})$=0.58 but the experimentally determined g factors are closer to g=0.8. It has been noted previously [160] that the g factors of proton orbits in the ^{132}Sn region are better reproduced with an increased effective orbital g factor. An effective orbital g factor of $g^{\rm eff}_\ell$=1.13 reproduces experimental data well, similar to the microscopically calculated value of $g^{\rm eff}_\ell$=1.11 suggested by Brown et al. [157]. This small change in the orbital g factor has a large impact on the single-particle g factor due to the large orbital angular momentum (ℓ=4) of the $g_{7/2}$ orbit. The decrease in the 2^+_1 g factor across the Te isotopes below N=82 is extremely rapid, becoming almost consistent with the collective limit of g=0.8Z/A (as discussed in Sec. 2.3) at ^{130}Te with only four neutron holes. A slower

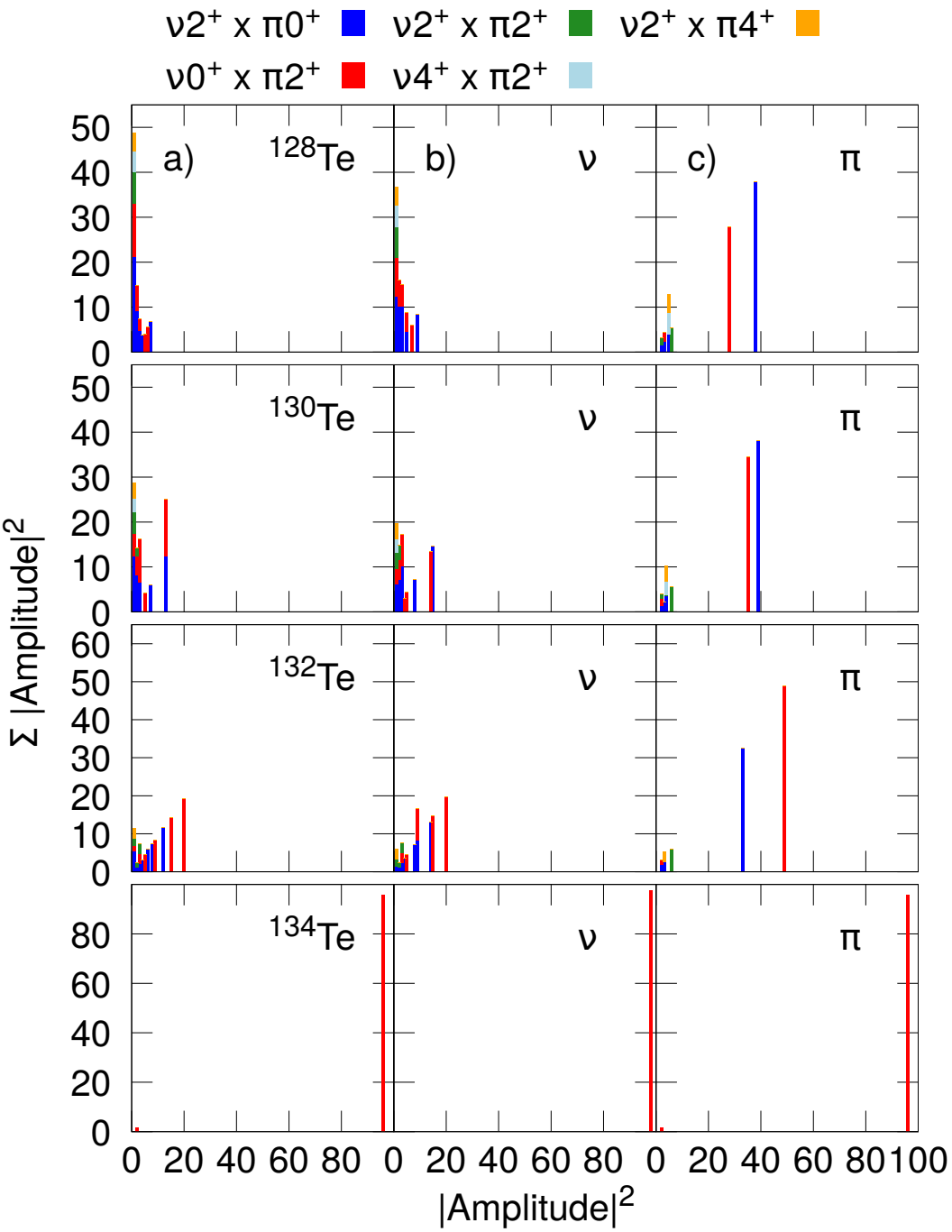

Figure 9.2: Squared amplitudes (%) of the wavefunction components comprising the 2_1^+ states in $^{128-134}$Te from shell-model calculations using the jj55pn interaction. In the left panels (a) the wavefunctions are split between every configuration, middle panels (b) show the wavefunction components in each neutron partition, and the right panels (c) shows the wavefunction components in each proton partition. See text for details.

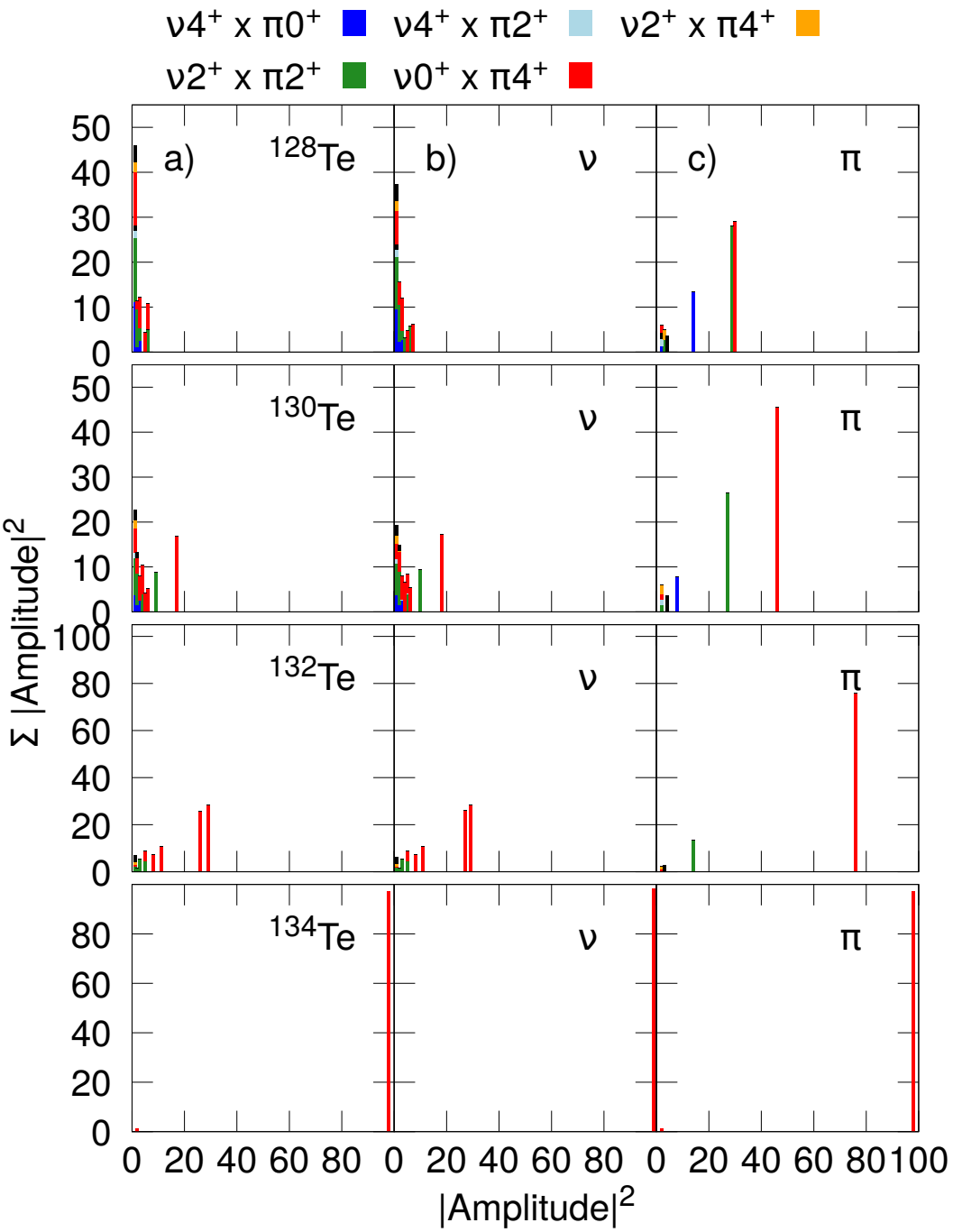

Figure 9.3: Squared amplitudes (%) of the wavefunction components comprising the 4_1^+ states in $^{128-134}$Te from shell-model calculations using the jj55pn interaction. In the left panels (a) the wavefunctions are split between every configuration, middle panels (b) show the wavefunction components in each neutron partition, and the right panels (c) shows the wavefunction components in each proton partition. See text for details.

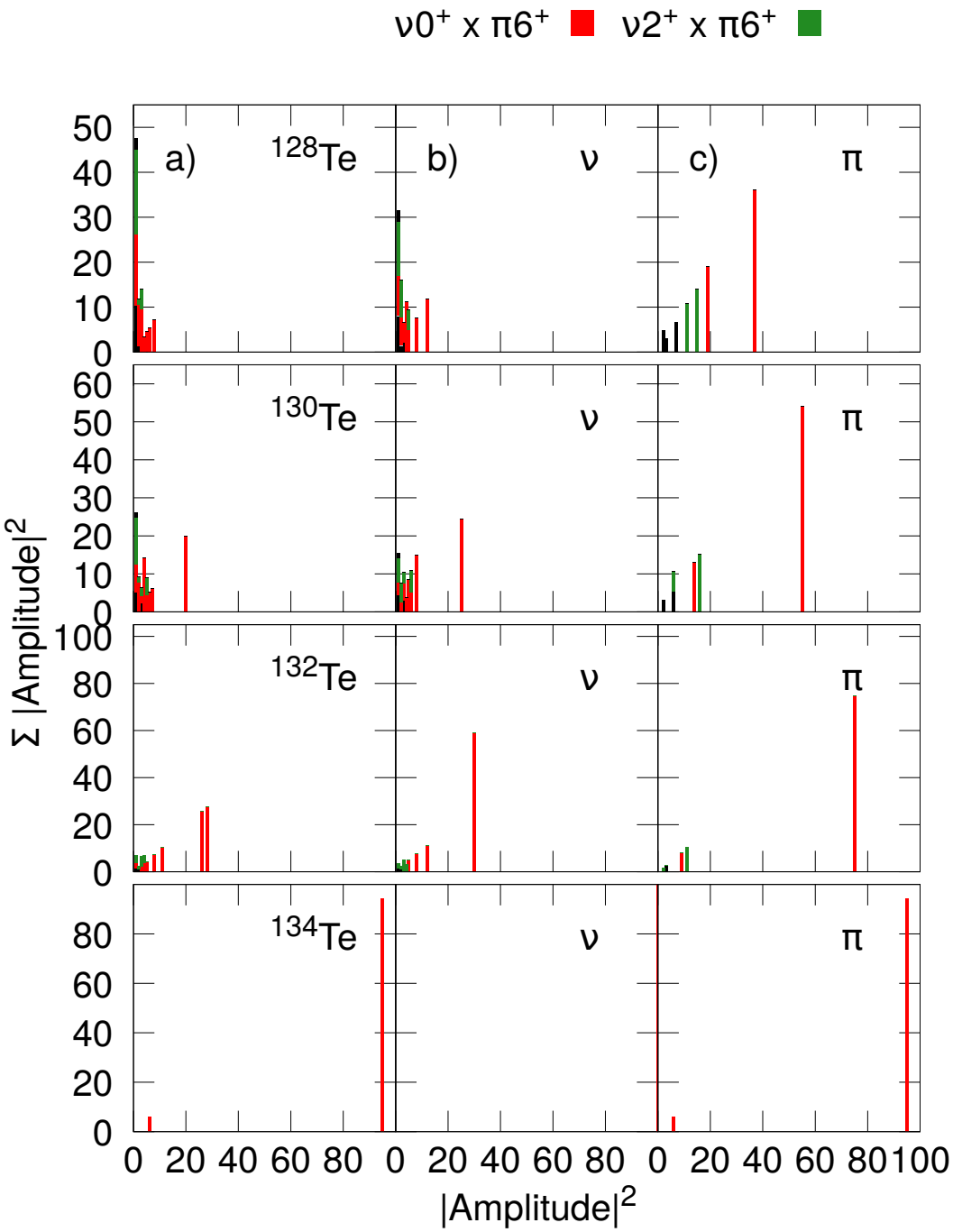

Figure 9.4: Squared amplitudes (%) of the wavefunction components comprising the 6_1^+ states in $^{128-134}$Te from shell-model calculations using the jj55pn interaction. In the left panels (a) the wavefunctions are split between every configuration, middle panels (b) show the wavefunction components in each neutron partition, and the right panels (c) shows the wavefunction components in each proton partition. See text for details.

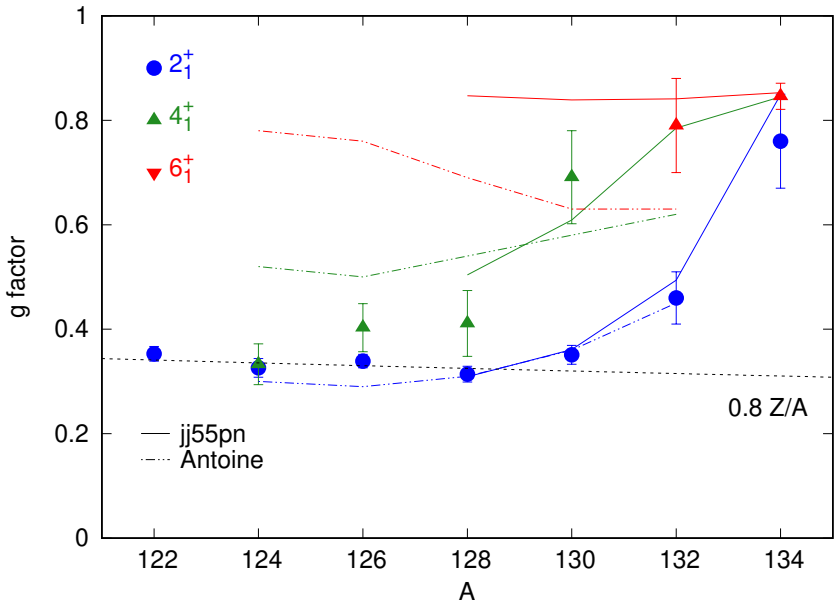

Figure 9.5: Tellurium g-factor systematics for 2_1^+, 4_1^+, and 6_1^+ states; $g(4_1^+)$ values for $^{124-130}$Te are from the present work. Other data are taken from Refs. [60; 61; 62; 63; 64; 65; 66]. Shell-model calculations using NushellX@MSU and the jj55pn interaction are shown with solid lines. Shell-model calculations performed with the Antoine code are shown with dotted lines.

decrease in the 4_1^+ g factor is observed. This is suggestive of reduced mixing in the 4_1^+ states compared to the 2_1^+ states.

The g factors predicted by the two interactions used for shell-model calculations agree quite closely for the 2_1^+ states. Further, the 2_1^+ g factors predicted by these calculations agree with the literature g factor values. These g-factors quickly reach the empirical collective limit of $0.8Z/A$. In the singly magic nuclide ^{134}Te, we observe experimentally [66] that the g factors of the measured 2_1^+ and 6_1^+ excited states are consistent with being equal, as would be expected for states made from the coupling of two $g_{7/2}$ protons in a seniority scheme. The values obtained from large-scale shell-model calculations using the jj55pn interaction agree with this observation and the predictions in a seniority scheme. While calculations performed using the interaction in the Antoine code do not reach ^{134}Te, the g factors of the 6_1^+ states do not follow the expected trends discussed above. Instead, the g factors of the 6_1^+ states increase as neutrons are removed.

The g factors of the 4_1^+ states converge to $g(2_1^+)$=$g(4_1^+)$=$0.8Z/A$ (the collective limit) more slowly than for the 2_1^+ state as the number of neutron holes increases. The shell-model calculations predict the observed splitting in the 2_1^+ and 4_1^+ g factors. It appears that the convergence to the collective limit in the 4_1^+ states occurs slightly more rapidly experimentally than in the shell-model calculations. A major factor in the expected decrease of the excited-state g factors is the increasing neutron component, starting from purely proton states in ^{134}Te. The spin-decomposition

into proton and neutron components is displayed in Fig. 9.6. The excited states with higher spins show more rapid reductions in the $|\pi J \otimes \nu 0\rangle$ component moving away from ^{134}Te. Additionally, the reduction of the $|\pi 2 \otimes \nu 0\rangle$ components in the 2_1^+ states correlates with an increase in configurations in which the spin is held entirely in the neutrons, with the largest component in ^{128}Te becoming $|\pi 0 \otimes \nu 2\rangle$. While the calculated $|\pi 2 \otimes \nu 0\rangle$ and $|\pi 4 \otimes \nu 0\rangle$ components are proportionally similar in both the 2_1^+ and 4_1^+ states, respectively, the large components in the 4_1^+ state (and higher-excited states) maintain a large proportion of their angular momentum in the proton components.

Previous shell-model calculations for $^{128-134}$Te performed by Teruya et al. [138] used a phenomenological interaction that underpredicted the g factors for the 2^+ states; however, the authors used the orbital g factors g_ℓ^π=1.0 and g_ℓ^ν=0.0 which (as discussed above) are lower than expected in the region. A comparison of experimental g factors and shell-model calculations is given in Table 9.1. The pattern of increasing g factors in higher spin states close to the neutron shell closure is observed in the calculations. The increasing g factor of the 6_1^+ states away from the closed shell is predicted in both the work of Teruya et al. and the present ANTOINE calculations but is not predicted in the calculations using the jj55pn interaction.

Predictions of the g factors of states in $^{130-134}$Te have also been made by Jakob et al. [137] using shell-model calculations with surface delta interactions. These early calculations predict g factors lower in magnitude than the jj55pn interaction for the 4_1^+ and 6_1^+ states. The predicted 2_1^+ g factors using the surface delta interactions decrease away from the closed shell much slower than the experimental values.

The shell-model-calculated g factors in Table 9.1 are consistent with a ratio of the g factors of the 4_1^+ and 6_1^+ states relative to the 2_1^+ state g factor close to unity near N=82. In the calculations $g(2_1^+)$ decreases rapidly away from N=82, while $g(4_1^+)$ and $g(6_1^+)$ do not see a similar decrease. The values quoted here from Jakob et al. [137] are from the calculations without truncation with the exception of the g factors of the 4_1^+ and 6_1^+ states in ^{130}Te, which, due to computational limitations, considered shell closures at N,Z=64.

9.1.3 Survey of g factors in transitional nuclides

Limited information on the g factors of excited states above the 2_1^+ states in transitional nuclei is available. Known g factors for selected nuclides in transitional regions are presented in Table 9.2. The Xe isotopes have been extensively studied previously [136] and, with two extra valence protons (Z=54) compared to the Te isotopes, the conclusions of earlier studies are directly relevant to the present study. It was noted in Ref. [136] that in the Xe isotopes at the N=82 shell closure the $g(4_1^+)/g(2_1^+)$ ratio is close to unity before an immediate large decrease, by a factor of $\sim$2, in the g factor of the 2_1^+ state towards the collective limit from $g(2_1^+)$=0.76(12) in ^{136}Xe to $g(2_1^+)$=0.35(5) in ^{134}Xe [163]. The 4_1^+ g factors decrease more slowly towards the collective limit. The $g(4_1^+)/g(2_1^+)$ ratio is much closer to unity, with both $g(4_1^+)$ and $g(2_1^+)$ near the collective limit in ^{130}Xe, the isotone of ^{128}Te. The g factors of the

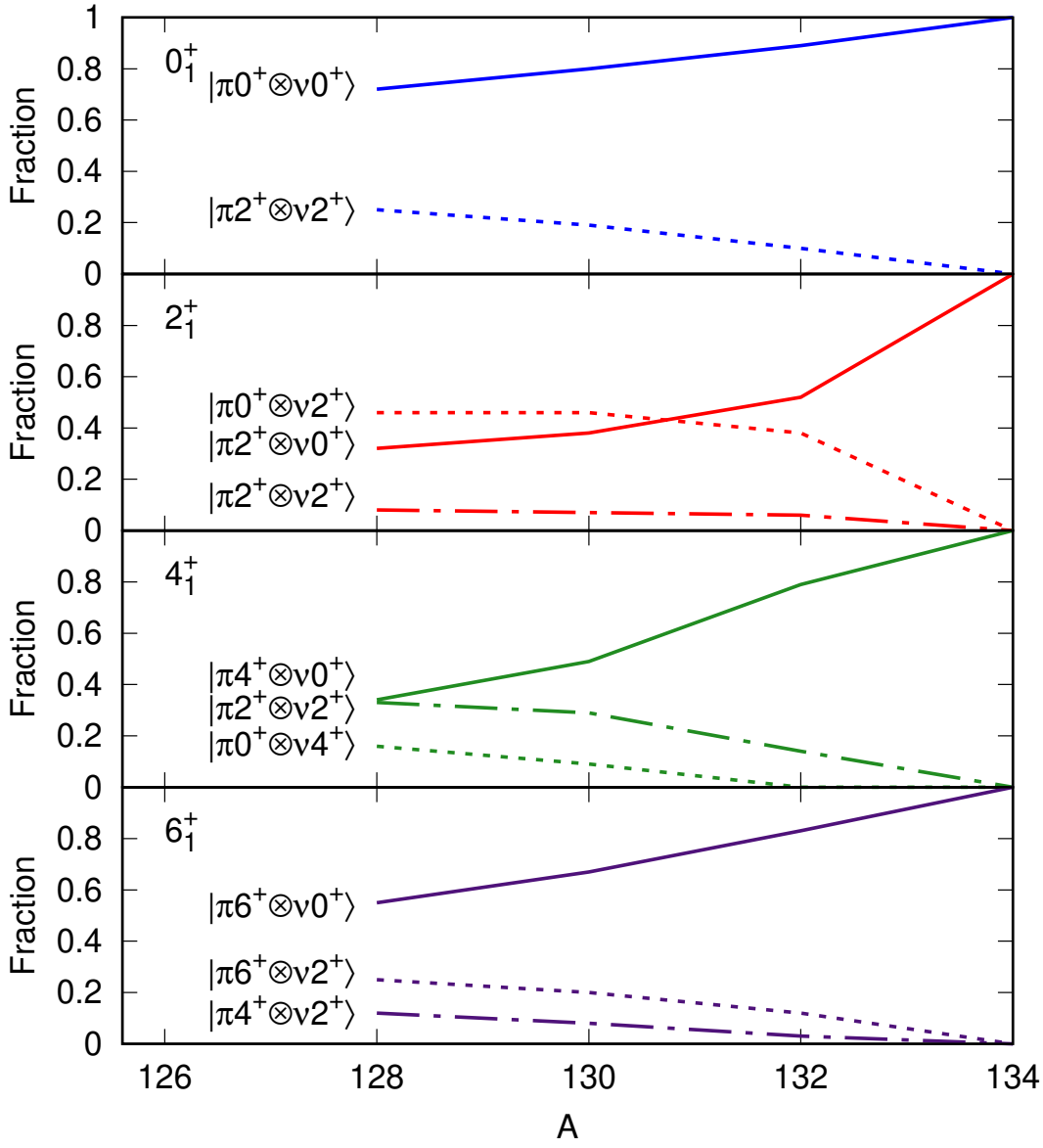

Figure 9.6: Proton-neutron spin decomposition versus mass number from shell-model calculations using the jj55pn interaction, showing results for the $0^+_{\text{g.s.}}$, 2^+_1, 4^+_1, and 6^+_1 states in $^{128-134}$Te.

Table 9.1: Comparison of experimental and shell-model g factors in $^{124-134}$Te. Experimental data are from the present work and Refs. [101; 71; 161; 162]. Shell-model predictions are given from present calculations and Refs. [137; 138]. Values from Ref. [137] are taken from calculations without truncation where possible.

$^{A}X_{N}$	I_i^π	g				
		Exp	jj55pn	ANTOINE	Ref. [137]	Ref. [138]
^{124}Te$_{72}$	2_1^+	+0.326(18)		+0.30		
	4_1^+	+0.33(4)		+0.52		
	6_1^+			+0.78		
^{126}Te$_{74}$	2_1^+	+0.339(13)		+0.29		
	4_1^+	+0.40(5)		+0.50		
	6_1^+			+0.76		
^{128}Te$_{76}$	2_1^+	+0.318(13)	+0.309	+0.31		+0.128
	4_1^+	+0.41(6)	+0.504	+0.54		+0.410
	6_1^+		+0.847	+0.69		+0.773
^{130}Te$_{78}$	2_1^+	+0.351(18)	+0.361	+0.36	+0.445	+0.146
	4_1^+	+0.69(9)	+0.609	+0.58	+0.766	+0.515
	6_1^+		+0.839	+0.63	+0.786	+0.712
^{132}Te$_{80}$	2_1^+	+0.46(5)	+0.494	+0.45	+0.448	+0.175
	4_1^+		+0.785	+0.62	+0.804	+0.608
	6_1^+	+0.79(9)	+0.841	+0.63	+0.807	+0.680
^{134}Te$_{82}$	2_1^+	+0.76(9)	+0.849		+0.858	+0.675
	4_1^+	$+0.70^{+0.55}_{-0.38}$	+0.845		+0.823	+0.678
	6_1^+	+0.846(25)	+0.853		+0.817	+0.683

4_1^+ states in the Xe isotopes appear to decrease at a similar rate with the number of neutron holes to the g factors in the Te isotopes.

The Mo isotopes allow for a study of the change in g factors from two isotopes, ^{92}Mo and ^{94}Mo. The g factors of the 2_1^+ and 8_1^+ are found to be similar in the singly magic isotope ^{92}Mo at $g(2_1^+)$=1.15(14) and $g(8_1^+)$=1.413(6), close to the value for $\pi g_{9/2}$. This behaviour is like that seen in ^{134}Te with $\pi g_{7/2}$. With the addition of two valence neutrons a marked decrease in the 2_1^+ g factor is observed to $g(2_1^+)$=+0.308(43) close to the collective limit. The g factor of the higher-excited 8_1^+ state in ^{94}Mo has a much smaller decrease to a value of $g(8_1^+)$=+1.137(15). While measurements of g factors above $g(2_1^+)$ further from the shell closure are not available, it is clear that the effect of the valence neutrons is much larger on the lower-spin state than the higher spin state. Similar observations may be made in the $^{142-146}$Nd isotopes, although in both of these cases the large number of valence protons complicates further discussion. If the Z=64 subshell closure is considered as one would a shell closure, then the Nd isotopes can be taken to have four valence proton holes, significantly reducing the complexity. The patterns in excited-state g factors then point to the role of $\nu f_{7/2}$ configurations in the low-spin yrast states. The persisting seniority structure of $\pi g_{7/2}$ configurations in Te and Xe isotopes is replaced by $\nu f_{7/2}$ configurations in ^{144}Nd. The smaller configuration-space of the Te isotopes and, to a lesser extent, the Xe isotopes, allows a much clearer picture of the microscopic origins of states, especially when shell-model calculations are available for comparison.

From this discussion it is clear that convergence of g factors toward the collective limit generally is much faster in the 2_1^+ states than in higher-excited states. It is not clear at this point whether the collectivity is developing in low-spin states first, or in low-energy states first. Difficulties can also arise in identifying collectivity, or states that can be considered collective. For example, the singly magic isotope ^{136}Xe has a transition strength from the first excited state of $B(E2; 2_1^+ \rightarrow 0_{\text{g.s.}}^+) = 10.5(16)$ W.u. [41], well above the 1 W.u. nominally expected for a particle-like transition, however, it would not usually be considered collective. Insights into these questions from shell-model calculations will be discussed anon.

9.1.4 Shell-model calculations of $B(E2)$ and $Q(2_1^+)$ values

The known transition strengths of the transitions from yrast states are displayed as a function of mass number in Fig. 9.7 along with shell-model calculations. The effective charges are assumed to be e_p=1.7e and e_n=0.8e in the jj55pn interaction calculations in Table 9.3. The $2_1^+ \rightarrow 0_{\text{g.s.}}^+$ transition strengths predicted for the higher-mass isotopes agree reasonably well with experimentally determined values in both shell-model calculations. The ANTOINE calculations for ^{124,126}Te predict $2_1^+ \rightarrow 0_{\text{g.s.}}^+$ transition strengths that are less than the experimental values. The only available comparison between $4_1^+ \rightarrow 2_1^+$ transition strengths determined experimentally and in the jj55pn interaction calculations is in ^{130}Te. In this case, the shell-model calculations slightly overpredict the transition strength. Using the lower effective neutron charge as discussed above leads to a significant decrease in the transition strengths

Table 9.2: Literature g factors for 2_1^+ and higher states for selected nuclei near the shell closures at N/Z=50 and 82.

${}^{A}_{Z}X_{N}$	I_i^π	$g(I_i^\pi)$	Ref.
${}^{92}_{42}Mo_{50}$	2_1^+	+1.15(14)	[164]
	8_1^+	+1.413(6)	[165]
${}^{94}_{42}Mo_{52}$	2_1^+	+0.308(43)	[164]
	8_1^+	+1.137(15)	[166]
${}^{130}_{54}Xe_{76}$	2_1^+	+0.334(11)	[137]
	4_1^+	+0.42(5)	[137]
${}^{132}_{54}Xe_{78}$	2_1^+	+0.314(12)	[137]
	4_1^+	+0.61(11)	[137]
${}^{134}_{54}Xe_{80}$	2_1^+	+0.354(7)	[137]
	4_1^+	+0.80(15)	[137]
${}^{136}_{54}Xe_{82}$	2_1^+	+0.766(45)	[137]
	4_1^+	+1.08(43)	[137]
${}^{142}_{60}Nd_{82}$	2_1^+	+0.844(73)	[167]
${}^{144}_{60}Nd_{84}$	2_1^+	+0.20(2)	[163]
	4_1^+	+0.13(4)	[163]
	6_1^+	−0.56(22)	[168]
${}^{146}_{60}Nd_{86}$	2_1^+	+0.29(3)	[163]
	4_1^+	+0.193(27)	[168]

Table 9.3: Transition strengths for the $4_1^+ \rightarrow 2_1^+$ transition are adopted from the present Coulomb-excitation measurement, and transition strengths for the $2_1^+ \rightarrow 0_{g.s.}^+$ transition are taken from Ref. [41]. Shell-model calculations using the jj55pn interaction (SM-1) and the ANTOINE calculations (SM-2) are presented for comparison (see text for details).

^{A}X	$B(E2; 2_1^+ \rightarrow 0_{g.s.}^+)$ (W.u.)			$B(E2; 4_1^+ \rightarrow 2_1^+)$ (W.u.)		
	Adopted	SM-1	SM-2	Adopted	SM-1	SM-2
^{124}Te	30.5(15)		24.7	39.9(9)		28.3
^{126}Te	25.3(5)		22.5	29.8(4)		25.3
^{128}Te	19.8(4)	18.9	18.4		24.9	19.1
^{130}Te	15.1(5)	14.0	14.0	15.3(3)	17.0	12.7
^{132}Te	10.4(9)	9.1	9.5		8.5	7.9
^{134}Te	5.08(20)	5.1			5.3	

calculated with the jj55pn interaction. The proton components are largely consistent between the calculations in the different isotopes while the large increases in transition strength come from the neutron components. The larger neutron effective charge is consistent with other studies in the region and so the e_n=0.8e results will be used in further discussion. The overpredicted transition strength using the standard effective charges is in contrast to the ANTOINE calculations; in this case the shell-model calculations for ^{130}Te slightly underpredict the transition strength while using similar effective charges. The lower-mass isotopes are observed also to have increased transition strengths over those in the ANTOINE calculations. Calculations performed on the lower-mass isotopes with the jj55pn interaction would be useful in the exploration of the onset of collectivity in the 4_1^+ states. Further from the closed shell at N=82, a higher degree of excitation across shell closures is expected. These excitations are not included in the model space of the calculations and so do not contribute to the calculated transition strengths in Table 9.3. This may be a factor contributing to the underestimation of the transition strengths, particularly at lower masses. In a recent study [169] of the neutron-rich $^{130-134}$Te isotopes with shell-model calculations using the extended pairing plus multipole-multipole force model, and including excitations over the N=82 shell closure, good agreement was found with the measured transition strengths in ^{132,134}Te. It is worth noting that this study used effective proton and neutron charges of e_p=1.5e and e_n=0.5e. This may suggest that including the extra $(f_{7/2}, p_{3/2})$ orbits above N=82 captures most of the effect that the core polarisability has on the effective charges. Due to computational limitations, the calculations for ^{130}Te in Ref. [169] did not include cross-shell excitations, which may explain the poorer agreement found in the study.

The shell-model calculated quadrupole moments in Table 9.4 are "more positive" than the experimentally observed quadrupole moments. The experimental and shell-model calculated quadrupole moments are displayed in Fig. 9.8. The experimentally determined quadrupole moments correspond to a small (but definite) prolate defor-

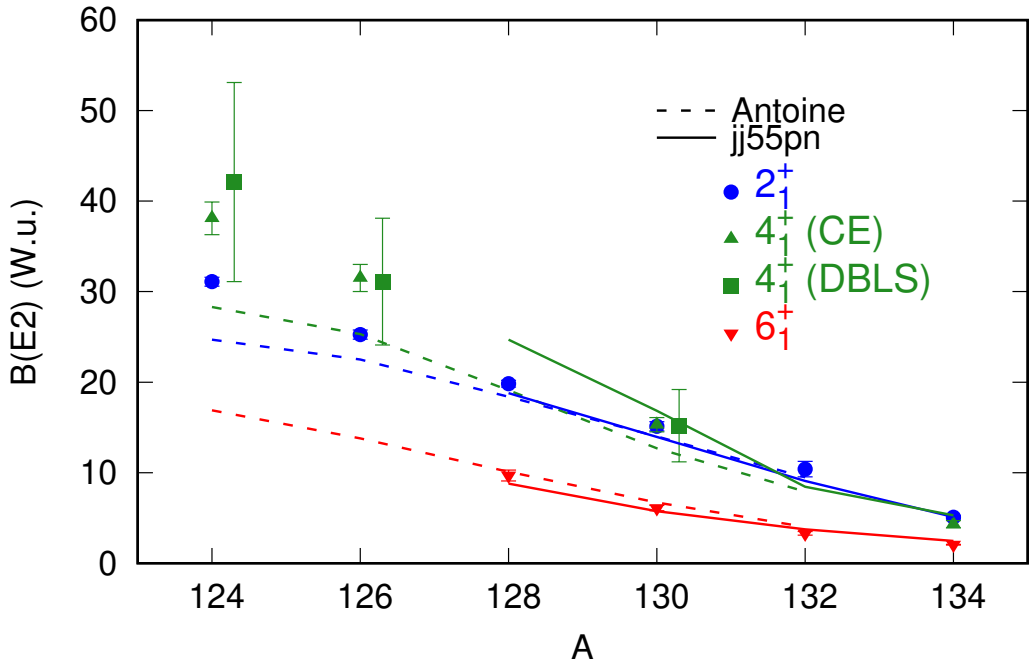

Figure 9.7: Systematics of $B(E2)$ values across the Te isotopes. Experimental data is presented from the present work and Refs. [41; 60; 61; 62; 63; 64; 65; 66]. The present shell-model calculations performed with NushellX@MSU and the jj55pn interaction are shown with solid lines. Results of the Antoine calculations are shown with dashed lines (see text for details).

Table 9.4: Experimental and shell-model quadrupole moments for 2_1^+ states in $^{124-134}$Te. Experimental data from Ref. [89].

^AX	$Q(2_1^+)$ (*e*b)		
	Ref. [89]	SM-1	SM-2
^{124}Te	−0.45(5)		−0.08
^{126}Te	−0.23(5)		+0.06
^{128}Te	−0.22(5)	+0.06	+0.09
^{130}Te	−0.12(5)	+0.12	+0.14
^{132}Te		+0.18	+0.17
^{134}Te		+0.12	

mation. The shell-model calculations predict a change from oblate shape close to the N=82 shell closure to a prolate shape at lower masses. A more rapid decrease in the quadrupole moment of the 2_1^+ state is observed from ^{126}Te to ^{124}Te, which is reproduced to a lesser extent in the shell-model calculations. Following the discussion in Ref. [170], it is possible to estimate the quadrupole moments in the axial-rotor prolate and oblate limits from the $B(E2)$ of the $2_1^+ \rightarrow 0_{\text{g.s.}}^+$ transition. These values are shown in the green dot-dashed lines in Fig. 9.8. The experimental values lie between the shell-model values and the prolate limit, clearly indicating triaxiality.

The large difference in the observed and calculated quadrupole moments in the investigated Te isotopes is indicative of missing components in the calculations that are required to create prolate deformations. It is unclear whether these observed differences in quadrupole moments are related to the observed excess in transition strengths over the shell-model calculated values, particularly in the Te isotopes nearer mid-shell. Since the observed differences in the experimental and calculated $E2$ moments are consistent across the investigated Te isotopes and the transition strength excess is seen primarily in the lower-mass isotopes, the deformation and collectivity in the Te isotopes appear to be less strongly linked in the shell-model calculations than would be expected.

In Fig. 9.9 the R_{42} ratio is compared to the ratio of the g factors of the 4_1^+ and 2_1^+ states for $^{124-130}$Te. A correlation is seen between the R_{42} ratio and the g-factor ratio, however, the R_{42} ratio is fairly constant over the range of isotopes measured, with a maximum of R_{42}=2.07 and a minimum of R_{42}=1.95. In contrast, the g-factor ratio changes by almost a factor of two over the same isotopes. The R_{42} ratio has often been used [172; 173] as an indicator of both structural changes and the development of collectivity; however, as seen in Fig. 9.9, the g-factor ratio is a much more sensitive indicator of the development of collectivity in these isotopes. This further confirms that one must be wary of relying too much on energy systematics in the investigation of nuclear structure.

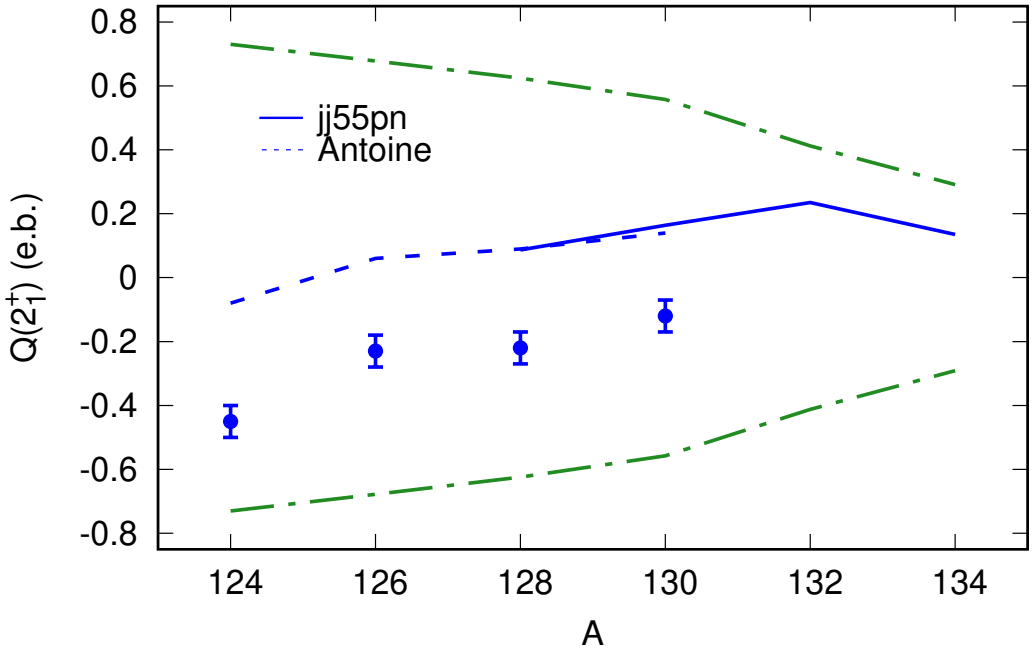

Figure 9.8: Tellurium $Q(2_1^+)$ systematics. Data is taken from Ref. [171]. The shell-model calculations performed with the jj55pn interaction are shown with solid lines, results of the ANTOINE calculations are shown with dashed lines. The oblate and prolate limits of the quadrupole moments based on the 2_1^+ state are shown with green, dot-dashed lines; see text for details.

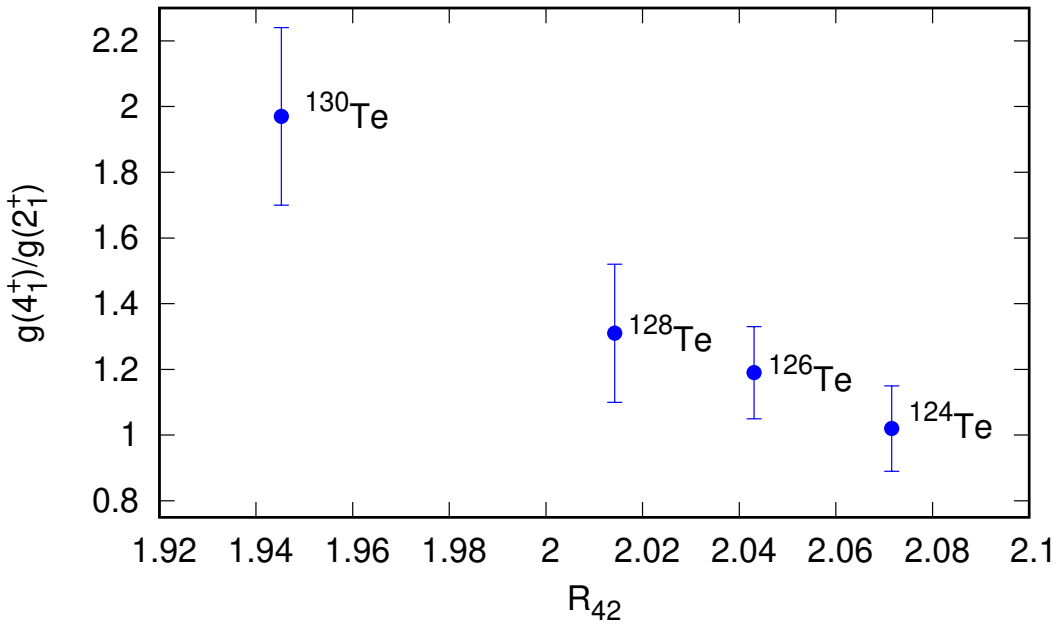

Figure 9.9: The comparison of R_{42} ratio ($E(4^+)/E(2^+)$) to $g(4^+)/g(2^+)$ across the measured Te isotopes.

9.1.5 Kumar-Cline sum rules and rotational invariants

Another approach to the determination of the nuclear shapes is the calculation of shape invariants from the Kumar-Cline sum rules, as discussed in Section 2.2. The extensive Coulomb-excitation measurements required for the determination of these values are not available over large regions of the nuclear chart. It is possible, however, to approach this procedure from a theoretical perspective, using shell-model-calculated matrix elements to determine the quadrupole deformation and triaxiality. We here use the shell-model calculations performed using the jj55pn interaction to calculate the shape invariants.

In Fig. 9.10 the convergence of the $\langle Q^2 \rangle$ shape invariant, calculated as given by Eqn. 2.7, is shown for the $0^+_{\text{g.s.}}$ state in red, and the 2^+_1 state in blue, for ^{132}Te, as higher energy states are included in the sum. Thirty states of each spin and parity were evaluated in the shell-model calculations of ^{132}Te. The highest-energy 2^+ state included in the sums is at $\sim$4.4 MeV. The sum does not appear to have converged fully, however, the last few individual components in the sum have become quite small. This can be seen in an equivalent convergence plot as a function of the maximum included index in Fig. 9.11. The sums have flattened significantly by the inclusion of the 10th states of each spin and parity, however, this hides the more rapid increase from the increased density of states at higher energies.

The asymmetry parameter δ is not directly calculated through the Kumar-Cline

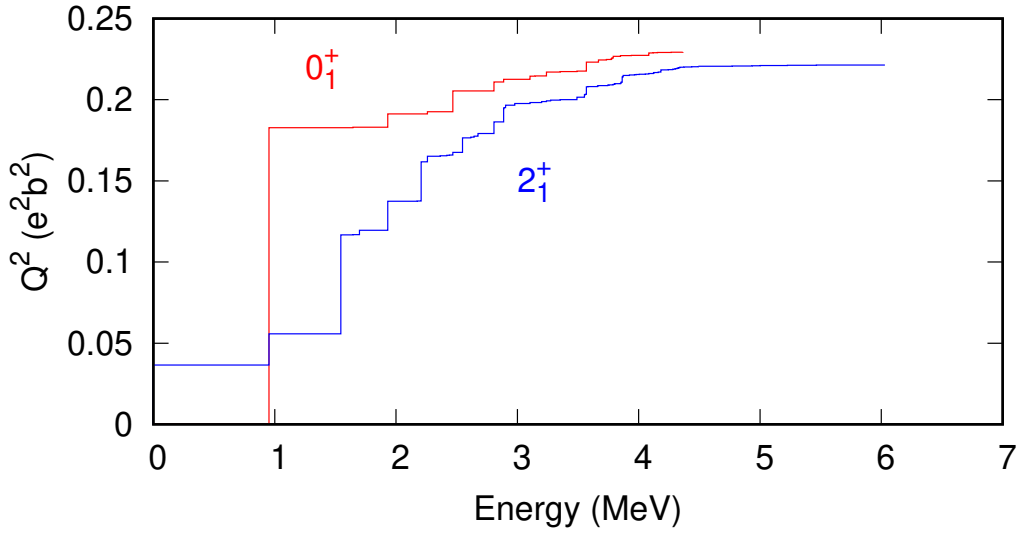

Figure 9.10: Convergence of $\langle Q^2 \rangle$ values as determined from Kumar-Cline sums [8] for the 0_1^+-, 2_1^+-, and 4_1^+-states in ^{132}Te from shell-model calculations in red, blue, and green, respectively. The sums are calculated including states up to the maximum energy shown on the x-axis.

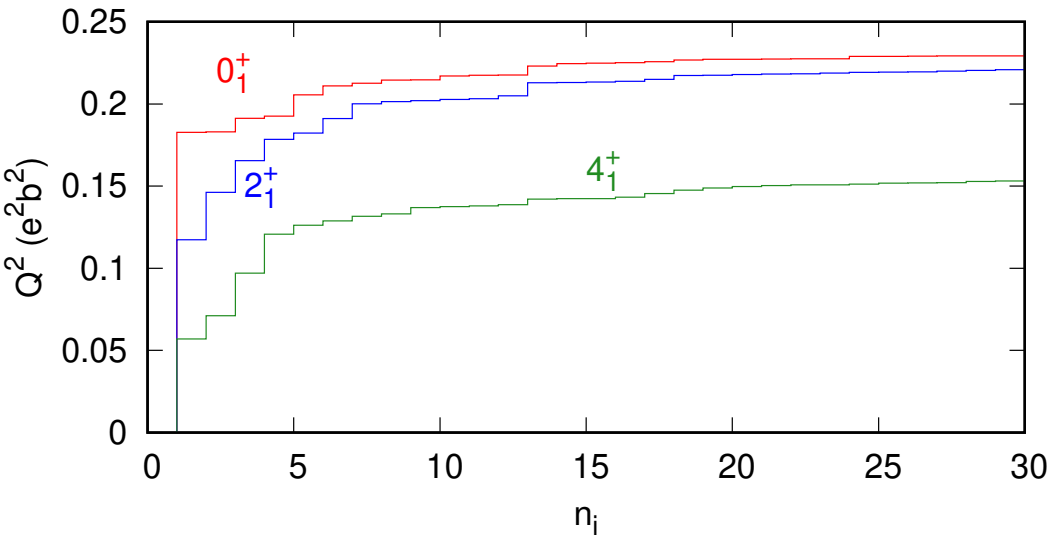

Figure 9.11: Convergence of $\langle Q^2 \rangle$ values as determined from Kumar-Cline sums [8] for the 0_1^+- and 2_1^+-states in ^{132}Te from shell-model calculations in red and blue, respectively. The sums are calculated including states up to the maximum index shown on the x-axis.

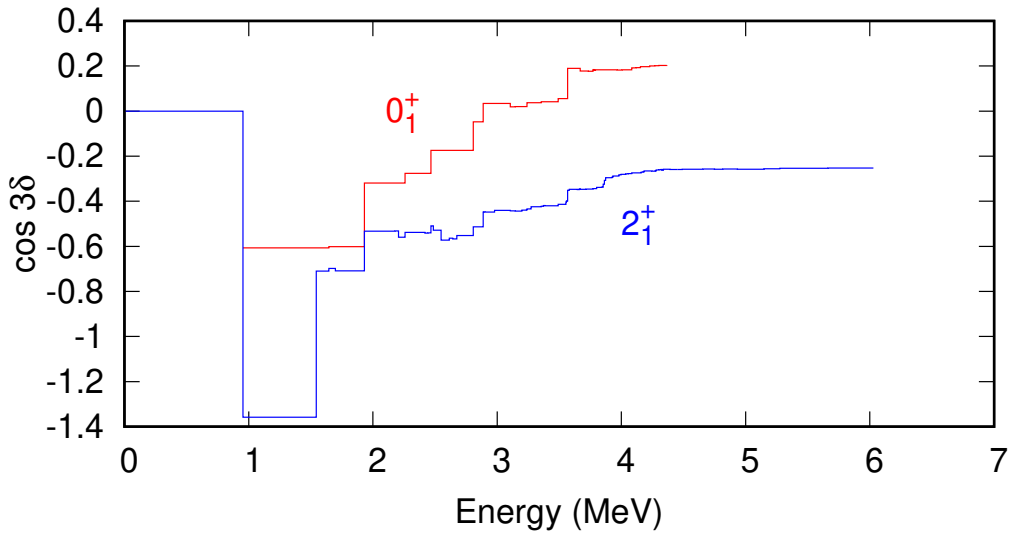

Figure 9.12: Incremental sum of $\langle \cos 3\delta \rangle$ as determined from Kumar-Cline sums [8] for the 0_1^+ state and the 2_1^+ state in ^{132}Te from shell-model calculations in red and blue, respectively.

sums. Instead, consistent with previous work [9], we define a new quantity

$$\langle \cos 3\delta \rangle = \frac{\langle Q^3 \cos 3\delta \rangle}{\langle Q^2 \rangle^{3/2}} \tag{9.1}$$

where $\langle Q^2 \rangle$ and $\langle Q^3 \cos 3\delta \rangle$ are the shape invariants as previously discussed (see Sec. 2.2). The effective asymmetry parameter is then extracted as

$$\delta = \frac{1}{3} \arccos \langle \cos 3\delta \rangle. \tag{9.2}$$

The convergence of $\langle \cos 3\delta \rangle$ from ^{132}Te shell-model calculations is displayed in Fig. 9.12. The line for the $0^+_{\text{g.s.}}$ state, in red, is reasonably stable including states up to 2^+_{30}, although a significant change is still seen from a single state close to 4 MeV. In contrast, the determined triaxiality of the 2_1^+ state seems to converge within the calculated states.

In more highly excited states care must be taken that enough states are included in the Kumar-Cline sums. The convergence of the shell-model calculated $\langle Q^2 \rangle$ parameters of the 0_4^+ and 2_4^+ states in ^{132}Te is displayed in Fig. 9.13 in red and blue, respectively. The deformation parameter of the 0_4^+ state has likely not converged within the number of states calculated. The only states that contribute to the $\langle Q^2 \rangle$ sum for a 0^+ state are the 2^+ states. States only contribute when they connect through the $E2$ operator which requires a total angular momentum of at least 2. The highest-energy 2^+ state calculated in the ^{132}Te shell-model calculations lies at $E(2^+_{30})$=4366 keV while the 0_4^+ state is predicted to appear at 2643 keV. The larger density of 2^+ states near

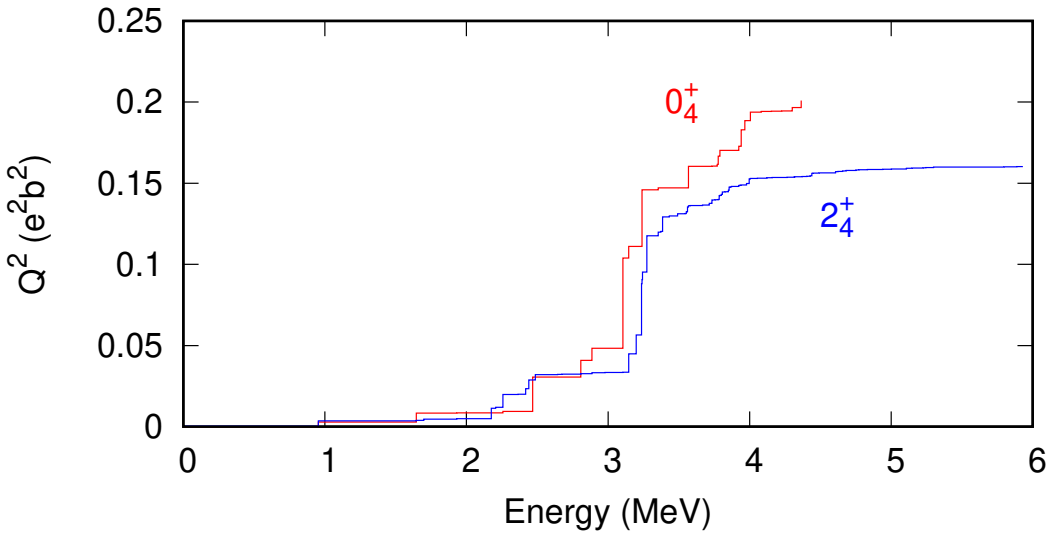

Figure 9.13: Convergence of $\langle Q^2 \rangle$ values as determined from Kumar-Cline sums for the 0_4^+- and 2_4^+-states in ^{132}Te from shell-model calculations in red and blue, respectively. The sums are calculated including states up to the maximum energy shown on the x-axis.

the 2_{30}^+ state suggests that many more states that would contribute to the sum could lie relatively close to the 0_4^+ and 2_{30}^+ states. The quadrupole shape invariant of the 2_4^+ state looks to have largely converged within the calculated states, however this may not be the case: there is a large gap in excitation energy between the regions in which the Kumar-Cline sums increase rapidly. It is possible that another region of rapid increase is found at higher energies. The energy range shown in Fig. 9.13 includes excitation energies above the 2_{30}^+ state where states of other spins are calculated to appear. The apparent decrease in the deformation of the higher-excited states is likely, therefore, due in part to not including more than thirty states in the shell-model calculations. A recent study of the convergence of shape invariants from shell-model calculations in the *sd* and *fp* shells [170] found that, in this model space, only a few intermediate states were required to capture the majority of contribution to the lowest-order sums. This is expected to be so for highly collective nuclei, and is expected to be less so for weakly collective nuclei. It is worth noting that, in *fp* shell nuclei, rotational bands emerge from shell-model calculations [174] while vibrational-like structures do not emerge in the same way. The slower convergence of the shell-model calculated Kumar-Cline sums likely indicates that the collectivity is building more slowly from single-particle characteristics in the ^{132}Sn region.

The shape invariants determined through the Kumar-Cline sums for the 0_1^+ states in ^{128,130,132,134}Te are shown in Fig. 9.14. They begin at the N=82 shell closure with small deformations. In virtually all cases the 0^+ states are seen to be highly triaxial. Moving further from the neutron shell closure, the deformations of the ground states of the even-even Te isotopes increase rapidly. The higher-excited 0^+ states show a

similar increase in the deformation with the excited states of the lower-mass isotopes generally more deformed than those in isotopes closer to the closed shell. An exception to this is ^{128}Te which has much lower deformations for the excited $0^+_{4,5}$ states, however only 10 states of each spin and parity were included in these calculations and so this may arise from not including the relevant 2^+ states.

The shell-model calculated shape invariants of the 2^+ states are shown in Fig. 9.15. The deformations of the 2^+ states in each of the even-even Te isotopes are similarly clustered in deformation and triaxiality to the 0^+ states. As expected, the cluster of 2^+ states increases in deformation away from the neutron shell closure. The 2^+_1 states in ^{128,130,132,134}Te are found to increase in deformation more rapidly than higher-excited states. It can also be seen that the deformation and shape parameters in ^{128}Te are reasonably close for the $0^+_{\text{g.s.}}$ and 2^+_1 states. This may indicate the beginning of a convergence to a collective behaviour in this isotope, akin to rotational motion at a fixed deformation.

The shape parameters for the 4^+ and 6^+ states are similarly highly clustered as shown in Figs. 9.16 and 9.17, respectively. The same pattern of increasing deformation away from the shell closure is observed.

It is common to consider the difference in predictions of shape parameters from lower- and higher-order sums in order to obtain a "variance" in the shape parameters [9]. It is worth noting that the variances in both the deformation and shape parameters are generally quite high for all calculated states. Most states have a variance in δ equivalent to at least 7° with many much larger. In particular, those for the calculated shape parameters in ^{134}Te for both the 0^+ and 2^+ states are all larger than 7° and up to 20°. It is therefore likely that any triaxiality in the region is soft rather than rigid. While the analysis of the shape parameters from Kumar-Cline sum rules is rigorous, the shapes in weakly collective nuclei are not expected to be well defined. However, the trends in the evolution of the shape parameter are instructive. The Bohr model shape parameters of the yrast states in ^{128,130,132,134}Te assuming an ellipsoidal deformed nucleus (β and γ) are displayed in Fig. 9.18. Transformations of the shape parameters were performed using Eqn. 2.9 and Eqn. 2.10. The higher-spin yrast states are consistently found to be at smaller deformation than the lower-spin states. The clustering of the states increases away from the shell-closure, which may be indicative of the nucleus acting more as a collective body.

9.1.6 Summary of the investigation of the Te isotopes

The development of collectivity in the Te isotopes has been explored though shell-model calculations with reference to $B(E2)$ and g-factor measurements, focussed on the 4^+_1 states across the isotopic chain. It has been seen that the collectivity develops more rapidly in low-lying, low-spin states than in higher-lying states. This is observed through the slower convergence of the 4^+_1 g factors to the collective limit than the 2^+_1 g factors and the slow increase of the $E2$ strength for the $4^+_1 \rightarrow 2^+_1$ transitions compared to the $2^+_1 \rightarrow 0^+_{\text{g.s.}}$ transition strength. Both of these trends are also observed in the shell-model calculations. The slower convergence of the 4^+_1 g factor may be

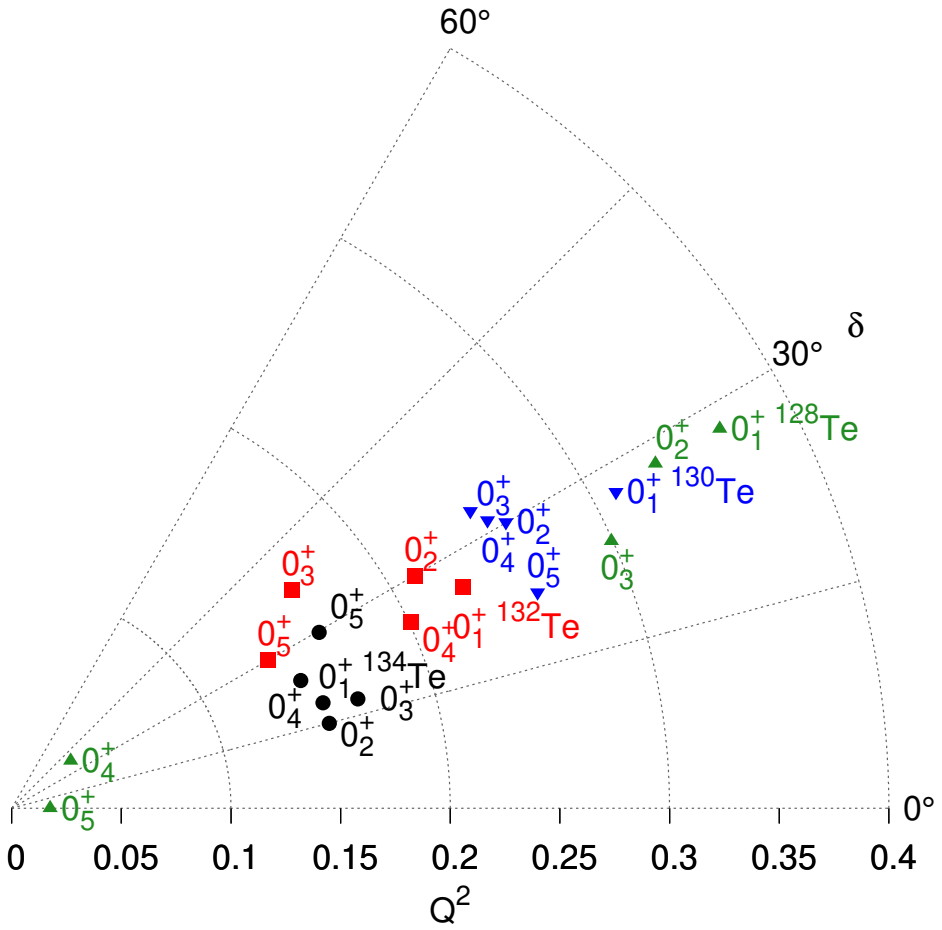

Figure 9.14: Shape parameters from Kumar-Cline sum rules based on shell-model calculations for 0^+ states in ^{128}Te (▲), ^{130}Te (▼), ^{132}Te (■), ^{134}Te (●).

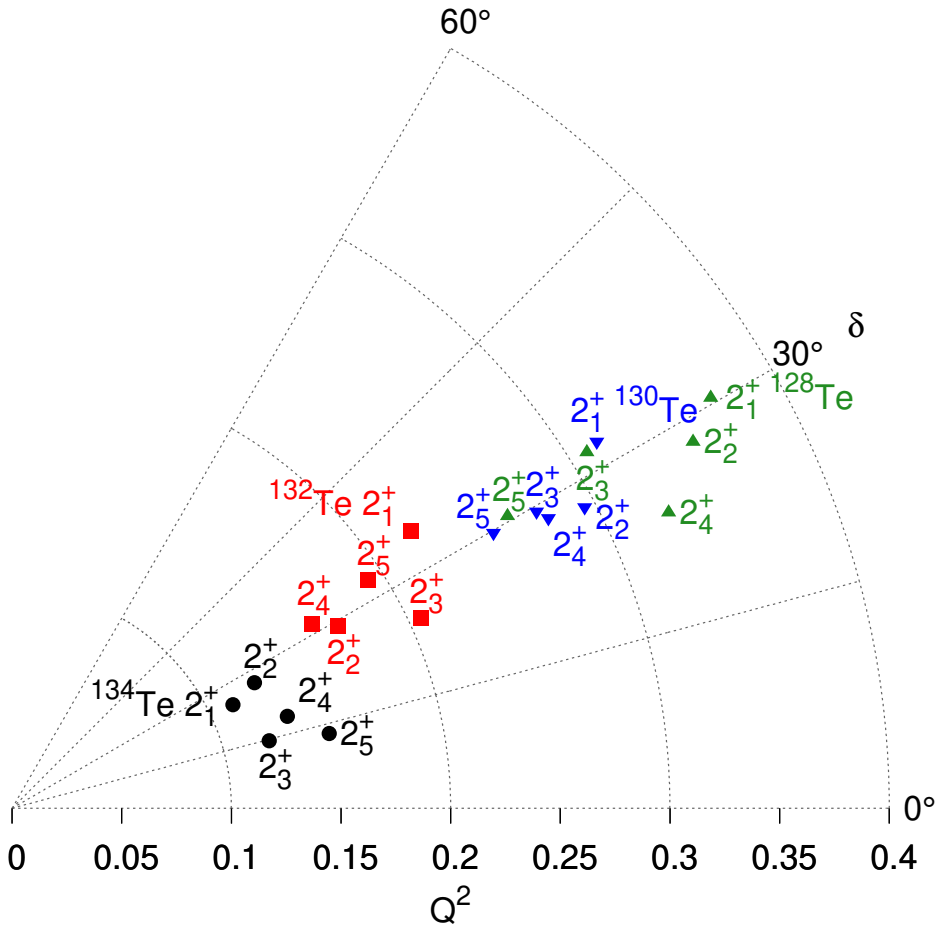

Figure 9.15: Shape parameters from Kumar-Cline sum rules based on shell-model calculations for 2^+ states in ^{128}Te (▲), ^{130}Te (▼), ^{132}Te (■), ^{134}Te (●).

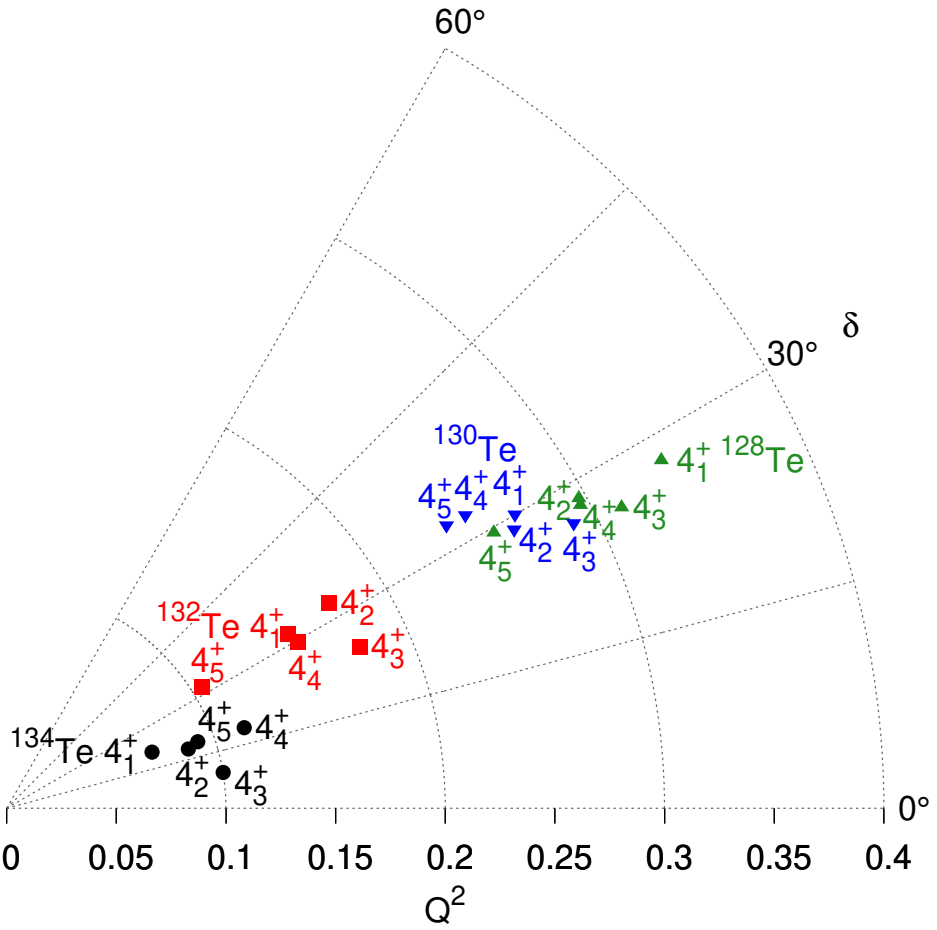

Figure 9.16: Shape parameters from Kumar-Cline sum rules based on shell-model calculations for 4^+ states in ^{128}Te (▲), ^{130}Te (▼), ^{132}Te (■), ^{134}Te (●).

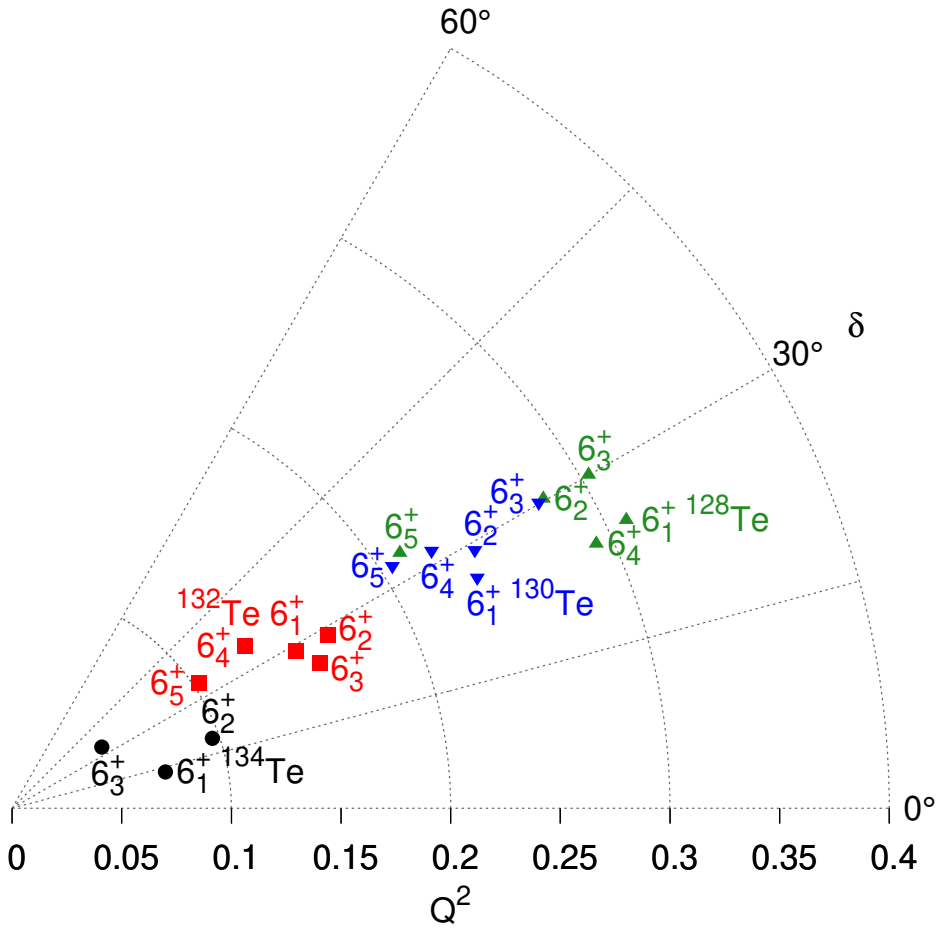

Figure 9.17: Shape parameters from Kumar-Cline sum rules based on shell-model calculations for 6^+ states in ^{128}Te (▲), ^{130}Te (▼), ^{132}Te (■), ^{134}Te (●).

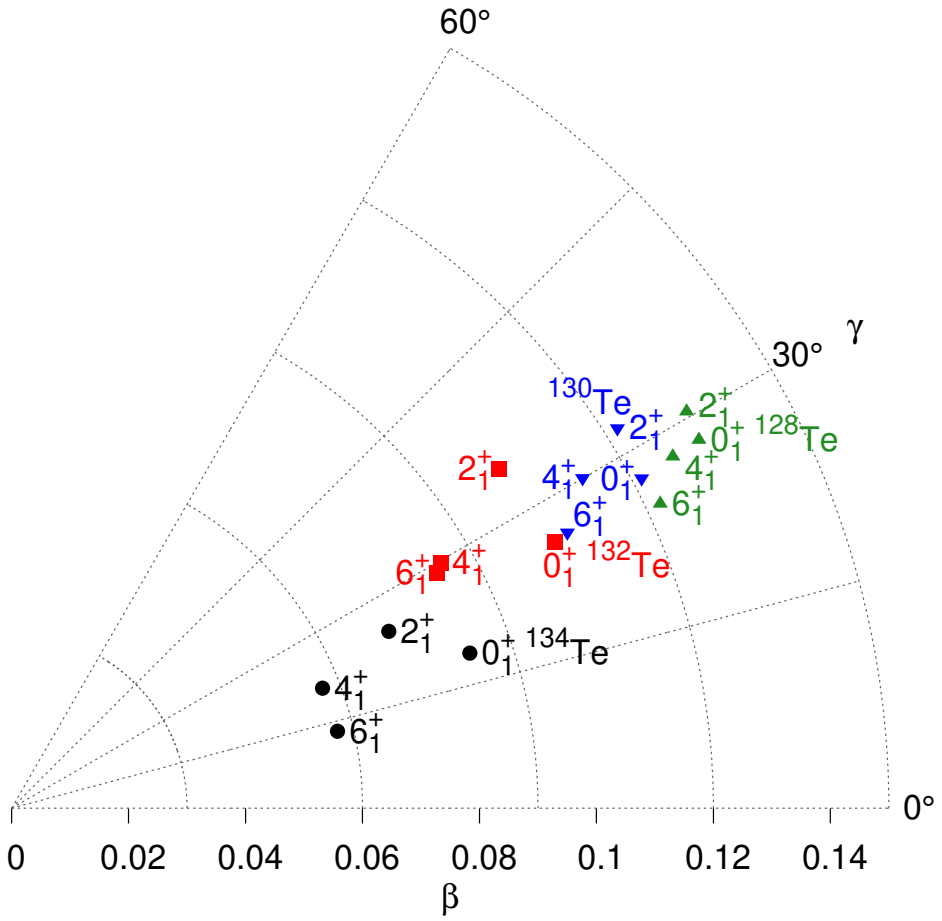

Figure 9.18: Bohr-model deformation parameters assuming an ellipsoidal deformed nucleus from Kumar-Cline sum rules based on shell-model calculations for yrast states in ^{128}Te (▲), ^{130}Te (▼), ^{132}Te (■), ^{134}Te (•).

attributed to less fragmentation of the wavefunction from the coupled $\pi g^2_{7/2}$ configuration which is dominant in singly magic ^{134}Te. In particular, less of the wavefunction is comprised of neutron-dominant (i.e. $J_\nu \neq 0$) configurations in the 4^+_1 states than in the 2^+_1 states.

The shell-model calculations support many of the indicators of the development of collectivity: the fragmentation of the wavefunction increases further from the N=82 shell closure, moreover the fragmentation occurs in a coherent way. This coherent fragmentation increases the $B(E2)$ values in a similar way to the values that have been measured in the present work. The sharing of angular momentum between protons and neutrons also increases, which can be observed in the g factors measured here and in previous works. Increasing deformation of the isotopes correlated with the enhanced transition strengths is observed both experimentally and through the shape invariants evaluated using the Kumar-Cline sum rules in the shell-model calculations, although the $E2$ moments calculated for the states are not in detailed agreement with experiment. It is posited that this may be due to the omission of particle-hole excitations across the shell-closure, which are expected to develop in collective nuclei. It was not possible to confirm the breakdown of the shell structure in the present measurements, however the measured quadrupole moments provide an avenue of exploration to investigate this phenomenon as cross-shell excitations are expected to produce larger deformations. Finally, the triaxial nature of the nucleus has been explored through the shape invariant from shell-model calculations, with most states in all investigated nuclides found to be highly non-axial (on average). Detailed measurements of transition strengths and quadrupole moments for a large number of excited states would be required to test this experimentally. Transfer reactions would also provide a method for the investigation of the nature of nuclear states as excitation of particle-like states would be enhanced over collective excitations.

Finally, it must be noted that the effective charges required in the shell-model calculations, i.e. e_p=1.7e and e_n=0.8e, are large. A deeper understanding of the origin of the effective charges must be sought in building a complete picture of the emergence of nuclear collectivity.

9.1.7 Collectivity in the Te isotopes

The increasing transition strengths and convergence of g factors to the collective limit are both indicators of emerging collectivity, however the potential that these observations are due purely to an increase in the number of valence nucleons and a sharing of angular momentum between protons and neutrons must be discussed. The proton and neutron contributions can be explored by comparison to the singly magic isotone of each nucleus. A comparison of $2^+_1 \rightarrow 0^+_{\text{g.s.}}$ transition strengths in the isotones of Sn, Te and Xe is given in Fig. 9.19. The transition strengths of the Sn isotopes can be seen to be relatively flat between N=54 and N=82. With two extra protons, the Te isotones have increased transition strength and the transition strengths begin to peak near the mid-shell isotopes of Te. The Xe isotopes have four valence protons and much larger transition strengths. In particular, a sharper peak

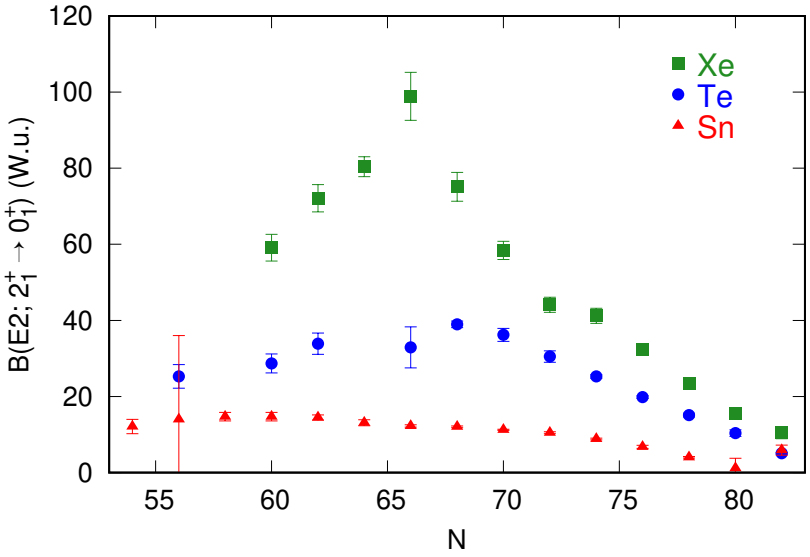

Figure 9.19: Comparison of the $2_1^+ \rightarrow 0_{g.s.}^+$ transition strengths in Sn, Te and Xe isotones. Data from Ref. [41].

in the transition strengths can be observed at the mid-shell at N=66. Shell-model calculations imply the mid-shell peak in the nuclides with valence protons is due to the coherent contribution of protons and neutrons to the transition strength [69].

However, a recent study of the Cd, Sn, and Te isotopes with a generalised seniority model reproduced the observed $B(E2)$ systematics [175]. In this view the increase in $E2$ strength near mid shell may not be a signature of increasing collectivity associated with proton-neutron correlations but rather a scaling with the particle number in a seniority scheme. There are three observations to make: (i) First, in Ref. [175] there is no discussion of the effective charges needed to describe the data. It appears that the seniority model is used to describe mass-dependent trends and that there is an arbitrary scaling to fit the data. In this case, the semiempirical description from the generalised seniority model is not necessarily in tension with the view of emerging collectivity from the shell-model calculations. (ii) The second remark is that the results of the present work show that there is an interplay of persistent seniority structure and collectivity that tends to break down the seniority structure in the Te and Xe isotopes. We therefore might expect that features of a generalised seniority model persist in weakly collective nuclei adjacent to the Sn isotopes. (iii) The final remark concerns the more general question of "What constitutes a collective $E2$ transition?". In other words, for an $E2$ transition between multinucleon states, how can one disentangle $E2$ strength that simply scales with the number of valence nucleons? The generalised seniority scheme may help address this question.

9.2 Collectivity in the Cd Isotopes

The Cd isotopes lie two protons below the Z=50 shell closure and thus have the same number of "valence protons" as the Te isotopes. While the shell in which the protons (holes) reside differs, the average long-range nucleon-nucleon interactions are likely to be similar between Cd and Te. Indeed, the lowest relevant configurations are the spin-orbit partners $\pi g^{n}_{7/2}$ and $\pi g^{-n}_{9/2}$ in Te and Cd, respectively. It is therefore expected that the same forms of collective structure may occur in both cases. Odd-mass isotopes can allow for detailed study into deformation and the nature of collectivity, which can be more difficult to determine in even-even nuclides. In particular, the properties of single-particle-like states give key insights into the deformation of the nucleus as the observations can often be interpreted through Nilsson schemes. The collective motion these nuclei experience can then be understood through the coupling of the single-particle degrees of freedom to the collective degrees of freedom. Decoupling the single-particle attributes from the collective attributes can be more difficult in even-even nuclides as the allowed coupling of nucleons in pairs can wash out some of the microscopic structure. The stable odd-mass Cd isotopes ^{111,113}Cd, with N=63,65 lie further from the shell closures at N=50 and N=82 than the Te isotopes discussed above. It may therefore be expected that the collective structures in the Cd isotopes discussed in this section would be more developed than those in the Te isotopes studied in this thesis.

The measured level scheme determined from the multi-step Coulomb-excitation measurement of ^{111}Cd does not show strong decay patterns that can be easily interpreted as rotational bands. In fact, most excited states are seen to decay to almost all of the lower-lying states to which they can decay via $M1$ or $E2$ transitions, without strong preferences for a particular decay path. Clearly, ^{111}Cd is not a well-defined rotational nuclide. However, the strong mixing between all states may be a hint as to the origins of deformation and collectivity. While only a few states were excited in the single-step Coulomb-excitation measurements of ^{111,113}Cd, it is instructive to compare the observed Coulomb-excited states between isotopes as these states are most likely to have quadrupole collectivity in common with the ground state.

Both ^{111}Cd and ^{113}Cd have a $1/2^+$ ground state. The g factor of the ground state of each nuclide is much more positive (i.e. a negative value which is smaller in magnitude) than the Schmidt g factor for an $s_{1/2}$ neutron. A reasonable explanation for the increase of the g factors of the ground states is configuration mixing associated with deformation of the nucleus. It has previously been shown that a small deformation is sufficient to explain the change in the g factors [82]. It is not clear how the change in the g factors would occur without deformation or sufficient configuration mixing as to correspond to deformation.

There are three low-lying $5/2^+$ states in both ^{111}Cd and ^{113}Cd. All three of these states were excited in the single-step Coulomb-excitation measurements of both ^{111}Cd and ^{113}Cd, with level schemes shown in Figs. 4.8 and 4.11, respectively. Each of these states has a distinctive character which will be discussed below.

The low-lying $5/2^+_1$ states in ^{111}Cd and ^{113}Cd are observed to have long lifetimes.

Based on g-factor measurements and the transition strengths to the ground state, these states must be associated with the $\nu d_{5/2}$ orbit [82]. The measured lifetimes of the $^{5}/_{2}^{+}_{1}$ states in ^{111}Cd and ^{113}Cd correspond to $^{5}/_{2}^{+}_{1} \rightarrow {}^{1}/_{2}^{+}_{\text{g.s.}}$ transition strengths of $B(E2)$=0.2218(19) W.u. [90] and $B(E2)$=0.372(25) W.u. [93], respectively. The transition strength is larger in ^{113}Cd than ^{111}Cd, however it is still smaller than the 1.0 W.u. estimate for a single-particle transition. The lifetime of the $^{5}/_{2}^{+}_{1}$ state is not known in ^{115}Cd so it is not clear that the trend would continue towards the mid shell at N=66 (^{114}Cd). Measurement of this value in ^{115}Cd would provide further information about the structure and the development of collectivity in the Cd isotopes.

The $^{5}/_{2}^{+}_{2}$ states in ^{111}Cd and ^{113}Cd were strongly populated in the Coulomb-excitation measurements, and have ground-state transitions with much larger $B(E2)$ values of 17.4(12) W.u. and 35.7(24) W.u., respectively. These states are likely collective and must be associated with the ground-state configuration (nominally $\nu s_{1/2}$) coupled with the 2^+ core excitation, irrespective of the nature of the core collectivity. The large increase in the transition strength from ^{111}Cd to ^{113}Cd is indicative of an increase in collectivity; this would correspond to larger deformations in the rotor model. A similar, albeit less pronounced, increase in transition strength of the $^{3}/_{2}^{+}_{1} \rightarrow {}^{1}/_{2}^{+}_{\text{g.s.}}$ transitions between ^{111}Cd and ^{113}Cd from 17.4(12) W.u. to 22.8(15) W.u. is also observed. The $^{3}/_{2}^{+}_{1}$ state can also be identified as the core excitation coupled to the ground-state configuration and so the increase in transition strength also suggests increasing collectivity.

The origin of the third excited $^{5}/_{2}^{+}$ state is less clear. Strong γ-decay branches are observed to both the ground state and the $^{5}/_{2}^{+}_{1}$ state; the state must therefore be of mixed character. The $^{5}/_{2}^{+}_{3} \rightarrow {}^{1}/_{2}^{+}_{\text{g.s.}}$ transition in ^{111}Cd has a transition strength of 5.5(4) W.u. which is neither clearly indicative of collectivity, nor of a single-particle excitation. In contrast to the pattern observed in the $^{3}/_{2}^{+}_{1} \rightarrow {}^{1}/_{2}^{+}_{\text{g.s.}}$ and $^{5}/_{2}^{+}_{2} \rightarrow {}^{1}/_{2}^{+}_{\text{g.s.}}$ transitions, it is also stronger than the $^{5}/_{2}^{+}_{3} \rightarrow {}^{1}/_{2}^{+}_{\text{g.s.}}$ transition in ^{113}Cd, which has a $B(E2)$ value of 2(1) W.u., measured in the present work. If these states can truly be identified with each other (as equivalent configurations), then the reduction in the transition strength in ^{113}Cd is against the naive expectations set by the increase in other transition strengths (suggesting increased collectivity). An explanation of the reduction of the transition strength may be a consolidation of the $E2$ collectivity of the $^{5}/_{2}^{+}$ states in a single state. In this case, the $E2$ collectivity appears to be shifting into the $^{5}/_{2}^{+}_{2}$ state. It has been noted that when states of a single spin and parity mix equally, a single state (with coherent mixing) lowers in energy [36]. If this result is applicable, then this may provide a pathway to stronger forms of collectivity.

The shell-model calculations of ^{111}Cd discussed in Sec. 6.3 are in good agreement with experiment. Further calculations of the higher-mass Cd isotopes would allow systematic study of the predicted wavefunctions and exploration of the nature of collectivity from the underlying nucleonic motion.

9.3 Emergence of collectivity in the Z=50 region

There are several factors that are acknowledged to be important in the development of collectivity. The coherent interaction of protons and neutrons can be observed in the increased transition strength towards the mid-shell Te isotopes. The shell-model calculated wavefunction decompositions show an increase in the neutron component of the angular momentum of the state along with the two valence protons. In particular, the 2_1^+ states observe a larger neutron spin component than the 4_1^+ states. This is observed experimentally in more rapid reduction in the g factors of the 2_1^+ state than in the g factors of the 4_1^+ states, which have a persisting seniority $g_{7/2}^2$ proton component. The explanation of the onset of collectivity that is seen is that the states develop collectivity individually as mixing increases, starting with the lower-spin states. As noted by Casten [36], the mixing of states of the same spin and parity with wavefunction components of the same relative phase leads to the lowering of the energy of the most coherently mixed state. This general feature would broadly explain why the observed collectivity appears in the low-lying states regardless of the nature of the state.

Simple collective models such as the triaxial-rotor model and the harmonic- or anharmonic-vibrator model have generally been used to describe weakly collective nuclides. We suggest here that the reason these models have had limited success in describing the weakly collective transitional nuclides is that the nucleus as a whole is not becoming collective. Rather, individual low-excitation states begin to develop collective character in turn as the number of valence nucleons increases. In this work, consistent with previous work, it appears that collectivity appears first in the lowest-energy and lowest-spin states. This scenario implies that any collective model that hopes to accurately predict the structure of weakly collective nuclei must therefore account for the reduced collectivity of states like the 4_1^+ and 6_1^+ states in the Te isotopes.

Conclusion

The nuclear structure and the onset of nuclear collectivity near ^{132}Sn has been investigated through the measurement of nuclear g factors and $E2$ transition strengths in selected stable Te and Cd isotopes. The emergence of collectivity is characterised by an increase in the measured transition strengths through the coherent motion of many nucleons, the fragmentation of the state wavefunctions between nucleon configurations, and the weakening of the nuclear shell structure.

The transition strengths measured through the Doppler-shift attenuation method and Coulomb excitation in ^{124,126,130}Te were presented in Chapters 7 and 8, and compared with shell-model calculations in Chapter 9. The transition strengths of the 4_1^+ states near the N=82 shell closure agree with the shell-model calculations, however the transition strengths increase faster in experiment than in the shell-model calculations. This indicates that the shell-model calculations do not fully capture the changes in nuclear structure and developing quadrupole collectivity. The reason could be that the calculations underestimate the fragmentation of the nuclear wavefunction within the valence space, or due to the calculations not including excitations from beyond the shell-model basis space (cross-shell excitations). It is not possible to distinguish between these two causes with the present data and calculations. The multi-step Coulomb-excitation measurements reported here were obtained as a by-product of other studies; dedicated measurements would be valuable, striving toward experimental evaluation of the Kumar-Cline sum rules. A next step would be to identify whether the excited 0^+ states, especially toward mid shell, show $E0$ and $E2$ strengths consistent with shape coexistence.

Previous systematic studies across isotopes in transitional regions have largely focussed on the emergence of collectivity through $E2$ transition strengths or on maintained seniority through g factor measurements. The present work has measured both $M1$ and $E2$ observables for the 4_1^+ states in the Te isotopes; this has allowed a clear difference to be seen in the relative collectivity of the excited states. A successful theoretical model that describes weakly collective nuclei must account for the differing levels of collectivity amongst the low-excitation excited states, which conform to neither simple collective or seniority structures.

The g factors of the 4_1^+ states in ^{124,126,128,130}Te were measured in Chapter 7 and discussed in Chapter 9. The g factors of the 2_1^+ states decrease rapidly towards the

collective limit as the number of neutrons moves away from the shell closure; the g factors of the 4_1^+ states decrease less rapidly than the 2_1^+ g factors. These trends in the g factors are a sign that the fragmentation of the wavefunction increases more rapidly in the 2_1^+ states than in the 4_1^+ states, and therefore collectivity is likely to build in lower-spin excitations before the higher-spin excitations. This interpretation was bolstered by comparison of the present results with shell-model calculations in which the fragmentation of the wavefunctions and mixing of proton and neutron configurations not coupled to spin zero in the lower-spin yrast states is higher than in the higher-spin states. The calculation of shape invariants based on Kumar-Cline sum rules also show a stronger dependence of the average deformation on the spin of the states rather than their energy.

The $E2$ transition strengths of low-lying states in ^{111,113}Cd were measured and presented in Chapter 4, and the results for ^{111}Cd were compared to shell-model calculations in Chapter 6, with a high level of agreement observed. Further, the results were also interpreted in terms of the Nilsson model and nuclear deformation. It was noted that the odd-mass nuclides provide the opportunity for extra sensitivity to aspects of the nuclear deformation and the nature of collective excitations due to their effect on the properties of the single-particle like states. A comparison of the obtained $B(E2)$ values and the predictions of the particle-vibration model show poor agreement in both ^{111}Cd and ^{113}Cd. Data from a ^{111}Cd multi-step Coulomb excitation measurement were analysed in Chapter 5 and it was determined that further measurements were required in order to extract useful transition strength information from the data. It is proposed that further measurements of the relevant mixing ratios, state lifetimes, state spins, and state parities must be performed before matrix elements can be extracted from such data. It is also suggested that dedicated experiments with lower-mass targets would provide useful data, and a measurement with a Pb target (for a period of longer than the present 90-minute calibration run data) would be required.

In conclusion, the emergence of nuclear collectivity west of ^{132}Sn has been explored through the measurement of single-particle characteristics from nuclear g-factor measurements across the Te isotopic chain, electric-quadrupole collectivity through $B(E2)$ measurements across the Te isotopic chain, and the nature of the emergent nuclear collectivity in the weakly collective, odd-mass Cd isotopes through the study of decay patterns. The path to nuclear collectivity from the underlying nucleonic motion has been explored through the fragmentation of nuclear wavefunctions, the interactions of protons and neutrons, and the deformation of states through calculated shape invariants from a shell-model basis. Further studies should be undertaken into the development of collectivity through the $E2$ strengths in weakly collective odd-mass nuclei and investigations of the breakdown of the nuclear shell model through transfer reaction studies. In addition, systematic multi-step Coulomb-excitation measurements of the even-even Te isotopes would allow calculation of the shape invariants from the Kumar-Cline sum rules. The preference for triaxiality in shell-model calculations should be tested experimentally. This is particularly interesting in the context of the recent interpretation of excited states in ^{110,112}Cd as a series

of rotational bands built on multiple shape coexisting states [125]. Development of a theoretical model which combines coupled particles and shape-coexisting structures may be helpful in the explanation of developing collectivity in odd-A systems.

Appendix A

Transfer-product and contaminant transitions in the Te g-factor measurements

In the transient-field g-factor measurements described in Chapter 7, transitions were seen from beam excitation, isotopic impurities in the target, and pickup reactions. Most of the observed transitions (see Table A.1) come from single-neutron pickup and isotopic impurities. The transition observed from ^{58}Ni is due to Coulomb excitation of the beam. Data sets are labelled according to the runs in Table 7.2. ^{123}Te and ^{125}Te are stable and present in small amounts in the targets. Assays of the material used in target preparation are given in Table A.2.

While ^{125}Te, and likely ^{123}Te (in trace amounts), are present in the isotopically enriched ^{126}Te target used in Run B, the observation of transitions from ^{59}Ni show that direct reactions between beam and target are occurring. Most of the transitions that are not from ^{124}Te in Run A are likely due to target impurities; no transitions from ^{59}Ni are observed in this data set. The isotopically enriched material used in the preparation of the ^{124}Te target has the largest isotopic impurities. The other odd-mass nuclides (^{127,129,131}Te, ^{131}I, ^{59}Ni) are unstable and do not occur naturally. They are therefore from reactions with the target. The contaminant transitions are most evident in the measurement of ^{130}Te. This is the least collective isotope and has the lowest Coulomb-excitation cross section, allowing other products to be observed more clearly.

Table A.1: Observed particle-γ coincident transitions from contaminants, reactions, and beam excitation. The data sets in which a transition is observed is denoted by the letter designating the run as given in Table 7.2. Level energies, and spin-parities are taken from Refs. [176; 177; 178; 179; 180; 181; 182]. Transition energies are those from the present measurements.

^{A}X	Run	I_i^π	E(I_i^π) (keV)	E(γ) (keV)	I_f^π	E(I_f^π) (keV)
^{123}Te	A	$\frac{3}{2}^+_1$	159.0	159.1	$\frac{1}{2}^+_1$	0
	A	$\frac{3}{2}^+_1$	440.0	440.1	$\frac{1}{2}^+_1$	0
	A	$(\frac{7}{2}^+_1)$	489.8	330.9	$\frac{3}{2}^+_1$	159.0
	A	$(\frac{5}{2}^+_1)$	505.4	346.4	$\frac{3}{2}^+_1$	159.0
	A	$(\frac{5}{2}^+_1)$		505.3	$\frac{1}{2}^+_1$	0
^{125}Te	A,B	$\frac{3}{2}^+_2$	443.6	408.1	$\frac{3}{2}^+_1$	35.5
	A,B	$\frac{3}{2}^+_2$		443.5	$\frac{1}{2}^+_1$	0
	A,B	$\frac{5}{2}^+_1$	463.4	427.9	$\frac{3}{2}^+_1$	35.5
	A,B	$\frac{5}{2}^+_1$		463.2	$\frac{1}{2}^+_1$	0
	B	$\frac{7}{2}^+_2$	636.1	600.9	$\frac{3}{2}^+_1$	35.5
	B	$\frac{7}{2}^+_3$	642.3	606.3	$\frac{3}{2}^+_1$	35.5
	A,B	$\frac{5}{2}^+_2$	671.4	635.8	$\frac{3}{2}^+_1$	35.5
^{127}Te	C,D	$\frac{1}{2}^+_1$	61.2	61.2	$\frac{3}{2}^+_1$	0
	C,D	$(\frac{9}{2}^-_1)$	340.9	252.7	$\frac{11}{2}^-_1$	88.2
	C,D	$\frac{5}{2}^+_1$	473.2	473.1	$\frac{3}{2}^+_1$	0
	C,D	$\frac{3}{2}^+_1$	501.9	440.7	$\frac{1}{2}^+_1$	61.2
	C,D	$\frac{3}{2}^+_1$		501.7	$\frac{3}{2}^+_1$	0
	C,D	$\frac{7}{2}^+_2$	924.0	923.6	$\frac{3}{2}^+_1$	0
^{129}Te	E,F	$\frac{1}{2}^+_1$	180.4	180.3	$\frac{3}{2}^+_1$	0
	E,F	$\frac{5}{2}^+_1$	544.6	544.4	$\frac{3}{2}^+_1$	0
	E,F	$\frac{5}{2}^+_2$	633.8	452.5	$\frac{1}{2}^+_1$	180.4
	E,F	$\frac{5}{2}^+_2$		633.2	$\frac{3}{2}^+_1$	0
	E,F	$\frac{1}{2}^+_2$	773.2	773.2	$\frac{3}{2}^+_1$	0
	E,F	$\frac{7}{2}^+_1$	813.0	812.9	$\frac{3}{2}^+_1$	0
	E,F	$\frac{3}{2}^+_2$	875.0	874.7	$\frac{3}{2}^+_1$	0

Continued on next page.

Table A.1 continued.

^{A}X	Run	I_i^π	E(I_i^π) (keV)	E(γ) (keV)	I_f^π	E(I_f^π) (keV)
	E,F	$\frac{5}{2}^+_3$	966.8	∼970	$\frac{3}{2}^+_1$	0
^{131}I	E,F	$\frac{5}{2}^+_1$	149.7	149.7	$\frac{7}{2}^+_1$	0
	F	$(\frac{3}{2}^+_1, \frac{5}{2}^+_1)$	602.0	492.5	$\frac{7}{2}^+_1$	149.7
^{58}Ni	A,B,C D,E,F	2^+_1	1454.2	∼1450	0^+_1	0
^{59}Ni	B,C D,E,F	$\frac{5}{2}^-_1$	339.4	∼338	$\frac{3}{2}^-_1$	0
	B,C D,E,F	$\frac{1}{2}^-_1$	464.9	∼460	$\frac{3}{2}^-_1$	0
	C,D E,F	$\frac{3}{2}^-_2$	878.0	∼875	$\frac{3}{2}^-_1$	0

Table A.2: Isotopic assay of materials used to create the targets in the transient-field measurements of $^{124-130}$Te.

$^{A}X_{\text{measured}}$	Target composition (%)							
	^{120}Te	^{122}Te	^{123}Te	^{124}Te	^{125}Te	^{126}Te	^{128}Te	^{130}Te
^{124}Te	<0.03	0.12	0.35	95.42	1.53	1.13	0.85	0.60
^{126}Te	<0.02	<0.02	<0.02	0.05	0.20	98.69	0.81	0.24
^{128}Te	<0.04	0.01	0.02	0.03	0.04	0.17	99.19	0.54
^{130}Te	<0.02	0.06	0.06	0.04	0.06	0.11	0.38	99.29

Appendix B

Wigner-Eckart theorem

The Wigner-Eckart theorem states that a matrix element of a spherical tensor, such as the electromagnetic transition strength, can be separated into a reduced matrix element which is independent of the magnetic substates, and a geometric component specified by an angular-momentum coupling coefficient:

$$\langle J_f M_f | T_{\lambda M} | J_i M_i \rangle = (-1)^{J_f - M_f} \begin{pmatrix} J_f & \lambda & J_i \\ -M_f & M & M_i \end{pmatrix} \langle f || T(\lambda) || i \rangle, \tag{B.1}$$

where $\langle f || T(\lambda) || i \rangle$ is the reduced matrix elements and the term in brackets is a Wigner-3j symbol.

Appendix C

Angular correlation formalism

Angular correlations from states with statistical tensor B_{kq} can be calculated using the formula

$$W(\theta_\gamma) = \sum_{kq} B_{kq}(\theta_p) Q_k F_k D^{k*}_{q0}(\Delta\phi, \theta_\gamma, 0), \tag{C.1}$$

where $D^{k*}_{q0}(\Delta\phi, \theta_\gamma, 0)$ is the Wigner D-matrix, F_k is dependent on the spins of the initial and final state and the multipolarity of the transition, and Q_k is the solid-angle attenuation coefficient.

The statistical tensors used in the calculations of the angular correlations were obtained from the de Boer-Winther code. The statistical tensors B_{kq} are obtained from the resulting statistical tensors from the calculations $\alpha^{(3)}_{kq}$ through

$$B_{kq} = \sqrt{2k+1}\rho_{kq} = \sqrt{2k+1}\frac{\alpha^{(3)}_{kq}}{\alpha^{(3)}_{00}}, \tag{C.2}$$

where α^3_{kq} is the output from the de Boer-Winther code with the z axis as the beam axis.

When a transition occurs the statistical tensors of the initial state can be propagated to obtain the statistical tensors of the fed state. To obtain the statistical tensor of the fed state the following equation was used:

$$B_{kq}(j) = B_{kq}(i) U_k(i \to j), \tag{C.3}$$

where [98]

$$U_k(J_i L_1 L_2 J_f) = \frac{1}{1+\delta^2}[u_k(J_i L_1 J_f) + \delta^2 u_k(J_i L_2 J_f)], \tag{C.4}$$

where δ is the mixing ratio of the transition and

$$u_k(J_i L_1 J_f) = (-)^{J_i + J_f - L_1}[(2J_i+1)(2J_f+1)]^{\frac{1}{2}} W(J_i J_i J_f J_f; k L_1). \tag{C.5}$$

The statistical tensors from the feeding from each higher state can then be used along with the directly excited statistical tensors to obtain an average statistical tensor used to calculate the shape of the experimental angular correlation. This calculation

occurs as

$$\langle B_{kq}(j)\rangle = \frac{N_j^0 B_{kq}(j) + \sum_{i>j,p} \prod_n N_i^0 b_{p_{n-1,n}} B_{kq}(i) U_k(p_{n-1} \to p_n)}{N_j^0 + \sum_{i>j,p} \prod_n b_{p_{n-1,n}} N_i^0}, \tag{C.6}$$

where i is the first state in the cascade, j is the final state in the cascade, p is the transition path from state i to state j and is given the subscript n to indicate the level along the path, $b_{p_{n-1,n}}$ is the branching ratio for the $n-1$ to n level step in the path, and N_i^0 is the direct population of the state i.

Appendix D

Solid attenuation coefficients

Angular correlation measurements are not performed using point-like γ-ray detectors. As such the measurement actually represents an average measurement over a range of detection angles, effectively reducing the anisotropy of the measured angular correlations. This effect is most prominent in measurements where the γ-ray detectors cover a large solid angle such as in the transient field g-factor measurements performed in the present work. A simple approximation to account for this geometrical solid angle is possible for cylindrical γ-ray detectors facing directly at the target position. This approximation was used in the angular correlation measurements used to test the validity of the calculated statistical tensors and the assumed detector positions. The so-called solid angle attenuation coefficient is given by

$$Q_k = \frac{\int_0^{\beta_{\max}} (1 - e^{-\mu x(\beta)}) P_k(\cos\beta)\, \sin\beta\, d\beta}{\int_0^{\beta_{\max}} (1 - e^{-\mu x(\beta)}) P_0(\cos\beta) \sin\beta\, d\beta}, \tag{D.1}$$

where β is the angle to the symmetry axis of the detector, P_k is the kth order Legendre polynomial, μ is the γ-ray absorption coefficient, and x is the length γ-ray detector at the angle β.

The detectors used for the g-factor measurements in the present work are not cylindrical. The cylindrical approximation is sufficient for testing the statistical tensors used in calculations, however, for the determination of the slopes used in the g-factor measurement, a the point-like angular correlations were numerically integrated over the actual detector geometry.

Bibliography

1. "Introduction and motivation," http://nucleartalent.github.io/Course2ManyBodyMethods/doc/pub/intro/html/intro.html, accessed: 04/11/2015.

2. R. Machleidt, Phys. Rev. C **63**, 024001 (2001).

3. S. G. Nilsson, *Binding states of individual nucleons in strongly deformed nuclei*, Tech. Rep. CERN-55-30. 16 (Det Kongelige Danske Videnskabernes Selskab, Matematisk-Fysiske Meddelelser, 1955).

4. J. A. Sheikh and K. Hara, Phys. Rev. Lett. **82**, 3968 (1999).

5. J. Sheikh, G. Bhat, G. Vakil, Y. Sun, and R. Palit, Phys. Rev. C **77**, 034313 (2008).

6. S. S. Tiwary, H. P. Sharma, S. Chakraborty, C. Majumder, G. H. Bhat, J. A. Sheikh, P. Baneerjee, S. Ganguly, S. Rai, Pragati, Mayank, S. Kumar, A. Kumar, S. S. Bhattacharjee, R. P. Singh, and S. Muralithar, The European Physical Journal A **55**, 163 (2019).

7. P. E. Garrett and J. L. Wood, Journal of Physics G: Nuclear and Particle Physics **37**, 064028 (2010).

8. D. Cline, Ann. Rev. Nucl. Part. Sci. , 683 (1986).

9. J. Srebrny, T. Czosnyka, C. Droste, S. Rohoziński, L. Próchniak, K. Zając, K. Pomorski, D. Cline, C. Wu, A. Bäcklin, L. Hasselgren, R. Diamond, D. Habs, H. Körner, F. Stephens, C. Baktash, and R. Kostecki, Nuclear Physics A **766**, 25 (2006).

10. P. J. Mohr, D. B. Newell, and B. N. Taylor, Rev. Mod. Phys. **88**, 035009 (2016).

11. K. S. Krane, *Introductory nuclear physics* (Wiley, New York, NY, 1988).

12. A. Bohr and B. Mottelson, *Nuclear Structure: Single-particle motion*, Nuclear Structure (W. A. Benjamin, 1969).

13. H. Morinaga and T. Yamazaki, *In-beam Gamma-ray Spectroscopy* (North-Holland Publishing Company, 1976).

14. K. Löbner, M. Vetter, and V. Hönig, Atomic Data and Nuclear Data Tables **7**, 495 (1970).

15. A. Bohr, B. Mottelson, W. B. (Firm), Ray, and C. C. S. Collection, *Nuclear Structure: Nuclear deformations*, Nuclear Structure (W. A. Benjamin, 1969).

16. L. Wilets and M. Jean, Phys. Rev. **102**, 788 (1956).

17. A. Davydov and G. Filippov, Nuclear Physics **8**, 237 (1958).

18. J. Allmond and J. Wood, Physics Letters B **767**, 226 (2017).

19. K. Hadyńska-Klęk, P. J. Napiorkowski, M. Zielińska, J. Srebrny, A. Maj, F. Azaiez, J. J. Valiente Dobón, M. Kici ńska Habior, F. Nowacki, H. Naïdja, B. Bounthong, T. R. Rodríguez, G. de Angelis, T. Abraham, G. Anil Kumar, D. Bazzacco, M. Bellato, D. Bortolato, P. Bednarczyk, G. Benzoni, L. Berti, B. Birkenbach, B. Bruyneel, S. Brambilla, F. Camera, J. Chavas, B. Cederwall, L. Charles, M. Ciemała, P. Cocconi, P. Coleman-Smith, A. Colombo, A. Corsi, F. C. L. Crespi, D. M. Cullen, A. Czermak, P. Désesquelles, D. T. Doherty, B. Dulny, J. Eberth, E. Farnea, B. Fornal, S. Franchoo, A. Gadea, A. Giaz, A. Gottardo, X. Grave, J. Grębosz, A. Görgen, M. Gulmini, T. Habermann, H. Hess, R. Isocrate, J. Iwanicki, G. Jaworski, D. S. Judson, A. Jungclaus, N. Karkour, M. Kmiecik, D. Karpiński, M. Kisieliński, N. Kondratyev, A. Korichi, M. Komorowska, M. Kowalczyk, W. Korten, M. Krzysiek, G. Lehaut, S. Leoni, J. Ljungvall, A. Lopez-Martens, S. Lunardi, G. Maron, K. Mazurek, R. Menegazzo, D. Mengoni, E. Merchán, W. Męczyński, C. Michelagnoli, B. Million, S. Myalski, D. R. Napoli, M. Niikura, A. Obertelli, S. F. Özmen, M. Palacz, L. Próchniak, A. Pullia, B. Quintana, G. Rampazzo, F. Recchia, N. Redon, P. Reiter, D. Rosso, K. Rusek, E. Sahin, M.-D. Salsac, P.-A. Söderström, I. Stefan, O. Stézowski, J. Styczeń, C. Theisen, N. Toniolo, C. A. Ur, R. Wadsworth, B. Wasilewska, A. Wiens, J. L. Wood, K. Wrzosek-Lipska, and M. Zięblíński, Phys. Rev. C **97**, 024326 (2018).

20. T. Naz, G. Bhat, S. Jehangir, S. Ahmad, and J. Sheikh, Nuclear Physics A **979**, 1 (2018).

21. J. B. Gupta and J. H. Hamilton, The European Physical Journal A **56**, 14 (2020).

22. J. Ha, T. Sumikama, F. Browne, N. Hinohara, A. M. Bruce, S. Choi, I. Nishizuka, S. Nishimura, P. Doornenbal, G. Lorusso, P.-A. Söderström, H. Watanabe, R. Daido, Z. Patel, S. Rice, L. Sinclair, J. Wu, Z. Y. Xu, A. Yagi, H. Baba, N. Chiga, R. Carroll, F. Didierjean, Y. Fang, N. Fukuda, G. Gey, E. Ideguchi, N. Inabe, T. Isobe, D. Kameda, I. Kojouharov, N. Kurz, T. Kubo, S. Lalkovski, Z. Li, R. Lozeva, H. Nishibata, A. Odahara, Z. Podolyák, P. H. Regan, O. J. Roberts, H. Sakurai, H. Schaffner, G. S. Simpson, H. Suzuki, H. Takeda, M. Tanaka, J. Taprogge, V. Werner, and O. Wieland, Phys. Rev. C **101**, 044311 (2020).

23. A. I. Levon, D. Bucurescu, C. Costache, T. Faestermann, R. Hertenberger, A. Ionescu, R. Lica, A. G. Magner, C. Mihai, R. Mihai, C. R. Nita, S. Pascu, K. P. Shevchenko, A. A. Shevchuk, A. Turturica, and H.-F. Wirth, Phys. Rev. C **100**, 034307 (2019).

24. P. E. Garrett, Journal of Physics G: Nuclear and Particle Physics **27**, R1 (2000).

25. C. Fahlander, A. Bäcklin, L. Hasselgren, A. Kavka, V. Mittal, L. Svensson, B. Varnestig, D. Cline, B. Kotlinski, H. Grein, E. Grosse, R. Kulessa, C. Michel, W. Spreng, H. Wollersheim, and J. Stachel, Nuclear Physics A **485**, 327 (1988).

26. A. Pasternak, J. Srebrny, A. Efimov, V. Mikhajlov, E. Podsvirova, C. Droste, T. Morek, S. Juutinen, G. Hagemann, M. Piiparinen, S. Törmänen, and A. Virtanen, The European Physical Journal A - Hadrons and Nuclei **13**, 435 (2002).

27. C. Mihai, A. A. Pasternak, S. Pascu, D. Filipescu, M. Ivaşcu, D. Bucurescu, G. Căta-Danil, I. Căta-Danil, D. Deleanu, D. G. Ghiţă, T. Glodariu, N. Mărginean, R. Mărginean, A. Negret, T. Sava, L. Stroe, G. Suliman, and N. V. Zamfir, Phys. Rev. C **83**, 054310 (2011).

28. T. Konstantinopoulos, P. Petkov, A. Goasduff, T. Arici, A. Astier, L. Atanasova, M. Axiotis, D. Bonatsos, P. Detistov, A. Dewald, M. J. Eller, V. Foteinou, A. Gargano, G. Georgiev, K. Gladnishki, A. Gottardo, S. Harissopulos, H. Hess, S. Kaim, D. Kocheva, A. Kusoglu, A. Lagoyannis, J. Ljungvall, R. Lutter, I. Matea, B. Melon, T. J. Mertzimekis, A. Nannini, C. M. Petrache, A. Petrovici, G. Provatas, P. Reiter, M. Rocchini, S. Roccia, M. Seidlitz, B. Siebeck, D. Suzuki, N. Warr, H. De Witte, and T. Zerrouki, Phys. Rev. C **95**, 014309 (2017).

29. A. Aprahamian, D. S. Brenner, R. F. Casten, R. L. Gill, and A. Piotrowski, Phys. Rev. Lett. **59**, 535 (1987).

30. A. Arima and F. Iachello, Annual Review of Nuclear and Particle Science **31**, 75 (1981), https://doi.org/10.1146/annurev.ns.31.120181.000451 .

31. D. Choudhury and J. Clemens, Nuclear Physics A **125**, 140 (1969).

32. Y. Varshni and S. Bose, Nuclear Physics A **144**, 645 (1970).

33. N. Kaffrell, N. Trautmann, G. Herrmann, and H. Ahrens, Phys. Rev. C **8**, 320 (1973).

34. J. J. Simpson, W. R. Dixon, and R. S. Storey, Phys. Rev. Lett. **31**, 946 (1973).

35. M. Saxena, R. Kumar, A. Jhingan, S. Mandal, A. Stolarz, A. Banerjee, R. K. Bhowmik, S. Dutt, J. Kaur, V. Kumar, M. Modou Mbaye, V. R. Sharma, and H.-J. Wollersheim, Phys. Rev. C **90**, 024316 (2014).

36. R. Casten, *Nuclear Structure from a Simple Perspective*, Oxford studies in nuclear physics (Oxford University Press, 1990).

37. N. Zamfir and R. Casten, Physics Letters B **260**, 265 (1991).

38. E. A. McCutchan, D. Bonatsos, N. V. Zamfir, and R. F. Casten, Phys. Rev. C **76**, 024306 (2007).

39. R. F. Casten, R. B. Cakirli, D. Bonatsos, and K. Blaum, Phys. Rev. C **102**, 054310 (2020).

40. K. Heyde and J. L. Wood, Rev. Mod. Phys. **83**, 1467 (2011).

41. B. Pritychenko, M. Birch, B. Singh, and M. Horoi, Atomic Data and Nuclear Data Tables **107**, 1 (2016).

42. D. Bucurescu, T. von Egidy, H.-F. Wirth, N. Mărginean, U. Köster, W. Schauer, I. Tomandl, G. Graw, A. Metz, R. Hertenberger, and Y. Eisermann, Nuclear Physics A **672**, 21 (2000).

43. H. Hua, C. Y. Wu, D. Cline, A. B. Hayes, R. Teng, R. M. Clark, P. Fallon, A. Goergen, A. O. Macchiavelli, and K. Vetter, Phys. Rev. C **69**, 014317 (2004).

44. J. A. Pinston, W. Urban, C. Droste, T. Rza ça Urban, J. Genevey, G. Simpson, J. L. Durell, A. G. Smith, B. J. Varley, and I. Ahmad, Phys. Rev. C **74**, 064304 (2006).

45. A. G. Smith, J. L. Durell, W. R. Phillips, W. Urban, P. Sarriguren, and I. Ahmad, Phys. Rev. C **86**, 014321 (2012).

46. J. Xiang, J. M. Yao, Y. Fu, Z. H. Wang, Z. P. Li, and W. H. Long, Phys. Rev. C **93**, 054324 (2016).

47. H. Abusara, S. Ahmad, and S. Othman, Phys. Rev. C **95**, 054302 (2017).

48. D. Doherty, J. Allmond, R. Janssens, W. Korten, S. Zhu, M. Zielińska, D. Radford, A. Ayangeakaa, B. Bucher, J. Batchelder, C. Beausang, C. Campbell, M. Carpenter, D. Cline, H. Crawford, H. David, J. Delaroche, C. Dickerson, P. Fallon, A. Galindo-Uribarri, F. Kondev, J. Harker, A. Hayes, M. Hendricks, P. Humby, M. Girod, C. Gross, M. Klintefjord, K. Kolos, G. Lane, T. Lauritsen, J. Libert, A. Macchiavelli, P. Napiorkowski, E. Padilla-Rodal, R. Pardo, W. Reviol, D. Sarantites, G. Savard, D. Seweryniak, J. Srebrny, R. Varner, R. Vondrasek, A. Wiens, E. Wilson, J. Wood, and C. Wu, Physics Letters B **766**, 334 (2017).

49. M. Sugawara, Phys. Rev. C **99**, 054323 (2019).

50. P.-A. Söderström, G. Lorusso, H. Watanabe, S. Nishimura, P. Doornenbal, G. Thiamova, F. Browne, G. Gey, H. S. Jung, T. Sumikama, J. Taprogge, Z. Vajta, J. Wu, Z. Y. Xu, H. Baba, G. Benzoni, K. Y. Chae, F. C. L. Crespi, N. Fukuda, R. Gernhäuser, N. Inabe, T. Isobe, A. Jungclaus, D. Kameda, G. D. Kim, Y.-K. Kim, I. Kojouharov, F. G. Kondev, T. Kubo, N. Kurz, Y. K. Kwon, G. J. Lane, Z. Li, A. Montaner-Pizá, K. Moschner, F. Naqvi, M. Niikura, H. Nishibata, A. Odahara, R. Orlandi, Z. Patel, Z. Podolyák, H. Sakurai, H. Schaffner, G. S. Simpson, K. Steiger, H. Suzuki, H. Takeda, A. Wendt, A. Yagi, and K. Yoshinaga, Phys. Rev. C **88**, 024301 (2013).

51. B. Bucher, H. Mach, A. Aprahamian, L. M. Robledo, G. S. Simpson, J. Rissanen, D. G. Ghiţă, B. Olaizola, W. Kurcewicz, J. Äystö, T. Eronen, L. M. Fraile, A. Jokinen, P. Karvonen, I. D. Moore, H. Penttilä, M. Reponen, E. Ruchowska, A. Saastamoinen, M. K. Smith, and C. Weber, Phys. Rev. C **98**, 064320 (2018).

52. S. H. Liu, J. H. Hamilton, A. V. Ramayya, A. Gelberg, L. Gu, E. Y. Yeoh, S. J. Zhu, N. T. Brewer, J. K. Hwang, Y. X. Luo, J. O. Rasmussen, W. C. Ma, A. V. Daniel, Y. T. Oganessian, and G. M. Ter-Akopian, Phys. Rev. C **84**, 014304 (2011).

53. S. Lalkovski, A. M. Bruce, A. M. Denis Bacelar, M. Górska, S. Pietri, Z. Podolyák, P. Bednarczyk, L. Caceres, E. Casarejos, I. J. Cullen, P. Doornenbal, G. F. Farrelly, A. B. Garnsworthy, H. Geissel, W. Gelletly, J. Gerl, J. Grębosz, C. Hinke, G. Ilie, D. Ivanova, G. Jaworski, S. Kisyov, I. Kojouharov, N. Kurz, N. Minkov, S. Myalski, M. Palacz, P. Petkov, W. Prokopowicz, P. H. Regan, H. Schaffner, S. Steer, S. Tashenov, P. M. Walker, and H. J. Wollersheim, Phys. Rev. C **88**, 024302 (2013).

54. R. Kumar and S. Sharma (2009) pp. 154 – 155.

55. N. Shimizu, T. Otsuka, T. Mizusaki, and M. Honma, Journal of Physics: Conference Series **20**, 65 (2005).

56. N. Shimizu, T. Otsuka, T. Mizusaki, and M. Honma, Journal of Physics: Conference Series **49**, 178 (2006).

57. B. Maheshwari, The European Physical Journal Special Topics **229**, 2485 (2020).

58. K. Kitao, Nuclear Data Sheets **75**, 99 (1995).

59. K. Kitao, Y. Tendow, and A. Hashizume, Nuclear Data Sheets **96**, 241 (2002).

60. T. Tamura, Nuclear Data Sheets **108**, 455 (2007).

61. J. Katakura and Z. Wu, Nuclear Data Sheets **109**, 1655 (2008).

62. J. Katakura and K. Kitao, Nuclear Data Sheets **97**, 765 (2002).

63. Z. Elekes and J. Timar, Nuclear Data Sheets **129**, 191 (2015).

64. B. Singh, Nuclear Data Sheets **93**, 33 (2001).

65. Y. Khazov, A. Rodionov, S. Sakharov, and B. Singh, Nuclear Data Sheets **104**, 497 (2005).

66. A. Sonzogni, Nuclear Data Sheets **103**, 1 (2004).

67. E. Mccutchan, Nuclear Data Sheets **152**, 331 (2018).

68. S. F. Hicks, J. R. Vanhoy, P. G. Burkett, B. R. Champine, S. J. Etzkorn, P. E. Garrett, S. W. Yates, and M. Yeh, Phys. Rev. C **95**, 034322 (2017).

69. C. Qi, Phys. Rev. C **94**, 034310 (2016).

70. T. von Egidy, C. Doll, J. Jolie, N. Warr, J. Kern, M. Crittin, and L. Genilloud, Nuclear Physics A **714**, 355 (2003).

71. B. Fogelberg, C. Stone, R. Gill, H. Mach, D. Warner, A. Aprahamian, and D. Rehfield, Nuclear Physics A **451**, 104 (1986).

72. J. Kotila, J. Suhonen, and D. S. Delion, Phys. Rev. C **68**, 014307 (2003).

73. J. Kumpulainen, R. Julin, J. Kantele, A. Passoja, W. H. Trzaska, E. Verho, J. Väärämäki, D. Cutoiu, and M. Ivascu, Phys. Rev. C **45**, 640 (1992).

74. D. Bandyopadhyay, C. C. Reynolds, S. R. Lesher, C. Fransen, N. Boukharouba, M. T. McEllistrem, and S. W. Yates, Phys. Rev. C **68**, 014324 (2003).

75. M. Kadi, N. Warr, P. E. Garrett, J. Jolie, and S. W. Yates, Phys. Rev. C **68**, 031306 (2003).

76. P. E. Garrett, K. L. Green, H. Lehmann, J. Jolie, C. A. McGrath, M. Yeh, and S. W. Yates, Phys. Rev. C **75**, 054310 (2007).

77. S. K. Chamoli, A. E. Stuchbery, S. Frauendorf, J. Sun, Y. Gu, R. F. Leslie, P. T. Moore, A. Wakhle, M. C. East, T. Kibédi, and A. N. Wilson, Phys. Rev. C **83**, 054318 (2011).

78. P. E. Garrett, J. Bangay, A. Diaz Varela, G. C. Ball, D. S. Cross, G. A. Demand, P. Finlay, A. B. Garnsworthy, K. L. Green, G. Hackman, C. D. Hannant, B. Jigmeddorj, J. Jolie, W. D. Kulp, K. G. Leach, J. N. Orce, A. A. Phillips, A. J. Radich, E. T. Rand, M. A. Schumaker, C. E. Svensson, C. Sumithrarachchi, S. Triambak, N. Warr, J. Wong, J. L. Wood, and S. W. Yates, Phys. Rev. C **86**, 044304 (2012).

79. L. Próchniak, P. Quentin, and M. Imadalou, International Journal of Modern Physics E **21**, 1250036 (2012), https://doi.org/10.1142/S021830131250036X .

80. J. C. Batchelder, N. T. Brewer, R. E. Goans, R. Grzywacz, B. O. Griffith, C. Jost, A. Korgul, S. H. Liu, S. V. Paulauskas, E. H. Spejewski, and D. W. Stracener, Phys. Rev. C **86**, 064311 (2012).

81. J. C. Batchelder, N. T. Brewer, C. J. Gross, R. Grzywacz, J. H. Hamilton, M. Karny, A. Fijalkowska, S. H. Liu, K. Miernik, S. W. Padgett, S. V. Paulaskas, K. P. Rykaczewski, A. V. Ramayya, D. W. Stracener, and M. Wolinska-Cichocka, Phys. Rev. C **89**, 054321 (2014).

82. A. E. Stuchbery, S. K. Chamoli, and T. Kibédi, Phys. Rev. C **93**, 031302 (2016).

83. T. Schmidt, K. L. G. Heyde, A. Blazhev, and J. Jolie, Phys. Rev. C **96**, 014302 (2017).

84. K. Nomura and J. Jolie, Phys. Rev. C **98**, 024303 (2018).

85. B. J. Coombes, A. E. Stuchbery, A. Blazhev, H. Grawe, M. W. Reed, A. Akber, J. T. H. Dowie, M. S. M. Gerathy, T. J. Gray, T. Kibédi, A. J. Mitchell, and T. Palazzo, Phys. Rev. C **100**, 024322 (2019).

86. P. E. Garrett, T. R. Rodríguez, A. Diaz Varela, K. L. Green, J. Bangay, A. Finlay, R. A. E. Austin, G. C. Ball, D. S. Bandyopadhyay, V. Bildstein, S. Colosimo, D. S. Cross, G. A. Demand, P. Finlay, A. B. Garnsworthy, G. F. Grinyer, G. Hackman, B. Jigmeddorj, J. Jolie, W. D. Kulp, K. G. Leach, A. C. Morton, J. N. Orce, C. J. Pearson, A. A. Phillips, A. J. Radich, E. T. Rand, M. A. Schumaker, C. E. Svensson, C. Sumithrarachchi, S. Triambak, N. Warr, J. Wong, J. L. Wood, and S. W. Yates, Phys. Rev. C **101**, 044302 (2020).

87. E. A. Coello Pérez and T. Papenbrock, Phys. Rev. C **92**, 064309 (2015).

88. A. Leviatan, N. Gavrielov, J. E. García-Ramos, and P. Van Isacker, Phys. Rev. C **98**, 031302 (2018).

89. N. Stone, Atomic Data and Nuclear Data Tables **111-112**, 1 (2016).

90. J. Blachot, Nuclear Data Sheets **110**, 1239 (2009).

91. J. Blachot, Nuclear Data Sheets **109**, 1383 (2008).

92. S. Kumar, J. Chen, and F. Kondev, Nuclear Data Sheets **137**, 1 (2016).

93. J. Blachot, Nuclear Data Sheets **111**, 1471 (2010).

94. J. Blachot, Nuclear Data Sheets **113**, 2391 (2012).

95. K. Alder and A. Winther, *Electromagnetic Excitation* (North-Holland, 1975).

96. D. Cline, T. Czosnyka, A. B. Hayes, P. Napiorkowski, N. Warr, and C. Y. Wu, "Gosia user manual for simulation and analysis of coulomb excitation experiments," (2012).

97. A. E. Stuchbery and M. P. Robinson, Nuclear Instruments and Methods in Physics Research Section A: Accelerators, Spectrometers, Detectors and Associated Equipment **485**, 753 (2002).

98. T. Yamazaki, Nuclear Data Sheets. Section A **3**, 1 (1967).

99. N. K. B. Shu, D. Melnik, J. M. Brennan, W. Semmler, and N. Benczer-Koller, Phys. Rev. C **21**, 1828 (1980).

100. A. E. Stuchbery, C. G. Ryan, H. H. Bolotin, and S. H. Sie, Phys. Rev. C **23**, 1618 (1981).

101. A. E. Stuchbery, A. Nakamura, A. N. Wilson, P. M. Davidson, H. Watanabe, and A. I. Levon, Phys. Rev. C **76**, 034306 (2007).

102. A. Blaugrund, Nuclear Physics **88**, 501 (1966).

103. J. F. Ziegler, M. Ziegler, and J. Biersack, Nuclear Instruments and Methods in Physics Research Section B: Beam Interactions with Materials and Atoms **268**, 1818 (2010), 19th International Conference on Ion Beam Analysis.

104. XIA, "Pixie-16 data sheet," (2019).

105. T. Vidmar, M. Korun, and A. Likar, Nuclear Instruments and Methods in Physics Research Section A: Accelerators, Spectrometers, Detectors and Associated Equipment **508**, 404 (2003).

106. J. F. Ziegler, U. Littmark, and J. P. Biersack, *The stopping and range of ions in solids* (Pergamon New York, 1985) p. 321.

107. T. Kibédi, T. Burrows, M. Trzhaskovskaya, P. Davidson, and C. Nestor, Nuclear Instruments and Methods in Physics Research Section A: Accelerators, Spectrometers, Detectors and Associated Equipment **589**, 202 (2008).

108. M. Esat, D. Kean, R. Spear, and A. Baxter, Nuclear Physics A **274**, 237 (1976).

109. K. P. Singh, D. C. Tayal, G. Singh, and H. S. Hans, Phys. Rev. C **31**, 79 (1985).

110. D. Eccleshall, B. Hinds, M. Yates, and N. Macdonald, Nuclear Physics **37**, 377 (1962).

111. F. McGowan, R. Robinson, P. Stelson, and J. Ford, Nuclear Physics **66**, 97 (1965).

112. W. Milner, F. McGowan, P. Stelson, R. Robinson, and R. Sayer, Nuclear Physics A **129**, 687 (1969).

113. S. Steadman, A. Kleinfeld, G. Seaman, J. De Boer, and D. Ward, Nuclear Physics A **155**, 1 (1970).

114. W. A. Gillespie, M. W. S. Macauley, A. Johnston, E. W. Lees, and R. P. Singhal, Journal of Physics G: Nuclear Physics **3**, L169 (1977).

115. K. Krane, Applied Radiation and Isotopes **105**, 278 (2015).

116. D. S. Andreev, A. P. Grinberg, K. I. Erokhina, V. S. Zvonov, and I. K. Lemberg, Izv.Akad.Nauk **SSSR**, Ser.Fiz. 36, 2172 (1972).

117. G. Savard, S. Baker, C. Davids, A. Levand, E. Moore, R. Pardo, R. Vondrasek, B. Zabransky, and G. Zinkann, Nuclear Instruments and Methods in Physics Research Section B: Beam Interactions with Materials and Atoms **266**, 4086 (2008), proceedings of the XVth International Conference on Electromagnetic Isotope Separators and Techniques Related to their Applications.

118. I. Lee, R. Clark, M. Cromaz, M. Deleplanque, M. Descovich, R. Diamond, P. Fallon, A. Macchiavelli, F. Stephens, and D. Ward, Nuclear Physics A **746**, 255 (2004), proceedings of the Sixth International Conference on Radioactive Nuclear Beams (RNB6).

119. C. Wu, D. Cline, A. Hayes, R. Flight, A. Melchionna, C. Zhou, I. Lee, D. Swan, R. Fox, and J. Anderson, Nuclear Instruments and Methods in Physics Research Section A: Accelerators, Spectrometers, Detectors and Associated Equipment **814**, 6 (2016).

120. K. A. Baskova, A. B. Vovk, T. M. Gerus, L. I. Gorov, A. M. Demidov, and V. A. Kurkin, *Study of γ-Rays from ^{111}Cd and ^{113}Cd from the Reactions (n, n'γ) and (n-bar(res), γ)*, Tech. Rep. IAE-4544/2 (1987).

121. Z. S. Nemeth, KFK **4888** (1991).

122. B. Rosner, Phys. Rev. **136**, B664 (1964).

123. T. Belgya, G. Molnár, and S. Yates, Nuclear Physics A **607**, 43 (1996).

124. N. Wang, F. A. Rickey, G. S. Samudra, P. C. Simms, and S. Zeghib, Phys. Rev. C **37**, 613 (1988).

125. P. E. Garrett, T. R. Rodríguez, A. D. Varela, K. L. Green, J. Bangay, A. Finlay, R. A. E. Austin, G. C. Ball, D. S. Bandyopadhyay, V. Bildstein, S. Colosimo, D. S. Cross, G. A. Demand, P. Finlay, A. B. Garnsworthy, G. F. Grinyer, G. Hackman, B. Jigmeddorj, J. Jolie, W. D. Kulp, K. G. Leach, A. C. Morton, J. N. Orce, C. J. Pearson, A. A. Phillips, A. J. Radich, E. T. Rand, M. A. Schumaker, C. E. Svensson, C. Sumithrarachchi, S. Triambak, N. Warr, J. Wong, J. L. Wood, and S. W. Yates, Phys. Rev. Lett. **123**, 142502 (2019).

126. N. Shimizu, (2013), arXiv:1310.5431 [nucl-th] .

127. O. Kavatsyuk, C. Mazzocchi, Z. Janas, A. Banu, L. Batist, F. Becker, A. Blazhev, W. Brüchle, J. Döring, T. Faestermann, M. Górska, H. Grawe, A. Jungclaus, M. Karny, M. Kavatsyuk, O. Klepper, R. Kirchner, M. La Commara, K. Miernik, I. Mukha, C. Plettner, A. Płochocki, E. Roeckl, M. Romoli, K. Rykaczewski, M. Schädel, K. Schmidt, R. Schwengner, and J. Żylicz, Eur. Phys. J. A **31**, 319 (2007).

128. T. Faestermann, M. Górska, and H. Grawe, Prog. Part. Nucl. Phys. **69**, 85 (2013).

129. J. Park, R. Krücken, D. Lubos, R. Gernhäuser, M. Lewitowicz, S. Nishimura, D. S. Ahn, H. Baba, B. Blank, A. Blazhev, P. Boutachkov, F. Browne, I. Čeliković, G. de France, P. Doornenbal, T. Faestermann, Y. Fang, N. Fukuda, J. Giovinazzo, N. Goel, M. Górska, H. Grawe, S. Ilieva, N. Inabe, T. Isobe, A. Jungclaus, D. Kameda, G. D. Kim, Y.-K. Kim, I. Kojouharov, T. Kubo, N. Kurz, G. Lorusso, K. Moschner, D. Murai, I. Nishizuka, Z. Patel, M. M. Rajabali, S. Rice, H. Sakurai, H. Schaffner, Y. Shimizu, L. Sinclair, P.-A. Söderström, K. Steiger, T. Sumikama, H. Suzuki, H. Takeda, Z. Wang, H. Watanabe, J. Wu, and Z. Y. Xu, Phys. Rev. C **96**, 044311 (2017).

130. D. T. Yordanov, D. L. Balabanski, M. L. Bissell, K. Blaum, A. Blazhev, I. Budinčević, N. Frömmgen, C. Geppert, H. Grawe, M. Hammen, K. Kreim, R. Neugart, G. Neyens, and W. Nörtershäuser, Phys. Rev. C **98**, 011303 (2018).

131. R. Machleidt, F. Sammarruca, and Y. Song, Phys. Rev. C **53**, R1483 (1996).

132. M. Hjorth-Jensen, T. T. Kuo, and E. Osnes, Physics Reports **261**, 125 (1995).

133. M. Hjorth-Jensen, (To be published).

134. P. Sarriguren, Phys. Rev. C **100**, 054306 (2019).

135. A. Stuchbery, J. Allmond, M. Danchev, C. Baktash, C. Bingham, A. Galindo-Uribarri, D. Radford, N. Stone, and C. Yu, Phys. Rev. C **96**, 014321 (2017).

136. E. E. Peters, A. E. Stuchbery, A. Chakraborty, B. P. Crider, S. F. Ashley, A. Kumar, M. T. McEllistrem, F. M. Prados-Estévez, and S. W. Yates, Phys. Rev. C **99**, 064321 (2019).

137. G. Jakob, N. Benczer-Koller, G. Kumbartzki, J. Holden, T. J. Mertzimekis, K.-H. Speidel, R. Ernst, A. E. Stuchbery, A. Pakou, P. Maier-Komor, A. Macchiavelli, M. McMahan, L. Phair, and I. Y. Lee, Phys. Rev. C **65**, 024316 (2002).

138. E. Teruya, N. Yoshinaga, K. Higashiyama, and A. Odahara, Phys. Rev. C **92**, 034320 (2015).

139. A. Stuchbery, A. Harding, D. Weisser, and N. Lobanov, Nuclear Instruments and Methods in Physics Research Section A: Accelerators, Spectrometers, Detectors and Associated Equipment **951**, 162985 (2020).

140. C. Gross, T. Ginter, D. Shapira, W. Milner, J. McConnell, A. James, J. Johnson, J. Mas, P. Mantica, R. Auble, J. Das, J. Blankenship, J. Hamilton, R. Robinson, Y. Akovali, C. Baktash, J. Batchelder, C. Bingham, M. Brinkman, H. Carter, R. Cunningham, T. Davinson, J. Fox, A. Galindo-Uribarri, R. Grzywacz, J. Liang, B. MacDonald, J. MacKenzie, S. Paul, A. Piechaczek, D. Radford, A. Ramayya, W. Reviol, D. Rudolph, K. Rykaczewski, K. Toth, W. Weintraub, C. Williams, P. Woods, C.-H. Yu, and E. Zganjar, Nuclear Instruments and Methods in Physics Research Section A: Accelerators, Spectrometers, Detectors and Associated Equipment **450**, 12 (2000).

141. K. Alder and A. Winther, *Coulomb Excitation: A Collection of Reprints*, Perspectives in Physics. A Series of Reprint Collections (Academic Press, 1966).

142. C. Stahl, J. Leske, M. Lettmann, and N. Pietralla, Computer Physics Communications **214**, 174 (2017).

143. A. Garzón, W. Rodriguez, F. Cristancho, and M. Tao, Computer Physics Communications **246**, 106854 (2020).

144. J. C. Wells and N. R. Johnson, *LINESHAPE: A Computer Program for Doppler Broadened Lineshape Analysis*, Tech. Rep. (1991).

145. J. M. Allmond, A. E. Stuchbery, C. Baktash, A. Gargano, A. Galindo-Uribarri, D. C. Radford, C. R. Bingham, B. A. Brown, L. Coraggio, A. Covello, M. Danchev, C. J. Gross, P. A. Hausladen, N. Itaco, K. Lagergren, E. Padilla-Rodal, J. Pavan, M. A. Riley, N. J. Stone, D. W. Stracener, R. L. Varner, and C.-H. Yu, Phys. Rev. Lett. **118**, 092503 (2017).

146. Y. Larochelle, A. Galindo-Uribarri, C. Baktash, W. Bennet, C. J. Gross, J. Johnson, J. Mas, J. McConnell, D. C. Radford, E. Padilla, and S. Pascual, in *APS April Meeting Abstracts*, APS Meeting Abstracts (2002) p. E10.001.

147. M. Macfarlane, S. Pieper, and A. N. L. P. Division, *PTOLEMY, a Program for Heavy-ion Direct-reaction Calculations* (Department of Energy [Office of Energy Research], Argonne National Laboratory, 1978).

148. F. Bosch and H. Spehl, Zeitschrift für Physik A Hadrons and Nuclei **280**, 329 (1977).

149. A. Abragam and R. V. Pound, Phys. Rev. **92**, 943 (1953).

150. T. Burrows, Nuclear Data Sheets **107**, 1747 (2006).

151. T. Churchill, "Investigation of tellurium-130 nuclear structure using inelastic neutron scattering," U.S.N.A., Trident Scholar Report (2003).

152. S. F. Hicks, A. E. Stuchbery, T. Churchill, D. Banyopadhyay, B. R. Champine, B. J. Coombes, C. M. Davoren, J. C. Ellis, W. M. Faulkner, S. R. Lesher, J. M. Mueller, S. Mukhopadhyay, N. Orce, M. D. Skubis, J. R. Vanhoy, and S. W. Yates, (To be published).

153. J. R. Vanhoy, J. A. Tanyi, K. A. Crandell, T. H. Churchill, S. F. Hicks, M. C. Burns, P. A. Roddy, N. V. Warr, T. B. Brown, and S. R. Lesher, Phys. Rev. C **69**, 064323 (2004).

154. S. F. Hicks, J. R. Vanhoy, and S. W. Yates, Phys. Rev. C **78**, 054320 (2008).

155. R. Stokstad and I. Hall, Nuclear Physics A **99**, 507 (1967).

156. M. Zielińska, L. P. Gaffney, K. Wrzosek-Lipska, E. Clément, T. Grahn, N. Kesteloot, P. Napiorkowski, J. Pakarinen, P. Van Duppen, and N. Warr, The European Physical Journal A **52**, 99 (2016).

157. B. A. Brown, N. J. Stone, J. R. Stone, I. S. Towner, and M. Hjorth-Jensen, Phys. Rev. C **71**, 044317 (2005).

158. L. Coraggio, L. De Angelis, T. Fukui, A. Gargano, and N. Itaco, Phys. Rev. C **95**, 064324 (2017).

159. D. C. Radford, C. Baktash, C. J. Barton, J. Batchelder, J. R. Beene, C. R. Bingham, M. A. Caprio, M. Danchev, B. Fuentes, A. Galindo-Uribarri, J. Gomez del Campo, C. J. Gross, M. L. Halbert, D. J. Hartley, P. Hausladen, J. K. Hwang, W. Krolas, Y. Larochelle, J. F. Liang, P. E. Mueller, E. Padilla, J. Pavan, A. Piechaczek, D. Shapira, D. W. Stracener, R. L. Varner, A. Woehr, C. H. Yu, and N. V. Zamfir, The European Physical Journal A - Hadrons and Nuclei **25**, 383 (2005).

160. A. E. Stuchbery, AIP Conference Proceedings **1625**, 52 (2014), https://aip.scitation.org/doi/pdf/10.1063/1.4901764 .

161. C. Goodin, N. J. Stone, A. V. Ramayya, A. V. Daniel, J. R. Stone, J. H. Hamilton, K. Li, J. K. Hwang, Y. X. Luo, J. O. Rasmussen, A. Gargano, A. Covello, and G. M. Ter-Akopian, Phys. Rev. C **78**, 044331 (2008).

162. A. Wolf and E. Cheifetz, Phys. Rev. Lett. **36**, 1072 (1976).

163. N. Stone, INDC(NDS)-0816 (2020).

164. P. F. Mantica, A. E. Stuchbery, D. E. Groh, J. I. Prisciandaro, and M. P. Robinson, Phys. Rev. C **63**, 034312 (2001).

165. O. Häusser, I. Towner, T. Faestermann, H. Andrews, J. Beene, D. Horn, D. Ward, and C. Broude, Nuclear Physics A **293**, 248 (1977).

166. T. Faestermann, F. Feilitzsch, R. S. Raghavan, C. Signorini, T. Yamazaki, C. V. K. Baba, D. B. Fossan, and D. Proetel, Zeitschrift für Physik A Atoms and Nuclei **273**, 157 (1975).

167. D. Bazzacco, F. Brandolini, K. Löwenich, P. Pavan, C. Rossi-Alvarez, E. Maglione, M. de Poli, and A. Haque, Nuclear Physics A **533**, 541 (1991).

168. J. Holden, N. Benczer-Koller, G. Jakob, G. Kumbartzki, T. J. Mertzimekis, K.-H. Speidel, C. W. Beausang, R. Krücken, A. Macchiavelli, M. McMahan, L. Phair, A. E. Stuchbery, P. Maier-Komor, W. Rogers, and A. D. Davies, Phys. Rev. C **63**, 024315 (2001).

169. H. K. Wang, S. K. Ghorui, Z. Q. Chen, and Z. H. Li, Phys. Rev. C **102**, 054316 (2020).

170. J. Henderson, Phys. Rev. C **102**, 054306 (2020).

171. N. Stone, *Table of Nuclear Electric Quadrupole Moments*, Tech. Rep. INDC(NDS)–0650 (2013).

172. J. Delaroche, M. Girod, J. Libert, H. Goutte, S. Hilaire, S. Péru, N. Pillet, and G. F. Bertsch, Phys. Rev. C **81**, 014303 (2010).

173. S. Peru and M. Martini, The European Physical Journal A **50** (2014), 10.1140/epja/i2014-14088-7.

174. H. L. Crawford, P. Fallon, A. O. Macchiavelli, A. Poves, V. M. Bader, D. Bazin, M. Bowry, C. M. Campbell, M. P. Carpenter, R. M. Clark, M. Cromaz, A. Gade, E. Ideguchi, H. Iwasaki, C. Langer, I. Y. Lee, C. Loelius, E. Lunderberg, C. Morse, A. L. Richard, J. Rissanen, D. Smalley, S. R. Stroberg, D. Weisshaar, K. Whitmore, A. Wiens, S. J. Williams, K. Wimmer, and T. Yamamato, Phys. Rev. C **93**, 031303 (2016).

175. B. Maheshwari, H. A. Kassim, N. Yusof, and A. K. Jain, Nuclear Physics A **992**, 121619 (2019).

176. S. Ohya, Nuclear Data Sheets **102**, 547 (2004).

177. J. Katakura, Nuclear Data Sheets **112**, 495 (2011).

178. A. Hashizume, Nuclear Data Sheets **112**, 1647 (2011).

179. J. Timar, Z. Elekes, and B. Singh, Nuclear Data Sheets **121**, 143 (2014).

180. Y. Khazov, I. Mitropolsky, and A. Rodionov, Nuclear Data Sheets **107**, 2715 (2006).

181. C. D. Nesaraja, S. D. Geraedts, and B. Singh, Nuclear Data Sheets **111**, 897 (2010).

182. M. S. Basunia, Nuclear Data Sheets **151**, 1 (2018).